

**The Preparation and Reactivity of Epitaxially  
Grown Iron Oxide Films: A Surface Science  
Investigation**

**Surin Saipanya PhD**

December 2007

**School of Chemistry, Cardiff University**

UMI Number: U584236

All rights reserved

INFORMATION TO ALL USERS

The quality of this reproduction is dependent upon the quality of the copy submitted.

In the unlikely event that the author did not send a complete manuscript and there are missing pages, these will be noted. Also, if material had to be removed, a note will indicate the deletion.



UMI U584236

Published by ProQuest LLC 2013. Copyright in the Dissertation held by the Author.  
Microform Edition © ProQuest LLC.

All rights reserved. This work is protected against  
unauthorized copying under Title 17, United States Code.



ProQuest LLC  
789 East Eisenhower Parkway  
P.O. Box 1346  
Ann Arbor, MI 48106-1346



## Declaration

I hereby declare that the work contained in this thesis is the result of my own personnel investigations, and that the results have not been previously accepted in substance for any degree or being currently in candidature for any degree

Signed.....*S. Saipanya*.....

S. Saipanya (Candidate)

Witnessed.....*A. F. Carley*.....

Dr. A. F. Carley (Supervisor)

Witnessed.....*P. R. Davies*.....

Dr. P. R. Davies (Supervisor)

I hereby give my consent that this thesis, if successful, may be made available for inter-library loan or photocopying, and that the title and abstract may be made available to outside organizations.

Signed.....*S. Saipanya*.....

S. Saipanya (Candidate)

## Abstract

The preparation and reactivity of epitaxially grown iron oxides on a Cu(100) substrate have been studied. An Fe adlayer grew epitaxially on the substrate with 2 domains with a square unit cell of sides 2.55 Å and 3.61 Å. The oxide is prepared by oxidizing Fe multilayers at temperature 850 K using a high and low heating rate. A low heating rate gives a thick film (10-14 Å) while a high heating rate gives a thinner (3-5 Å) film. Both conditions give a well-ordered surface. However, the Cu substrate was not oxidized in this low-pressure/high-temperature oxidation treatment. Fe<sub>3</sub>O<sub>4</sub>(100) and (111) surfaces are identified by the chemical composition of the surface from XP spectra and features of LEED and STM images such as the excellent long-range epitaxy, antiphase domain boundary strips and hexagonal superstructures.

Au clusters were vapor-deposited on iron oxide Fe<sub>3</sub>O<sub>4</sub>, oxidized Cu and clean Cu surfaces. It was found that the clusters grow in a 3D mode (Stranski-Krastanov) on the oxidized substrate but in a layer-by-layer mode (Frank van der Merwe) on clean Cu. On the iron oxide the Au nanoparticles have an average diameter of 30-50 Å and are ~10 Å high. Annealing experiments show that the Au clusters are rather stable in the system and form well-defined hexagonal microcrystals. STS showed that the Au clusters on the oxide substrate show nonmetallic properties. LEED and STM show that Au grows epitaxially on clean Cu.

Iron oxide (Fe<sub>3</sub>O<sub>4</sub>) and Au modified iron oxide surfaces were used for studies of the chemistry of acrylic acid, CO<sub>2</sub>-rich CO<sub>2</sub>-O<sub>2</sub> mixtures and NH<sub>3</sub>-rich NH<sub>3</sub>-O<sub>2</sub> mixtures at room temperature. The adsorption of acrylic acid on thin and thick iron oxide surfaces and Au modified thin and thick iron oxide surfaces resulted in carboxylate formation and vinyl adsorption together with the desorption of CO<sub>2</sub> and ethylene at 500 K. Au nanoparticles on the oxide did not enhance the acid reaction on the surface.

However, Au clusters on oxide films increased the surface reaction of small molecules such as CO<sub>2</sub> (acid) and NH<sub>3</sub> (base). STM results show the edges of the iron oxide islands and the top of Au nanoparticles are more reactive as their rims turn uneven after adsorption.

## **Acknowledgements**

I would like to show my appreciation to the following persons:

Dr. A. F. Carley and P. R. Davies, my supervisors, for giving me the opportunity to study postgraduate research. Also for their continued support and advice throughout my time spent at Cardiff and for being patient to understand my English with a Thai accent.

Ministry of Science and Technology, Thailand for their financial support and providing me with the chance to undertake this research.

To the guys in the lab who made working a lot easier, more interesting and more fun. Particular thanks are owed to Dr. D. J. Morgan for his constant enthusiasm, excellent technical assistance, computer software, ever present willingness to help in any way possible and his frequently funny jokes.

Many thanks go to students; in particular my Thai friends and Sharon Huxter in Cardiff who have helped keep a healthy balance between study and play.

Lastly I would like to thank those closest to me. Chartklar, your love and support means everything to me. To my family in particular my mom, dad and Khun Yaai Ruang-rueng's family (in Khlong-Poh, Uttaradit), my never-ending thanks. You always support me in what way I have done. I could not have done it without you.

# **Contents**

## **Chapter 1**

### **Introduction to Surfaces**

1.1 Surface sites	1
1.2 Relaxation and reconstruction of surfaces	1
1.3 Catalysis and surfaces	2
1.4 Adsorption on surfaces	3
1.5 Stress and strain	3
1.6 Type of Interfaces	4
1.7 Solid-on-solid growth	4
1.8 Nonequilibrium growth modes	6
References	8

## **Chapter 2**

### **Experimental Details**

2.1 Introduction: spectroscopic techniques for surfaces studies	9
2.2 X-ray Photoelectron spectroscopy (XPS)	9
2.2.1 Introduction	9
2.2.2 The basic principles	10
2.2.3 Photoemission process	11
2.2.3.1 Primary process	12
2.2.3.2 Secondary process or fate of the core-hole	12
2.2.3.3 Final state effects	14
2.2.3.4 Chemical Shift in XPS	16
2.3.4 Chemical Analysis by XPS	17
2.3.5 X-ray photoelectron spectrometer	22
2.3 Low energy electron diffraction (LEED)	25
2.3.1 Real lattices and reciprocal lattices	27
2.3.2 Diffraction and Ewald sphere construction	28
2.3.3 Surface structures and notation	32
2.3.4 Overlayer structures	33

2.3.5 Overlayer structure interpretation from LEED	36
diffraction patterns	
2.3.6 LEED instrument	38
2.4 Scanning Tunneling Microscopy (STM)	39
2.4.1 Introduction	39
2.4.2 Basic principles of solid	40
2.4.3 Principles of STM operation	42
2.4.4 Scanning tunneling spectroscopy (STS)	45
2.4.5 Instrumentation for Scanning Tunneling Microscopy	47
2.4.6 Tip preparation	50
2.5 Ultrahigh vacuum techniques	50
2.5.1. Principles of ultrahigh vacuum techniques	50
2.5.2 Vacuum requirement for analysis equipment	52
2.5.3 Pumps for UHV	52
2.5.4 Pressure measurement	55
2.5.5 Material and construction for UHV system	57
2.5.6 Chemical analysis of the gas in the system	57
2.6 Instrumentals in experiments	59
2.6.1 Components of the machine	59
References	61

## **Chapter 3**

### **Iron Oxide Thin Film**

3.1 Introduction iron-oxide crystal structures	63
3.2 Literature reviews of iron oxide preparation in ultra high vacuum	69
3.3 Experimental details	70
3.4 Result and discussion	71
3.4.1 Fe on Cu:	71
Characterization of Fe film on Cu(100) by XPS, LEED, STM	
3.4.2 Thin iron oxide preparation	79
3.4.2.1 Characterisation of iron oxide by XPS	79
3.4.2.2 Characterisation of iron oxide by LEED	82
3.4.2.3 Characterization of iron oxide by STM	91

3.4.3 Characterization of thick iron oxide	107
3.5 Conclusions	109
References	112

## **Chapter 4**

### **Gold Nanoparticles Deposited on Iron Oxide**

4.1 Introduction to gold nanoparticles deposited on iron oxide	114
4.2 Literature reviews: Au nanoparticles supported on substrates	115
4.3 Experimental details	116
4.4 Characterization of Au deposited on iron oxide films	116
4.4.1 Characterization of Au deposited on thin iron oxide films (~5 Å thick)	117
4.4.1.1 XPS results	117
4.4.1.2 STM results	118
4.4.2 Characterization of Au on thick iron oxide film (10-15 Å)	124
4.4.2.1 XPS results	124
4.4.2.2 LEED results	124
4.4.2.3 STM results	126
4.5 Characterization of Au on an oxidized Cu surface	132
4.5.1 XPS results	132
4.5.2 LEED results	133
4.5.3 STM results for oxidized Cu	135
4.5.4 STM results for Au deposited on oxidized Cu(100) surface	136
4.6 Characterization of Au on a clean Cu(100) surface	142
4.6.1 XPS results	142
4.6.2 LEED results	143
4.6.3 STM results	144
4.7 Conclusion	145
References	148

## Chapter 5

### Reactions on iron oxide surfaces

5.1 Introduction to reactions on iron oxide surfaces	149
5.2 Literature review of reactions on iron oxide surfaces	149
5.3 Reaction of acrylic acid on thin iron oxide ( $\text{Fe}_3\text{O}_4$ , 3-4 Å) and thick iron oxide ( $\text{Fe}_3\text{O}_4$ , 7-14 Å)	152
5.3.1 Introduction	152
5.3.2 Experimental details	152
5.3.3 Reaction of acrylic acid on a thin iron oxide surface ( $\text{Fe}_3\text{O}_4$ , 3-4 Å)	153
5.3.3.1 XPS results	153
5.3.3.2 LEED results	157
5.3.3.3 STM results	157
5.3.4 Reaction of acrylic acid on thick iron oxide ( $\text{Fe}_3\text{O}_4$ , 7-14 Å)	162
5.4 Reaction of acrylic acid on thin and thick iron oxide films in the presence of Au nanoparticles	168
5.4.1 Reaction of acrylic acid on thin iron oxide supported Au nanoparticles	168
5.4.2 Reaction of acrylic acid on thick iron oxide supported Au nanoparticles	169
5.5 Reaction of iron oxide and Au modified iron oxide surfaces with $\text{CO}_2$	173
5.5.1 Introduction and literature review	173
5.5.2 Experimental details	175
5.5.3 Results and discussion	175
5.5.3.1 Reaction of iron oxide surfaces with $\text{CO}_2$ rich $\text{CO}_2$ - $\text{O}_2$ mixtures	176
5.5.3.2 Reaction of Au modified iron oxide surface with $\text{CO}_2$ rich $\text{CO}_2$ - $\text{O}_2$ mixtures	179
5.5.3.3 Reaction of regenerated thick iron oxide surface with $\text{CO}_2$ rich $\text{CO}_2$ - $\text{O}_2$ mixtures	181

5.6 Reaction of iron oxide and Au modified iron oxide surfaces with NH <sub>3</sub>	184
5.6.1 Introduction	184
5.6.2 Experimental details	184
5.6.3 Reaction of iron oxide with NH <sub>3</sub> -rich NH <sub>3</sub> -O <sub>2</sub> mixtures	185
5.6.4 Reaction of Au modified iron oxide surfaces with NH <sub>3</sub> -rich NH <sub>3</sub> -O <sub>2</sub> mixtures	188
5.7 Conclusions	191
References	192

## Chapter 6

### Conclusion

Conclusion	194
------------	-----



## Chapter 1

### Introduction to Surfaces

Surfaces are important in many ways to everyday life, for example they are important in sensors, corrosion, electronic device technology, pollution catalytic converters and energy conversion. One of the most economically important areas in which the surface is crucial is heterogeneous catalysis [1]. Study of surfaces and their behavior needs some general knowledge of surface chemistry. In this chapter, some key ideas relating to the experimental surface studies will be described.

#### 1.1 Surface sites

A surface consists of a mixture of terraces (flat regions) and defects [2]. There are many types of defect as in Fig 1.1 such as steps, kinks and point defects.

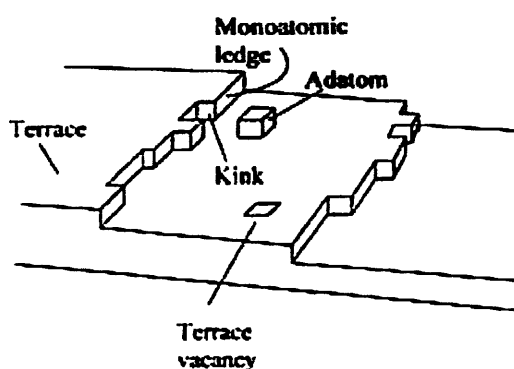


**Fig 1.1** Schematic diagram of defects found at the terrace or a step [2].

#### 1.2 Relaxation and reconstruction of surfaces

If the surface free energy is sufficiently large, relaxation and reconstruction are needed to reduce the free energy of the surface [2]. Both processes may occur with clean surfaces in ultrahigh vacuum (UHV).

**Relaxation:** is a small rearrangement of the surface layer. There is no change in periodicity or symmetry of surface. The effect results in the distance of first and second layer becoming slightly smaller than the bulk.

**Reconstruction:** involves a change in the periodicity of surface structure. It can be an obviously observable effect for example; the missing row model of reconstruction (110) fcc metal surface to minimize surface free energy.

### 1.3 Catalysis and surfaces

Catalysis can be divided into 2 types [3]: heterogeneous and homogeneous catalysis.

**Heterogeneous catalysis:** the catalyst and reactant are in different phases.

**Homogeneous catalysis:** the catalyst and reactant are in the same phases.

In heterogeneous catalysis, the efficiency of the process depends on the nature of the interface. Moreover, the nature of the top layer of atoms determines how fast a catalytic reaction takes place and small amount of additives can reduce or enhance the reaction.

**Poison additives:** block active sites on the surface of the catalyst resulting in a reduced reaction rate. They are generally electron acceptor elements such as Cl, S and C.

**Promoter additives:** enhance the catalyst activity by developing reactions at the sites adjacent to the promoter. They are often electron donor elements such as K, Cs and La.

Heterogeneous reactions occur at the interface (where the phases meet) between phases such as solids and liquids or gases and solids. Gas-solid interfaces are our interest due to the solid surface which immobilizes adsorbed gas, and molecules can be deposited without losing them as a product. As the surface is the first phase for reaction occurring but bonding at the surface is different than that in the bulk, therefore, surface atoms simply cannot satisfy bonding conditions in the same way as bulk atoms. The study of surface atoms will reveal the important mechanisms of the reaction on the interface.

### 1.4 Adsorption on surfaces

Adsorption is the term used to describe the process in which that the molecules (adsorbate) form a bond to the surface (adsorbent) [2]. Desorption is the reverse of adsorption. There are 2 types of adsorption.

**Chemisorption:** strong adsorption, a chemical bond breaks in the reactant and makes a new bond with the surface. It is characterized by an exchange of electrons between the adsorbate and the adsorbent.

**Physisorption:** weak adsorption, it involves attractive force such as van der Waals and mainly electrostatic polarization effect between the adsorbate and the adsorbent. Heat of physisorption ( $-\Delta H_{phy}^o < 35 \text{ kJ mol}^{-1}$ ) is lower than that of chemisorption ( $-\Delta H_{chem}^o > 35 \text{ kJ mol}^{-1}$ ).

### 1.5 Stress and strain

The understanding of adsorbate-induced the strain and surface tension gives the useful information of the different modes of layer growth [1, 4].

Consider solid B sitting on the substrate surface A. If the two solids form an interface that is indistinguishable from the rest of the crystal, the interface is perfectly matched geometrically. If the size of material is a big difference then they would not match. The lattice mismatch expressed in terms of the lattice constants  $a_A$  and  $a_B$  of two materials, is

$$\varepsilon = \frac{a_A - a_B}{a_B}$$

Stress is a force per unit area, defined by

$$\text{Stress} = \frac{F}{A}$$

where  $F$  is force and  $A$  is area.

There are three types of forces at the interface. If the material either side of the interface expands into the neighbors, this stress is called compression. A compressive force pushes on the interface. If the material on either side of the interface contracts away from the interface, this stress is called tension. A tensile force pulls away from the surface. Both compressive and tensile forces are opposite in direction and directed

perpendicular to the interface. A third force is a force parallel to the interface, called shearing stress.

When a non-rigid lattice is deformed by stress, the deformation of the stressed material is called strain. Either compressive or tensile forces onto the lattice lead to the change of length. Strain is defined by

$$\text{Strain} = \frac{\Delta l}{l}$$

In case of tension, the Young's modulus is defined by

$$Y = \frac{\text{stress}}{\text{strain}} = \frac{Fl}{A\Delta l}$$

The amount of strain at the interface of two materials depends on the relative sizes of two materials (e.g. lattice constant), lattice symmetry, relative strengths of the A-A, B-B and A-B interactions and thermal coefficient.

## 1.6 Type of Interfaces

There are three types of interfaces formed as shown in Fig 1.2 [4]. If there is no mixing of two materials it called a sharp interface. If one material is soluble in the other, then it can diffuse into the other material and create a region of a mixture of compositions. It called a non-abrupt interface. If A and B can form a stable compound, it is called reactive interface. In this case 2 interfaces rather than one interface are grown.

When growth occurs on a crystalline substrate, the overlayer may grow either as crystalline or as amorphous. A special case of growth is epitaxial growth in which the overlayer takes on the same structure as the substrate. There are 2 types of epitaxy. The overlayer and the substrate are the same material, called homoepitaxy or the overlayer and the substrate are different, called heteroepitaxy.

## 1.7 Solid-on-solid growth

The strain resulting from lattice mismatch gives several modes of film growth [4]. The observation of equilibrium structures can be summarized as follows (Fig 1.3);

**Layer-by-layer(Frank-van der Merwe) growth:** It is generally high crystalline quality. Film atoms more strongly bond to the substrate than to each other.

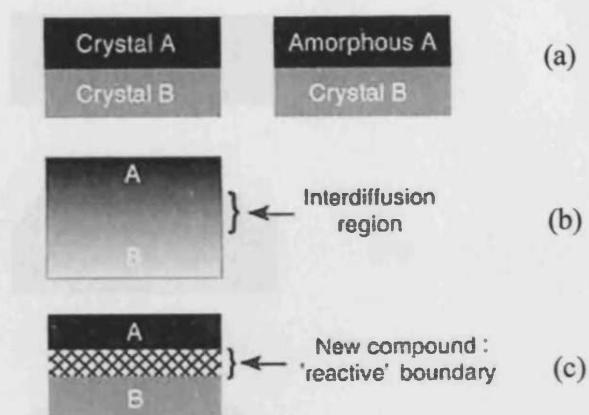


**Fig 1.2** Interface of 2 materials: (a) sharp interface, (b) nonabrupt interface and (c) reactive interface [4].

The system is lattice matching nearly zero ( $\epsilon \approx 0$ ) and balanced interactions are required. The substrate is wetted by the adsorbate.

**Layer plus island (Stranski-Krastanov) growth:** it general occurs after 1-4 atomic layer thicknesses. After that thickness the overlayer can't grow as the wetting layer (strained structure) but three-dimensional island (less strained structure).

**Three-dimensional island (Volmer-Weber) growth:** This growth mode occurs when the adsorbate is non-wetting due to the adsorbate-adsorbate interactions being stronger than adsorbate-substrate interactions.

In general the equilibrium structure of overlayers depends on some parameters:

- Relative strengths of adsorbate-adsorbate and adsorbate-substrate interactions
- Lattice matching of substrate and overlayer
- Strain field: relaxation in the substrate and islands
- Temperature: surface energies and reconstructions change by temperature

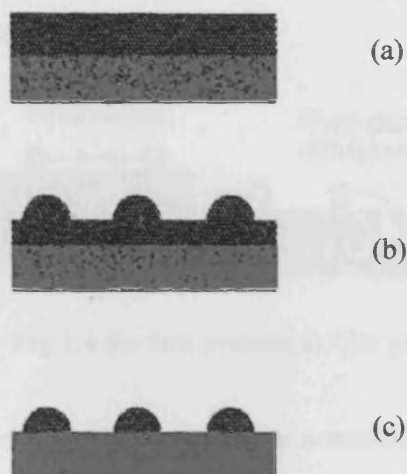


**Fig 1.3** Equilibrium growth mode : (a) layer-by-layer growth (Frank-van der Merwe), (b) layer and island growth (Stranski-Krastanov) and (c) island growth (Volmer-Weber) [4].

### 1.8 Nonequilibrium growth modes

The driving force of the growth mode transition is thermodynamic rather than kinetic [4]. Two important parameters (temperature and pressure) drive a system away from equilibrium. The temperature of the substrate controls the diffusion and desorption rates of adsorbates (i.e. sticking coefficient). The pressure of the gas phase controls the impingement rate of adsorbing atoms. Therefore, the growth is controlled by thermodynamic or kinetic factors depending on the experimental conditions. If the temperature is low the probability of island creation is high. The size and the shape of islands are determined by the kinetics of adsorption and diffusion. When the driving force of the growth mode transition is kinetic rather than thermodynamic then evidence of nonequilibrium growth is found. Kinetic factors control the relative rates of, terrace diffusion, accommodation of atoms at steps, nucleation, diffusion across steps and deposition for the film morphology illustrated in Fig 1.4. It was found that diffusion across a terrace is easier than diffusion across a step and diffusion in the step-down direction is easier than diffusion in the step-up direction because of lower activation barrier.

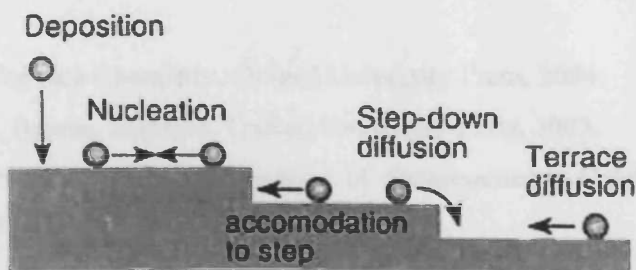


Fig 1.4 Surface process in film growth [4].

Three growth modes are distinguished for nonequilibrium growth (Fig 1.5):

**Step-flow growth:** there is no interlayer transport and terrace diffusion is so fast, all atoms reach a step before the island can be grown.

**Layer growth by island coalescence (2-dimensional growth):** The nucleation of islands is fast. The limitation of this mode is no island nucleates on the layer until the earlier layer is complete.

**Multilayer growth (3-dimensional growth):** islands nucleate on top of unfinished layers because of the limitation of the interlayer transport. The higher the amount of deposition, the larger the number of islands on islands.

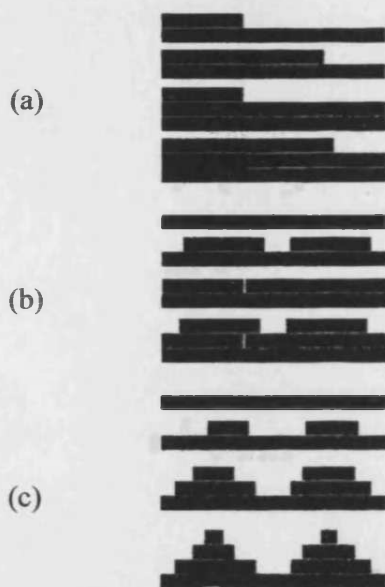


Fig 1.5 Nonequilibrium growth mode: (a) step-flow growth, (b) layer growth by island coalescence and (c) multilayer growth [4].

**Reference:**

- [1] E. M. McCash, Surface Chemistry, Oxford University Press, 2004.
- [2] G. Attard and C. Barnes, Surfaces, Oxford University Press, 2003.
- [3] M. Bowker, The Basis and Applications of Heterogeneous Catalysis, Oxford University Press, 2004.
- [4] K. W. Kolasinski, Surface Science: Foundations of Catalysis and nanoscience, John Willey & Sons LTD, 2001.



## Chapter 2

### Experimental Details

#### 2.1 Introduction: spectroscopic techniques for surfaces studies

Surface characterization needs techniques to probe surface properties at the molecular level [1]. It must reveal detailed information of geometric structure, chemical composition and electronic properties. Many questions need to be answered such as what type of atoms are on the surface and how much, where atoms are situated, bond lengths and bond angles in adsorbates or how surface bonds influence surface reactivity. To answer those questions, a combination of several characterization techniques could provide some functional information. X-ray photoelectron spectroscopy (XPS) gives surface chemical information and Low Energy Electron Diffraction (LEED) and scanning tunneling microscopy (STM) surface structure. Moreover, the system needs to stay clean long enough for probing; the ultrahigh vacuum UHV system and the accessory instruments in the laboratory are also described.

#### 2.2 X-ray Photoelectron spectroscopy (XPS)

##### 2.2.1 Introduction

XPS was developed around 1960 into a sophisticated analytical method by Kai Siegbahn and his colleagues [1- 5] in Sweden. The work of this group in Uppsala was honored by the awarding of the 1981 Nobel Prize in physics to K. Siegbahn. Since this technique could determine the chemical difference between a metal, its oxide or non-metallic elements, this technique was named “electron spectroscopy for chemical analysis” or the acronym ESCA.

Around 1970 the first UHV instruments became commercially available. XPS is perhaps the most versatile and generally applicable surface spectroscopic technique.

### 2.2.2 The basic principles

Photoelectron spectroscopy (PES) uses photo-ionization and analysis of the emitted photoelectrons to study the surface composition and electronic state [1-8]. According to the source of exciting radiation, PES is divided into two categories: X-ray photoelectron spectroscopy (XPS), using X-ray (200-2000 eV) radiation to examine core-levels of electron in atoms and ultraviolet photoelectron spectroscopy (UPS), using vacuum UV (10-45 eV) radiation to examine valence levels of atoms in a solid. UPS accesses only the molecular orbital or valence levels of the sample whereas XPS allows ionization of both valence and core-level shells.

If an atom A absorbs a photon of a well-defined energy  $h\nu$  (the energy of a photon is given by the Einstein equation  $E = h\nu$ , where  $h$  is Planck constant  $6.62 \times 10^{-34}$  Js and  $\nu$  is a frequency (Hz) of the radiation), there is a finite probability that it will absorb a photon and use the energy discharged to emit an electron from an electron level in the atom [6]. The kinetic energy (KE) of photoelectron is a characteristic of the orbital from which it has been removed (Fig 2.1).

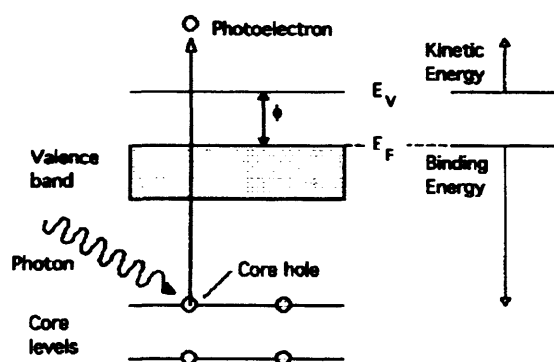
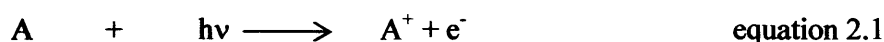


Fig 2.1 Diagram of photoemission process [ 7 ].

PES involves the photoelectric effect as defined by Albert Einstein in 1905. Photons of a defined energy strike on the solid and absorption of this photon causes the ejection of a photoelectron, called the photoionisation process or photoelectric effect. The aim of photoelectron spectroscopy is to detect the electrons generating a spectrum consisting of a number of electrons  $n(E)$  versus kinetic energy (KE)

Conservation of energy from equation 2.1 requires that

$$E(A) + h\nu = E(A^+) + E(e^-) \quad \text{equation 2.2}$$

Since the electron's energy is presented as kinetic energy (KE) this can be rearranged to give the following expression for the KE of the photoelectron.

$$KE = h\nu - [E(A^+) - E(A)] \quad \text{equation 2.3}$$

Where  $E(A)$  is the total energy of the initial state of system, that is the ground state of the neutral atom and  $E(A^+)$  is the energy of the final state of the system, which is the ionized species. The final term,  $[E(A^+) - E(A)]$ , representing the difference in energy between the ionized and neutral atoms, is commonly called the binding energy (BE) of the electron.

The binding energy of photoelectron is simply the difference between initial state (atom with  $n$  electrons) and final state (atom with  $n-1$  electrons (ion)). This is the frozen orbital approximation, assumed by Koopman's theorem. Measured BE's and calculated orbital energies are different by 10-30 eV because the frozen orbital approximation is not accurate due to electron rearrangement to shield the core hole.

A diagram representation of measured and calculated orbital energy is shown in Fig 2.2

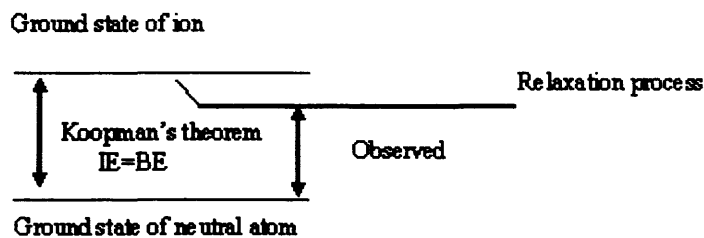


Fig 2.2 A diagram of comparing measured and calculated BEs [6].

### 2.2.3 Photoemission process

From Fig 2.2 the equation 2.3 can be written

$$KE = h\nu - IP \quad \text{for gas} \quad \text{equation 2.4}$$

$$KE = h\nu - BE - \phi \quad \text{for solid} \quad \text{equation 2.5}$$

Ionization energy, IP (or ionization energy (IE)), is the energy needed to remove an electron from a gaseous atom or ion. Binding energy, BE, is a measure of the energy required to free electrons from their atomic orbital. The work function,  $\phi$  ( $E_{vac} - E_{femi}$ ), is the minimum energy that must be given to an electron to free it from

the surface. Kinetic energy, KE, is an excess energy given to the electron.

The process is divided into primary process and secondary processes described as follows.

### 2.2.3.1 Primary process

#### Photoionization process



An atom absorbs a photon and generates an excited ion by distributing out an electron with finite energy [3]. The kinetic energy of the electron is equal to the difference between the photon energy and the binding energy. A schematic of photoionization process is shown in Fig 2.3.

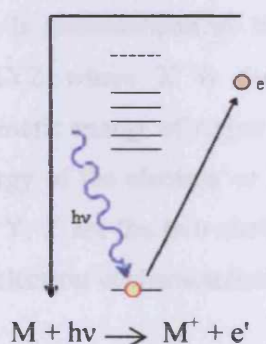


Fig 2.3 Schematic diagram of photoionization process [6].

### 2.2.3.2 Secondary process or fate of the core-hole

A core hole is formed after initial photoelectric event results in an excited ionic state. This ion state leads to either X-ray fluorescence or a radiation-less process known as an Auger emission.

#### (1) X-ray fluorescence

The excited ion relaxes to generate a photon and a ground state ion by an electron falling from a higher orbital to fill the core-hole (Fig 2.4) and the energy released as electromagnetic radiation or X-ray fluorescence process.

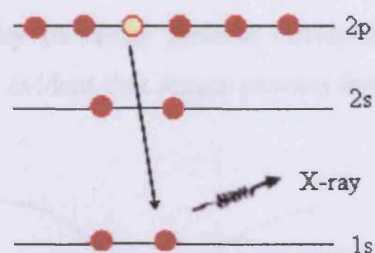


Fig 2.4 Schematic diagram of X-ray fluorescence process [6].

## (2) Auger electron emission

The core-hole created may be neutralized by an electron transition from an electron level of lower binding energy [1]. The quantum of energy  $\Delta E$  equals to the difference in binding energy between the core hole and down electron. A third electron which can escape into the vacuum with the a well-defined KE is termed the Auger electron. This process is characterized by the three orbitals involved and is designated conventionally XYZ where X is the initial shell from which the photoelectron is emitted the kinetic energy of Auger electron [4]. The electron kinetic energy is independent of energy of the electron or incident radiation because it is a secondary process (Fig. 2.5). Y, Z are the two shells containing the final vacancies. The kinetic energy of Auger electron is characteristic only of the binding energies of electrons within the atom.

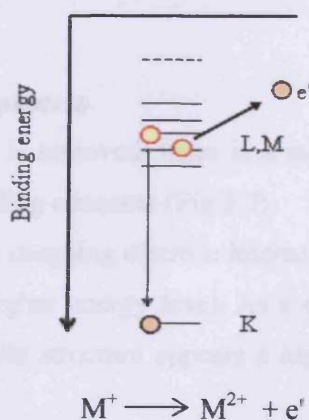
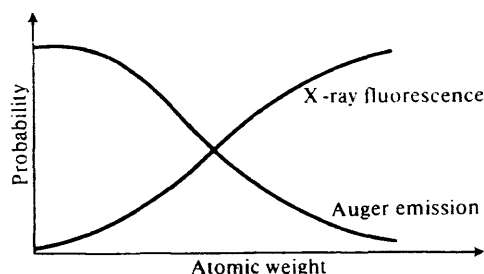


Fig 2.5 Secondary process diagram of Auger electron decay [6].

Auger emission and X-ray fluorescence are competitive decay mechanisms and the relative probability of either process occurring is dependent on atomic number. From Fig 2.6 it is evident that Auger process dominates for elements of low atomic number.



**Fig 2.6** Relative probabilities of X-ray fluorescence and Auger electron emission [9].

### 2.2.3.3 Final state effects

The core-level of the remaining electrons in the ionized atom are influenced by the core-hole potential giving to a variety of final states and therefore there is the additional structure in XP spectrum.

#### (1) Relaxation shifts

The removal of an electron from an atomic shell results in a hole of positive charge. The electron in the systems relaxes themselves to minimize the energy. The result is outgoing electron traveling with an additional amount of kinetic energy, and hence reduced binding energy.

#### (2) Shake-up and Shake-off process

When a core electron is removed, there is a sudden change in the effective charge due to the loss of shielding elements (Fig 2.7).

**Shake-up satellite:** the outgoing electron interacts with a valence electron and excites it (shake it up) to a higher energy level. As a consequence the energy core-electron is reduced and satellite structure appears a higher apparent binding energy than the parent photoelectron.



**Shake-off:** the valence electron is ejected from the ion completely (to the continuum). Appears as a broadening of the core level peak or contributes to the inelastic background.

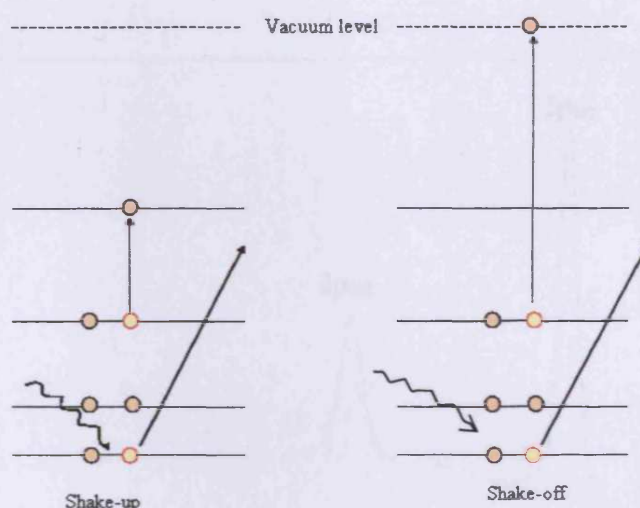


Fig 2.7 Schematic diagram of shake-up and shake-off processes [ 6].

### (3) Multiplet Splitting

After photoionisation unpaired electron from a filled core-shell and any unpaired electrons in the system could interact resulting in a spectrum observed as 2 peaks. The intensities of the two resulting XP lines are proportional to  $2s+1$ . For example, the lithium (Li) ground state structure  $1s^2 2s$  has total spin 0 and 1 resulting in 2 electrons in the ion state with spin anti-parallel and parallel with intensity 3:1.

### (4) Spin-orbit splitting

Spin-orbital coupling is the magnetic interaction between the spin of an electron and its orbital angular momentum. After photoionization the remaining unpaired electron may have its spin vector,  $s$ , parallel or anti-parallel to its orbital angular momentum vector,  $l$ , resulting in two final states of different energy and total angular momentum quantum number,  $j = l \pm \frac{1}{2}$ . The parallel state is the lowest in energy. For instance (Fig 2.8) ionization of the 2p level in Cu ( $l=1$ ) leads to 2 peaks designated  $2p_{3/2} (j = 1 + \frac{1}{2})$  and  $2p_{1/2} (j = 1 - \frac{1}{2})$  and separated by 19.5 eV. The intensity of the components are proportional to  $(2j+1)$  so that the relative intensities ( $2p_{3/2}$  :

$2p_{1/2}$ ) should equal 4:2 (or 2:1). The level of highest  $j$  value has the larger hole-life time and hence by the uncertainty principle it has a narrower full-width at half maximum (FWHM).

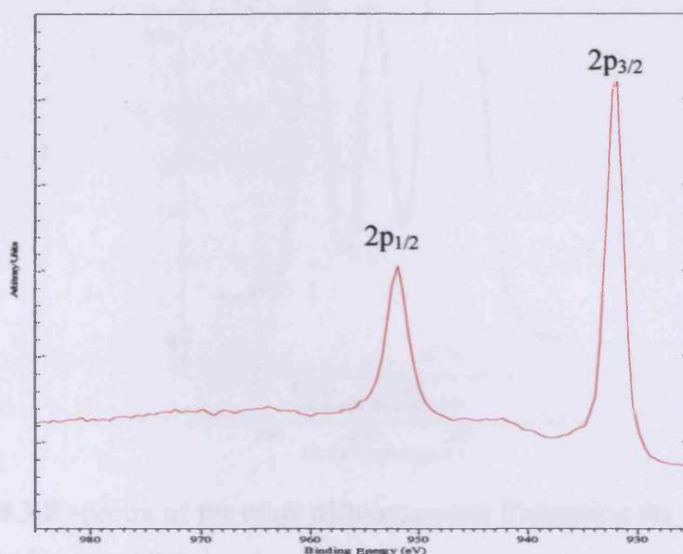


Fig 2.8 Splitting of the Cu (2p) XP spectrum.

#### 2.3.3.4 Chemical Shift in XPS

The energy of an orbital is sensitive to the chemical environment of atom. The chemical shift is related to the overall charge on the atom. Three main factors affecting the chemical shift are (1) number of substituents, (2) substituent electronegativity and (3) formal oxidation state.

One of the most important features which determine XP binding energies is the chemical environment of atoms. The local charge and potential changes cause binding energy shifts, called chemical shifts, in the core levels. Fig 2.9, an example of chemical shifts is shown in the C1s XP spectrum of ethyl-trifluoroacetate. The molecule contains four C atoms in four different chemical surroundings. The electronegativity of the F atom is highest in the molecule therefore, the C atom bonded with the F atom gives a chemical shift to highest binding energy in XP spectra.



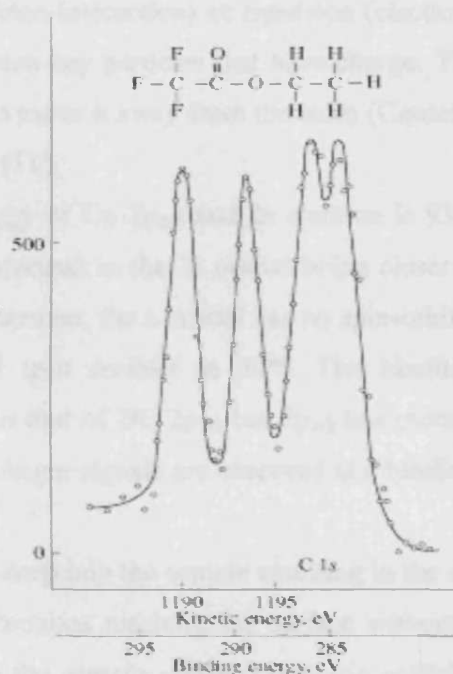


**Fig 2.9** XP spectra of the ethyl trifluoroacetate illustrating the chemical shifts of the 1s level of carbon [10].

### 2.3.4 Chemical Analysis by XPS

#### (1) Qualitative Analysis

It is clear that no photoemission occurs if  $IP > h\nu$  for gases whereas in the case of a solid photoemission can not occur if  $BE + \phi > h\nu$ . In general, photoemission will yield a polychromatic or polyenergetic flux of electrons due to the presence of different species of electrons in the given atom, molecule or solid. For different orbitals of an atom, photoelectron peak intensities are different depending on the atomic cross-section for photoelectric absorption, probability of escape of the photoelectron without collision and probability of detection by the instrument. Since each element has a unique set of core levels photoemission can be used as a fingerprint technique. For example, the atomic number of Cu is 29. The electron configuration is  $1s^2 2s^2 2p^6 3s^2 3p^6 3d^{10} 4s^1$  and the XP spectrum in Fig 2.10 shows binding energies of electrons in the different orbitals. At the atomic level, binding energy is derived from electrostatic interactions. This interaction is either long rang

attraction (electron – proton interaction) or repulsion (electron-electron and proton - proton interaction) between any particles that have charge. The amount of energy to be given to an electron to move it away from the atom (Coulombic potential) is called the binding energy (BE) [11].

The binding energy of Cu 2p<sub>3/2</sub> and 2s electron is 932.7 eV and 1096.7 eV, respectively due to the electron in the 2s orbital being closer to the nucleus than the 2p<sub>3/2</sub> electron orbital. Moreover, the s orbital has no spin-orbital split, singlet whilst p orbital is a spin-orbital split doublet in XPS. The binding energy of the 2p<sub>1/2</sub> component is higher than that of BE 2p<sub>3/2</sub> but 2p<sub>3/2</sub> has more electron population or cross section than 2p<sub>1/2</sub>. Auger signals are observed at a binding energy between 500-800 eV.

X-rays penetrate deep into the sample resulting in the observed peak. Electron emission results from electrons reaching the surface without inelastic scattering. If electrons emitted within the sample undergo inelastic collisions then the energy of electrons reduced, resulting in background counts. Moreover, the background intensity at high binding energies is larger than at lower binding energy as shown in Fig 2.10.

## (2) Quantitative Analysis

The calculation of surface concentration of adsorbates from photoelectron data is done using the modified form of the equation proposed by Madey et al. [12], and discussed in detail by Carley and Roberts [13]. Scofield's tabulation [14] of subshell photoionization cross sections is used for the calculation. Carley-Roberts equation is the following

$$\sigma_a = \frac{I_a \mu_s E_a N \rho_s \lambda \cos \phi}{I_s \mu_a E_s M} \quad \text{equation 2.7}$$

where:  $\sigma_a$  = concentration of adsorbate (cm<sup>-2</sup>),  $I_a$  = adsorbate line intensity,  $I_s$  = substrate intensity,  $E_a / E_s$  = kinetic energy of photoelectrons,  $\mu_a / \mu_s$  = modified Scofield photoionisation cross sections,  $\lambda$  = mean free path of electrons within substrate,  $\rho_s$  = density of surface,  $\phi$  = angle of collection with respect to the surface

normal,  $M$  = relative atomic mass of substrate,  $N$  = Avogadro's constant ( $6.02 \times 10^{23}$  atoms  $\text{mol}^{-1}$ )

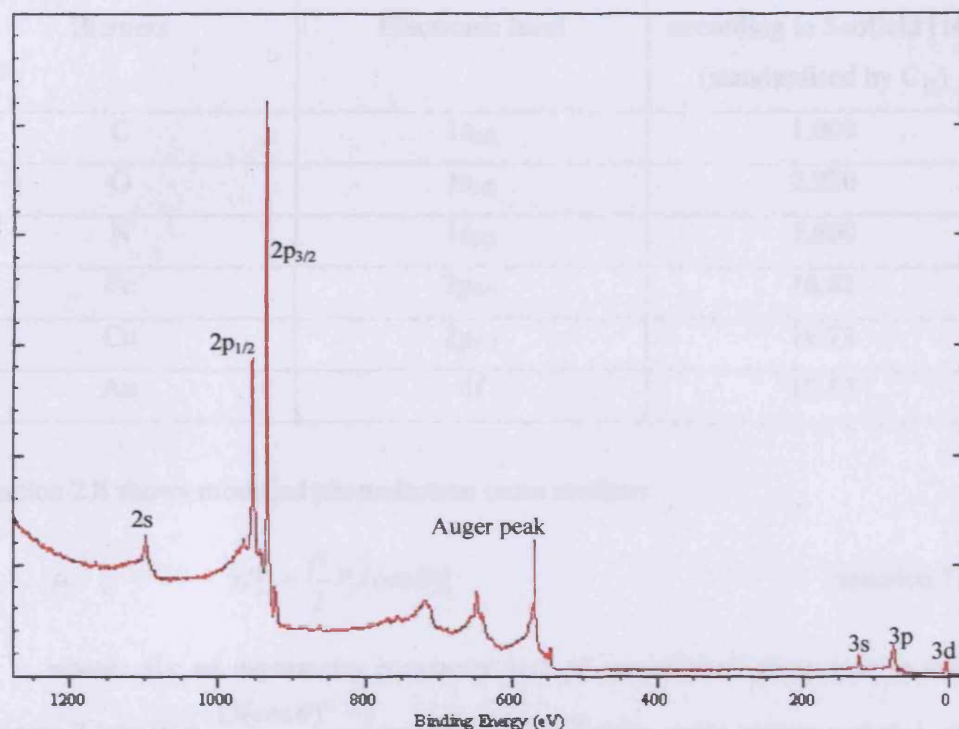


**Fig 2.10** A wide scan of a Cu 2p XP spectrum from Cu(100) excited by Al ( $K\alpha$ ) radiation at  $E = 1486.6$  eV.

We shall see how it is possible to choose values for each of these parameters and to conduct XPS quantitative analysis.

### (i) Ionisation Cross-Section

As the creation of the photoelectron when the sample is irradiated by photons is the first process, the probability of photoelectron creation directly contributes to the observed photoemission intensity. The probabilities are directly related to the ionization cross sections. Calculated by J. H. Scofield [14], Table 2.1 presents a value of cross-section of elements for a source Al ( $K\alpha$ )

**Table 2.1** Ionisation cross-sections of elements for a source Al (K $\alpha$ )

Element	Electronic level	Ionization cross-section according to Scofield [14] (standardised by C <sub>1s</sub> )
C	1s <sub>1/2</sub>	1.000
O	1s <sub>1/2</sub>	2.930
N	1s <sub>1/2</sub>	1.800
Fe	2p <sub>3/2</sub>	10.82
Cu	2p <sub>3/2</sub>	16.73
Au	4f	17.12

Equation 2.8 shows modified photoelectron cross sections

$$\mu = \mu' \left[ 1 - \frac{\beta}{2} P_2(\cos \theta) \right] \quad \text{equation 2.8}$$

where:  $\beta$  = an asymmetry parameter and  $\mu'$  unmodified photoelectron cross section;  $P_2(\cos \theta) = \frac{(3(\cos \theta)^2 - 1)}{2} = -0.1694$ ,  $\theta = 62^\circ$  (the angle between photon and photoelectron direction)

$$\begin{aligned}
 \text{Therefore, } \mu_C &= 1.00 [1 - (2/2) \times (-0.1694)] = 1.1694 \\
 \mu_O &= 2.93 [1 - (2/2) \times (-0.1694)] = 3.426 \\
 \mu_N &= 1.80 [1 - (2/2) \times (-0.1694)] = 2.105 \\
 \mu_{Cu} &= 16.73 [1 - (1.41/2) \times (-0.1694)] = 18.73 \\
 \mu_{Fe} &= 10.82 [1 - (1.45/2) \times (-0.1694)] = 12.14 \\
 \mu_{Au} &= 17.12 [1 - (1.03/2) \times (-0.1694)] = 18.61
 \end{aligned}$$

## (ii) Mean free path of the electrons

The mean free path of electrons represents the mean distance that electrons can travel between inelastic interaction, depending on the kinetic energy of electron and the sample nature [15].

$\lambda_s$  = escape depth of photoelectrons through the substrate (For Cu is 7.6 Å)

$$\lambda_s = \varepsilon / a(\ln \varepsilon + b) \quad \text{equation 2.9}$$

Where a and b depend on the electron concentration, in case of Cu with kinetic energy 554 eV ( Please note : Al anode gives energy 1487 eV, binding energy of Cu 2p is 932 eV So, the kinetic energy of electron is 554 eV).  $a = 23.6$  and  $b = -3.21$

$$= 554 / 23.6 (\ln 554 - 3.21)$$

$$= 7.55 \text{ Å}$$

$$M_s = \text{molar mass of the substrate (Cu = 63.54 g/mol)}$$

$$\sigma_s = \text{substrate density (Cu = 8.96 g/cm}^3\text{)}$$

The surface concentration calculation of C, O, Fe, N in experiments are

$$\sigma_C = 2.41 \times 10^{17} \times \frac{I_{C1s}}{I_{Cu2p3/2}} \quad \text{equation 2.10}$$

$$\sigma_O = 6.03 \times 10^{16} \times \frac{I_{O1s}}{I_{Cu2p3/2}} \quad \text{equation 2.11}$$

$$\sigma_{Fe} = 1.38 \times 10^{16} \times \frac{I_{Fe3/2}}{I_{Cu2p3/2}} \quad \text{equation 2.12}$$

$$\sigma_N = 1.10 \times 10^{17} \times \frac{I_{N1s}}{I_{Cu2p3/2}} \quad \text{equation 2.13}$$

$$\sigma_{Au} = 1.60 \times 10^{16} \times \frac{I_{Au4f}}{I_{Cu2p3/2}} \quad \text{equation 2.14}$$

### (3) Thickness of overlayer calculation

The intensity decay is an exponential first-order decay law characteristic for the travel of radiation through matter (Beer-Lambert law) [1]. Therefore, the intensity of electrons of kinetic energy ( $E$ ) will be reduced as a function of distance into the solid. The equation is

$$I(d) = I(o) \exp\left(\frac{-d}{\lambda(E)}\right) \quad \text{equation 2.15}$$

Where  $I(d)$  and  $I(o)$  are intensity after and before the primary electron beam has traveled a distance,  $d$ .  $\lambda(E)$  is the inelastic mean free path (IMFP), which is shown how far an electron can travel (on average) before losing energy. For an angle of incidence  $\theta$  to the surface, the expression is

$$I(d) = I(o) \exp\left(\frac{-d}{\lambda \cos \theta}\right) \quad \text{equation 2.16}$$

Fig 2.11 shows the effective path length ( $d_{\text{eff}}$ ) for an electron in a solid

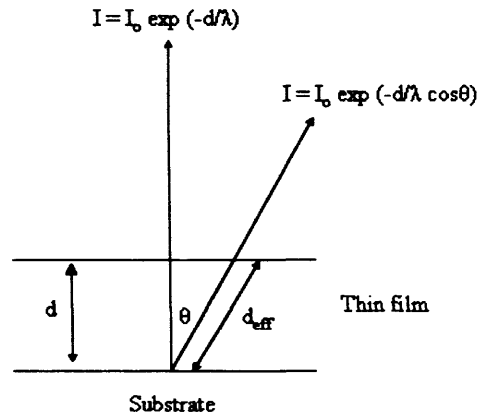


**Fig 2.11** Schematic diagram of the effective path length ( $d_{\text{eff}}$ ) for an electron in substrate [1].

The equation used to calculating the prepared overlayer thickness is,

$$I(d) = I(o) \exp\left(\frac{-d}{7.6}\right) \quad \text{equation 2.17}$$

where:  $\lambda_{\text{Cu}} = 7.6 \text{ \AA}$  and  $\theta = 0$ .

### 2.3.5 X-ray photoelectron spectrometer

The simplest form of electron spectrometer consists of the sample under investigation, primary radiation source and an electron energy analyzer. All are operating in an ultra high vacuum (UHV) system.

The schematic arrangement of photoelectron spectrometer is shown in Fig. 2.12 below

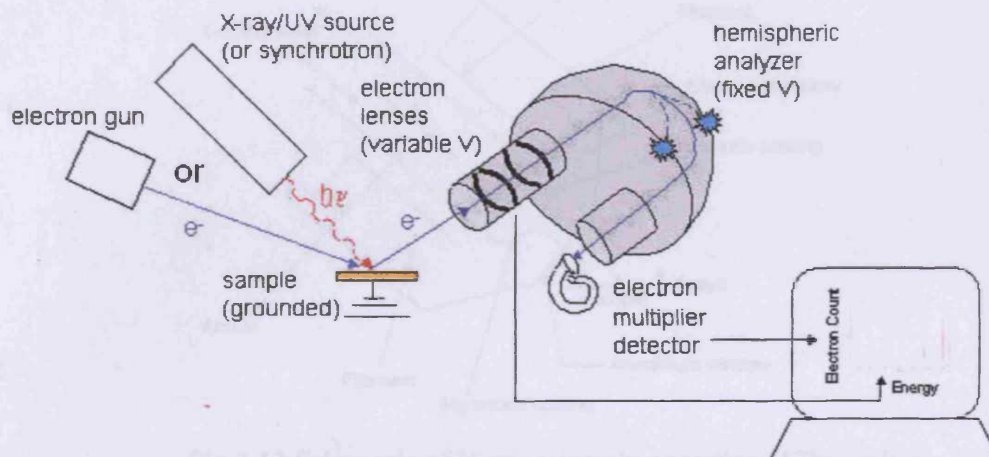


**Fig 2.12** Schematic diagram of the operation of an X-ray photoelectron spectrometer [16].

The basic requirements for a photoelectron spectrometer are:

### (1) The source of energy radiation

In the experiment, the X-ray source, DAR 400 (Fig 2.13), (Omicron nanotechnology), has twin anodes Mg K $\alpha$  (1253.6 eV) or Al K $\alpha$  (1486.6 eV) that allow either of them to be selected. The heated filament gives electrons to bombard the selected surface of an anode at high positive potential. The focus ring and the nose cone direct the electron to be hit in the certain area. Cooling water is used to prevent Al and Mg evaporation.

### (2) The electron energy analyzer

The electron energy analyzer (Fig 2.14), EA 125 spectrometer, consists of : (1) a multi-element electrostatic lens with 30 mm working distance to collect and focus electrons on the entrance of hemisphereical energy analyzer, (2) slit sets at the entrance to the energy analyzer change the transmission characteristics and resolution of the analyzer, (3) a hemisphereical energy analyzer, (4) slit set at the exit of the energy analyzer corresponding to the number of electron multipliers in the detector and (5) detector consisting of an array of 7 chaneltron electron multipliers.



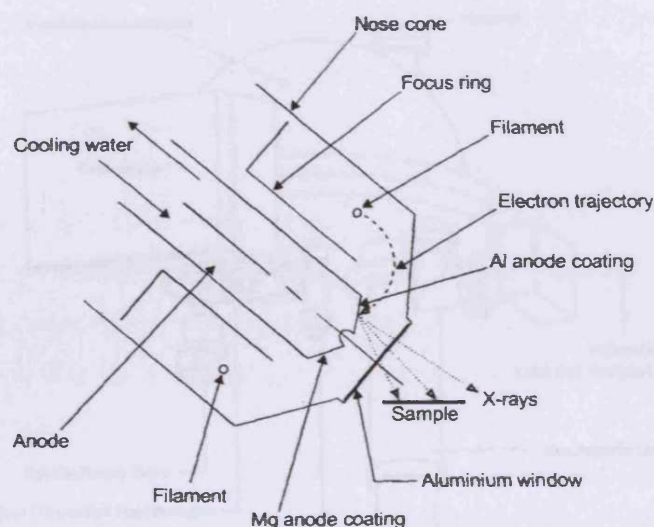


Fig 2.13 Schematic of X-ray source in operation [17].

### (3) The electron detector

Seven channel electron multipliers (Channeltron) are laid across the exit plane of the analyzer. The channeltron amplifies the current of a single electron by a factor of about  $10^8$ . The small current pulse from the output of the Channeltron is passed through a vacuum feedthrough and goes to the preamplifier, and then the signal is passed to a pulse counter for processing and production of an electron energy spectrum.

Due to the short inelastic mean free path of the photoemitted electron, XPS measurements analyze the outmost atomic layers of the surface. This means that electron spectroscopy is truly a surface sensitive analysis method. It is non-destructive and it can apply to all solid material except H and He, including insulators such as polymers and glasses.

### (4) The high vacuum environment

In order to get rid off the interference from gas phase collision and surface contamination, UHV conditions are necessary.



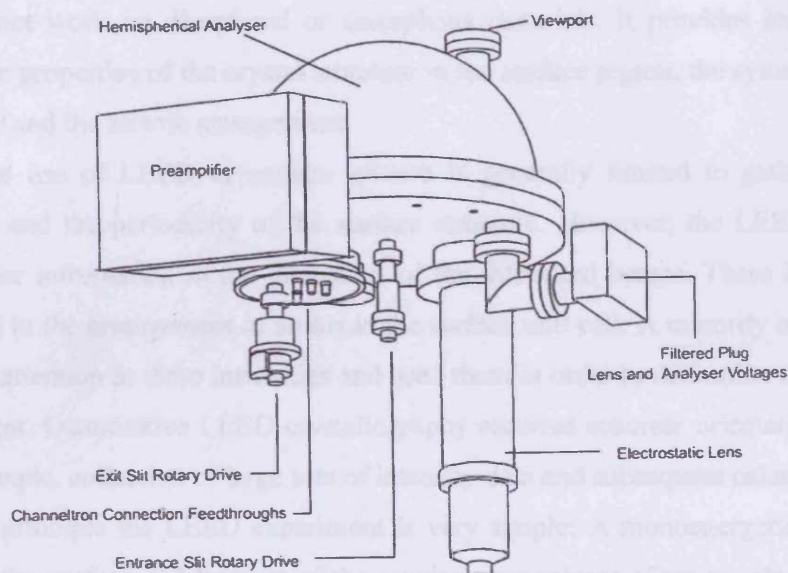


**Fig 2.14** The EA 125 hemispherical analyzer major components [18].

### 2.3 Low energy electron diffraction (LEED)

Surface structure is not equivalent to a simple termination of the bulk structure. In simple cases only the distance between the first few atomic layers is changed (multilayer relaxation). Frequently the arrangement of atoms within a layer is modified and this can reduce the translational symmetry of the surface (surface reconstruction). In addition to atomic displacements, atoms can be removed or added, bonds may be broken or new ones can be established. In the case of the surface of a chemical compound, the chemical stoichiometry can be changed by segregation, depletion, or substitutive adsorption (chemical relaxation and reconstruction). X-Ray diffraction was already well-known as a crystallographic technique, but X-rays are weakly scattered by matter and therefore penetrate deeply into the crystal. Low energy electron diffraction (LEED) is used for surface diffraction studies.

In LEED, electrons analyzed in the energy range 20-600 eV, are back-scattered by the electrons on surface atoms [1, 19-21]. Electrons in this energy range have de Broglie wavelengths similar to the interatomic spacing between atoms at the surfaces and may diffract if the atoms on the surface are periodic. This technique is suitable for long-range order determination, size and symmetry of surface unit cell,

but does not work on disordered or amorphous materials. It provides information about three properties of the crystal structure in the surface region, the symmetry, the periodicity and the atomic arrangement.

The use of LEED in surface science is generally limited to gathering the symmetry and the periodicity of the surface structure. However, the LEED pattern contains the information in the intensities of the diffracted beams. These intensities are related to the arrangement of atoms in the surface unit cell. A minority of workers have paid attention to these intensities and used them in order to determine the atomic arrangement. Quantitative LEED crystallography requires accurate orientation of the surface sample, collection of large sets of intensity data and subsequent calculations.

In principle the LEED experiment is very simple: A monoenergetic electron beam hits the surface and because of the regular arrangement of atoms, electrons are diffracted back in discrete directions determined by the lateral periodicity.

The modified de Broglie equation estimates the wavelength of electrons [19]:

$$\lambda \text{ (\AA)} = \frac{\sqrt{150.4}}{\sqrt{E(\text{eV})}} \quad \text{equation 2.18}$$

where  $E(\text{eV})$  is the kinetic energy of electron.

From equation 2.18 the de Broglie wavelengths are in the range 0.7 – 2.5 Å for kinetic energies between 50 and 200 eV which is comparable to inter-atomic distances. Moreover, electrons with 50-200 eV energy penetrate only < 20 Å to the surface. LEED is considered to be a surface geometrical structure probe due to the reasons of the limitation of penetration depth and suitable wavelength.

The penetration depth of electrons will vary in different materials, The result of many experiments show that this depth does not vary significantly until the incident beam energy is over 200 eV. From Fig 2.15, the energy of incident electrons of 50-200 eV is very acceptable for LEED experiments.

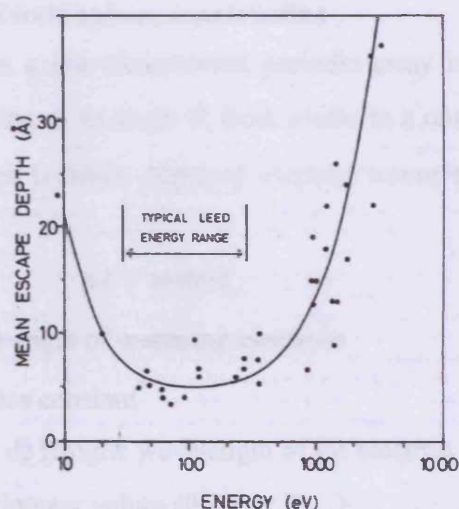


**Fig 2.15** Universal curve of the inelastic mean free path of electrons in a solid varies with its kinetic energy [19].

### 2.3.1 Real lattices and reciprocal lattices

Diffraction depends on the spacing of the surface. A convenient method to depict diffraction is using of the reciprocal lattice. In 2-dimensions, the vectors in real lattice are defined as  $a$  and  $b$  and the vectors in the reciprocal lattice  $a^*$  and  $b^*$  as in Fig.2.16. Note that  $a^*$  is perpendicular to  $b$  and  $b^*$  is perpendicular to  $a$ . Consider two sets of planes of real lattice at the right angle and with spacing  $a$  and  $b$ . The rules above applied produce two points in the reciprocal lattice, related to the origin  $O$  by  $a^*$  and  $b^*$ .

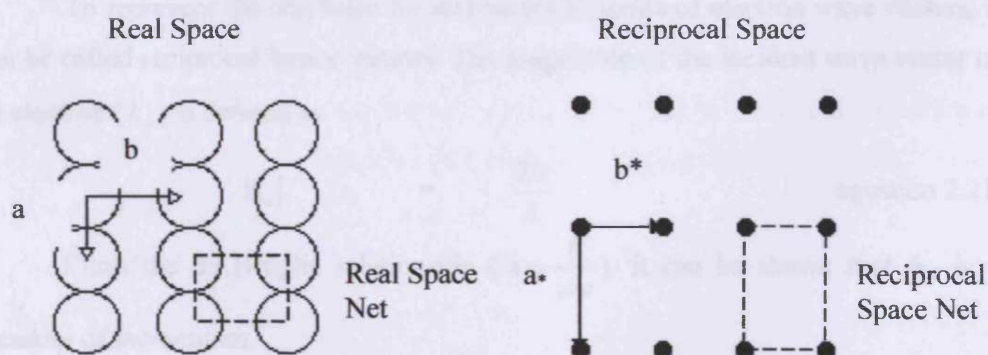


**Fig 2.16** Vector of real lattice and reciprocal lattice.



### 2.3.2 Diffraction and Ewald sphere construction

Diffraction from a one-dimensional periodic array is shown in Fig 2.17. It shows electrons scattering at an angle  $\theta_a$  from atoms in a one-dimensional array. For constructive interference between scattered electron waves can be written as Bragg equation

$$n\lambda = a \sin \theta_a \quad \text{equation 2.19}$$

$\theta_a$  is the angle of scattering electrons

$a$  is lattice constant

$\lambda$  is the de Broglie wavelength of the electron

$n$  is an integer values (0,  $\pm 1$ ,  $\pm 2$  ...)

Rearrangement gives  $\sin \theta_a = \frac{n\lambda}{a}$  equation 2.20

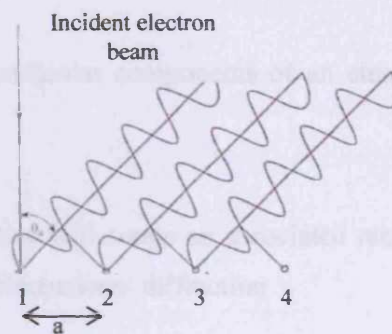


Fig 2.17 One-dimensional array diffraction [1].

To represent the condition for diffraction in terms of electron wave vectors, it can be called reciprocal lattice vectors. The magnitude of the incident wave vector of an electron ( $k_o$ ) is defined as

$$|k_o| = \frac{2\pi}{\lambda} \quad \text{equation 2.21}$$

From the de Broglie relationship ( $\lambda = \frac{h}{mv}$ ), it can be shown that  $k_o$  is a measure of momentum.

$$|k_o| = \frac{2\pi(mv)}{h} \quad \text{equation 2.22}$$

Substituting of equation 2.20 into equation 2.21 gives

$$|k_o| \sin \theta_a = \frac{2\pi m}{a} \quad \text{equation 2.23}$$

$|k_o| \sin \theta_a$  is the component of momentum parallel to the surface of incident electron ( $k_{||}$ ). From equation 2.23 the parallel momentum can be exchanged in the units of  $2\pi/a$ , the magnitude of the one dimensional reciprocal lattice vector as in Fig 2.18.

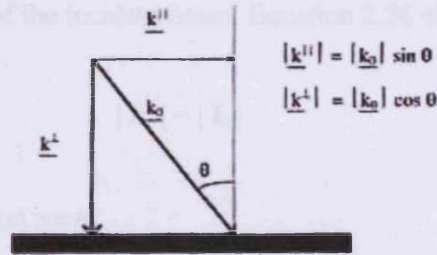


**Fig 2.18** Parallel and perpendicular components of an electron with incident wave vector  $k_o$  [1].

Every real space lattice will create an associated reciprocal lattice, using the following set of rules for 2-dimensional diffraction

$$\mathbf{M} = n\mathbf{a}^* + r\mathbf{b}^* \quad \text{equation 2.24}$$

$$\mathbf{a}^* = 2\pi/|\mathbf{a}| \quad ; \quad \mathbf{b}^* = 2\pi/|\mathbf{b}| \quad ; \quad \mathbf{a} \cdot \mathbf{b}^* = \mathbf{a}^* \cdot \mathbf{b} = 0 \quad ; \quad \mathbf{a} \cdot \mathbf{a}^* = \mathbf{b} \cdot \mathbf{b}^* = 1 \quad \text{equation 2.25}$$

where  $\mathbf{a}$  and  $\mathbf{b}$  are the elementary vectors of the surface two-dimensional unit cell,  $\mathbf{a}^*$  and  $\mathbf{b}^*$  are the elementary vectors of the corresponding reciprocal lattice,  $n$  and  $r$  are an integer values ( $0, \pm 1, \pm 2 \dots$ )

Equation 2.25 states that a small distance in real space becomes a large distance in reciprocal space, vice versa, Moreover,  $\mathbf{a}$  and  $\mathbf{b}$  are perpendicular to the direction of  $\mathbf{a}^*$  and  $\mathbf{b}^*$  respectively.

Ewald sphere is centered on the sample surface with a radius equal to the reciprocal of the wavelength of the incident electrons. The radius of the Ewald sphere is equal to the magnitude of the  $k_o$  vector, which is the reciprocal of the wavelength of the incident electrons. The  $k_i$  vector, corresponds to an allowed diffraction condition, and the  $G$  vector is the difference between the  $k$  and  $k_o$  vectors. In this figure, the  $k$  vector is the specular beam. Diffraction conditions are satisfied where the rods of reciprocal lattice intersect the Ewald sphere. Therefore, the magnitude of a vector from the origin of the Ewald sphere to the intersection of any reciprocal lattice rods is equal in magnitude to that of the incident beam. Equation 2.26 shows

$$|k_o| = |k_i| \quad \text{equation 2.26}$$

where :  $k_o$  is incident electron wave

$k_i$  is electron wave vector at any intersection of reciprocal lattice with Ewald sphere

An arbitrary vector,  $G$ , defines the reciprocal lattice vector between the ends of any two  $k$  vectors. Vector  $G$  is used to finding distance between arbitrary planes in the crystal. Vector  $G$  is calculated using Equation 2.27

$$G = |k_i| - |k_o| \quad \text{equation 2.27}$$

Using the Ewald sphere construction is a simple method to find the number of diffracted beams emerging from a surface at a given energy.

Consider a 2-dimensionnal crystal of square array, suppose the radiation beam with wavelength  $\lambda$  imposes on the surface; a vector  $k$  with length  $\frac{1}{\lambda}$  represents the radiation. To calculate the number of diffracted beams from a Cu{110} surface at 100 eV given that the lattice constant of Cu is 3.61Å

1) Calculate the de Broglie wavelength and the corresponding wave vector of the incident electron (equation 2.21)



$$\lambda = \left( \frac{150.4}{100 \text{ eV}} \right)^{\frac{1}{2}} = 1.227 \text{ \AA}$$

$$\text{From (equation 2.21)} |k_o| = \frac{2\pi}{\lambda} = 5.12 \text{ \AA}^{-1}$$

2) Construct the two-dimensional reciprocal lattice of the surface using the equations listed under equation 2.23

For Cu(110) surface (Fig 2.22)

$$|a| = \frac{3.61}{\sqrt{2}} = 2.55 \text{ \AA}$$

$$\therefore |a^*| = \frac{2\pi}{2.55} = 2.416 \text{ \AA}^{-1}$$

$$|b| = 3.61 = 3.61 \text{ \AA}$$

$$\therefore |b^*| = \frac{2\pi}{3.61} = 1.741 \text{ \AA}^{-1}$$

3) Choose a reciprocal lattice point as the origin (0,0)

4) Draw a circle radius  $|k_o|$  (5.12 \AA) centered at the origin

The total number of diffracted beams from the surface is simply given by the number of reciprocal lattice points contained within the circle. In this case, the number of diffracted beams is 21 (Fig 2.19).

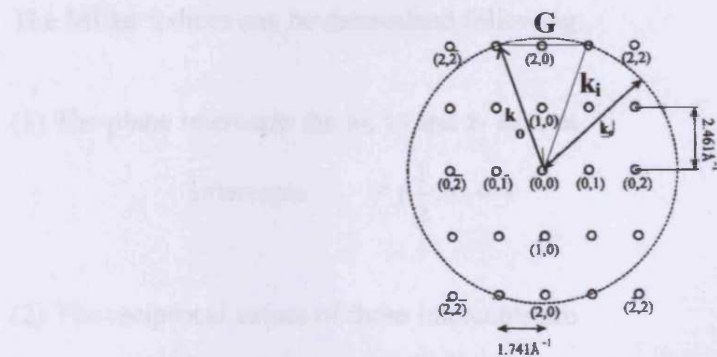


**Fig 2.19** Ewald sphere construction of Cu(110) surface with electron energy 100 eV [1].

### 2.3.3 Surface structures and notation

Crystal structure is a unique arrangement of atoms in a crystal, composed of a unit cell which is periodically repeated in three dimensions to generate a lattice. The well-defined surfaces consist of atoms in a limited number of well-defined sites. Surface structures may be varied by changing the angle at which the surface is cut with respect to the basic unit cell axes. Surface planes in the crystal are defined by the Miller indices. Simple cubic (sc), face-centered cubic (fcc) and body-centered cubic (bcc) surfaces are described by three integers ( $x, y, z$ ) while the hexagonal closed packed (hcp) structure has 4 integers ( $w, x, y, z$ ). Fig 2.20 shows an example defining the Miller indices of a plane. Three perpendicular Cartesian axes, labeled  $x, y$  and  $z$ , define a simple cubic lattice (lattice constant  $a$ ).

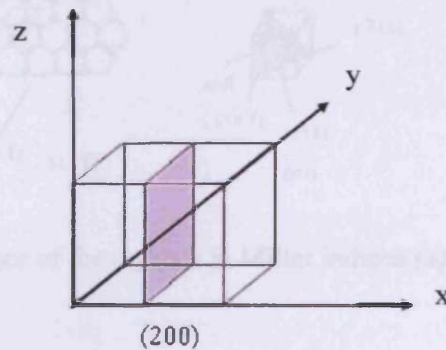


**Fig 2.20** The (200) plane of a simple cubic lattice.

The Miller indices can be determined following:

- (1) The plane intercepts the  $x$ -,  $y$ - and  $z$ - axes at

$$\text{Intercepts} = \left( \frac{1}{2}, \infty, \infty \right)$$

- (2) The reciprocal values of those intercepts are

$$\text{Reciprocals} = \left( \frac{1}{1/2}, \frac{1}{\infty}, \frac{1}{\infty} \right) = (2, 0, 0)$$

Fig 2.21 shows the principal low index planes of an fcc crystal as (100), (110) and (111).



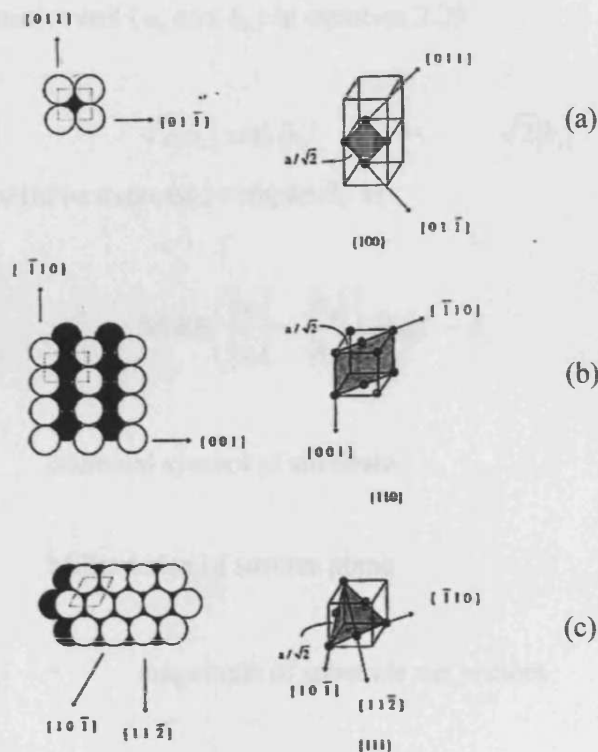


**Fig 2.21** Low index planes of fcc crystals in Miller indices (a) (100), (b) (110) and (c) (111) plane [1].

### 2.3.4 Overlayer structures

There are two ways of naming overlayer structures [1, 19]: Wood's notation and in matrix notation. The lattice vectors  $a_0$  and  $b_0$  of overlayer can be described in term of the substrate lattice vectors  $a_s$  and  $b_s$ . Fig 2.22(a) shows an adsorbate overlayer on a square fcc(100) substrate.

$$|a_0| = 2|a_s| \quad \text{and} \quad |b_0| = 2|b_s| \quad \text{equation 2.28}$$

Therefore, the over layer unit cell in Fig 2.22(a) is a (2×2) (primitive two by two) overlayer. Fig 2.22(b) is a c(2×2)(centered two by two) overlayer due to overlayer contains an atom in the center. In Fig 2.22(b), overlayer unit cell could also be referred to as  $(\sqrt{2} \times \sqrt{2})R45^\circ$  (root two by root two rotated  $45^\circ$ ), the overlayer unit

cell in term of primitive cell ( $a_0$  and  $b_0$ ) in equation 2.29

$$|a_0| = \sqrt{2}|a_s| \text{ and } |b_0| = \sqrt{2}|b_s| \quad \text{equation 2.29}$$

Wood's notation could be expressed completely as

$$S(hkl) \left( \frac{|a_0|}{|a_s|} \times \frac{|b_0|}{|b_s|} \right) - R \alpha^\circ - A \quad \text{equation 2.30}$$

where S = chemical symbol of substrate

(hkl) = Miller index of surface plane

$|a_s|$  and  $|b_s|$  = magnitude of substrate net vectors

$|a_0|$  and  $|b_0|$  = magnitude of overlayer net vectors

$\alpha$  = angle between overlayer and substrate (absent  $\alpha = 0$ )

A = chemical symbol of overlayer (No S and A for a clean surface)

Supposed S is Cu(100) and A is O atom, therefore

Cu(100)(2×2)-O from Fig 2.22(a)

Cu(100)c(2×2)-O or Cu(100)( $\sqrt{2} \times \sqrt{2}$ )R45°-O from Fig 2.22(b)

Note that the absence of p in Wood's notation means a primitive cell of overlayer. Now we consider how matrix notation of the overlayer in Fig 2.22 can be

written. Defining the primitive overlayer vectors ( $a_o$  and  $b_o$ ) in term of a linear combination of primitive unit vectors of substrate ( $a_s$  and  $b_s$ ). Equation 2.28 can be rewritten as

$$a_o = 2a_s + 0b_s \quad \text{equation 2.31}$$

$$b_o = 0a_s + 2b_s \quad \text{equation 2.32}$$

$$\begin{pmatrix} a_o \\ b_o \end{pmatrix} = \begin{pmatrix} 2 & 0 \\ 0 & 2 \end{pmatrix} \begin{pmatrix} a_s \\ b_s \end{pmatrix} \quad \text{equation 2.33}$$

Matrix notation is  $\text{Cu}(100) - \begin{pmatrix} 2 & 0 \\ 0 & 2 \end{pmatrix} - \text{O}$

From Fig 2.22(b), it can be written

$$a_o = 1a_s + 1b_s \quad \text{equation 2.34}$$

$$b_o = -1a_s + 1b_s \quad \text{equation 2.35}$$

$$\begin{pmatrix} a_o \\ b_o \end{pmatrix} = \begin{pmatrix} 1 & 1 \\ -1 & 1 \end{pmatrix} \begin{pmatrix} a_s \\ b_s \end{pmatrix} \quad \text{equation 2.36}$$

Matrix notation is  $\text{Cu}(100) - \begin{pmatrix} 1 & 1 \\ -1 & 1 \end{pmatrix} - \text{O} \quad \text{equation 2.37}$

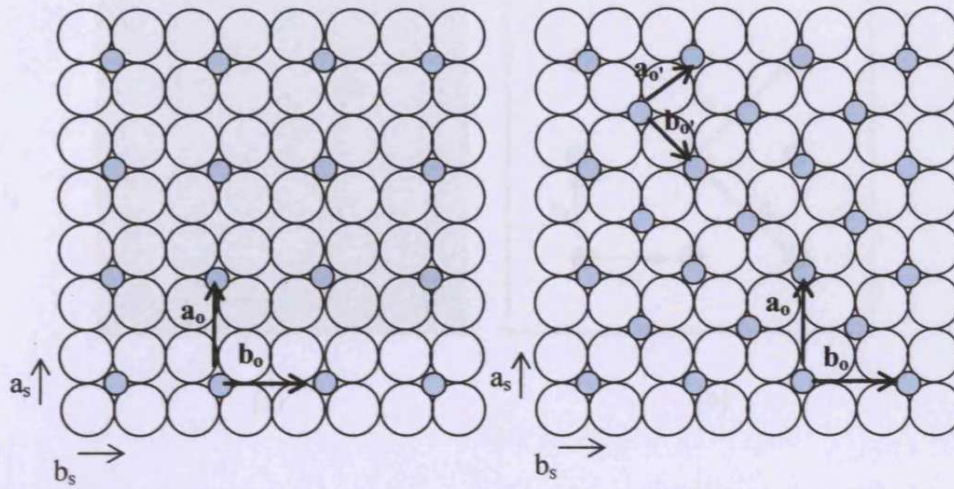


**Fig 2.22** The overlayer structure on fcc(100): (a) p(2×2) or  $M = \begin{bmatrix} 2 & 0 \\ 0 & 2 \end{bmatrix}$  and (b) c(2×2) or  $(\sqrt{2} \times \sqrt{2})R45^\circ$  or  $M = \begin{bmatrix} 1 & 1 \\ -1 & 1 \end{bmatrix}$ .

### 2.3.5 Overlayer structure interpretation from LEED diffraction patterns

The overlayer unit cell in real space can be derived from the reciprocal lattice in LEED pattern by manipulation of matrices. Suppose adsorption of atoms (e.g. O atoms) on Cu(100) gives the LEED pattern in Fig 2.23(a), and Fig 2.23(b) is the real space structure. The blue spots represent the Cu unit cell and the red spot additional spots due to the overlayer.

It can be determined as follows:

- (1) Write the reciprocal unit cell vectors of the overlayer in terms of the reciprocal space vectors of the substrate

$$a_o^* = m_{11}^* a_s^* + m_{12}^* b_s^* \quad a_o^* = \frac{1}{2} a_s^* - \frac{1}{2} b_s^* \quad \text{equation 2.38}$$

$$b_o^* = m_{21}^* a_s^* + m_{22}^* b_s^* \quad b_o^* = \frac{1}{2} a_s^* + \frac{1}{2} b_s^* \quad \text{equation 2.39}$$

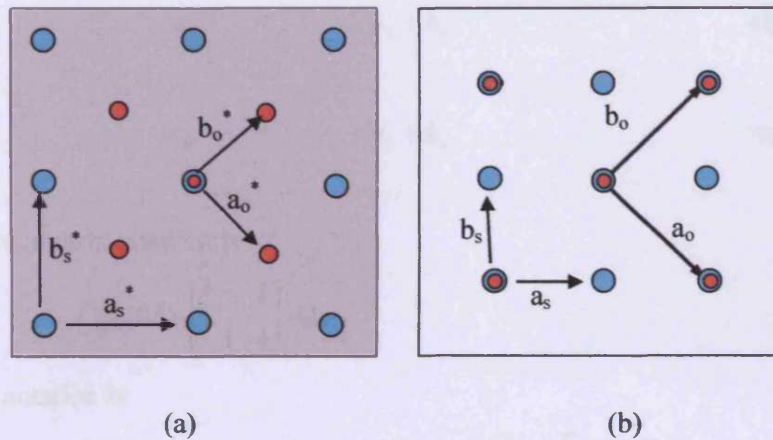


**Fig 2.23** Diagram of (a) reciprocal space of overlayer in LEED pattern (b) real space over layer on the Cu(100) substrate.

Matrix,  $M^* = \begin{bmatrix} m_{11}^* & m_{12}^* \\ m_{21}^* & m_{22}^* \end{bmatrix} = \begin{bmatrix} 1/2 & -1/2 \\ 1/2 & 1/2 \end{bmatrix}$  equation 2.40

(2) Convert the reciprocal space to real space

$$M = ([M^*]^{-1})^t = \frac{1}{\det M^*} \begin{bmatrix} M_{22}^* & -M_{21}^* \\ -M_{12}^* & M_{11}^* \end{bmatrix} \quad \text{equation 2.41}$$

$$\det M^* = (m_{22}^* \cdot m_{11}^*) - (m_{21}^* \cdot m_{12}^*) \quad \text{equation 2.42}$$

$$M = \frac{1}{1/4 + 1/4} \begin{bmatrix} 1/2 & 1/2 \\ -1/2 & 1/2 \end{bmatrix} = \begin{bmatrix} 1 & 1 \\ -1 & 1 \end{bmatrix} \quad \text{equation 2.43}$$

Hence

$$\text{or } \begin{bmatrix} a_o \\ b_o \end{bmatrix} = \begin{bmatrix} 1 & 1 \\ -1 & 1 \end{bmatrix} \begin{bmatrix} a_s \\ b_s \end{bmatrix} \quad \text{equation 2.44}$$

$$a_0 = a_s + b_s \quad \text{equation 2.45}$$

$$b_0 = -a_s + b_s \quad \text{equation 2.46}$$

Therefore, matrix notation is

$$\text{Cu(100)} - \begin{bmatrix} 1 & 1 \\ -1 & 1 \end{bmatrix} - \text{O}$$

Wood's notation is

$$\text{Cu(100)} - \text{c}(2 \times 2) - \text{O} \text{ or } \text{Cu(100)} - \text{p}(\sqrt{2} \times \sqrt{2})\text{R}45^\circ - \text{O}$$

### 2.3.6 LEED instrument

LEED uses the wave nature of electrons. These, with energies between 20 and 200 eV are incident in the form of a thin beam onto a surface, as shown in Fig 2.24. The electrons will be partially reflected by the layers of a crystalline sample [25]. The periodic arrangement of the atoms in the crystalline material determines the direction into which electrons are diffracted. These back-diffracted electrons are made visible on a phosphor screen. A camera is used to take images from the screen and store those images on a PC. One of the advantages of electron diffraction is that electrons cannot travel very far in solids. The electrons we see on the screen are therefore diffracted from the near surface region of the sample. This means that LEED is a surface sensitive technique but it also requires that the surface is very clean so that we must work in vacuum in order to keep gases from sticking to the surface.

A monochromatic electron beam can be generated by an electron gun with energy in the range 0 – 1000 eV. The sample must be an electrical conductor connected to earth to prevent charging when the beam hits the sample. After undergoing diffraction, electrons back scattered from the surface go towards a series of concentric meshes or grids. The outer most and inner most grids are earthed to ensure that the electrons travel free in that region. The inner pair of grids act as a cut-off filter and are held at a negative potential  $(-E_p + \Delta V)$ , where  $\Delta V$  is normally in the range 0 – 10 V. This ensures that only elastically scattered electrons arrive at the

detector, S (the phosphor screen with positive bias  $\sim 6$  kV). The diffracted electrons (elastically scattered) and secondary electrons (inelastically scattered) are back-scattered towards the LEED optics in the field free region. The spots come from the diffracted electrons while the secondary electrons give a dark background.

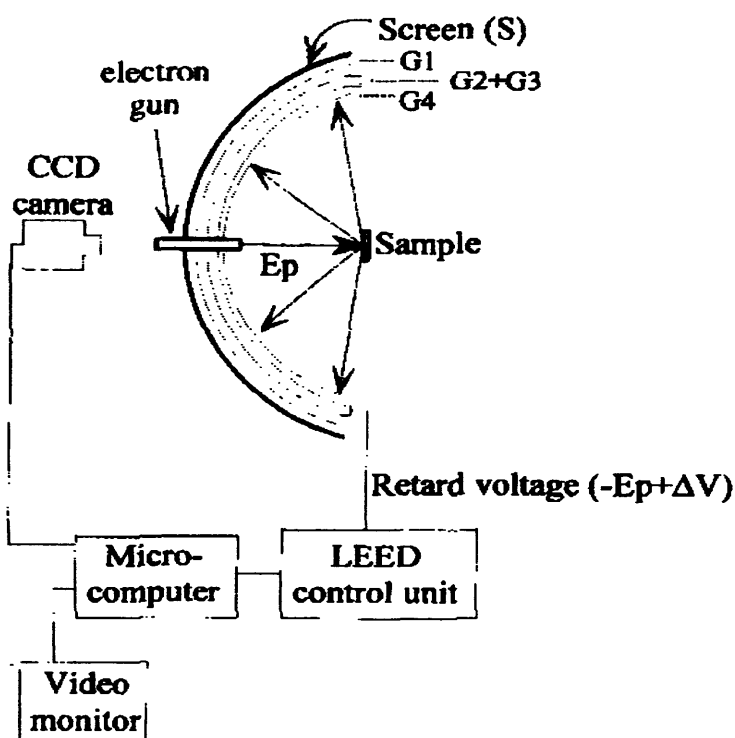


Fig 2.24 Schematic of LEED apparatus [1].

The image is captured on photographic film or monitored with a video camera.

## 2.4 Scanning Tunneling Microscopy (STM)

### 2.4.1 Introduction

The Scanning Tunneling Microscope (STM) was developed by Gerd Binnig and Heinrich Rohrer at the IBM Zurich Research Laboratory in the early 80's. Their accomplishment which won them a Nobel Prize in 1986 utilized the basics of quantum mechanics and produced a revolutionary method for determining surface



structure atom by atom [22-24], and these instruments have become established it as one of the most important techniques in surface investigations. Moreover, they have been used to fabricate surface structures ranging from  $\sim 100$  nm down to atomic dimensions.

### 2.4.2 Basic principles of solid

The technique is based on quantum mechanical tunneling between the very top atom of a sharp metal tip and the surface atoms of a conducting solid. The tip is separated (usually by vacuum) by a few angstroms from the sample surface, enabling a tunneling current to flow. Since the electrical current is necessary, both the sample and the tip should be conducting. The tunneling current is determined by the overlap of wave functions between the sample and the tip. Fig 2.25 shows the electronic structure of a solid (insulator, semiconductor and metal).

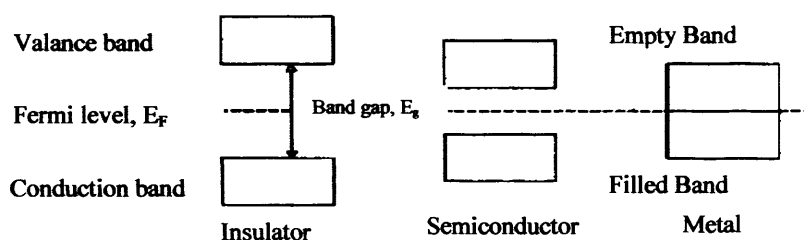


**Fig 2.25** Electronic structure of solid [25].

The top filled band is called the valence band. The bottom empty band is called the conduction band. The energy level between the filled-empty bands is called the Fermi level,  $E_F$ . The surface electronic structure is shown in Fig 2.26. The energy level of a

free electron is called the vacuum level,  $E_v$ .

The energy required to move an electron from  $E_F$  to  $E_v$  at the surface (Fig 2.26) is called the work function,  $\phi$ . The work function depends on the material, crystal face, adsorbate, external electric fields and reconstruction. Fig 2.27 shows the wave function inside a solid and outside a solid. The electron density decays exponentially away from the surface.



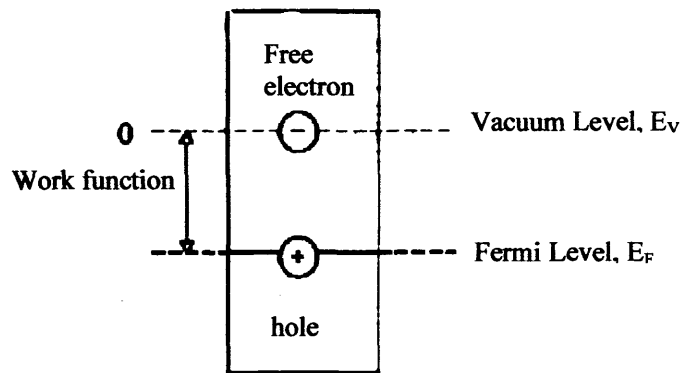


**Fig 2.26** The surface electronic structure [25].

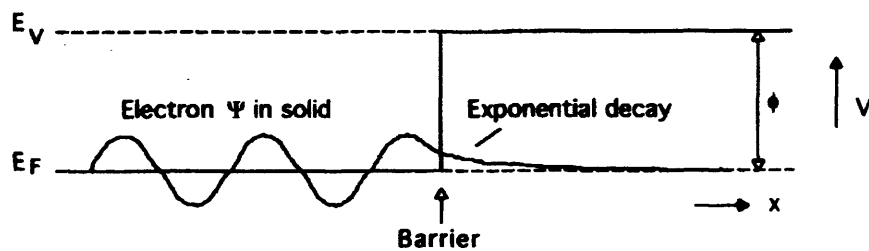


**Fig 2.27** Wave function inside a solid and outside a solid [25].

Tunneling occurs if two metals are brought in close proximity (Fig 2.28).

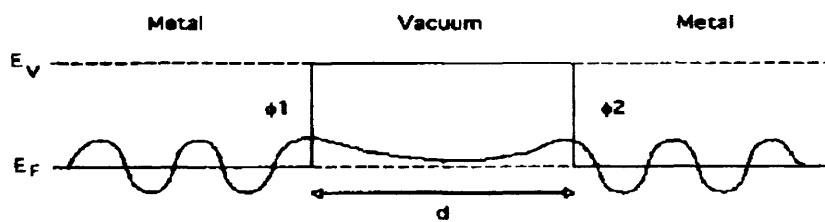


**Fig 2.28** The wave function of two solids [25].

When a potential  $V(\text{ext})$  is applied to one metal to drive electrons one way (metal 1 negative) tunneling occurs from filled states within  $V(\text{ext})$  of  $E_F$  in the left-hand metal  $\rightarrow$  empty states at  $E_F$  in the right-hand metal, (Fig 2.29).

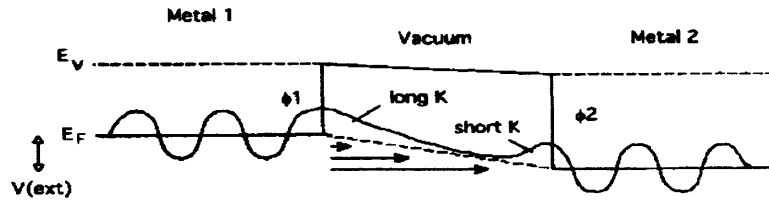


Fig 2.29 Illustration of between metals [25].

### 2.4.3 Principles of STM operation

Understanding the process of electron flow between the tip and surface is used to interpret STM images. Fig 2.30(a) represents the position in which two metals are not connected. The Fermi energies of the left-hand,  $E_F^L$  and right-hand,  $E_F^R$  metal have their characteristic values, as given in equation 2.47

$$\phi = E_{vac} - E_F \quad \text{equation 2.47}$$

$E_F$  = Fermi energy

$E_v$  = Vacuum energy

The offset in the Fermi energies is equal to the difference of work function of two metals

$$\phi_c = E_F^L - E_F^R \quad \text{equation 2.48}$$

$\phi_c$  = Contact potential

$E_F^L$  = Fermi energy of left-hand metal

$E_F^R$  = Fermi energy of right-hand metal

The solid line represents the potential barrier between two separated metals. When the metals are brought closer together the Fermi energies of the two metals are not equal (different metals), therefore an electric field exists in the vacuum between the metals. All electronic states up to  $E_F$  are full; the unoccupied state is empty. Therefore, no current can flow between the two metals in the absence of an applied bias (Fig 2.30(b)). The direction of flow of current can be controlled by adjusting the potential difference between two metals. If the two metals are brought sufficiently close, the wave functions of the electrons in the two metals overlap and tunneling can occur (Fig 2.30(c) and (d)).

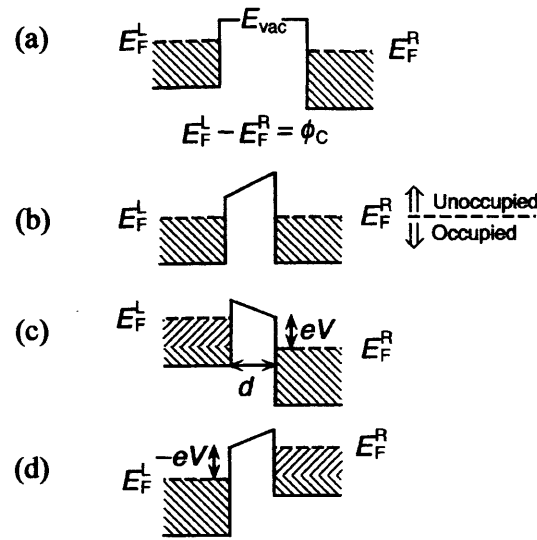


**Fig 2.30** Fermi and vacuum levels for two metals: (a) isolated metals; (b) electrical contact in an absence of applied bias; (c) and (d) applied bias [23].

As electrons always flow from occupied states to unoccupied states, therefore, STM represents a convolution of the density of states of occupied and unoccupied electron states between the tip and the sample surface.

STM is an imaging technique that gives 3 dimensional real space images. This technique allows the measurement of the localized geometric and electronic structure, and atomic resolution may be accomplished. The image is acquired by scanning a tip over the sample surface. While scanning, the tip does not make a contact with the sample.

Once the sharp tip and the surface are close enough their wave functions overlap and a finite probability exists that electron can cross the barrier when a bias is applied between sample and the tip. The resulting current,  $I$  is

$$I = C \rho_t \rho_s e^{s\phi^{1/2}} \quad \text{equation 2.49}$$

where  $C$  is a constant

$\rho_t$  and  $\rho_s$  are electronic density of tip and sample

$\phi$  is a parameter related to the barrier between tip and sample

$s$  is the distance between tip and sample

Tunneling is sensitive to electronic structure, the convolution of filled density of states of the left-handed metal (-) and empty density of states of the right-handed metal (+). The tunneling current depends exponentially on the gap and the barrier height. So if we increase/decrease the separation by a few angstrom ( $\text{\AA}$ ), the tunneling current would change one order of magnitude. For a metal tip and a metal sample, changing the bias voltage changes the direction of the current. Tunneling current is a very sensitive function of tunneling gap (space between tip and sample) as in Fig 2.31. If one metal is also a sharp tip, most of  $I_{\text{tunnel}}$  will travel through a terminal atom, giving atomic scale resolution.

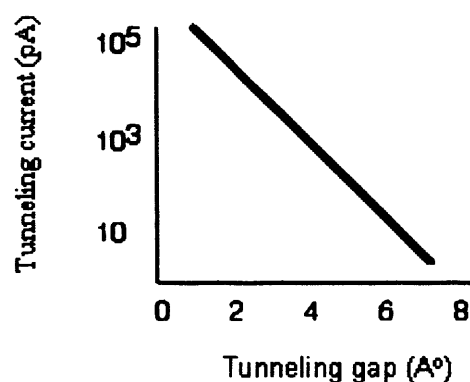


Fig 2.31 Graph of tunneling current against tunneling gap [25].

An electron can only tunnel if there is an unoccupied state with the same energy in the other electrode. In case of a negative potential on the sample the occupied states generate the current, whereas in case of a positive bias the unoccupied states of the sample are of importance.

STM can be operated in 2 modes: constant current and constant height mode.

### (1) Constant current mode

A feedback mechanism is used to maintain a constant current while a constant bias is applied between the tip and the sample. This mode (Fig 2.32) needs a constant tip-sample current while the tip is scanned over the sample; the vertical position of tip is altered to maintain constant current. The piezoelectric element is used to control the motion in the three directions (x, y and z). The linear voltage ramps applied to the

x and y piezoelectric element makes the tip move over the surface. The change of vertical tip position constructs the image, representing a constant charge density contour of the sample.

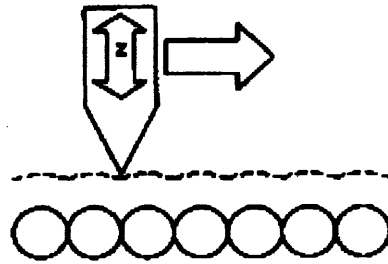


Fig 2.32 The constant current mode of STM [25].

## (2) Constant height mode

This mode (Fig 2.33) needs constant height and applied bias at the same time. Topographic structure varying with the sample-tip separation results in a variation of current while the tip scans over the sample. In this case, the current, related to the charged density, provides the image.

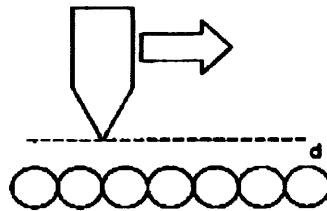


Fig 2.33 The constant height mode of STM [25].

Constant current mode can produce contrast directly related to electron charge density profile; it works slowly but works for rough surfaces while the constant height mode provides a fast scan but it only works well for flat areas. However, atomic resolution image are possible obtained under the optimum condition e.g. sharp tip and a clean sample.

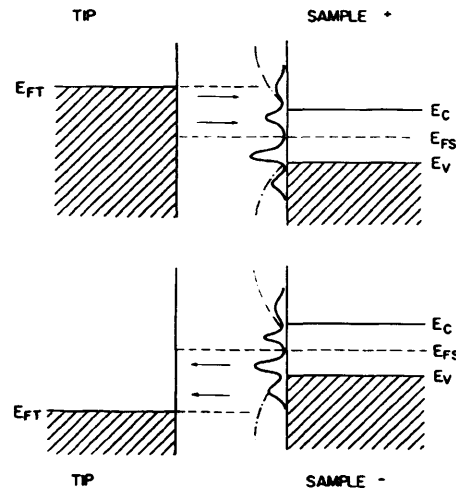
### 2.4.4 Scanning tunneling spectroscopy (STS)

STS in STM provides electronic information about the sample by probing the electron density of the surface as a function of bias. There are 2 methods to acquire spectroscopic information.

(1) Point spectroscopy: move the tip to the interesting point of the surface, switch off the feedback mechanism, scan the tip bias and record the result variation in current. Fig 2.34 shows the idealized band structure and current flow in STS. Occupied and unoccupied energy states can be probed by this ramped bias. The magnitude of current at a specific voltage directly relates to the density of states of the sample at that energy. The constant  $C$  is a linear function of voltage. Spectroscopy data can be related to the sample electronic structure ( $D_s$ )

$$\frac{I}{V} = C * D_s e^{-1.025Z\phi^{1/2}} \quad \text{equation 2.50}$$

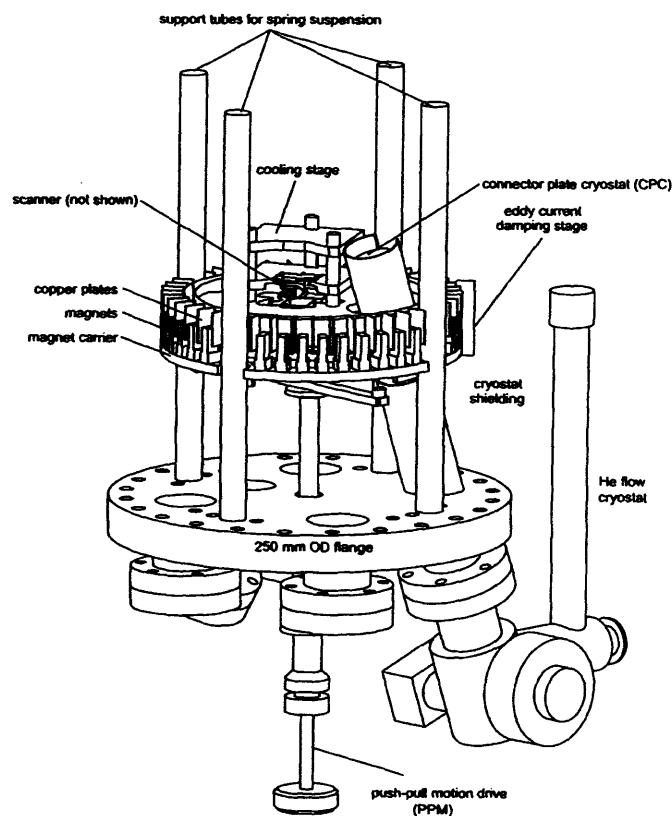
(2) Obtain spectroscopic information involving collection of images at various biases. It can be achieved by changing the bias and recording the current at several values of applied bias.



**Fig 2.34** Schematic diagram of tunneling spectroscopy, Note the tip is a metal with continuous occupation to the Fermi level and the sample is a semiconductor. The shaded area represents the occupied state region [23].

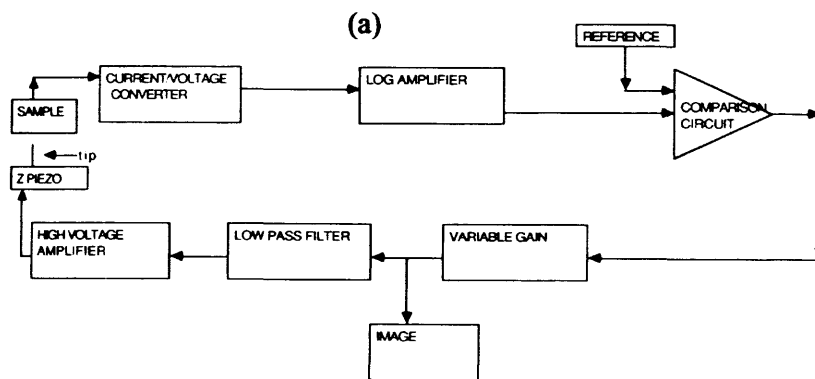
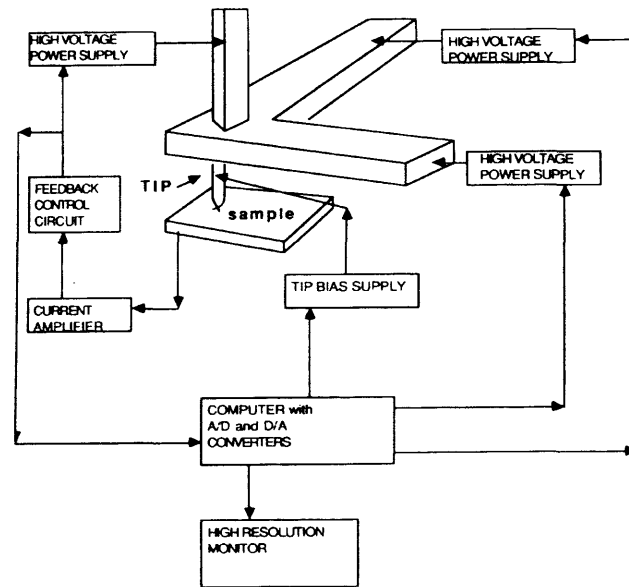
### 2.4.5 Instrumentation for Scanning Tunneling Microscopy

Fig 2.35 shows a schematic of the STM stage of the spectrometer



**Fig 2.35** Side view of the VT STM (Omicron) [26].

Fig 2.36 shows features of the STM control circuits. The high-voltage power supplies connected to the x and y piezoelectric elements are programmed with coordinated ramp functions to execute scanning. The low-voltage power supply provides the sample-tip bias and is programmable for spectroscopy measurements. The tunneling current can be amplified by 7-10 orders of magnitude. It needs to be done as close as possible to the tunnel junction to avoid noise incorporated into the signal before amplification. The output of the amplified current enters the feedback controller which compares the value to a reference.



(b)

**Fig 2.36** Schematic diagram of STM in (a) and the feedback control circuit is expanded in (b) [20].



The monoatomically sharp tip (W, Pt, Ir) is mounted on a 3 D drive. The tip diameter has a pronounced effect on the image. The electronics control  $V$  (0-3 V) and measure  $I$  (1 pA-10nA). The resistance of the gap is approximately  $10^7$ - $10^{10}\Omega$ . The sample-tip separation typically is 2 – 5 Å. Figure 2.37 shows a diagram of a working STM.

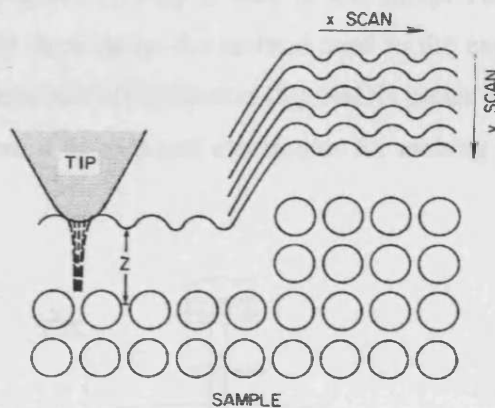


Fig 2.37 Schematic diagram of the imaging process of STM [24].

The movement of the tip in  $x$ ,  $y$  and  $z$  directions (Fig 2.38) is controlled by the piezoelectric scanner. The tip holder consists of three piezoceramic tubes that can creep on the surface (jerk motion), and central piezoelectric leg attached to the tip whose motion can be controlled by the voltage (usually periodic saw-tooth voltage) applied to it.

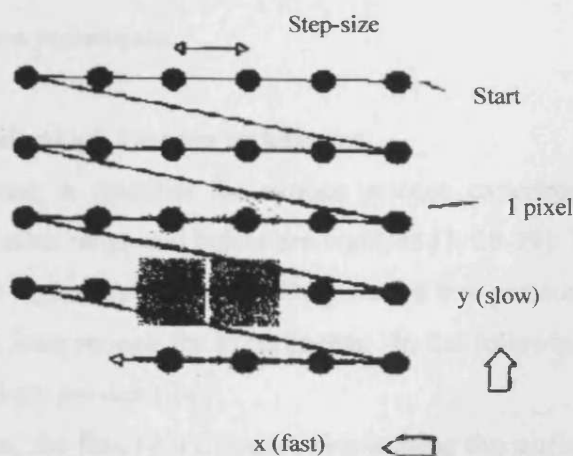
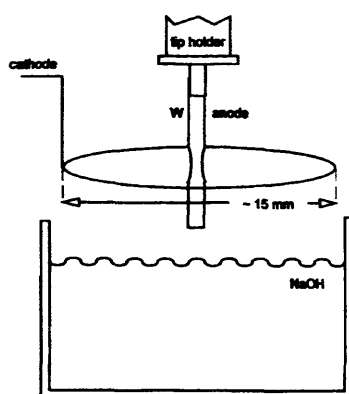


Fig 2.38 Computer control movement of the tip in  $x$  and  $y$  directions controlled by the piezoelectric scanner [25].

### 2.4.6 Tip preparation

The single atom at the tip termination is generally regarded to be necessary for imaging at atomic resolution [5, 27]. STM tips are sometimes made from cut pieces of high purity metal wire, but a standard method for STM tip production is electrochemical etching. The tungsten (W) tip is used in this study. The diagram of the tip preparation is in Fig 2.39 showing as the method used in the experiment, called DC etching 'lamella'. It consists of NaOH solution (8 g NaOH pellet in 100 mL distilled or de-ionized water), 0.38mm  $\phi$  W wire and electronics for etching device (Tip Etching Kit, Omicron).



**Fig 2.39** Schematic diagram of Etching 'lamella' [24] (Tip Etching Kit, Omicron).

## 2.5 Ultrahigh vacuum techniques

### 2.5.1. Principles of ultrahigh vacuum techniques

A clean surface is essential for surface science experiments. This means pressures in the  $10^{-9}$  mbar range and below are required [3, 28-29]. This low pressure system is called ultra-high vacuum (UHV). Only such a low pressure will assure that a surface stays clean long enough for experiments. In the following, some essential parts of UHV technology are described.

In the vacuum, the flux ( $F$ ) of molecules striking the surface of unit area at given pressure,  $P$

$$F = \frac{2.63 \times 10^{20} P(\text{Pa})}{\sqrt{M(\text{g/mole})T}} \quad \text{atoms.cm}^{-2}\text{s}^{-1} \quad \text{equation 2.51}$$

Where M is molecular mass in the units of the atomic mass constant

P is pressure; 1 torr = 1.33 mbar = 133 Pascal

**Table 2.2** Flux ( $F$ ) of gases at pressure of  $10^{-6}$  mbar and a temperature of 300 K [29]

Molecule	Molecular Mass (M)	F ( $\text{cm}^{-2} \text{s}^{-1}$ )
H <sub>2</sub>	2	$1.1 \times 10^{15}$
H <sub>2</sub> O	18	$3.6 \times 10^{14}$
CO	28	$2.9 \times 10^{14}$
O <sub>2</sub>	32	$2.7 \times 10^{14}$
CO <sub>2</sub>	44	$2.3 \times 10^{14}$

Table 2.2 shows the flux of gas at pressure of  $10^{-6}$  mbar and temperature of 300 K. As surface atom concentration are approximately  $10^{15}$  atoms per square centimeter, it means if every gas molecule under the above conditions sticks on the surface a monolayer is formed in a few seconds.

Mean free path ( $\lambda$ ) is the average distance that particle travels between collisions with other particles.

$$\lambda = \frac{kT}{\sqrt{2}\pi d^2 P} \quad \text{equation 2.52}$$

where  $T$  is temperature,  $P$  is the pressure and  $d$  is the molecular diameter

Therefore, in a UHV system the mean free path of molecule is meters. It means that it is more likely the molecule in the UHV system hits the walls of the vacuum chamber rather than another molecule.

### 2.5.2 Vacuum requirement for analysis equipment

Under normal high – vacuum conditions ( $\sim 10^{-6}$  mbar) a clean surface would become rapidly covered with contaminants from the residual gas atmosphere. In surface science studies it is necessary to reduce the rate at which gas molecules adsorb.

Not only to keep the sample surface clean but also to use the techniques for surface analysis requires a UHV system. For XPS photoelectrons should be able to travel from sample to energy analyzer without collision with residual gas molecules and  $10^{-5}$  -  $10^{-6}$  mbar will be sufficient. A high vacuum is also required to prevent electrical discharge in the X- ray source and electron detector. LEED also need UHV for operation.

### 2.5.3 Pumps for UHV

The base vacuum in UHV is determined by gas emitted from the walls of the apparatus and from the equipment inside the chamber. The diagram of the pumping in the UHV system (Fig 2.40) consists of roughing pump, turbo-molecular pump, ion pump, titanium sublimation pump as described below.

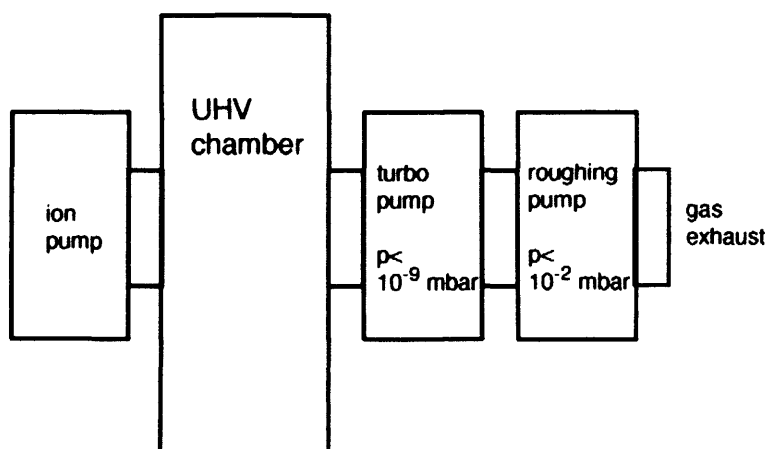
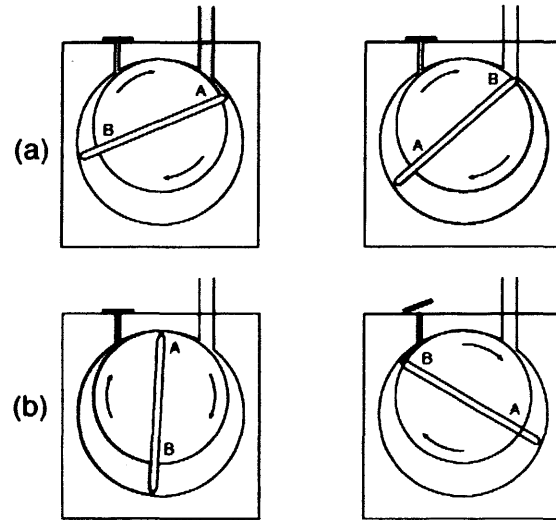


Fig 2.40 Schematic diagram of pumping for a UHV system [29].

(1) **Oil rotary pumps** ( $1 \text{ atm} - 10^{-3}$  mbar), this pump removes gases from the turbo molecular pump chamber. The pump consists of a wheel with blades on its perimeter lubricated with oil (Fig 2.41). The blades trap air molecules from vacuum vessel

between the wheel and wall by rotating of the wheel. After that the air molecules transports to an exhaust pump by a one-way valve. The rotary pump works well when the pressure is high enough to let a gas flow through the pump. When the mean free path of molecule is very long the turbo-molecular pump is required (second stage).



**Fig 2.41** Schematic diagram of an oil-sealed rotary vane pump [29] : (a) gas from the vacuum system enters into the pump and (b) the gas are expelled to the pump exhaust.

Firstly, a rotary oil pump is used to decrease the pressure from 1 atm to  $10^{-2}$  mbar. After that, turbo molecular pump works to decrease the pressure down to  $<10^{-9}$  mbar.

**(2) Turbo molecular pumps** usually employed to operate from  $10^{-1}$  to  $10^{-9}$  mbar. A turbo pump consists of several planes of blades which rotate at extremely high velocities, when the blades spin and hit molecules they are moved towards the exhaust pump. The gas molecule collides with fast moving blade to achieve low pressure (Fig 2.42). The speed of blades has to be fast, typical values are up to 100 krpm.

Once the low pressure has been achieved it can also be maintained by another type of pump, called an ion pump.

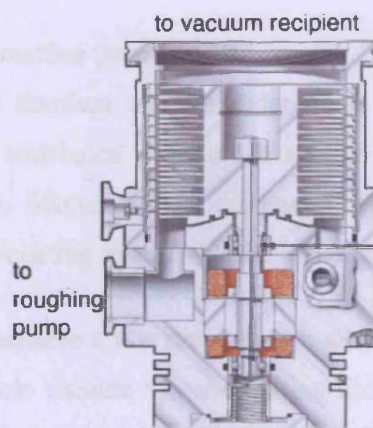


Fig 2.42 Schematic diagram of a turbo-molecular pump [30].

(3) **Ion-pumps**, pressure range of  $10^{-5}$ - $10^{-10}$  mbar. The pump consists of 2 titanium plates with a titanium cell construction (Fig 2.43). The gas molecules, ionized by the high potential between anode and cathode then go into the pump. Electrons move towards the cells and the ions go to one of the plates. The magnetic field causes electrons and ions to move in a circle. The ionization probability is increased by the presence of the magnetic field which makes the electrons travel in a twist motion. The ion can be buried when they hit the titanium cathode. Moreover, the Ti, sputtered off the cathodes, can react with the residual gas and increase the pumping effect. The ion pump does not eliminate gas from the system, but binds the residual molecule gas.

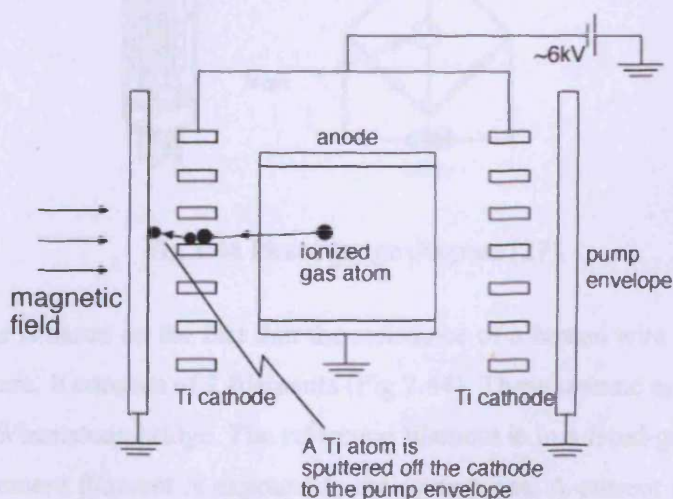


Fig 2.43 Schematic of an ion pump [29].

### (3) Titanium sublimation pump (TSP)

An alloy of titanium and molybdenum is mounted in a carrier, designed to have low electrical resistance. Titanium is sublimed immediately after passing a high current through the filament. This sublimated evaporant then covers the chamber walls. The titanium coating reacts with the active gas and removes it from the system.

In order to achieve a low pressure in a short time it is necessary to do a called bake-out of the whole vacuum system. During the bakeout the system is heated to at least 100-200 °C for period of time (at least 24h). The heating causes a fast removal of the impurities adsorbed on the walls of the vacuum system (mostly water).

### 2.5.4 Pressure measurement

There are 2 methods for pressure measurement in UHV system: Pirani gauge and ion gauge.

(1) **Pirani gauge** is used to monitor low pressure (1 atm –  $10^{-3}$  mbar)

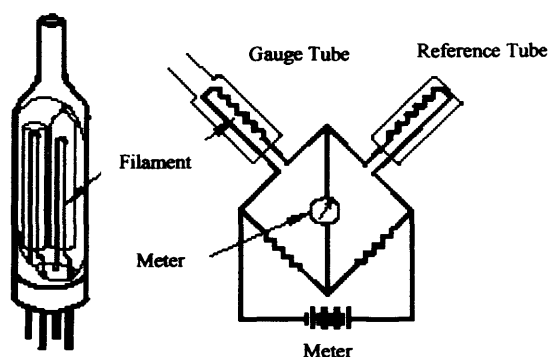


Fig 2.44 Pirani gauge diagram [27].

This gauge is based on the fact that the resistance of a heated wire depends on the wire temperature. It consists of 2 filaments (Fig 2.44). These operate as resistances in two arms of a Wheatstone bridge. The reference filament is in a fixed-gas pressure, while the measurement filament is exposed to the system gas. A current through the bridge heats both filaments. Gas molecules hit the heated filament and conduct away



some of the heat. At high pressures the wire will be cooled by collisions with the residual gas whilst at low pressure the temperature of the wire rises. If the gas pressures around the measurement filament are not identical to that around the reference filament, the bridge is unbalanced and the degree of unbalance is a measure of the pressure. The measurement principle allows these gauges to cover a total range from 1 atm to  $10^{-3}$  mbar; not very good for  $P > 1$  mbar.

(2) **Ion gauges**, used to measure pressures in range  $10^{-4} - 10^{-11}$  mbar consists of 3 components: a filament (tungsten), a grid (anode) and a collector (Fig 2.45).

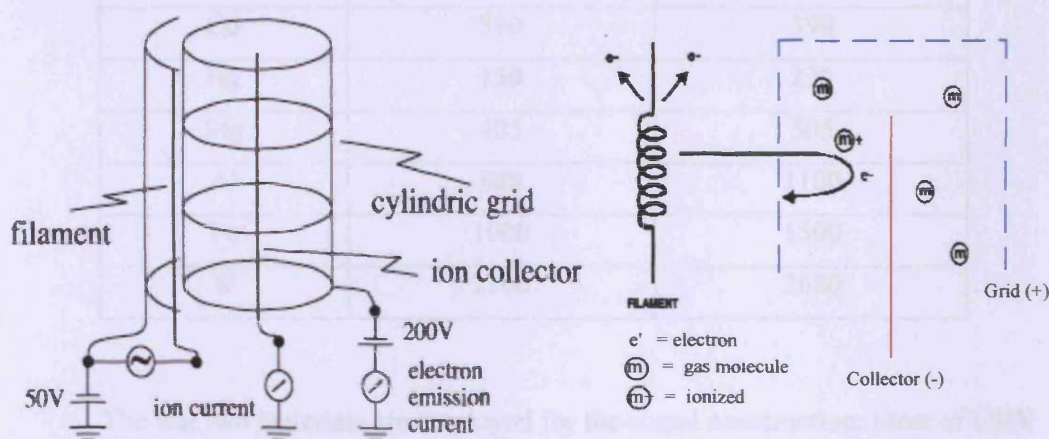


Fig 2.45 Diagram of (a) ion gauge and (b) a process of measurement [29].

A current through the filament causes the generation of electrons inside the cylindrical cage. These electrons are accelerated through a potential of approximately 150 V towards the grid and collide with any gas molecules to produce positive charged ions. These ions are attracted to the negatively charged tungsten wire (the collector). The current of positive ions to the collector is directly proportional to the pressure of molecules within the anode. The ion gauge can be used in for pressures between  $10^{-4}$  and  $10^{-11}$  mbar.



### 2.5.5 Material and construction for UHV system

All materials in UHV system must be tolerate high temperature during bake-out and the vapor pressure of materials has to be low at normal operating temperature. Table 2.3 gives the temperatures in K to generate a certain vapor pressure.

**Table 2.3** The temperatures in K to generate a vapor pressure [27]

element	Temperature (K) at $P=10^{-10}$ mbar	Temperature (K) at $P=10^{-6}$ mbar
Na	310	400
Zn	355	450
Cd	310	390
Hg	150	230
Mg	405	505
Al	860	1100
Fe	1000	1300
W	2160	2680

The last two materials are employed for the actual construction. Most of UHV chambers are made of stainless steel (iron-carbon alloy with some chromium), all filaments are made of tungsten and electrical insulators are made of ceramics.

A UHV chamber has many circular flanges where windows or apparatus with the same flange type can be bolted on. These flanges have sharp edges profiled on their working sides. There is a leak-tight seal between the two flanges, made by placing a copper gasket between the edges. It is required to use a copper gasket because of the bake-out at high temperature.

### 2.5.6 Chemical analysis of the gas in the system

The chemical composition of the residual gas in the chamber needs to be measured, and also the impurity of gas used for experiment for leak checking. The test

can be done by direct a flow of He gas on the suspected leak from outside the system. If there is a partial pressure of He presence inside, the leak can be found.

A quadrupole mass spectrometer (MS), consists of three sections (Fig 2.46). First, residual gas molecules are ionized in the ionizer, and these ions are then accelerated and focused to the second part called an electrical quadrupole field. The last is the detector containing an electron multiplier leading to an amplification of the signal.

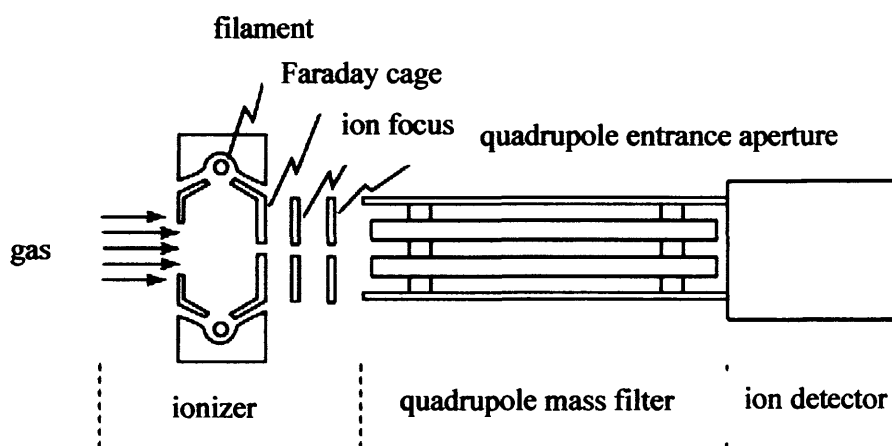


Fig 2.46 A quadrupole mass spectrometer [29].

The main residual gases in the chamber are  $H_2$ ,  $H_2O$ ,  $CO$  and some  $CO_2$ . After the bake-out of the system, the partial pressure of water will be reduced and the total pressure will be dominated by  $CO$  and  $H_2$ .

## 2.6 Instrumentals in Experiments

4 of main chambers are connected by 3 gate valves (---) in the UHV system in Fig 2.47.

### 2.6.1 Components of the machine

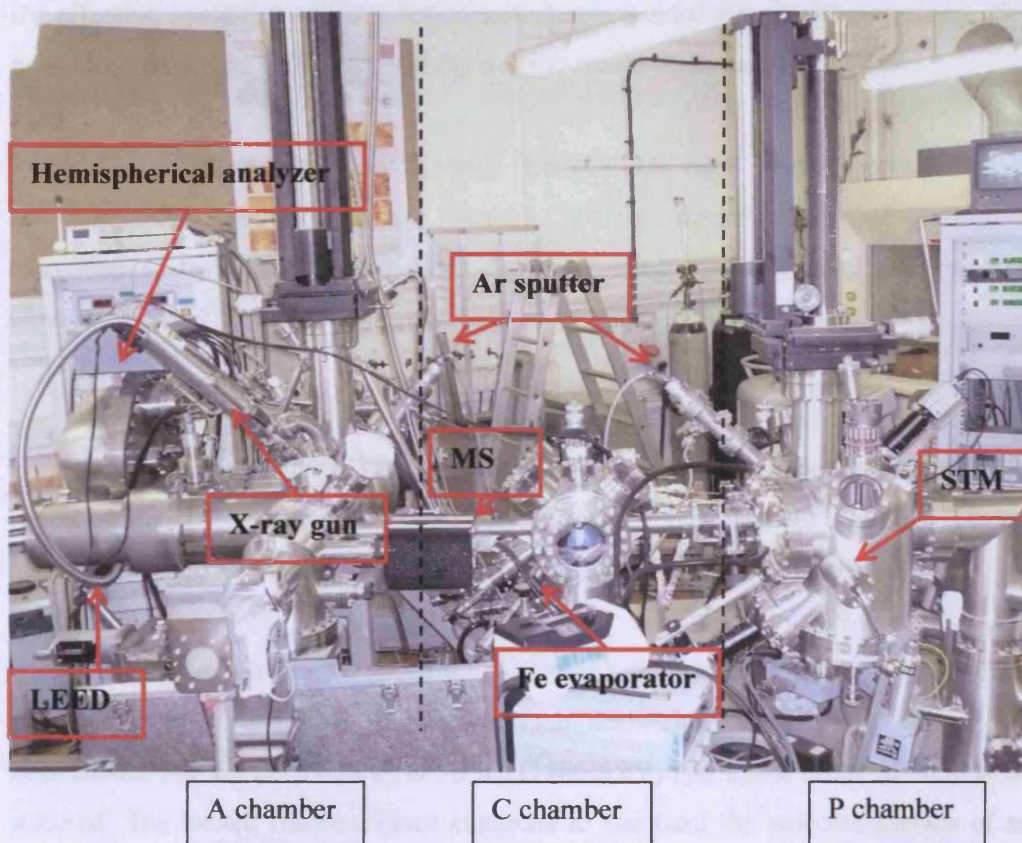


**Fig 2.47** Components of instruments in experiment.

There are 4 main chambers in the UHV system

- (1) Preparation Chamber (P Chamber): E-beam and  $\text{Ar}^+$  sputtering gun and the gas line ( $\text{Ar}$ ,  $\text{O}_2$ ,  $\text{CO}_2$ ,  $\text{NH}_3$  and acrylic acid)
- (2) Center Chamber (C Chamber): Fe evaporator
- (3) Analysis Chamber (A Chamber): XPS, LEED and  $\text{Ar}^+$  sputtering gun
- (4) STM Chamber: STM

The devices relating to the experimental studies are briefly described as follows

**(1) Ar<sup>+</sup> ion sputtering** (Omicron ISE 10 Sputter Ion Source) to clean the sample, the ionization is done by electron bombardment. High beam energy is used for effective sputtering while a low beam energy is used for sensitive samples. The broad ion beam with a flat top intensity can get uniform sputtering.

**(2) E-beam heating** (Omicron, EBHC) the high voltage power supply accelerates the electron from the filament. Most of kinetic energy of electron is converted to heat the filament. This device is used for annealing, performed in chamber P.

**(3) Fe evaporator** (Omicron UHV evaporator EFM 3), Fe is evaporated from a Fe rod (cleanliness 99.999 %), achieved by electron bombardment heating. The operating conditions are high voltage current 10 mA, flux monitor current 6 nA and high voltage 800 V. Fe was deposited on the Cu(100) substrate in the C chamber.

**(4) XP spectrometer** (DAR400, Omicron), the surface chemical composition was analyzed by using XPS. The Omicron nanotechnology spectrometer source, has twin anodes Mg K $\alpha$  (1253.6 eV) or Al K $\alpha$  (1486.6 eV) that allow either of them to be selected. The heated filament gives electrons to bombard the selected surface of an anode at high positive potential. EA125 energy analyzer (Omicron) is used with an electron pass energy of hemispherical analyzer 50 eV.

**(5) LEED** (LEED, Omicron SPECTARLEED) was used to study the structure of sample films. The images were recorded employing a computer controlled video camera.

**(6) STM** (VT STM Omicron), is mounted in the small UHV-chamber (STM chamber). The STM images are collected as constant current topographies (CCT's), they are signified in brown-tone images.

**References:**

- [1] G. Attard and C. Barnes, *Surfaces*, Oxford University Press, 2003.
- [2] J. M. Walls and R. Smith, *Surface Science Techniques*, PERGAMON, Loughboough University of Technology, Leicestershire, UK, 1<sup>st</sup>, 1994.
- [3] G. Ertl, J. Kupperts, *Low Energy Electrons and Surface Chemistry*, VCH Verlagsgesellschaft mbH, 2<sup>nd</sup>, 1985.
- [4] A. F. Carley, Chapter 2: Photoelectron Spectroscopy, *Electron Spectroscopic Studies of Solid Surfaces*, Ph.D, 1980., University of Bradford.
- [5] D. J. Morgan, Chapter 2: Spectroscopic and Theoretical Studies of Multifunctional Hydrocarbon at Cu(110) surface, Ph.D, 2002., Cardiff University.
- [6] <http://www.fysik.uu.se/AoM/Teaching/ElecSpec/ElecSpec.html>  
This text is a version of the course Electron Spectroscopy lectured by L.Karlsson at Department of Physics Uppsala University 1981-1995.
- [7] <http://www.cem.msu.edu/~cem924sg/Topic09.pdf>  
Introduction to Surface Analysis, Michigan state University
- [8] R. H. Williams, G. P. Srivastava and I T Mc Govern, *Rep. Prog. Phys.*, 43, 1980.
- [9] R. P. H. Gasser, *An introduction to Chemisorption and Catalysis by Metals*, Clarendon Press, Oxford, 1985, 148
- [10] K. Siegbahn, *Proc. R. Soc. Lond. A* **33** (1970) 268.
- [11] P. W. Atkins, *Physical Chemistry*, 5<sup>th</sup> ed, Oxford University Press, Oxford, 1944.
- [12] T. E. Madey, J. T. Yates, Jr. and N. E. Erickson, *Chem. Phys. Lett.* **19** (1973) 487.
- [13] A. F. Carley and M. W. Roberts, *Proc. Roy. Soc. Lond. A.*, **363** (1978) 403.
- [14] J. H. Scofield, *J. Elect. Spec Rel. Phen.* **8** (1976) 129.
- [15] D. E. Penn, *J. Elec. Spec. Rel. Phenom.* **9** (1976) 29.
- [16] [www.chem.queensu.ca/~horton/Resear3.jpg](http://www.chem.queensu.ca/~horton/Resear3.jpg)
- [17] DAR400 X-ray source and power supply, version 2.0, November 21, 2000
- [18] EA 125 Energy Analyzer, User's Guide, Omicron Nanotechnology, version 2.1, July 11, 2002.

- [19] L. J. Clarke, Surface crystallography an introduction to low energy electron diffraction, , John Willey & Sons, 1985.
- [20] R. P. H. Gasser, An introduction to chemisorption and catalysis by metals, Clarendon Press, Oxford 1985.
- [21] M. P. Seah, W. A. Dench, Surf. Interf. Anal. 1 (1979) 2.
- [22] J. M. Walls and R. Smith, Surface Science Techniques, Pergamon, 1994.
- [23] D. A. Bonnell, Scanning Tunneling Microscopy and Spectroscopy, Theory, Techniques and Application, VCH, New York, 1993.
- [24] K. W. Kolasinski, Surface Science foundations of Cataylysis and Nanoscience, John Willey&Sons, UK, 2002.
- [25] <http://www.cem.msu.edu/~cem924sg/LibraryPapers.html>
- [26] VT STM user's Guid, version 1.7, March 26, 2002, Omicron Nanotechnology
- [27] Tip Etching Kit (Omicron) , version 1.1, October 29, 1998.
- [28] G. A. Somorjai, Introduction to Surface Chemistry and Catalysis, John Willey & Sons, 1994.
- [29] [http://www.vacgen.com/asp/catalogue.asp?url=http%3A//www.vacgen.com/catalogue/section-8/page08\\_06.htm&frame=1](http://www.vacgen.com/asp/catalogue.asp?url=http%3A//www.vacgen.com/catalogue/section-8/page08_06.htm&frame=1)
- [30] [http://whome.phys.au.dk/~philip/q1\\_05/surflec/node7.html](http://whome.phys.au.dk/~philip/q1_05/surflec/node7.html)

## Chapter 3

### Iron Oxide Thin Film

#### 3.1 Introduction iron-oxide crystal structures

Metal oxides are an important class of materials that are involved in environmental science, electrochemistry, magnetism and other chemical process. One of the most important applications is heterogeneous catalysis [1]. Metal oxides are used for many organic compound syntheses via selective oxidation, dehydrogenation and other chemical processes. Acidic and basic sites in oxide ionic compounds may control their surface properties. The understanding of the atomic mechanism of a catalytic reaction is very important for catalyst development.

The complexity of metal oxides is a big problem for surface science. Impurities contained in single crystal samples are even harder to control in a surface study. Most metal oxides are electric insulators preventing electron spectroscopy or scanning tunneling microscopy measurements (STM). The thermal conductivity and temperature management by thermocouple is poor. To avoid these problems making thin oxide films grown on a conducting substrate would aid surface science characterization.

Iron oxide is one of the most important oxides commercially. It has a high selectivity for many reactions. FeO (wüstite),  $\alpha$ -Fe<sub>2</sub>O<sub>3</sub> (hematite) and Fe<sub>3</sub>O<sub>4</sub> (magnetite) are 3 common natural iron oxides. Iron oxide film preparation and the study of a Fe<sub>3</sub>O<sub>4</sub> film and its reactivity is one of the aims of this research. In this Chapter iron oxide preparation in UHV is mainly discussed.

Iron oxides are formed in different stoichiometries and crystal structures in different conditions and specific iron oxide formation can be made by using proper temperature treatment and oxygen atmosphere from the oxide phase diagram [1]. The iron-oxygen phase diagram is shown in Fig. 3.1.

Fe<sub>1-x</sub>O (wüstite) [1, 2] forms in a sodium chloride structure containing four formula units in a cubic unit cell. The O<sup>2-</sup> anions form a closed-packed fcc sublattice

with octahedrally coordinated  $\text{Fe}^{2+}$  cations located in the interstitial O sites of the structure. Under thermal equilibrium this phase is stable at temperature above 843 K

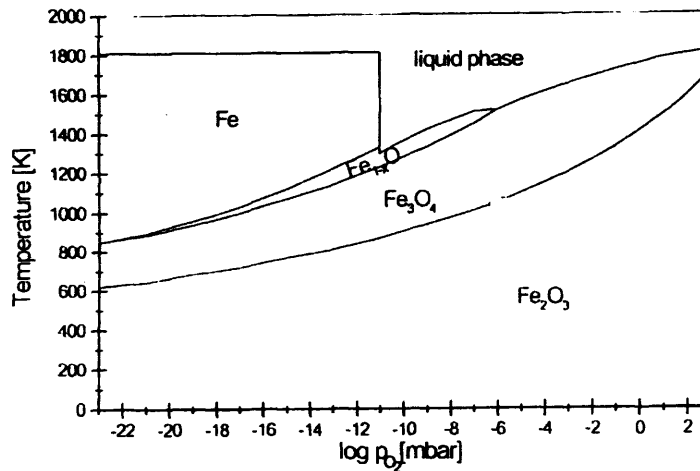


Fig 3. 1  $p$  (oxygen) - temperature diagram of iron -oxygen system [1].

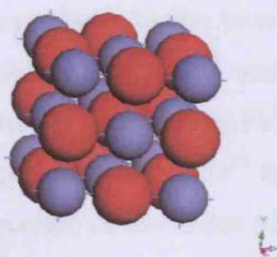
whilst at lower temperature it converts to metal and  $\text{Fe}_3\text{O}_4$ . Hence, this oxide must be made at temperature greater than 843 K. The wüstite is normally a large deviation stoichiometry,  $\text{Fe}_{1-x}\text{O}$ , with  $x$  varying by 5-10% depending on  $\text{O}_2$  partial pressure and temperature. The whole FeO structure is shown in Fig 3.2(a). The low index (100), (110) and (111) surfaces of FeO are also explained.

FeO(100) in Fig 3.2(b) shows the  $3.06 \text{ \AA}$  square unit cell of Fe and O atoms and each layer is  $2.16 \text{ \AA}$  high. The  $3.16 \times 4.3 \text{ \AA}^2$  rectangular unit cell of Fe and O atoms in Fig 3.2(c) is FeO(110) and  $3.06 \text{ \AA}$  hexagonal unit cell of Fe and O in FeO(111) plane shows in Fig 3.2(d). Along the [111] direction the Fe and O(111) planes form the cubic ABC stacking sequence with an interlayer distance of  $1.25 \text{ \AA}$ . Fe layer is  $1.25 \text{ \AA}$  high and the height of each layer of both Fe and O atoms is  $2.50 \text{ \AA}$ .

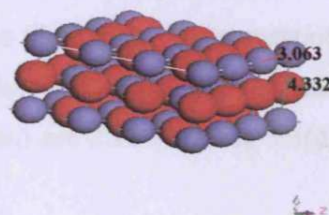
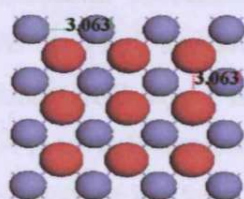
$\alpha\text{-Fe}_2\text{O}_3$  (hematite) [1, 2] is the only oxidized form of iron that is stable at room temperature in thermodynamic equilibrium with  $\text{O}_2$  atmosphere from phase diagram in Fig 3.1. The O anions form a hcp lattice with ABAB stacking with  $\text{Fe}^{3+}$  in interstitials. The lattice constant of  $\alpha\text{-Fe}_2\text{O}_3$  is  $5.03 \text{ \AA}$  (Fe-Fe interatomic distance). Low index planes of this oxide are not explained further here due to conditions in the experiment leading only to reduced forms of iron oxide.



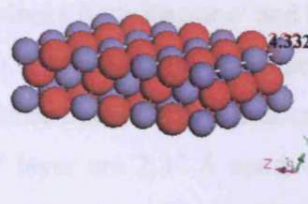
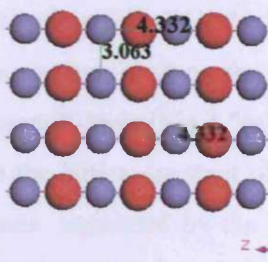
## (a) FeO



## (b) FeO(100)



## (c) FeO(110)



## (d) FeO(111)

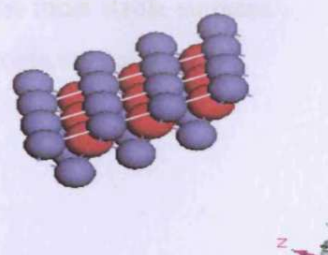
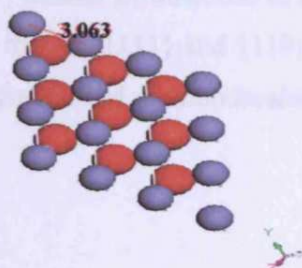


**Fig 3.2** (a) FeO wüstite crystal in NaCl structure. A perspective top and side views of FeO in (b) FeO(100) , (c) FeO(110) and (d) FeO(111) surface structure space ( red represents oxygen atoms and blue iron atoms).

$\text{Fe}_3\text{O}_4$  (magnetite) [1, 2] crystallizes in the inverse spinel structure. The O anions form a close-packed fcc sublattice with  $\text{Fe}^{2+}$  and  $\text{Fe}^{3+}$  located in interstitial sites. The tetrahedral interstitial sites are occupied by  $\text{Fe}^{3+}$  ions while the octahedral interstitial sites are occupied by equal numbers of  $\text{Fe}^{2+}$  and  $\text{Fe}^{3+}$ . The unit cell has a lattice constant of 8.396 Å. The structure of low index planes (100), (110) and (111) of  $\text{Fe}_3\text{O}_4$  is clarified in Fig 3.3.

The  $\text{Fe}_3\text{O}_4(100)$  plane in Fig 3.3(b) has two alternating layers (A and B) as a stacking series. The tetrahedral coordinated  $\text{Fe}^{3+}$  ions is in A-layer, while the octahedral coordinated  $\text{Fe}^{2+}$  and  $\text{Fe}^{3+}$  ions are in B-layer in Fig 3.3(c). The separation between neighboring planes (A-B layer) is 1.05 Å, while the separation between successive like planes (A-A or B-B interplanar separation) are 2.10 Å in Fig 3.3(d) and (e). Fe-Fe interatomic distance is 5.94 Å.

The  $\text{Fe}_3\text{O}_4(110)$  plane is shown in Fig 3.4. The atomic distance of Fe-Fe is 5.14 Å with each layer 2.9 Å high.

In the  $\text{Fe}_3\text{O}_4(111)$  plane (Fig 3.5), the hexagonal O planes form a cubic ABC stacking order. Fe layers alternately sit on the O(111) planes both Kagome' and three mix-trigonal (three hexagonal) layer (Fig 3.5(a) and (b)). The atomic Fe-Fe distance is 5.94 Å corresponding to the lattice constant of the 2-dimensional surface unit cell of  $\text{Fe}_3\text{O}_4(111)$ . O(111) planes separated by the Kagome' layer are 2.37 Å apart while O(111) planes are separated by 2.48 Å apart in the three mix-trigonal layers. Then the distance between every second O layer is 4.85 Å corresponding to the distance between equivalent (111) surface terminations of  $\text{Fe}_3\text{O}_4$ .

It has been said that the {111} and {110} planes are the most stable surfaces of  $\text{Fe}_3\text{O}_4$ , leading to octahedral and rhombodecahedral macroscopic crystal form [1].

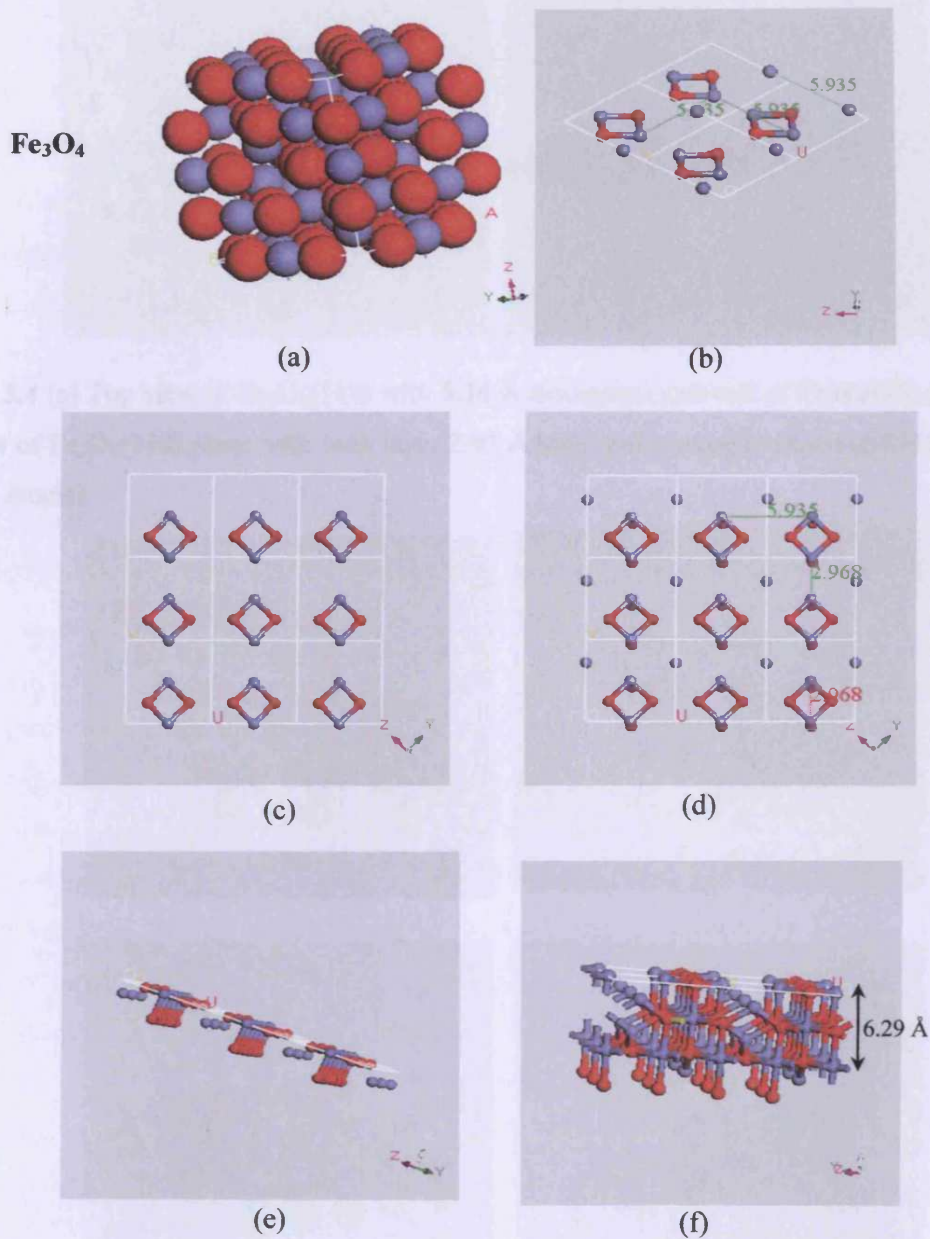


**Fig 3.3** (a)  $\text{Fe}_3\text{O}_4$  crystal in inverse spinel structure; (b) perspective top views of  $\text{Fe}_3\text{O}_4(100)$  BA layer with 5.94 Å Fe unit cell; (c) Fe in octahedral interstitial sites with 1.049 Å high in this layer; (d) Fe in octahedral and tetrahedral sites in AB layer; (e) the side view of BA layer with distance 2.099 Å high and (f) BABABA stacking in [100] with distance 6.295 Å (red represents oxygen atoms and blue iron atoms).



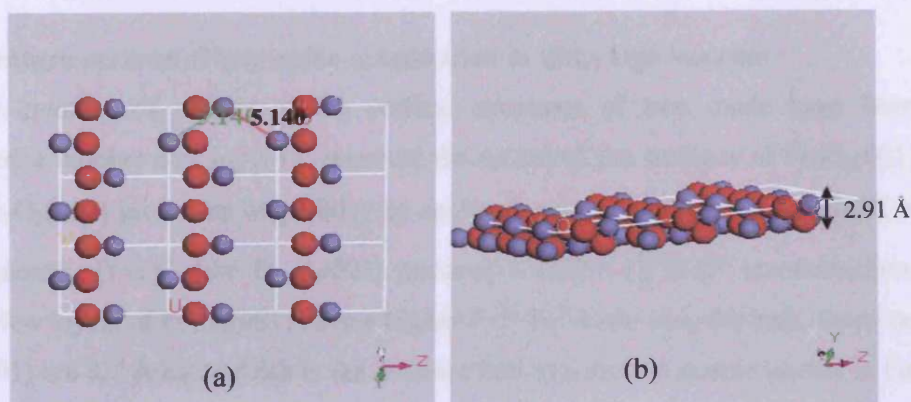


**Fig 3.4** (a) Top view of  $\text{Fe}_3\text{O}_4(110)$  with 5.14 Å hexagonal unit cell of Fe and (b) side view of  $\text{Fe}_3\text{O}_4(110)$  plane with each layer 2.91 Å high (red = oxygen atoms and blue = iron atoms).

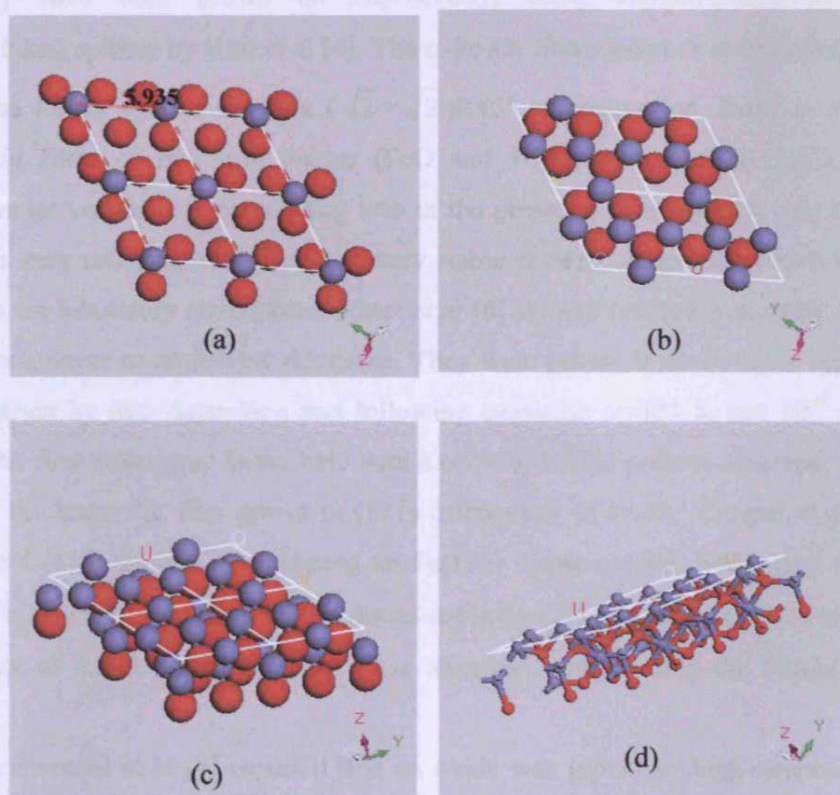


**Fig 3.5** Perspective side and top views of  $\text{Fe}_3\text{O}_4(111)$  (a) Mix-trigonal layer (b) Kagome' layer (c) 4.85 Å high between equivalent (111) surface terminations of  $\text{Fe}_3\text{O}_4$  (d) Fe ions in octahedral and tetrahedral sites in the side view (red = oxygen atoms and blue = iron atoms).

### 3.2 Literature reviews of iron oxide preparation in ultra high vacuum

A number of studies of the surface structures of iron oxide have been conducted. Chamber and Joyel [2] reported the nature of the surfaces of  $\text{Fe}_3\text{O}_4(001)$  and  $\gamma\text{-Fe}_2\text{O}_3(001)$  grown on  $\text{MgO}(001)$  by molecular beam epitaxy.  $\gamma\text{-Fe}_2\text{O}_3(001)$  is unambiguously  $(1 \times 1)$  while  $\text{Fe}_3\text{O}_4(001)$  assumes a  $(\sqrt{2} \times \sqrt{2})\text{R}45^\circ$  reconstruction. The top few layers of  $\text{Fe}_3\text{O}_4(001)$  have a higher  $\text{Fe}^{3+}/\text{Fe}^{2+}$  ratio than the bulk. Steps on  $\text{Fe}_3\text{O}_4(001)$  are 2.1 Å high which is the distance between similar atomic planes in the inverse spinel structure of magnetite. Fonin et al [3] studied *in situ*  $\text{Fe}_3\text{O}_4(100)$  thin films on  $\text{MgO}(100)$  single crystals by STM. An atomically resolved  $(\sqrt{2} \times \sqrt{2})\text{R}45^\circ$  wavelike surface atomic structure observed. Moreover,  $\alpha\text{-Fe}_2\text{O}_3(0001)$  and  $\text{Fe}_3\text{O}_4(001)$  have been grown on  $\text{Al}_2\text{O}_3(0001)$  using oxygen-plasma-assisted molecular beam epitaxy by Kim et al [4]. The  $\alpha\text{-Fe}_2\text{O}_3$  film surface is unreconstructed whereas the  $\text{Fe}_3\text{O}_4$  surface shows a  $(\sqrt{2} \times \sqrt{2})\text{R}45^\circ$  reconstruction. Ruby et al [5] formed thin films of two iron oxides ( $\text{FeO}$  and  $\text{Fe}_3\text{O}_4$ ) prepared on  $\text{MgO}(100)$  substrate under vacuum by evaporating iron in the presence of oxygen. It was found that  $\text{FeO}$  is very unstable while  $\text{Fe}_3\text{O}_4$  is very stable at room temperature even when exposed to the laboratory atmosphere. Ritter et al [6] studied ordered iron oxide films from submonolayer to multilayer thickness. They were grown layer-by-layer on a Pt (100) substrate by iron deposition and following oxidation at 900 K and  $10^{-6}$  mbar oxygen. The first monolayer forms  $\text{FeO}$  with a  $c(2 \times 10)$  LEED pattern observed. With increasing thickness the film grows in (111) orientation of  $\text{Fe}_3\text{O}_4$ . Cappus et al [7] prepared  $\text{FeO}(111)$  surface by oxidizing an  $\text{Fe}(110)$  single crystal. Fellows et al [8] prepared  $\text{Fe}_3\text{O}_4$  (111) formation on a reduced  $\alpha\text{-Fe}_2\text{O}_3$  (112'3) substrate. STM shows step heights of 4.8 Å which separate these terraces corresponding the  $\text{Fe}_3\text{O}_4(111)$  surface.

Karunamuni et al [9] reported that an oxide was grown by high-temperature oxidation of Fe films deposited on a  $\text{Cu}(001)$  substrate. Oxidation was accomplished by annealing the sample to 810 K in presence of oxygen. It was found that  $\text{Fe}_{1-x}\text{O}$  (111) forms for initial iron coverages below 2 ML and that  $\text{Fe}_3\text{O}_4(111)$  forms for thicker initial Fe coverages. Pflitsh et al [10] reported that  $\text{Fe}_2\text{O}_3(111)$  could be prepared by oxidising a smooth epitaxial 5 ML Fe film on  $\text{Cu}(110)$  at 400 K.  $\text{Fe}_2\text{O}_3$  decomposed at 950 K to  $\text{FeO}(111)$ . Weiss et al [1] studied  $\text{FeO}(111)$ ,  $\text{Fe}_3\text{O}_4(111)$

and  $\alpha\text{-Fe}_2\text{O}_3(0001)$  oxide grown epitaxially on a Pt(111) substrate. Iron oxide is produced at  $10^{-6}$  mbar  $\text{O}_2$ ; the first layer forms an FeO-like hexagonal iron-oxygen bilayer containing an  $\text{Fe}^{2+}$  species. At the higher coverage  $\text{Fe}_3\text{O}_4(111)$ , containing  $\text{Fe}^{2+}$  and  $\text{Fe}^{3+}$  species surface termination is formed. Order  $\alpha\text{-Fe}_2\text{O}_3(0001)$  multilayer films contains only  $\text{Fe}^{3+}$  species were prepared by high-pressure oxidation at 30 mbar. Qin et al [11] studied oxidation of the Fe(111) surfaces at oxygen partial pressure of  $1\text{-}5\times 10^{-7}$  torr resulted in the formation of  $\text{Fe}_2\text{O}_3$  and  $\text{Fe}_3\text{O}_4$  at 300 K. At 500 K, the predominant oxide phase was  $\text{Fe}_3\text{O}_4$ .

From these studies, it is clear that iron oxide film formation depends on oxygen exposure, heat treatment and substrate. The copper single crystal is an ideal substrate for iron oxide growth due to a good lattice match, resistance to oxidation, and suitability for performing XPS, LEED and STM.

### 3.3 Experimental Details

The Cu(100) single crystal was cleaned using cycles of  $\text{Ar}^+$  ion sputtering at 1000 eV for 30 min, (Omicron ISE 10 Sputter Ion Source). The ionization is done by electron bombardment. High beam energy is for effective sputtering while low beam energy is for sensitive samples. The broad ion beam with a flat top intensity can get uniform sputtering. Due to Cu being soft, the operating conditions are beam energy  $E = 1000$  V and electron emission current  $I_E = 10\text{mA}$ , extractor voltage is 515 V, focus 820 V and argon pressure is  $5 \times 10^{-6}$  mbar. With this condition, the beam diameter is about 18 mm. Annealing to 870 K for 60 min followed; 2-3 cycles were needed to clean the Cu substrate crystal. The cleaning step was performed in chambers P and A.

The 6-10 ML Fe films were grown with an evaporation rate of  $0.25\text{ MLmin}^{-1}$ . (Omicron UHV evaporator EFM 3), Fe is evaporated from a Fe rod (cleanliness 99.999 %), achieved by electron bombardment heating. The operating conditions are high voltage current 10 mA, flux monitor current 6 nA and high voltage 800 V. During evaporation the pressure increased up to a value between 2 and  $5\times 10^{-9}$  mbar and the Cu(100) substrate was kept at room temperature (295 K). Fe deposition is performed in the C chamber.

Oxide films were produced by oxidizing an Fe multilayer deposited on Cu(100). The sample was exposed to oxygen at a pressure of  $10^{-6}$  mbar at room

temperature and simultaneously, the sample was heated at a slow rate to 850 K and maintained at this temperature for 10 min. The sample was then cooled at a slow rate to 480 K. Oxygen exposure was stopped at around 520 K. All oxygen doses refer to the ion gauge reading in the chamber P.

At every stage of the experiment the surface was analyzed in chamber A at a base pressure  $\sim 10^{-9}$  mbar. The surface chemical composition was analyzed by using XPS. The X-ray Al K $\alpha$  source (DAR 400, Omicron) used in this experiment has a primary energy 1486.6 eV. An EA125 energy analyzer (Omicron) with electron pass energy of hemispherical analyzer was 50 eV is used. The electron collecting angle with respect to the Cu(100) surface plane was set to 90 degree.

The low-energy electron diffraction (LEED, Omicron SPECTARLEED) was used to study the structure of sample films. The images were recorded employing a computer controlled video camera.

The STM is mounted in the small UHV-chamber (chamber C). The working pressure of the system during the STM measurements was well below  $10^{-11}$  mbar. The STM images are collected as constant current topographies (CCT's), they are signified in brown-tone images. The values of the sample bias voltage and the tunneling current are noted in the image.

### 3.4 Results and discussion

#### 3.4.1 Fe on Cu: Characterization of Fe film on Cu(100) by XPS, LEED and STM

In this section, the characterization of 6-10 ML Fe films on Cu(100) will be discussed using XPS, LEED and STM information to understand the formation of the geometric structure and chemical composition on the surface.

The factors affecting Fe growth mode are substrate temperature, flux of Fe evaporation and technique [2, 12].

Fig 3.6 shows an Fe film on Cu(100) wide scan survey XP spectrum. The substrate was contaminated by carbon and oxygen (Surface concentration is  $\sim 2-3 \times 10^{-14}$  cm $^{-2}$ , XPS). The XP spectra of those contaminations are not shown here.

6 ML Fe on Cu(100) surface gives an Fe 2p<sub>3/2</sub> peak at 706.9 eV. The specific scan of XP spectra are slightly asymmetric (in Fig 3.7) because of a coupling with the conduction electrons [13]. Moreover, it has been stated that the electronic relaxation effects in the resonant photoemission process would also give an asymmetric peak. As the photoenergy is turned through the energy corresponding to a transition from the initial ground state to the tightly bond core-hole to bond valence intermediate state. The formation of a core hole was studied by Doniach and Sunjic [9]. If the lifetime of intermediate state is long the electron will have enough time to adjust towards the fully released intermediate state. This effect mostly occurs in rare earth metals having a strong resonant enhancement. The electrons in d and f orbitals show this effect while electrons in p orbitals as in Fe can hardly be observed because it is less localized than the d and f orbital of rare earth metals.

The thickness of the Fe films is computed [14] from the Cu(2p<sub>3/2</sub>) intensity decay following an exponential first-order decay law typical for the travel of radiation through the Cu substrate

$$I(d) = I_0 \exp \left( \frac{-d}{\lambda \cos \theta} \right) \quad \text{equation 3.1}$$

where  $I(d)$  is the intensity after the primary electron beam has traveled a distance,  $d$ , through the solid and  $I_0$  is the initial beam intensity before interaction with the solid,  $\lambda(E)$  is the inelastic mean free path (IMFP).

The inelastic mean free path is 7.57 Å for Al anode excitation of Cu 2p. The thickness of Fe on Cu substrate was about 12 – 20 Å. The step height of Fe is about 1.7 Å. By XP spectra, the Fe films on Cu(100) were about 6 – 10 ML. This thickness was used to prepare iron oxide which will be discussed in the next section.

The structure of 6 - 10 ML Fe films on Cu(100) was studied by LEED and STM at room temperature. LEED patterns are shown in Fig. 3.8. The quality of the Fe film is high as evidenced by the STM image in Fig 3.10. At this coverage, the Fe films tend to have the same fcc structure as Cu(100) substrate, confirmed by LEED patterns.



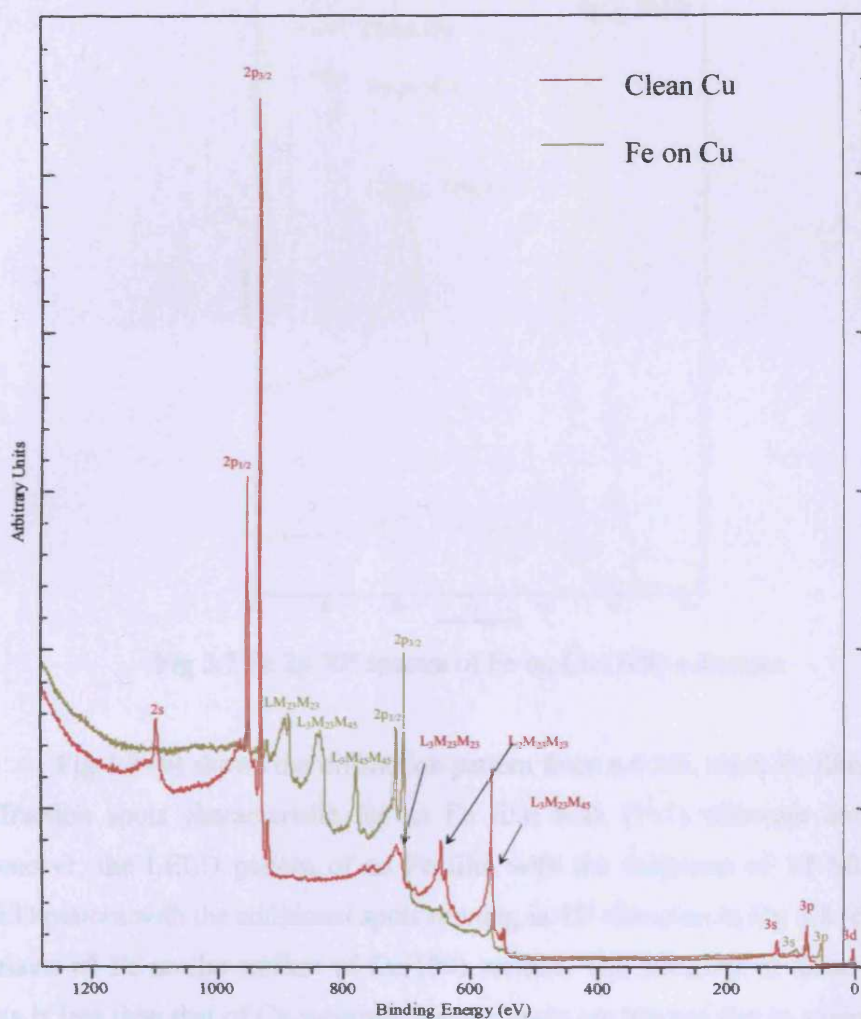


**Fig 3.6** Wide scan XPS spectra of clean Cu and 6 ML Fe on Cu(100) substrate.

The epitaxial iron films are strained because of the mismatch between bcc iron, which should have a lattice constant of 3.58 Å at 300 K and the fcc Cu substrate with a lattice constant of 3.61 Å [15]. It has been pointed out that strained fcc iron films on Cu(100) are metastable for two reasons [16]. They are metastable since they are grown in the wrong structure, specifically with an fcc structure instead of bcc structure. Furthermore, the films are metastable because of strained growth due to the 0.7 % mismatch between bcc iron and fcc copper. The strain energy between the fcc iron films and analogous films with bcc structure increases in each supplementary layer of fcc iron grown on the Cu(100) substrate.

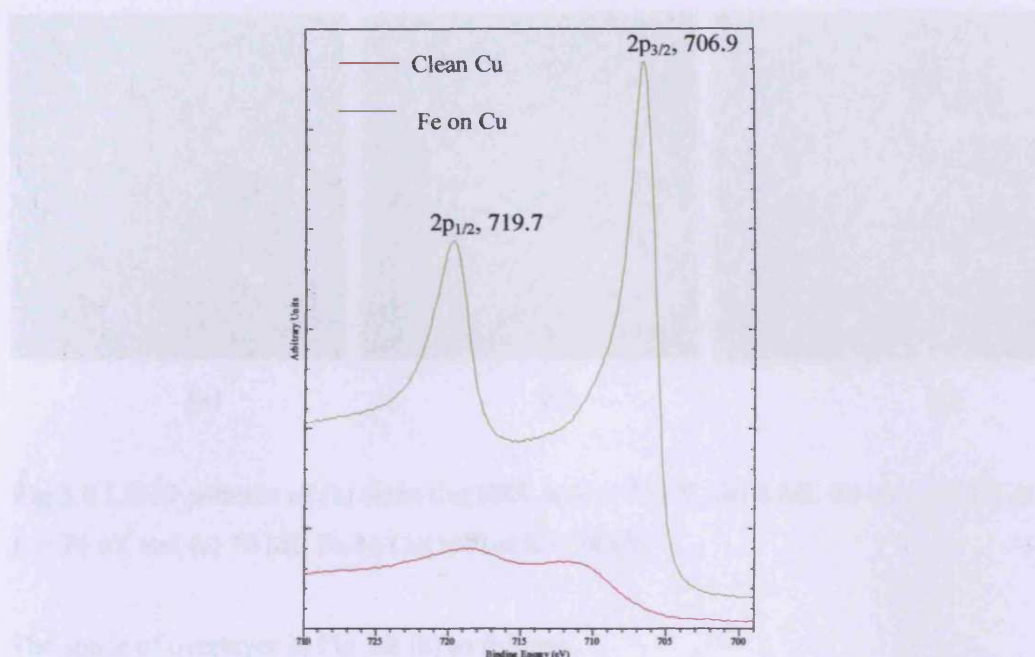
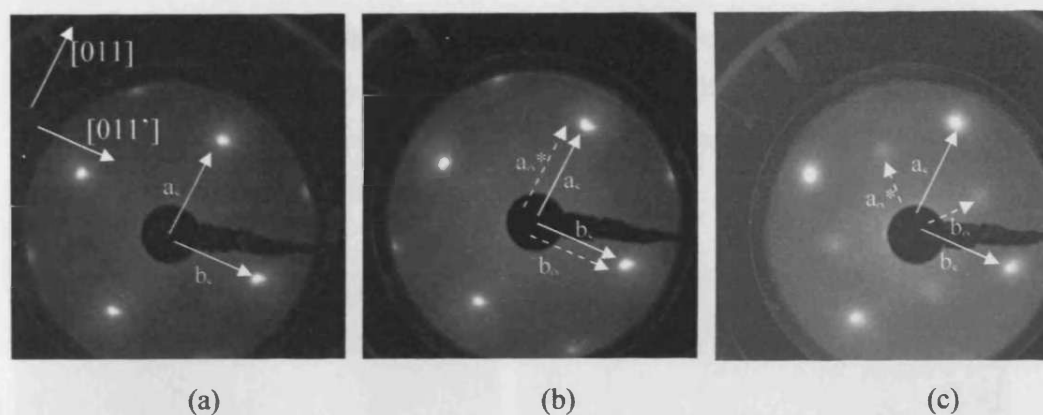


Fig 3.7 Fe 2p XP spectra of Fe on Cu (100) substrate.

Fig 3.8 (b) shows the diffraction pattern from a 6 ML thick Fe film at 295 K. Diffraction spots characteristic for an Fe film with  $(1 \times 1)$  structure are acquired. Moreover, the LEED pattern of an Fe film with the thickness of 10 ML shows a LEED pattern with the additional spots running in  $45^\circ$  direction in Fig 3.8 (c), due to 2 domains of Fe on the surface of Cu(100) surface. The intensity of those additional spots is less than that of Cu substrate and the spots are blurred due to again the small mismatch of Fe and Cu.

The diffraction pattern for 6 ML Fe on Cu recorded using LEED is a  $p(1 \times 1)$  pattern with respect to the clean Cu substrate, indicating true pseudomorphic growth of Fe films. It has previously been reported that for a thickness range below approximately 9 ML a sharp  $p(1 \times 1)$  pattern is found with respect to the clean Cu substrate [17]. This pattern remains  $1 \times 1$  with this coverage indicating that the development of Fe is epitaxial; however the spots become more diffuse.

Manipulation of matrices [14] can be used to derive the unit cell of the Fe overlayer in real space of the Cu (100) clean surface



**Fig 3.8** LEED patterns of (a) clean Cu(100) at  $E = 75$  eV (b) 6 ML Fe on Cu(100) at  $E = 74$  eV and (c) 10 ML Fe on Cu(100) at  $E = 70$  eV.

The space of overlayer in Fig 3.8 (b) as follows

$$a_o = 1 a_s + 0 b_s \quad \text{equation 3.2}$$

$$b_o = 0 a_s + 1 b_s$$

The space of overlayer in fig 3.8 (c) as follows

$$a_o = 1 a_s + 1 b_s \quad \text{equation 3.3}$$

$$b_o = -1 a_s + 1 b_s$$

From equation 3.2 and 3.3, Fe might be grown on square unit cell of Cu with distance either  $2.55 \text{ \AA}$  or  $3.61 \text{ \AA}$ . Possible real space structures are shown in Fig 3.9.

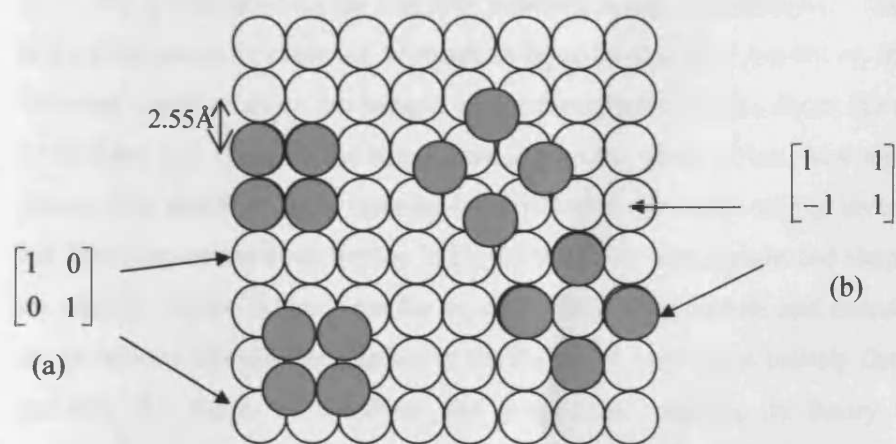


**Fig 3.9** Possible real space structures of Fe (a)  $p(1 \times 1)$  (from Fig 3.8 (b)) and (b)  $(\sqrt{2} \times \sqrt{2}) R45^\circ$  (from Fig 3.8 (c)) or  $c(2 \times 2)$  on Cu(100) substrate.



Fig 3.10 shows that three dimensional islands of Fe grown on Cu(100). This is possibly due to a relaxation of strain of Fe overlayers (the bcc structure is stable for Fe atoms at room temperature) or to carbon and oxygen contamination of the surface after the rather long deposition time (25 min).

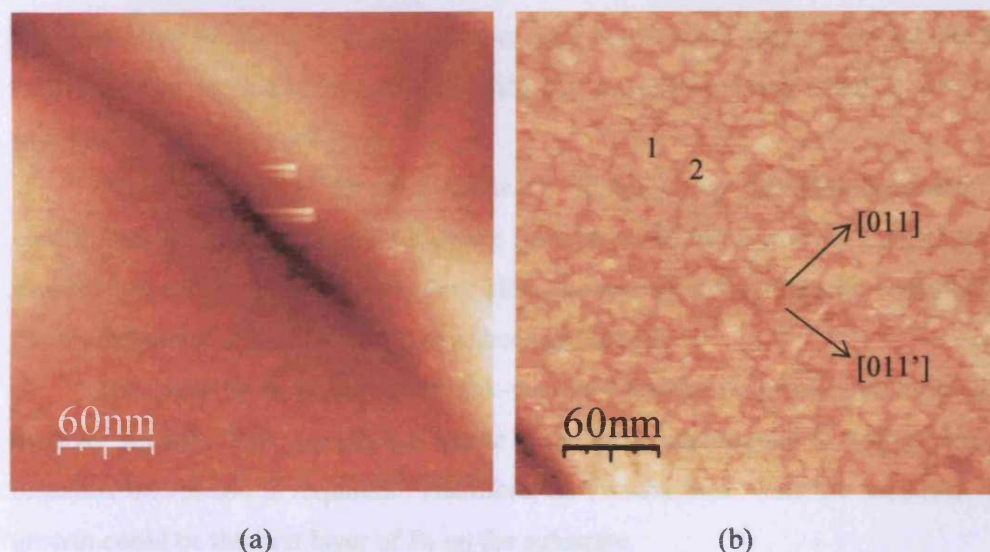


**Fig 3.10** STM images of 6 ML Fe deposited (a) on the step and (b) on the big terrace of Cu (100) substrate at 300 K ( $3000 \times 3000 \text{ \AA}^2$  nm, 1.1 nA, 0.76 V).

Fe is deposited on the Cu(100) substrate using an evaporator. The small flux of Fe evaporation is expected to result in layer-by-layer Fe growth on the substrate. However, large areas of the sample in the topographic image show 3D islands (Fig 3.10(a) and (b)). Those STM images are shown for films which show a  $(1 \times 1)$  LEED pattern. The deviation from layer-by-layer to island such as 2 atomic layers (labeled 1 and 2) is seen on the main terrace in Fig 3.10(b). The size, height and shape of islands are slightly square-like and similar to each other. The smooth and round-step edges are as isolated islands. The surface of the Fe island area is not entirely flat because of probably the rough Cu substrate and evaporation process. In theory the surface consists of the flat region (called terrace) and defects (step, kink and point defects). Due to atoms on the surface tend to move around there might be a Cu island in some area of the substrate and then arriving Fe atoms on the surface might cluster on a

substrate-like island. The big cluster or island might consist of Fe and Cu or Fe islands over Cu islands. Those events might be the cause of a rough island surface.

It was also reported [17] that the initial process of Fe epitaxy on Cu is an exchange of arriving Fe atoms with the surface of Cu that indicates the newly arrived Fe atoms must diffuse either on the surface or within the top layer of the Cu substrate. The mismatch of Cu and Fe is smaller at high temperature than at low temperature [18]. Previous literature data also suggests that segregation may occur at the Fe/Cu interface at room temperature.

The growth of a film on a surface is controlled by the thermodynamics for equilibrium growth mode or by kinetics for non-equilibrium growth [12]. If the Fe evaporation rate in experiment is very slow the growth film might be controlled by thermodynamics. 3 growth modes have been described:

(1) Layer-by-layer growth (Frank-van der Merwe): Fe growth might be layer-by-layer growth. This growth can occur if the lattice difference is nearly zero and balanced interaction is required. Therefore, an Fe adsorbate wets the substrate. This growth could be the first layer of Fe on the substrate.

(2) Layer and island growth (Stranski-Krastanov): After the wetting layer grow about 1-4 monolayer thickness. The overlayer, which has a strong interaction with the surface, can not grow in the strained structure.

(3) Island growth (Volmer-Weber): After the 10 ML Fe adsorbate might be non-wetting due to Fe-Fe interactions being stronger than Fe-Cu interaction. This growth might be occurred if the Fe development carries on.

In Fig 3.11, the occurrence of two-dimensional Fe islands with atomically flat tops are clearly visible indicating layer and island growth mode. The profiles in Fig 3.11 (b) and (c) are an atomic layer (2 Å) growing simultaneously. The Cu and Fe step heights are about 1.8 and 1.7 Å, respectively. A step height of the island close to a monatomic step ~2 Å high is measured.

Subsequently, the epitaxial 6-10 ML Fe film on Cu(100) develops by layer and island growth (Stranski-Krastanov). These surfaces were used for iron oxide preparation for the next experiment.

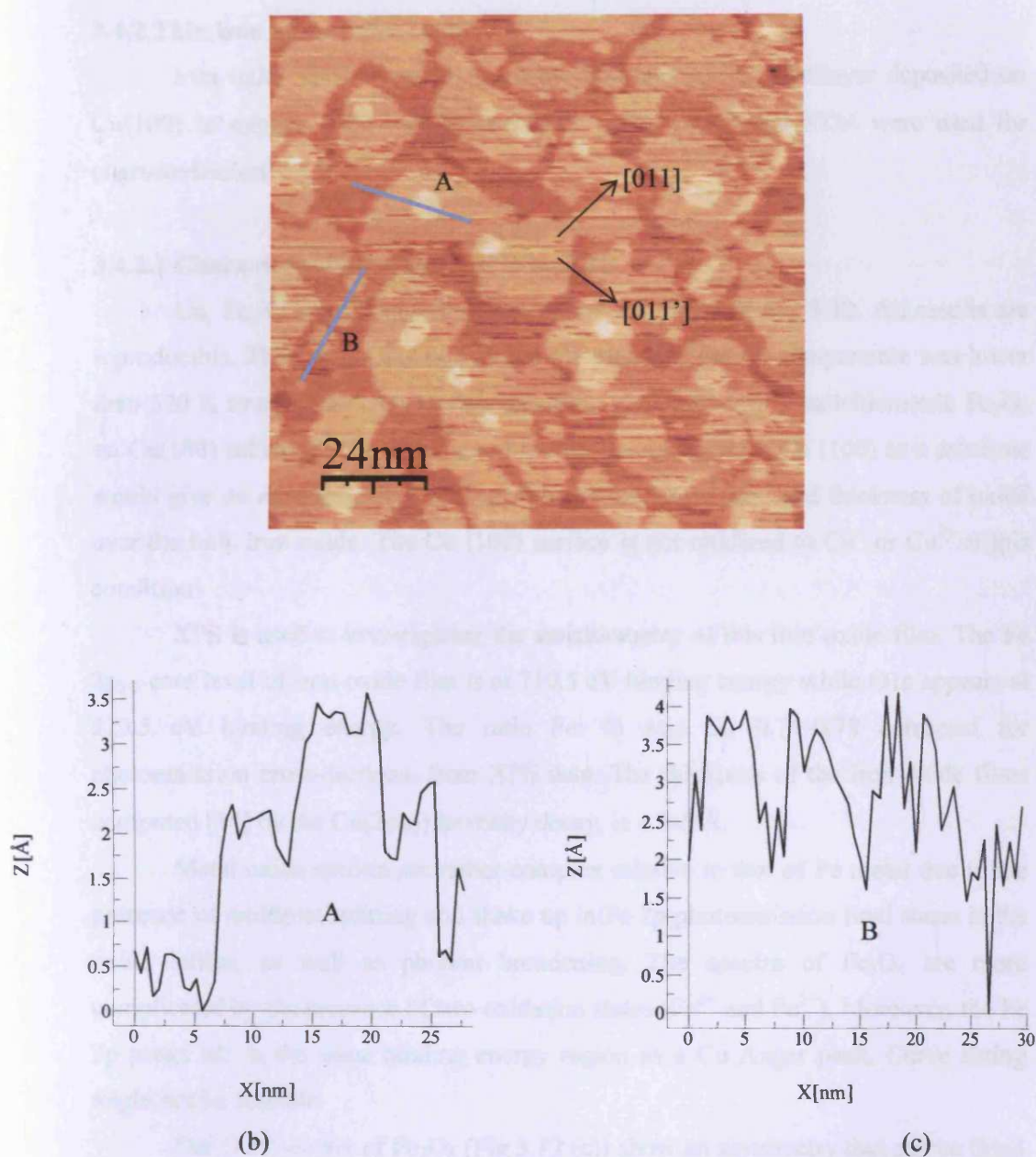


**Fig 3.11** (a) STM image of Fe film ( $1220 \times 1220 \text{ \AA}^2$ , 0.44 nA, 0.87 V) and a profile of an Fe islands in (b) A area and (c) B area.

### 3.4.2 Thin iron oxide preparation

Iron oxide films were prepared by oxidizing an Fe multilayer deposited on Cu(100) in oxygen ( $\sim 10^{-6}$  mbar) at 850 K. XPS, LEED and STM were used for characterization.

#### 3.4.2.1 Characterisation of iron oxide by XPS

Cu, Fe, O and C photoemission peaks are shown in Fig 3.12. All results are reproducible. The oxygen gas was turned off when the sample temperature was lower than 520 K to avoid an oxygen-rich condition to produce fully stoichiometric  $\text{Fe}_2\text{O}_3$  on Cu(100) substrate. The use of an ultra-thin Fe overlayer on Cu (100) as a substrate would give an advantage in the control of the oxidation state and thickness of oxide over the bulk iron oxide. The Cu (100) surface is not oxidized to  $\text{Cu}^+$  or  $\text{Cu}^{2+}$  at this condition.

XPS is used to investigating the stoichiometry of this thin oxide film. The Fe  $2p_{3/2}$  core level of iron oxide film is at 710.5 eV binding energy while O1s appears at 529.5 eV binding energy. The ratio Fe: O was ca. 0.74-0.78 corrected for photoemission cross-sections, from XPS data. The thickness of the iron oxide films computed [14] by the Cu( $2p_{3/2}$ ) intensity decay, is  $\sim 3\text{-}5$  Å.

Metal oxide spectra are rather complex relative to that of Fe metal due to the presence of multiplet splitting and shake up in Fe 2p photoemission final states in the oxide lattice, as well as phonon broadening. The spectra of  $\text{Fe}_3\text{O}_4$  are more complicated by the presence of two oxidation states ( $\text{Fe}^{2+}$  and  $\text{Fe}^{3+}$ ). Moreover, the Fe 2p peaks are in the same binding energy region as a Cu Auger peak. Curve fitting might not be feasible.

The O 1s spectra of  $\text{Fe}_3\text{O}_4$  (Fig 3.12 (c)) show an asymmetry that can be fitted to a second peak shifted 0.7 eV to a higher binding energy relative to the lattice O 1s. It has been published [2] that O 1s spectra in  $\text{RuO}_2$  grown on  $\text{TiO}_2(110)$  have very similar asymmetries. The metal core-level photoemission measured for this oxide also shows strong final-state effects, which could lead the O 1s photoelectron also displaying the asymmetry. However, the O 1s binding energy is fixed at 529.5 eV because the O 1s binding energy is in general not sensitive to oxidation of the iron [19, 20, 21 and 22]. The Fe 2p line shape is complex and inherently broad, and the



chemical shift between  $\text{Fe}^{2+}$  and  $\text{Fe}^{3+}$  peaks is too small to be resolvable with our system. However, there are two features in these spectra which give useful information on the Fe oxidation state. The first feature is the full width at half maximum (FWHM) of the Fe  $2p_{3/2}$  peak and the second is a satellite feature at binding energy 718 eV which is associated with  $\text{Fe}^{3+}$  photoemission. The broad peak for the  $\text{Fe}_3\text{O}_4$  film is consistent with the mixture of  $\text{Fe}^{2+}$  and  $\text{Fe}^{3+}$  cations whilst  $\text{Fe}_2\text{O}_3$  contains only  $\text{Fe}^{3+}$  cations. It has been found that the Fe  $2p_{3/2}$  FWHM values for  $\text{Fe}_3\text{O}_4$  and  $\alpha\text{-Fe}_2\text{O}_3$  are 3.65 and 2.30 eV, respectively [2]. Fig 3.12(b) shows Fe 2p spectra with the Auger peak of Cu subtracted showing a very small satellite at a binding energy of 718.5 eV. This suggests that iron oxide film would be  $\text{Fe}_3\text{O}_4$ . The broad Fe  $2p_{3/2}$  (FWHM  $\sim 4.3$  eV) also suggests  $\text{Fe}_3\text{O}_4$ . The nature of this oxide will be confirmed by the LEED and STM results later. It cannot directly identify what type of iron oxides on the surface from those considerations because there is no standard sample to be used as a reference in this experiment and the  $\text{Fe}^{3+}$  satellite is in the same position as the Cu Auger peak. The LEED result gives the long-range structure of thin film. It will be discussed later.

The Cu  $L_3M_{4,5}M_{4,5}$  Auger peaks and the Cu  $2p_{3/2}$  peak attributable to  $\text{Cu}_2\text{O}$  or CuO were not found during the preparation of the iron oxide, indicating that the oxidation of the Cu(100) substrate to  $\text{Cu}_2\text{O}$  or CuO did not occur. Therefore, the decrease of the Cu  $2p_{3/2}$  peak intensity is only due to the formation of the iron oxide overlayer.

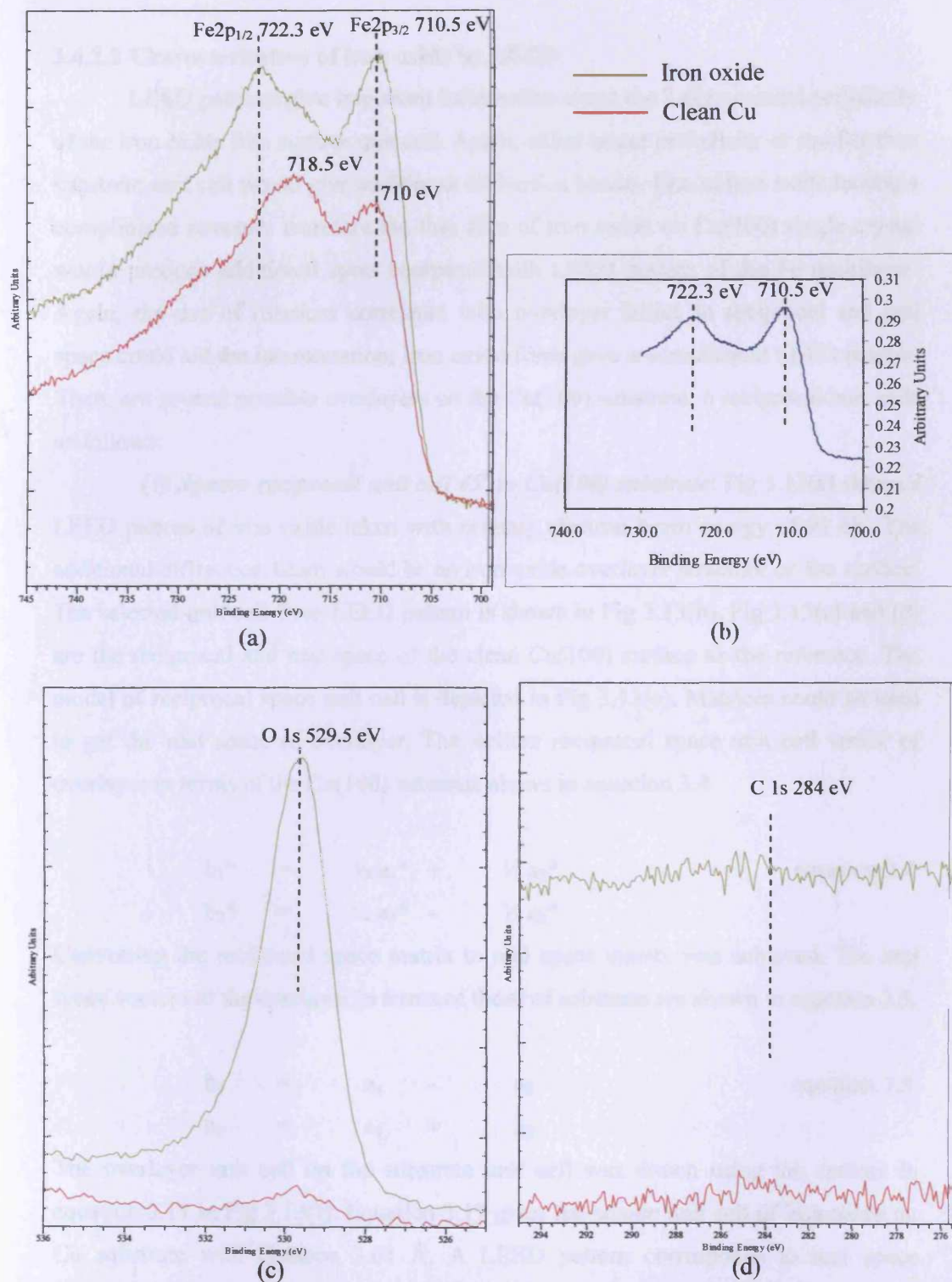


**Fig 3.12** XPS spectra of (a) Fe 2p and Auger peak of Cu, (b) Fe 2p subtracted Cu Auger peak background and (c) and (d) are O 1s and C 1s of iron oxide film and clean Cu surface, respectively.

### 3.4.2.2 Characterisation of iron oxide by LEED

LEED patterns give important information about the 2-dimensional periodicity of the iron oxide film surface unit cell. Again, either larger periodicity or smaller than substrate unit cell would give additional diffraction beams. Due to iron oxide having a complicated structure therefore the thin film of iron oxide on Cu(100) single crystal would produce additional spots compared with LEED pattern of the Fe multilayer. Again, the use of matrices correlated with overlayer lattice in reciprocal and real space could aid the interpretation. Iron oxide films gave a complicated LEED pattern. There are several possible overlayers on the Cu(100) substrate. 6 reciprocal unit cells as follows:

(1) **Square reciprocal unit cell  $45^\circ$  to Cu(100) substrate:** Fig 3.13(a) shows a LEED pattern of iron oxide taken with primary electron beam energy of 91 eV. The additional diffraction beam would be an iron oxide overlayer structure on the surface. The selected unit cell from LEED pattern is shown in Fig 3.13(b). Fig 3.13(c) and (d) are the reciprocal and real space of the clean Cu(100) surface as the reference. The model of reciprocal space unit cell is depicted in Fig 3.13(e). Matrices could be used to get the real space of overlayer. The written reciprocal space unit cell vector of overlayer in terms of the Cu(100) substrate shows in equation 3.4

$$\begin{aligned} b_1^* &= \frac{1}{2} a_1^* + \frac{1}{2} a_2^* \\ b_2^* &= \frac{1}{2} a_1^* - \frac{1}{2} a_2^* \end{aligned} \quad \text{equation 3.4}$$

Converting the reciprocal space matrix to real space matrix was achieved. The real space vectors of the overlayer in terms of those of substrate are shown in equation 3.5.

$$\begin{aligned} b_1 &= a_1 - a_2 \\ b_2 &= a_1 + a_2 \end{aligned} \quad \text{equation 3.5}$$

The overlayer unit cell on the substrate unit cell was drawn using the vectors in equation 3.17 in Fig 3.13(f). Equation 3.17 gives the square unit cell of iron oxide on Cu substrate with distance 3.61 Å. A LEED pattern corresponds to real space structure  $(\sqrt{2} \times \sqrt{2}) R 45^\circ$  or  $c(2 \times 2)$  or  $\begin{bmatrix} 1 & -1 \\ 1 & 1 \end{bmatrix}$  with respect to Cu(100) substrate.

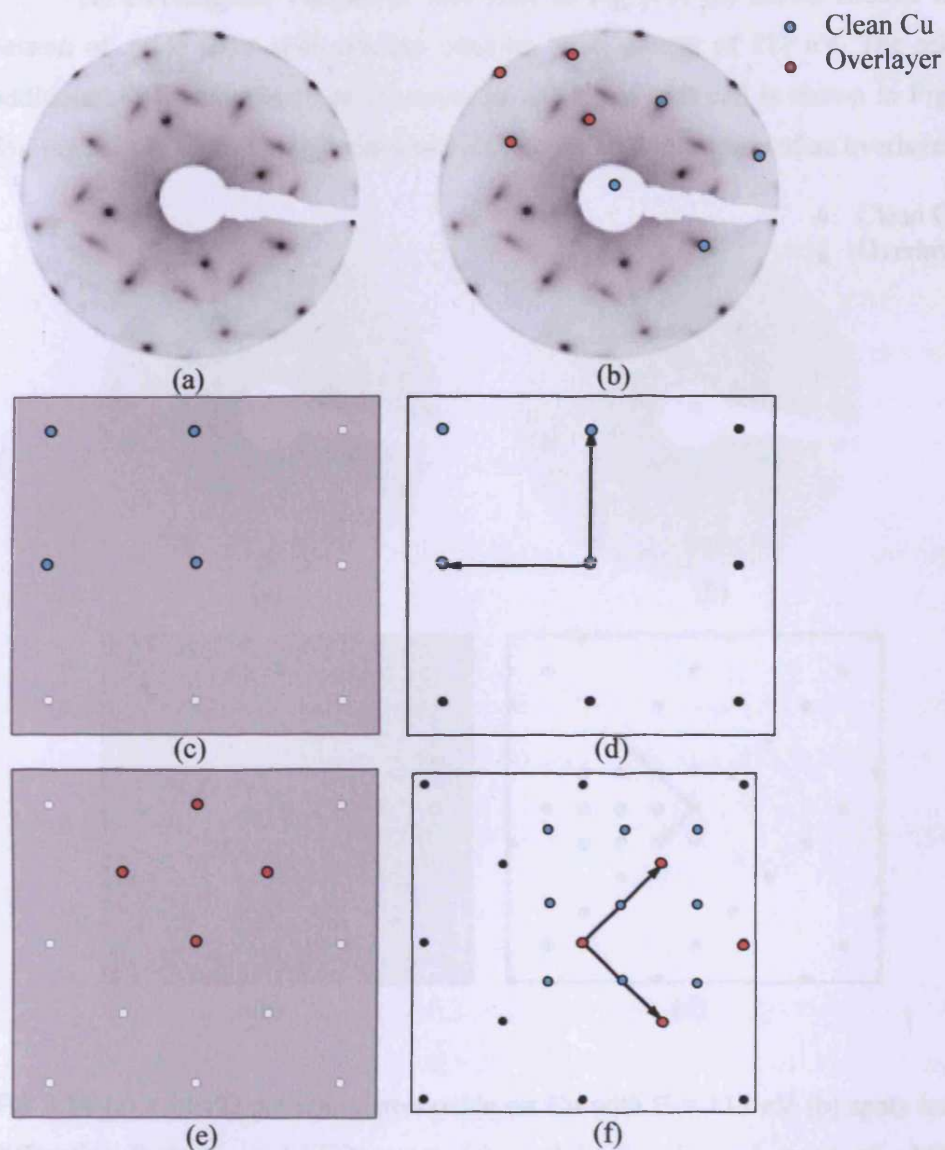


**Fig 3.13** (a) a LEED pattern of iron oxide on Cu at  $E = 91$  eV (b) spots indicate diffraction features on LEED screen ( red and blue spots represents overlayer and Cu substrate, respectively) , (c) and (d) correspond to reciprocal and real space of clean Cu , respectively, (e) reciprocal space of the iron oxide beams and (f) real space structure  $\text{Cu}(100)-(\sqrt{2} \times \sqrt{2}) R 45$  or  $\text{Cu}-(100)-c(2 \times 2)$  or  $\text{Cu}-(100)-\begin{bmatrix} 1 & -1 \\ 1 & 1 \end{bmatrix}$  for iron oxide on  $\text{Cu}(100)$ .



(2) **Rectangular reciprocal unit cell:** in Fig 3.14 (a) shows another LEED pattern of oxide taken with primary electron beam energy of 117 eV. The selected additional diffraction beam of overlayer as reciprocal unit cell is shown in Fig 3.14 (b). Fig 3.14 (c) and (d) are the model of reciprocal and real space of an overlayer.

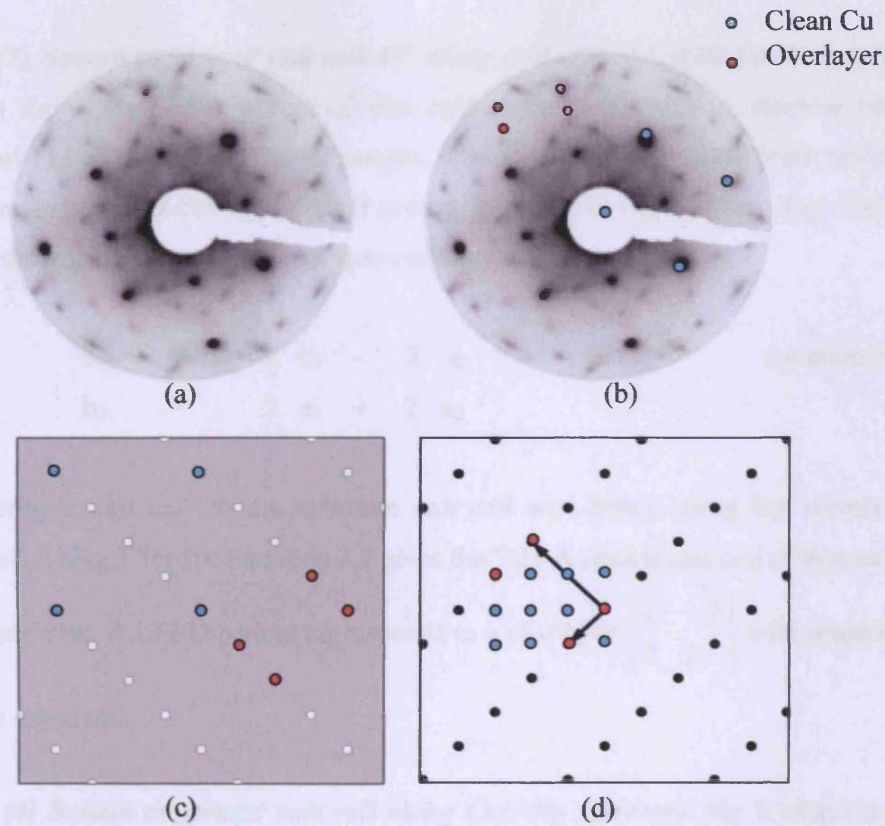


**Fig 3.14** (a) a LEED pattern of iron oxide on Cu with  $E = 117$  eV (b) spots indicate diffraction features on LEED screen (c) model of reciprocal space of additional diffraction beams and (d) possible real space structure  $\text{Cu}(100)-(2\sqrt{2} \times \sqrt{2})\text{R}45^\circ$  or

$\text{Cu}(100)-\begin{bmatrix} 2 & 2 \\ -1 & 1 \end{bmatrix}$ -iron oxide.

The real space vectors of the oxide overlayer are shown in equation 3.6.

$$\begin{aligned} b_1 &= 2a_1 + 2a_2 \\ b_2 &= -1a_1 + 1a_2 \end{aligned} \quad \text{equation 3.6}$$

From equation 3.6 gives the  $7.21 \times 3.61$  Å rectangular unit cell of iron oxide on Cu substrate. A LEED pattern corresponds to a  $(2\sqrt{2} \times \sqrt{2})R45^\circ$  or  $\begin{bmatrix} 2 & 2 \\ -1 & 1 \end{bmatrix}$  with respect to the Cu(100) substrate.

**(3) Square reciprocal unit cell  $45^\circ$  along unit cell of Cu(100) substrate:** Fig 3.15 (a) shows the LEED pattern of iron oxide taken with primary electron beam energy of 113 eV in another area of sample. The additional diffraction beam selected for the reciprocal unit cell from LEED pattern is shown in Fig 3.15(b). Fig. 3.15(c) and (d) show the reciprocal and real space of an overlayer.

$$\begin{aligned} b_1 &= 2 a_1 - 2 a_2 \\ b_2 &= 2 a_1 + 2 a_2 \end{aligned} \quad \text{equation 3.7}$$

The overlayer unit cell on the substrate unit cell was drawn using the vectors in equation 3.7 (Fig 3.15(d)). Equation 3.7 gives the  $7.21$  Å square unit cell of iron oxide on Cu substrate. A LEED pattern corresponds to a  $c(4 \times 4)$  or  $\begin{bmatrix} 2 & -2 \\ 2 & 2 \end{bmatrix}$  with respect to Cu(100) substrate.

**(4) Square reciprocal unit cell along Cu(100) substrate:** Fig 3.16(a) shows the LEED pattern of iron oxide taken with primary electron beam energy of 63 eV. Fig 3.16(b) shows the additional diffraction beams of the reciprocal unit cell of overlayer. Fig. 3.16(c) and (d) show the reciprocal and real space of the overlayer.

$$\begin{aligned} b_1 &= 2 a_1 + 0 a_2 \\ b_2 &= 0 a_1 + 2 a_2 \end{aligned} \quad \text{equation 3.8}$$

The overlayer unit cell on the substrate unit cell was drawn using the vectors in equation 3.8 ( Fig 3.16 (d)). Equation 3.8 gives the square unit cell of iron oxide on Cu substrate with distance  $5.1 \times 5.1$  Å<sup>2</sup>

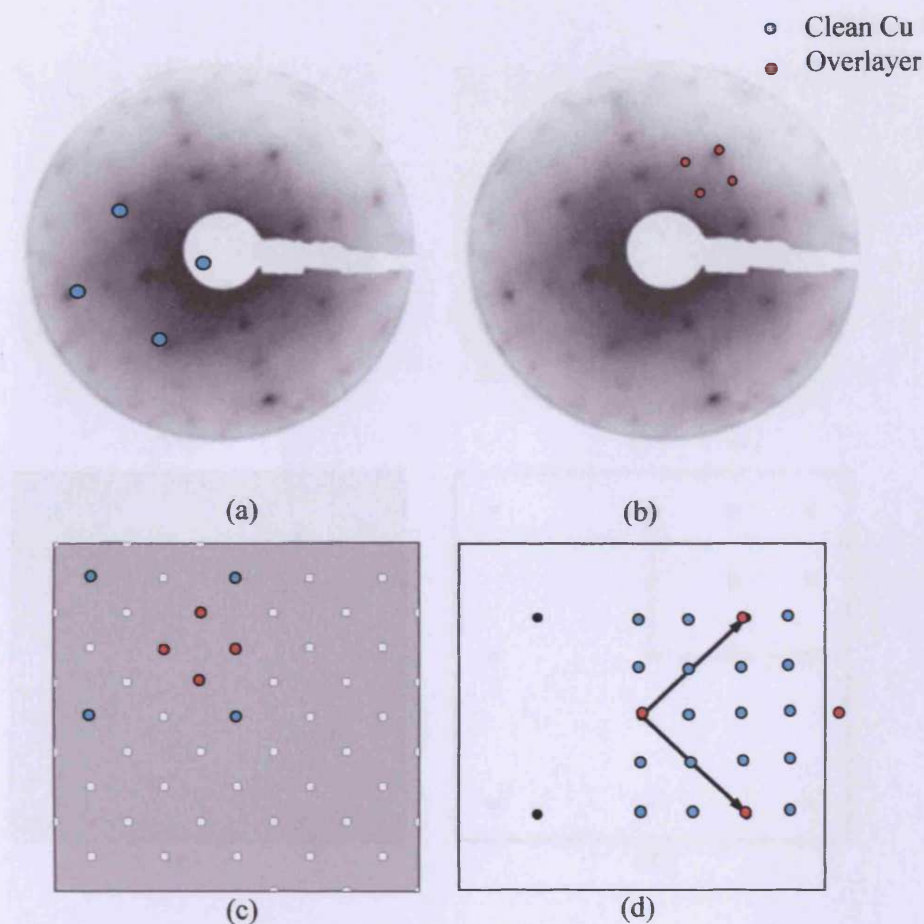


**Fig 3.15** (a) a LEED pattern of iron oxide on Cu at  $E = 113$  eV (b) spot indicate diffraction features on LEED screen (c) model of reciprocal space of additional diffraction beams and (d) possible real space structure Cu(100)-c(4×4) or Cu-(100)- $\begin{bmatrix} 2 & -2 \\ 2 & 2 \end{bmatrix}$ -iron oxide. The overlayer unit cell is  $7.21 \times 7.21 \text{ \AA}^2$ .

**(5) Hexagonal reciprocal unit cell** Fig 3.17(a) shows the LEED pattern of reciprocal unit cell of iron oxide taken with primary electron beam energy of 91 eV. Some selected spots are not really clear because the spots are so close to the center of the screen. The additional picture (Fig 3.17(b)) is clearly seen. The selected additional diffraction beam of the reciprocal unit cell of the overlayer is shown in Fig 3.17(b). Fig 3.17(c) and (d) shows the model of reciprocal and real space of the overlayer.



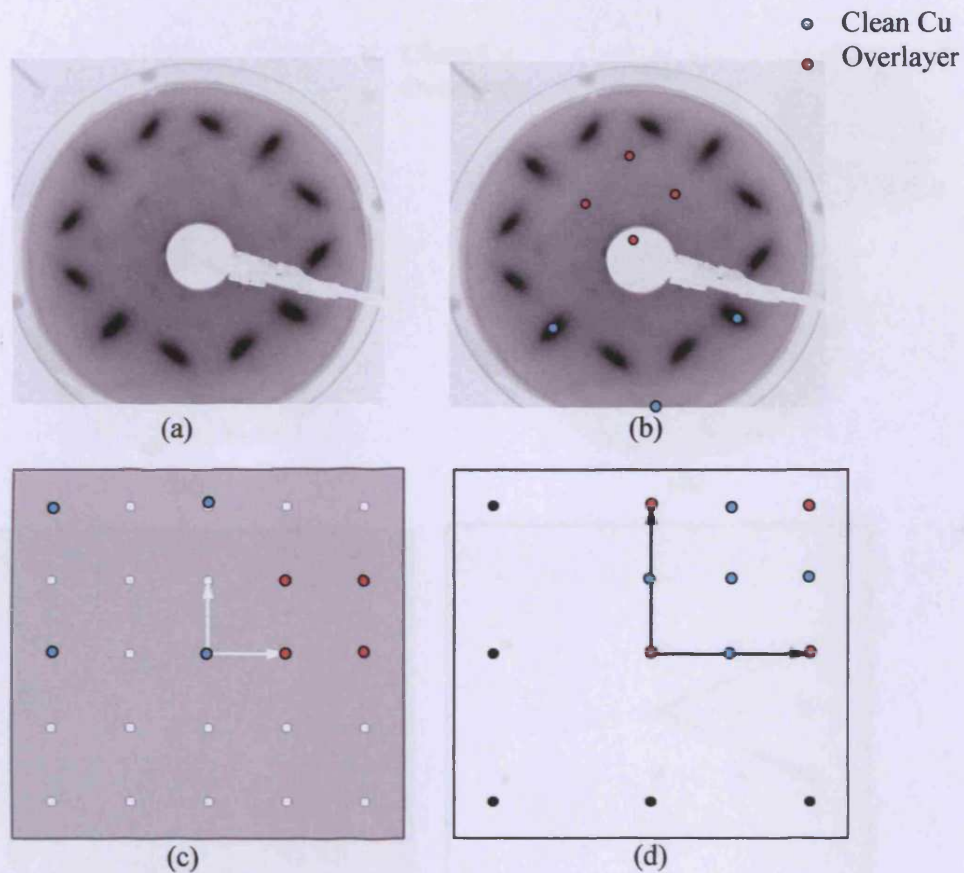


**Fig 3.16** (a) a LEED pattern of iron oxide on Cu and  $E = 63$  eV (b) spots indicate diffraction features on LEED screen (c) model of reciprocal space of an iron oxide and (d) possible real space structure Cu(100)-p(2×2) or Cu-(100)- $\begin{bmatrix} 2 & 0 \\ 0 & 2 \end{bmatrix}$ -iron oxide. The square unit cell of overlayer with  $5.1 \times 5.1 \text{ \AA}^2$ .

$$\begin{aligned} b_1 &= 2a_1 - 1a_2 \\ b_2 &= 2a_1 + 1a_2 \end{aligned} \quad \text{equation 3.9}$$

The overlayer unit cell on the substrate unit cell in Fig 3.17(d) was drawn using the vectors in equation 3.9. From equation 3.9 gives the  $5.7 \text{ \AA}$  hexagonal unit cell of iron oxide on Cu substrate.

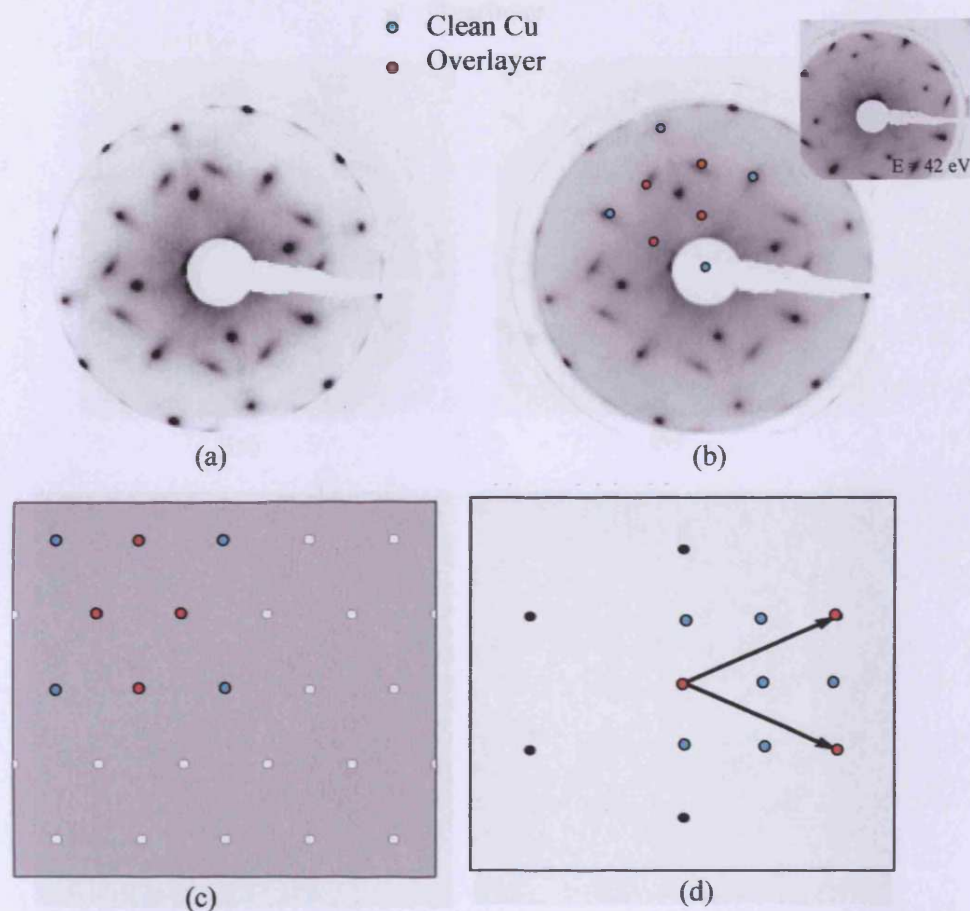


**Fig 3.17** (a) a LEED pattern of iron oxide on Cu with  $E = 91$  eV (b) selected diffraction of overlayer on LEED screen (c) model of reciprocal space of additional diffraction beams and (d) possible real space structure  $\text{Cu}(100)\text{-c}(4\times 2)$  or  $\text{Cu-(100)-}\begin{bmatrix} 2 & -1 \\ 2 & 1 \end{bmatrix}$ -iron oxide with unit cell  $5.7 \text{ \AA}$ .

**(6) 2 domains of square reciprocal unit cell:** Fig 3.18 (a) shows the LEED pattern of reciprocal unit cell of iron oxide taken with primary electron beam energy of 42 eV. The additional diffraction beam of the reciprocal unit cell from the LEED pattern is shown in Fig 3.18(b). Fig 3.18 (c) and (d) shows the reciprocal and real space of an overlayer.

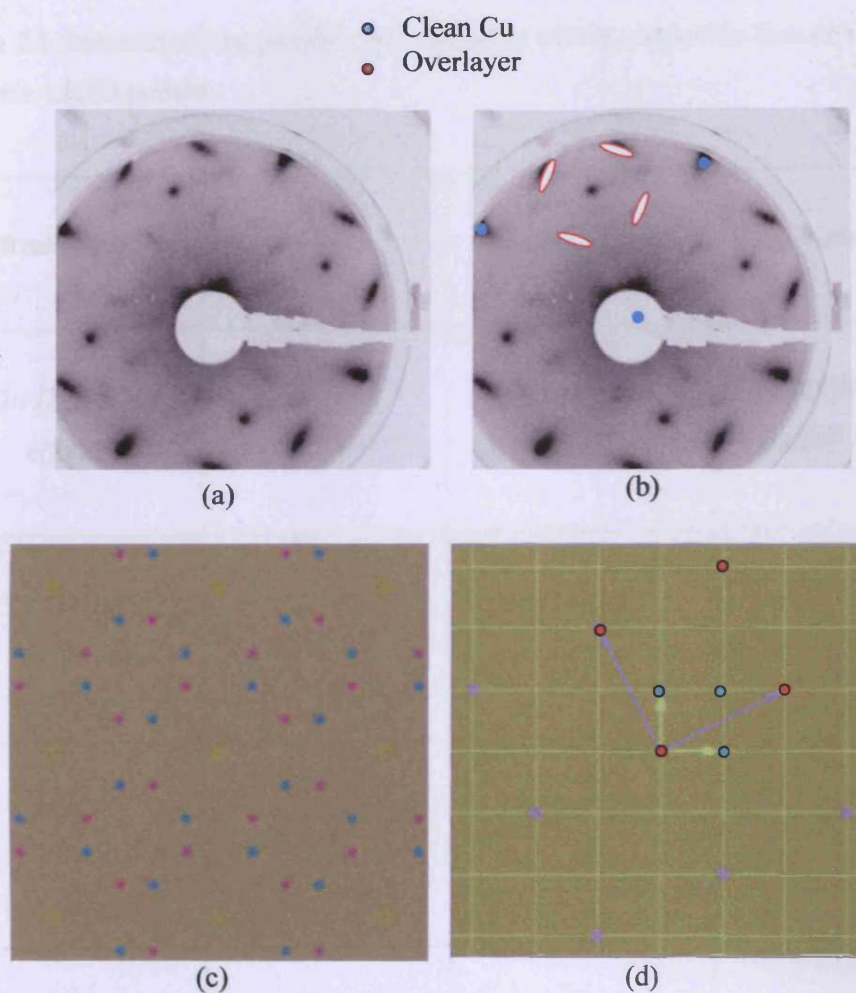


**Fig 3.18** (a) a LEED pattern of iron oxide on Cu at  $E = 42$  eV (b) selected diffraction features on LEED screen (c) model of reciprocal space of additional diffraction beams and (d) possible real space structure  $\text{Cu}(100)-(\sqrt{5} \times \sqrt{5})\text{R}26.6^\circ$  or  $\text{Cu}-(100)-\begin{bmatrix} 2 & 1 \\ -1 & 2 \end{bmatrix}$ -iron oxide. The square unit cell of overlayer is about  $5.71 \times 5.71 \text{ \AA}^2$ .

$$\begin{aligned}
 b_1 &= 2 a_1 + 1 a_2 \\
 b_2 &= -1 a_1 + 2 a_2
 \end{aligned}
 \qquad \text{equation 3.10}$$

The overlayer unit cell on the substrate unit cell was drawn using the vectors in equation 3.10 (Fig 3.18 (d)). Equation 3.10 gives the square unit cell of iron oxide on Cu substrate with distance  $5.1 \text{ \AA}$ .



**Table 3.1** Summary of the possible real structures of iron oxide thin film on Cu (100) from the LEED pattern

Real space	Matrix	Possible unit cell	Iron oxide model
$(\sqrt{2} \times \sqrt{2})R45^\circ$ or $c(2 \times 2)$	$\begin{bmatrix} 1 & -1 \\ 1 & 1 \end{bmatrix}$	$3.61 \times 3.61$ $\square$	FeO(100) with $3.06 \times 3.06 \text{ \AA}^2$
$(2\sqrt{2} \times \sqrt{2})R45^\circ$	$\begin{bmatrix} 2 & 2 \\ -1 & 1 \end{bmatrix}$	$7.21 \times 3.61$ $\square$	-
$c(4 \times 4)$	$\begin{bmatrix} 2 & -2 \\ 2 & 2 \end{bmatrix}$	$7.21 \times 7.21$ $\square$	-
$p(2 \times 2)$	$\begin{bmatrix} 2 & 0 \\ 0 & 2 \end{bmatrix}$	$5.10 \times 5.10$ $\square$	Fe <sub>3</sub> O <sub>4</sub> (100) with $5.94 \times 5.94 \text{ \AA}^2$
$c(4 \times 2)$	$\begin{bmatrix} 2 & -1 \\ 2 & 1 \end{bmatrix}$	$5.70 \times 5.70$ $\diamond$	Fe <sub>3</sub> O <sub>4</sub> (111) with $5.94 \times 5.94 \text{ \AA}^2$ and Fe <sub>3</sub> O <sub>4</sub> (110) with $5.10 \times 5.10 \text{ \AA}^2$

There are various new diffraction features due to the orientations of the oxide. Domains are less well-ordered giving rise to set of streak perpendicular to each other. This LEED structure is a part of hexagonal, rectangular and square lattice that is well-oriented relative to the Cu(100) substrate shown in Table 3.1. Some of the two sets of spots indicate that there are two equally domains. The LEED patterns are different in different areas on the surface of the Cu substrate indicating different oxide formation on the Cu substrate (The sample was moved when LEED pattern were taken several times).

Some promising unit cells of prepared iron oxide surface corresponding to surface model of  $\text{Fe}_{1-x}\text{O}(100)$  having 3.06 Å square unit cell,  $\text{Fe}_3\text{O}_4(100)$  having 5.94 Å square unit cell and  $\text{Fe}_3\text{O}_4(111)$  having 5.94 Å hexagonal unit cell. From the LEED interpretation in Table 3.1, the prepared thin iron oxide films surface probably are  $\text{Fe}_{1-x}\text{O}(100)$  (3.61 Å square unit cell),  $\text{Fe}_3\text{O}_4(100)$  (5.71 Å square unit cell) and  $\text{Fe}_3\text{O}_4(111)$  (5.70 Å hexagonal unit cell). The unit cell sizes are not perfectly matched with the standard iron oxide model, however the small mismatch results in streaks as observed. The combination of techniques will help us point out what type of oxide is made from this experimental condition. The STM result will be discussed next to support XPS and LEED result.

#### 3.4.2.3 Characterization of iron oxide by STM

From the XPS and LEED results,  $\text{Fe}_3\text{O}_4$  is the most likely iron oxide film prepared from this experiment. The topography of the prepared iron oxide surface was studied by STM.  $\text{Fe}_3\text{O}_4$  crystallizes in the inverse spinel structure.  $\text{Fe}^{2+}$  and  $\text{Fe}^{3+}$  cations locate in the interstitial sites of the O anion close-packed fcc sublattice.  $\text{Fe}^{3+}$  ions are in tetrahedral holes while equal numbers of  $\text{Fe}^{2+}$  and  $\text{Fe}^{3+}$  ions are in octahedral holes. As mentioned before the  $\text{Fe}_3\text{O}_4(111)$  surface is stable and normally occurs on obviously grown crystals [1]. In  $\text{Fe}_3\text{O}_4(111)$ , the hexagonal O planes form a cubic ABC stacking order. Fe layers alternately sit on the O(111) planes either Kagome' or three mix-trigonal (three hexagonal). O(111) planes are separated by the Kagome' layer with 2.37 Å apart while O planes are separated by 2.48 Å apart in the three mix-trigonal layers. Then a distance between every second O layer is 4.85 Å corresponding to the distance between equivalent (111) surface terminations of  $\text{Fe}_3\text{O}_4$ .

$\text{Fe}_3\text{O}_4(100)$  surface is another possible iron oxide formed on  $\text{Cu}(100)$  substrate. It might be formed perfectly on  $\text{Cu}(100)$  substrate corresponding to the LEED pattern (square unit cell with  $5.94 \times 5.94 \text{ \AA}^2$ ). The  $\text{Fe}_3\text{O}_4(100)$  plane has two alternating layers (A and B) as a stacking series. The tetrahedral coordinated  $\text{Fe}^{3+}$  ions are in the A-layer, while the octahedral coordinated  $\text{Fe}^{2+}$  and  $\text{Fe}^{3+}$  ions are in the B-layer. The separation between neighboring planes (A-B layer) is  $1.05 \text{ \AA}$ , while the separation between successive like planes (A-A or B-B interplanar separation) are  $2.10 \text{ \AA}$ .

STM images in Fig 3.19 show the dramatic change in a large area on the Cu substrate after an Fe multilayer was oxidized at  $850 \text{ K}$  in a presence of  $\text{O}_2$  ( $10^{-6} \text{ mbar}$ ). XPS of iron oxide prepared in this coverage is reproducible and STM images collected also show reproducibility. In the wide area scans, pseudo-hexagonal superstructure, antiphase domain boundary strips and bare Cu are decorated over the  $\text{Cu}(100)$  substrate. The edges of Fe/Cu steps and Fe islands before high-temperature oxidation were rough however after oxidation the surface becomes well defined.

The oxide is extremely ionic with an interatomic bond strength almost 10 times of that Cu substrate [9]. When the oxide forms, the Cu substrate migrates to form a large flat area to minimize the surface energy. There is a competition between large oxide crystallites forming and a desire to minimize step-step repulsive energy. The morphology observed in STM images result from equilibrium on the surface.

In Fig 3.19(a) iron oxide overlayer islands with atomically high iron oxide terraces, integral multiplies high and bare Cu substrate region coexist on the image. Some bare Cu area (as confirmed by XPS) was obtained in these STM images despite the oxidation at high temperature. The clean  $\text{Cu}(100)$  substrate terrace was obtained with terraces separated by monoatomic steps with  $\sim 1.8\text{-}2 \text{ \AA}$ . Most substrate area is covered by iron oxide terraces  $\sim 5 \text{ \AA}$  high, which corresponds to the distance between equivalent (111) surface terminations of  $\text{Fe}_3\text{O}_4$ . Some coverage exhibits a double height of  $\sim 4.8 \text{ \AA}$  indicating 2 layers of  $\text{Fe}_3\text{O}_4(111)$ . The thickness of the iron oxide film is about  $3\text{-}5 \text{ \AA}$ ; XPS results agree with this STM result. Hexagonal and triangular-shaped islands with height between  $5$  and  $10 \text{ \AA}$  were regularly observed.

In Fig 3.19(b), rows of antiphase domain boundary strips in different directions  $[011]$  and  $[011']$  coexist with the hexagonal and triangular islands indicating those oxide strips grown and aligned with the Cu(100) substrate structure. The size of a strip is about  $50 \text{ \AA}$  wide and  $2.1 \pm 0.2 \text{ \AA}$  high. Fascinatingly, those strips are perpendicular to each other along the Cu(100) substrate direction as square unit cell of Cu(100).

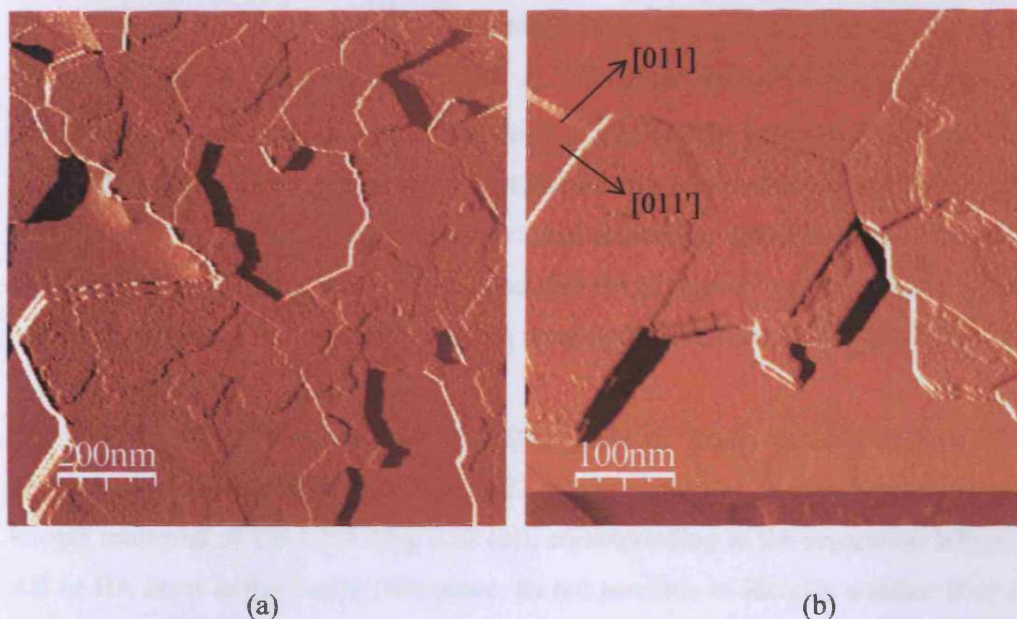


**Fig 3.19** STM large scale images of iron oxide overlayer on Cu(100) substrate in (a)  $1000 \times 1000 \text{ nm}^2$  (1.1V, 3 nA) and (b)  $500 \times 500 \text{ nm}^2$  (0.7V, 1 nA).

Fig 3.20 (a) and (b) show a closer view of iron oxide surface. The driving force for the surface morphology change is oxide formation. Three different regions coexist in the images. They were formed to the order strips denoted (1), the pseudo-hexagonal superstructures along  $[011]$  denoted (2) and the disorder of the round iron oxide structures denoted (3). The pseudo-hexagonal superstructure has  $50 \text{ \AA}$  hexagonal spacing while the disorder particle has size randomly between  $20 - 50 \text{ \AA}$ . The height of superstructure could not be measured due to all the Cu(100) substrate surface being fully covered by iron oxide film. However, the line profile of particle denoted (d) and (e) (Fig 3.20 (c)) are ca.  $1.2-1.4$  and  $2.1 \text{ \AA}$  high, respectively. Moreover, the big round hollow ( $400 \text{ \AA}$  diameters) observed in Fig 3.20 (a) may be a

defect on the substrate.

Fascinatingly, strips ( $\text{Fe}_3\text{O}_4(100)$ ) are underneath the hexagonal structures (denoted as  $\text{Fe}_3\text{O}_4(111)$ ). Strips might be the first layer of iron oxide formation on  $\text{Cu}(100)$  surface. The next layer could be either strips or hexagonal structure. As mentioned before the  $\text{Fe}_3\text{O}_4(111)$  is a stable iron oxide surface therefore, the next layer of oxide tends to be  $\text{Fe}_3\text{O}_4(111)$ .

The pseudo- hexagonal superstructure is not only obtained in the partial area of the terrace but also acquired as the big terrace in Fig 3.21. The separation of individual bright round structures is  $\sim 50 \text{ \AA}$ . Triangular-shaped islands of hexagonal superstructure with atomically flat  $\sim 5 \text{ \AA}$  high in Fig 3.21(b) correspond to the  $\text{Fe}_3\text{O}_4(111)$  termination. The superstructure could be clearly seen in the current image (Fig 3.21(c)). 2 layers of hexagonal superstructures formed as triangular shape are also depicted in Fig 3.21(d). It has been reported that the hexagonal superstructure in STM image could result from a Moiré pattern, a rectangular overlayer mismatched with the square Cu lattice [9].

The (100) plane is another possible plane of  $\text{Fe}_3\text{O}_4$  on this surface. The antiphase domain boundary strips (Fig. 3.22 (a)) are separated by step heights that are integer multiples of  $1.0\text{-}1.5 \text{ \AA}$  (Fig 3.22 (b)), corresponding to the separation between AB or BA layer in the  $\text{Fe}_3\text{O}_4(100)$  plane. Its not possible to identify whether B or A layer is on the top surface from such a big area in Fig 3.22. The pucker edge hollows  $0.8 \text{ \AA}$  deep might be oxygen adsorbed on the bare Cu.



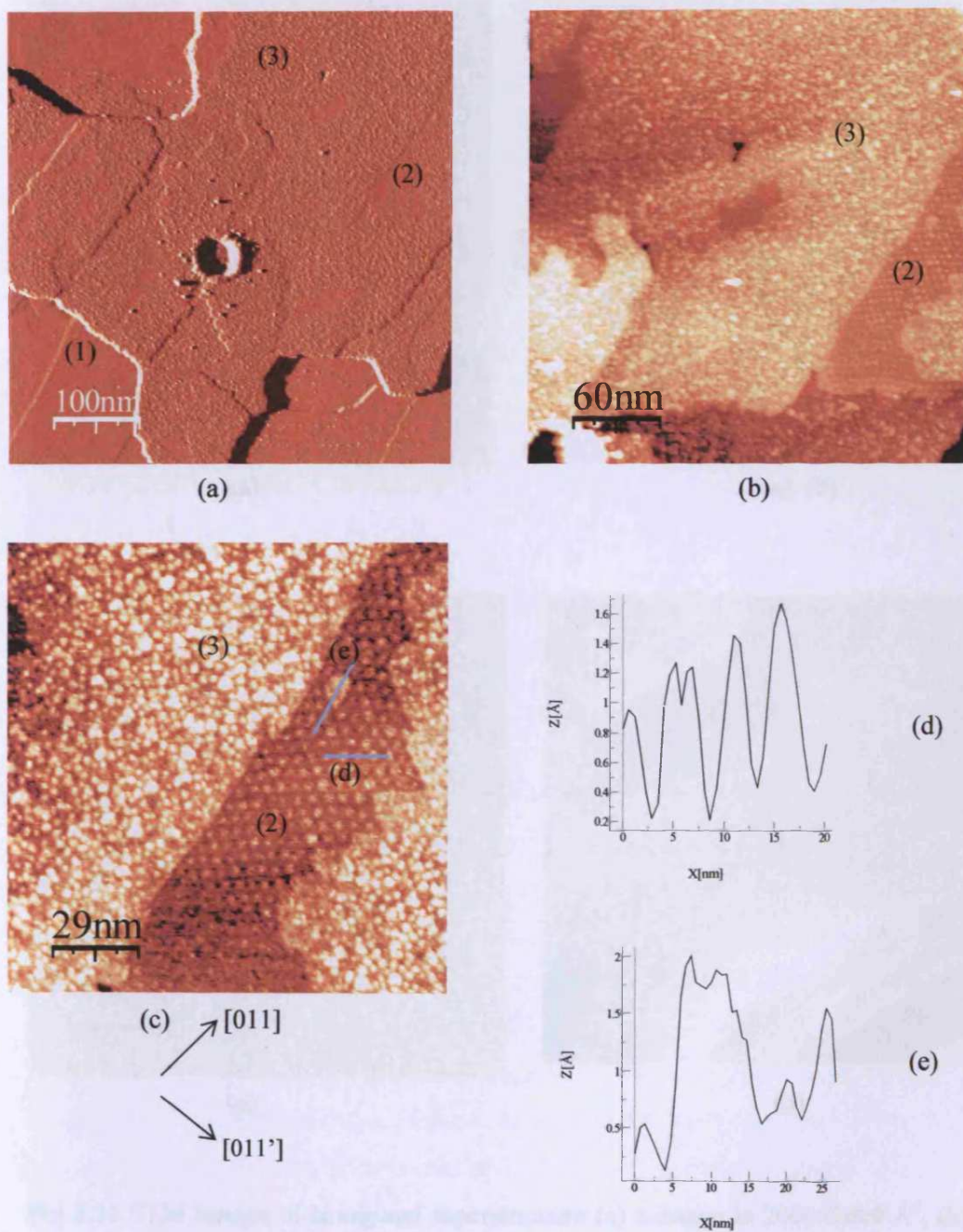


**Fig 3.20** STM images show strips, hexagonal superstructure and disordered particles which are in (a) i-image  $5000 \times 5000 \text{ \AA}^2$ , (b) z-image  $3000 \times 3000 \text{ \AA}^2$ , (c) closer image  $1400 \times 1400 \text{ \AA}^2$  and (d) and (e) lines profile of superstructure. (1V, 1.7nA).

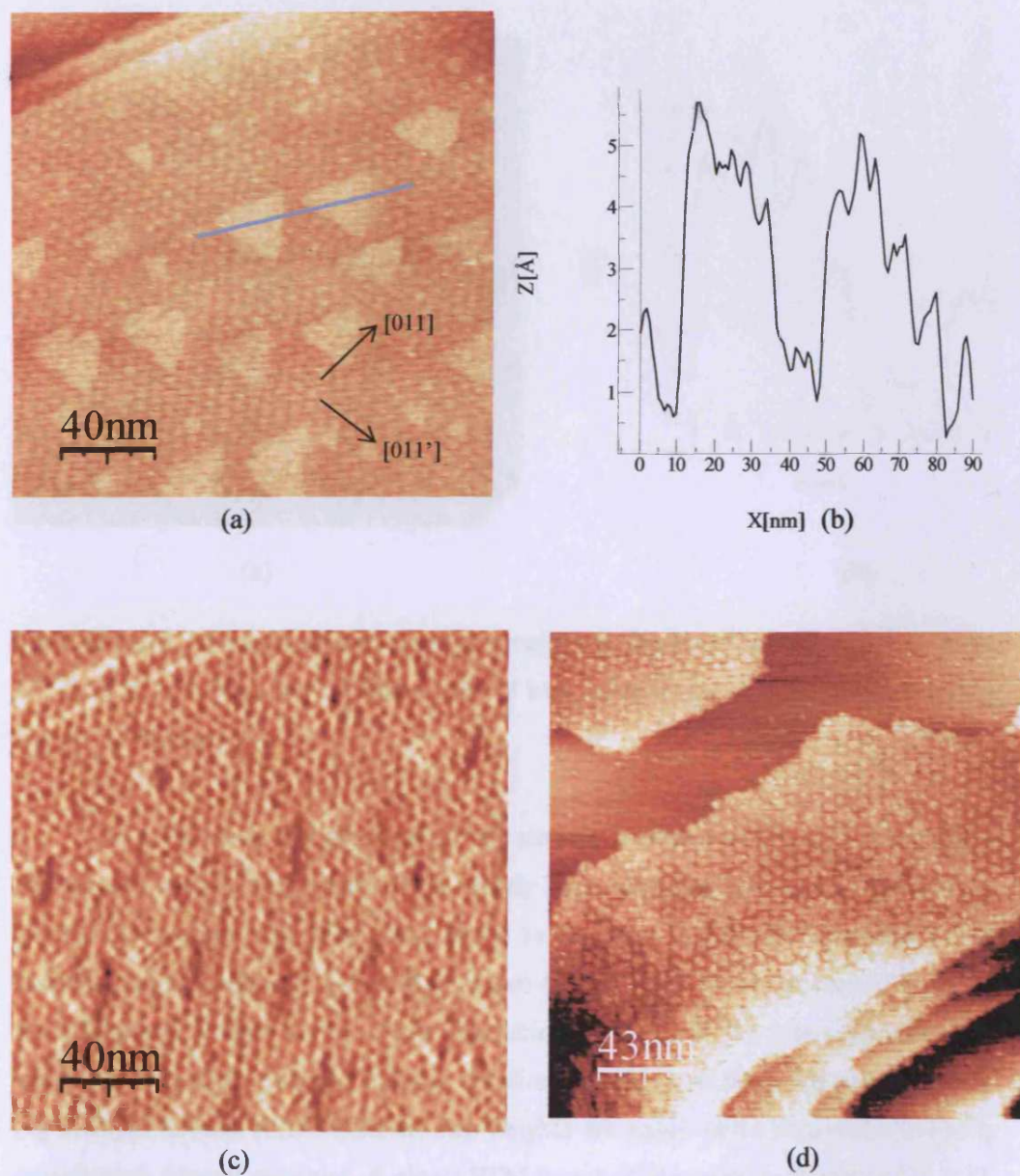


**Fig 3.21** STM images of hexagonal superstructure (a) z-image in  $2000 \times 2000 \text{ \AA}^2$ , (b) line profile of triangular island, (c) current image in  $2000 \times 2000 \text{ \AA}^2$  and (d) 2 layers of superstructure of iron oxide in  $2200 \times 2200 \text{ \AA}^2$  (1V, 1.1 nA).



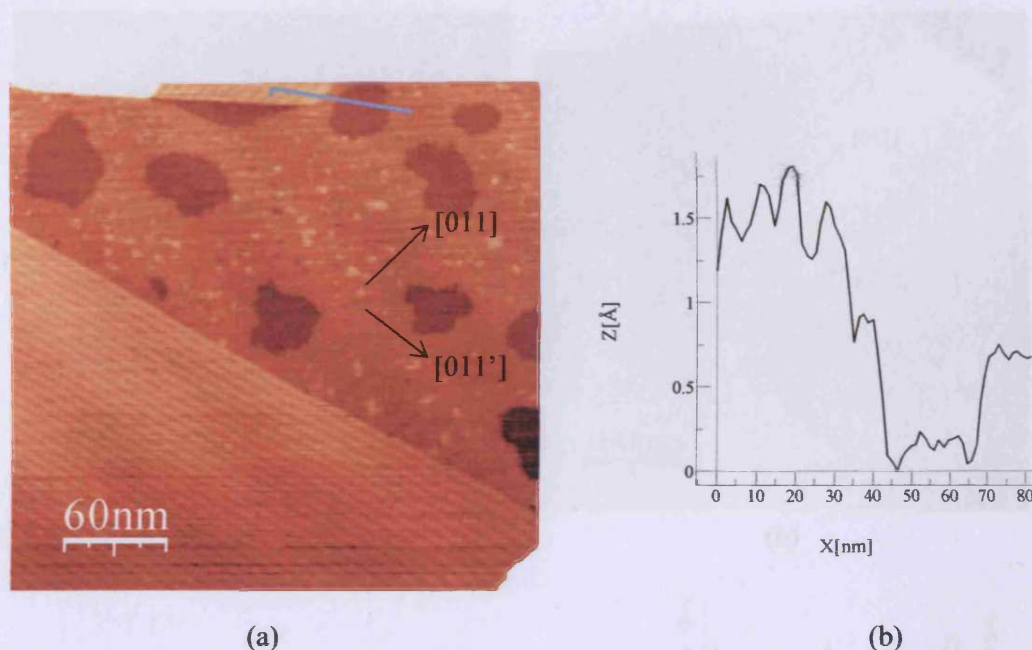


**Fig 3.22** (a) STM image of iron oxide strips close to the bare Cu surface ( $3000 \times 3000 \text{ Å}^2$ , 0.86 V, 0.89 nA) and (b) line profile of iron oxide strips with surface of bare Cu and pit on surface.

An STM overview of a  $\text{Fe}_3\text{O}_4(100)$  surface is shown in Fig 3.23. Atomically flat terraces with the step edges can be clearly seen, revealing a layer-by-layer growth mode. The average step height was found to be about  $2.1 \text{ Å}$  corresponding to the distance between adjacent A-A or B-B planes of bulk  $\text{Fe}_3\text{O}_4(100)$  structure. The strips are different directions in Fig 3.23(a). Reducing the strain in the iron oxide structure resulted in remarkable double strips in the direction [011] on the strips area shown in Fig 3.23(b). Several small different step heights for oxide strips obtained indicate a complicated internal structure. A closer STM image of the strips is shown in Fig 3.23 (c). The different contrast of strips indicates different heights; the darkest being the lowest and the lightest the highest. The ends of these oxide strips are also obtained. These ends of oxide strip show the oxide growth, which allows the structure of oxide layer to be analyzed. The  $50 \text{ Å}$  width of the overlayer strips (lighter strips) are on a gap between strips underneath (darker strips) with  $2.1 \text{ Å}$  heights again corresponding to an  $\text{Fe}_3\text{O}_4$  termination.

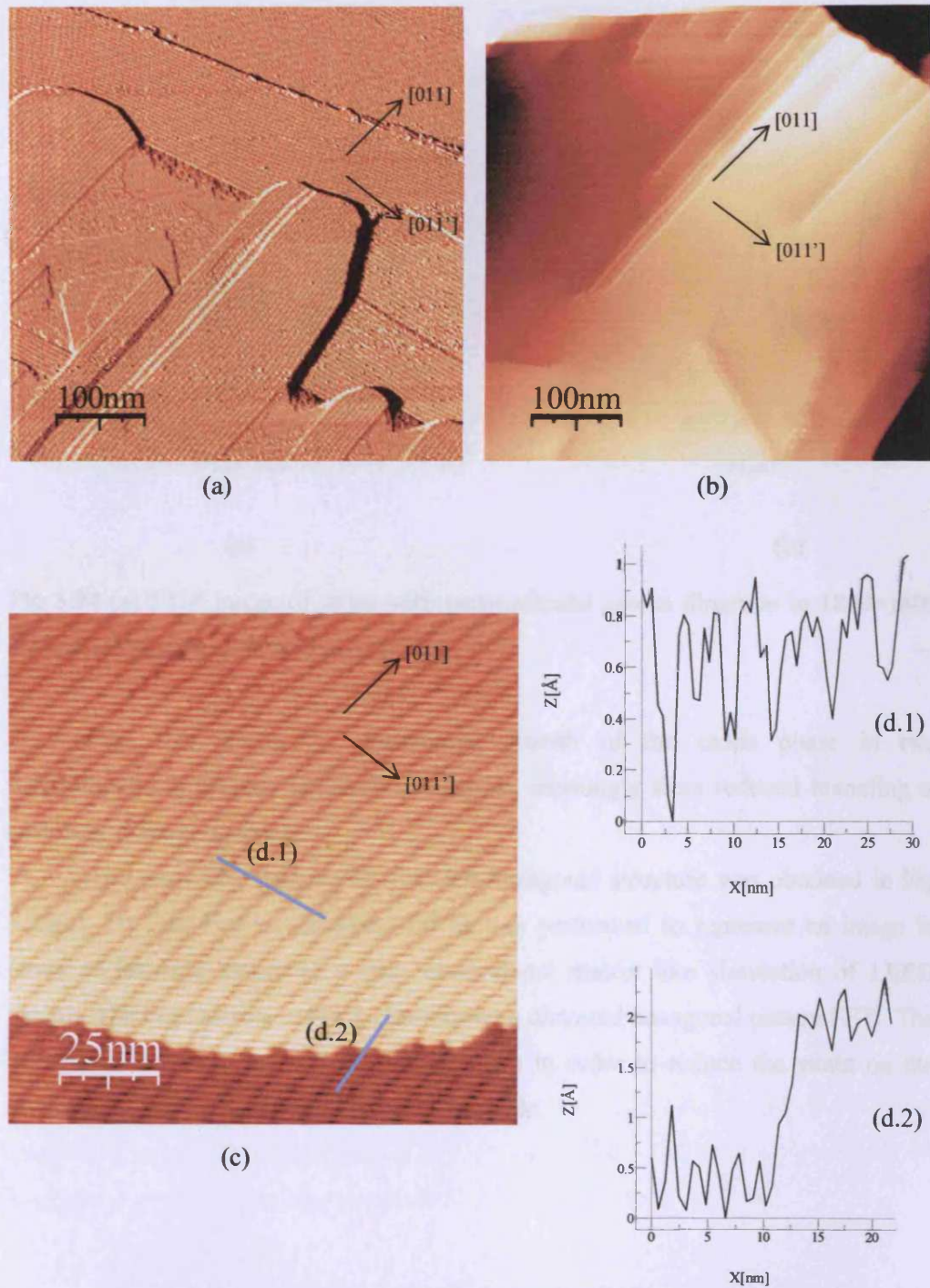


**Fig 3.23** STM images of (a) iron oxide strips in different direction ( $5000 \times 5000 \text{ \AA}^2$ ) (1.3V, 1.2nA), (b) several double strips run on the ordered strips in  $5000 \times 5000 \text{ \AA}^2$ , (c) closer STM image shows 2 layers of iron oxide strips ( $1200 \times 1200 \text{ \AA}^2$ ) (1.5nA, 1V) and (d.1) and (d.2) line profile of oxide strips ( $\sim 2 \text{ \AA}$ ).



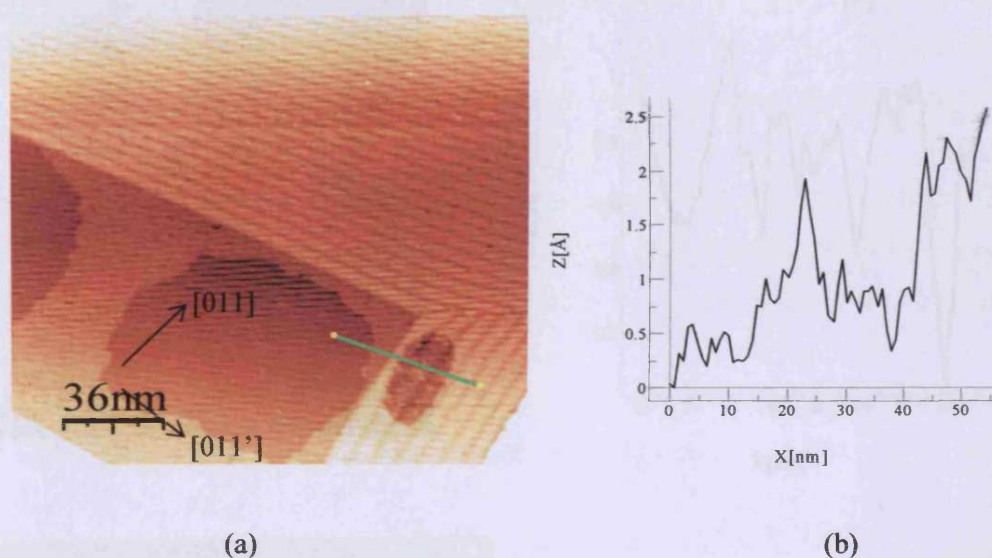


**Fig 3.24** (a) STM image of strips with perpendicular grown direction in  $1800 \times 1800$  Å, 1nA, 1V and (b) line profile of strips.

Fig. 3.24 shows the preferential growth of the oxide phase in two perpendicular directions. These dark strips are seemingly from reduced tunneling at antiphase domain boundaries.

The wave-like features of distorted hexagonal structure was obtained in Fig 3.25(a). 2D Fast Fourier transform (FFT) was performed to represent an image in terms of intensity values in a two-dimensional matrix like simulation of LEED pattern. The inset picture in Fig 3.25(a) shows a distorted hexagonal pattern FFT. The hexagonal structures are in wave-like features in order to reduce the strain on the surface. Fig 3.25(c) is a closer image of the oxide.

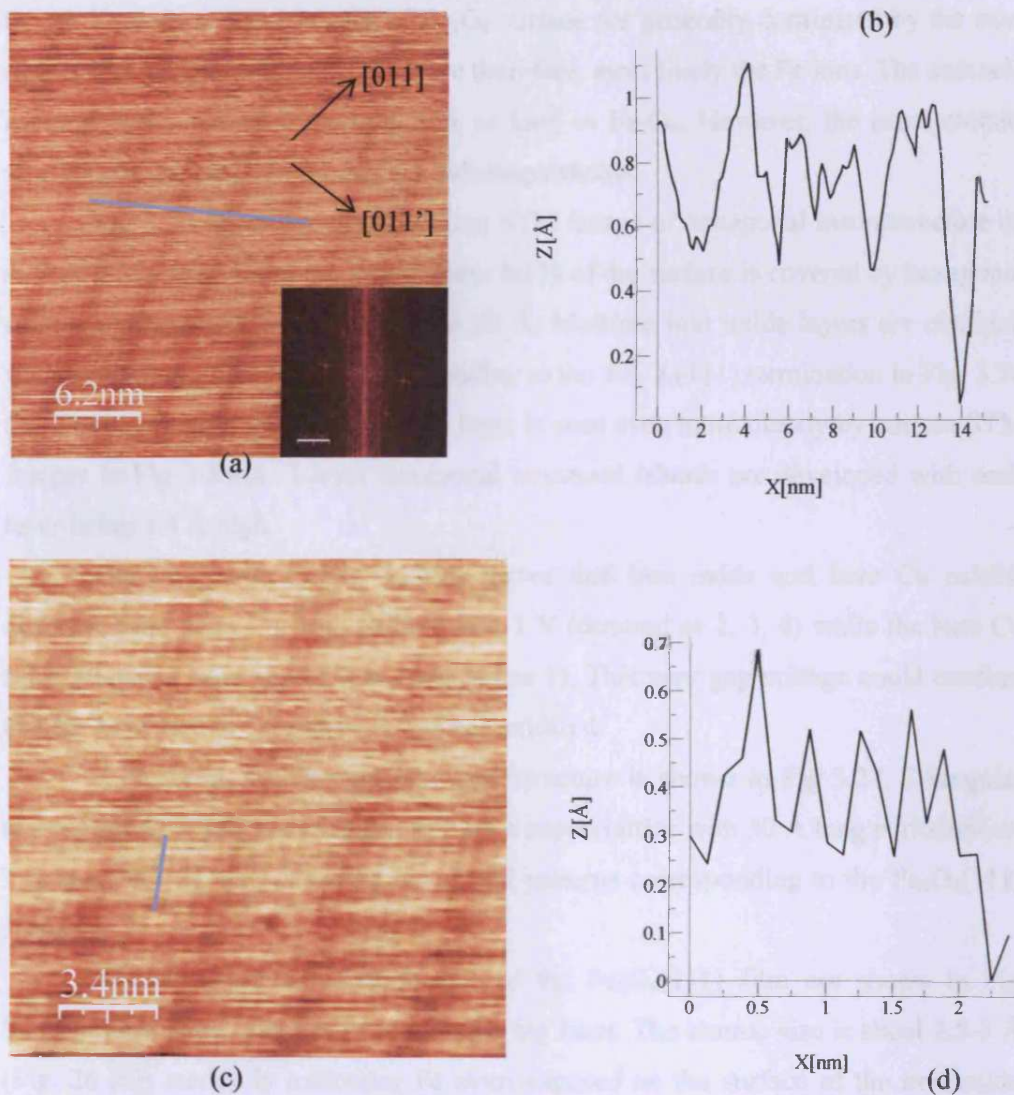


**Fig 3.25** (a) Atomic resolved STM image of iron oxide strips in  $310 \times 310 \text{ \AA}^2$  (b) line profile of wave-like structure (c) a closer image of (a) and (d) line profile of the structure in rows of wave-like structure ( $-0.2 \text{ V}$ ,  $0.32 \text{ nA}$  ).

The  $5 \text{ \AA}$  periodicity of the wave-like features with  $40 \text{ \AA}$  wide (Fig 3.25) were found over a length of the atomic structure. It has been reported that such a long-range order is established at room temperature due to the metal- insulator transition on the surface [24]. Calculations of band structure for  $\text{Fe}_3\text{O}_4$  by Zang and Satpathy [3] reveal that the O 2p orbitals lie below the Fermi level and the bands near  $E_f$  are primarily of

Fe 3d. Therefore, STM images of  $\text{Fe}_3\text{O}_4$  surface are generally dominated by the iron cation. The bright spots in Fig 3.25 are therefore, most likely the Fe ions. The unit cell is more like a distorted hexagon 5 Å as long as  $\text{Fe}_3\text{O}_4$ . However, the exact atomic structure of the  $\text{Fe}_3\text{O}_4$  surface is not indistinguishable.

Fig 3.26 (a) shows the large area STM image of hexagonal macrostructure of an iron oxide film. From the image about 60 % of the surface is covered by hexagonal structure plates with the lateral length 50 Å. Multiple iron oxide layers are obtained with atomic steps 4.8 Å high corresponding to the  $\text{Fe}_3\text{O}_4(111)$  termination in Fig. 3.26 (b). The topography of the iron oxide layer is seen even more clearly by current STM images in Fig 3.26(c). 3 layer hexagonal structural islands are developed with each layer being 4.8 Å high.

The I-V curve in Fig 3.26(d) shows that iron oxide and bare Cu exhibit different band gaps. For iron oxide this is 1 V (denoted as 2, 3, 4) while the bare Cu substrate has a band gap of zero (denoted as 1). This zero gap voltage could confirm that the bare area of Cu substrate was not oxidized.

A closer-up new hexagonal superstructure is shown in Fig 3.27. Triangular and hexagonal plates are arranged to form a superlattice with 50 Å long periodicities. The inset is a 2D-FFT showing hexagonal patterns corresponding to the  $\text{Fe}_3\text{O}_4(111)$  surface.

Atomic -resolved STM images of the  $\text{Fe}_3\text{O}_4(111)$  film are shown in Fig 3.28(a). Obviously many atoms are on the big facet. The atomic size is about 2.5-3 Å (Fig. 26 (b)) randomly indicating Fe atom exposed on the surface of the iron oxide film. The 2D-FFT in Fig 3.28(b) shows the 2 hexagonal patterns. The small hexagonal unit cell in Fig 3.28 (b) denotes the hexagonal superstructure and the big hexagonal unit cell denotes hexagonal arranged atoms in big hexagonal superstructures.



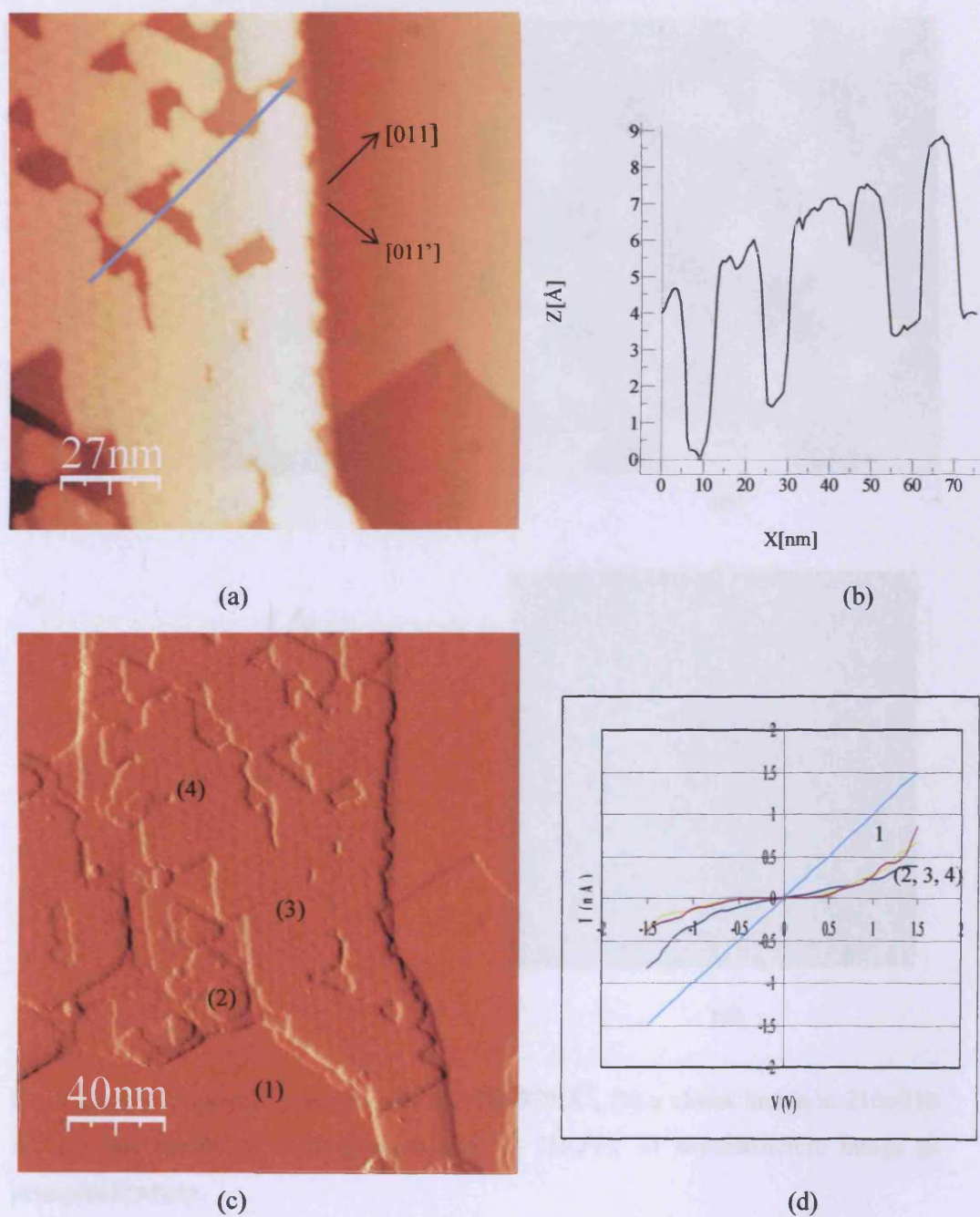


**Fig 3.26** (a) STM image of iron oxide hexagonal structure in  $1400 \times 1400 \text{ \AA}^2$  (1 V, 0.48 nA), (b) line profile of hexagonal topmost structure, (c) current STM image in  $2000 \times 2000 \text{ \AA}^2$  (1 V, 0.48 nA) and (d) IV-curve from (c).

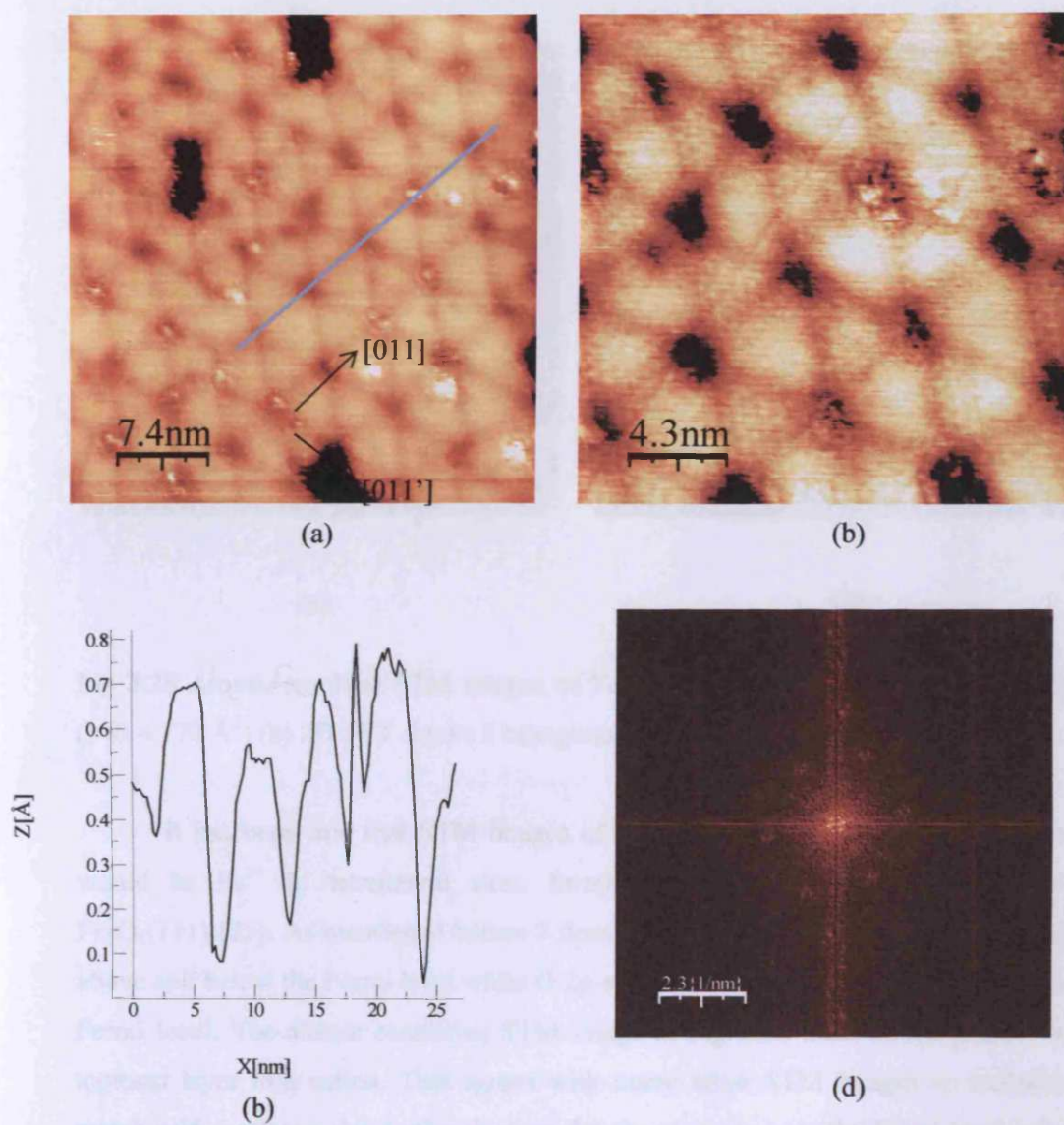


**Fig 3.27** (a) Hexagonal superstructure in  $370 \times 370 \text{ \AA}^2$ , (b) a closer image in  $210 \times 210 \text{ \AA}^2$ , (c) line profile of superstructure and (d) 2D-FFT of superstructure image as hexagonal pattern.



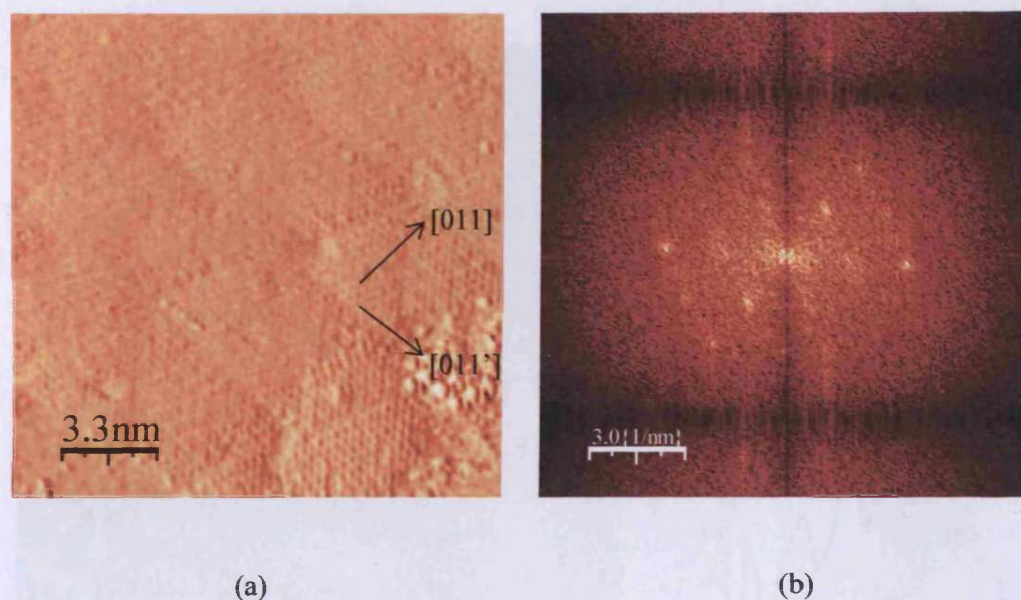


**Fig 3.28** Atomic-resolved STM images of  $\text{Fe}_3\text{O}_4(111)$  (a) Fe atoms in the big facet ( $170 \times 170 \text{ \AA}^2$ ) (b) 2D-FFT shows 2 hexagonal structures on surface.

It has been said that STM images of the topmost of  $\text{Fe}_3\text{O}_4(111)$  termination would be  $\text{Fe}^{3+}$  in tetrahedral sites, forming a hexagonal surface lattice with  $\text{Fe}_3\text{O}_4(111)$  [25]. As mentioned before 2 dominant states of Fe are located intimately above and below the Fermi level while O 2p-states are generally located far below the Fermi level. The atomic resolution STM image in Fig 3.28 must be the position of topmost layer iron cation. This agrees with many other STM images on transition metal oxide surfaces, due to the electron density of states near the Fermi level being generally dominated by the metal orbital band.

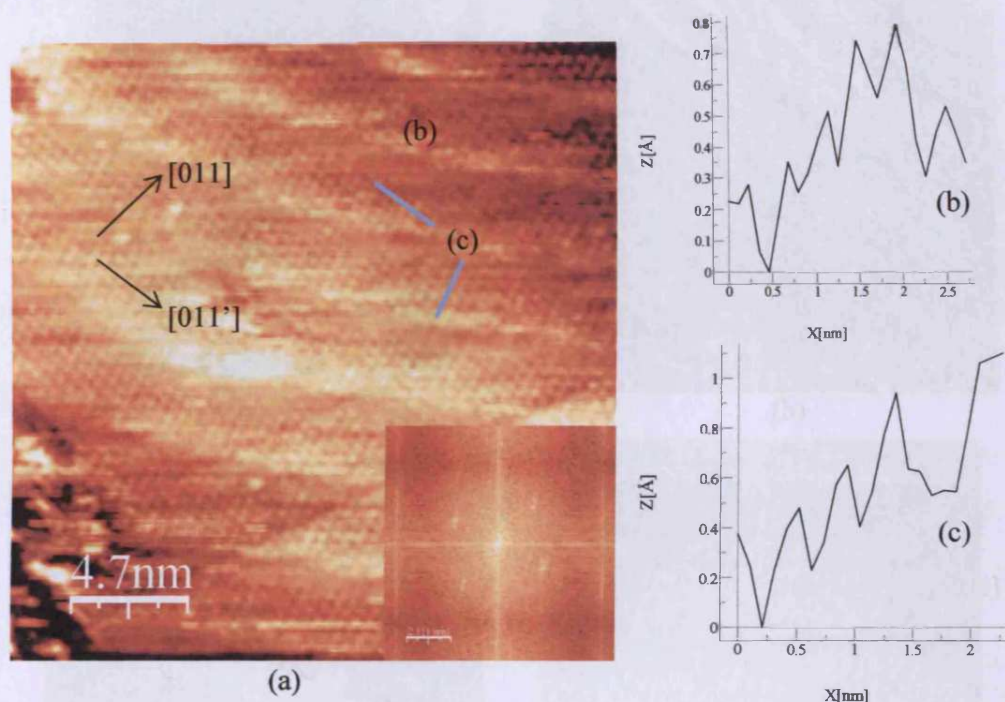


**Fig 3.29** (a) STM image with rectangular pattern in  $240 \times 240 \text{ \AA}^2$  (0.70 nA, 1V) and (b) and (c) line profile of the structure.

Another higher resolution image taken from the oxide terrace is shown in Fig 3.29. Atomically resolved rows running  $15^\circ$  compared with  $[011]$  directions are clearly visible. A rectangular lattice was occasionally observed with a spot-to-spot separation of  $\sim 3.5 \times 5.5 \text{ \AA}$ . Neither of them is the likely unit cell of the  $\text{Fe}_3\text{O}_4$  surface. This STM image might be a Moiré pattern.

Defect found in large views of antiphase domain boundary strips in different directions are shown in Fig 3.30(a), (b) and (c) images. The staircase-like defects are shown in Fig. 3.30 (c) and (d).

Consequently, XPS, LEED and STM results confirm that iron oxide prepared in 850 K and  $10^{-6}$  mbar  $\text{O}_2$  could be  $\text{Fe}_3\text{O}_4(111)$  coexisting with  $\text{Fe}_3\text{O}_4(100)$ .



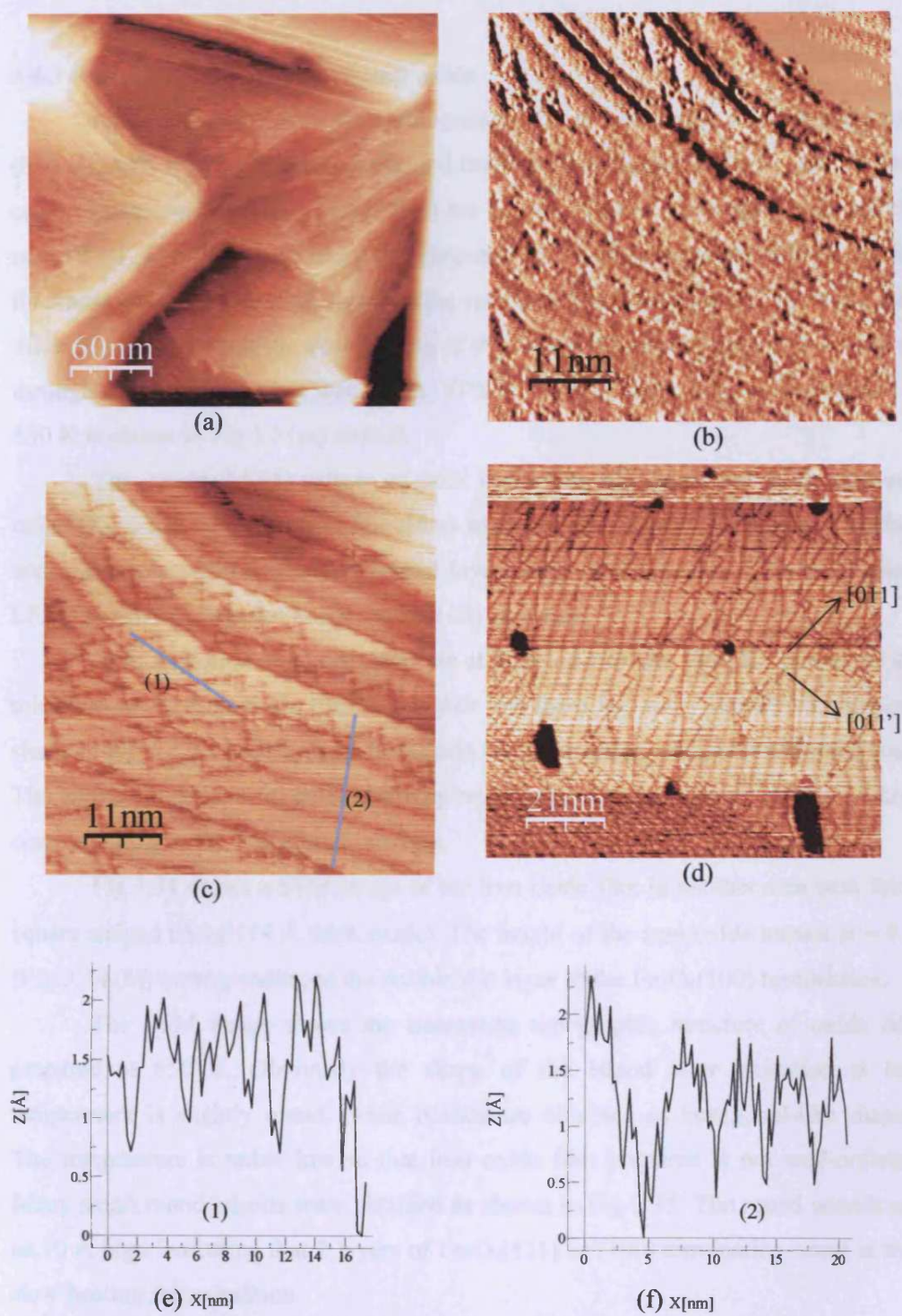


**Fig 3.30** STM images of (a) strips of iron oxide in different direction in a large area ( $3000 \times 3000 \text{ \AA}^2$ ,  $-0.1 \text{ v}$ ,  $0.2 \text{ nA}$ ), (b) and (c) closer i- and z-STM images with  $540 \times 540 \text{ \AA}^2$  ( $-0.15 \text{ V}$ ,  $0.2 \text{ nA}$ ), (d) a view of the 'pit' in iron oxide strips ( $110 \times 110 \text{ \AA}^2$ ) and (e) and (f) line profile of the defect on the strips.

### 3.4.3 Characterization of thick iron oxide

After the oxidation of Fe multilayers on Cu substrate with lower heating rate (850 K), XPS (Fig 3.31) result confirmed that the oxide formed is  $\text{Fe}_3\text{O}_4$ . The binding energy positions of  $\text{Fe}(2p_{3/2})$  and  $\text{O}(1s)$  are 710.6 and 529.7 eV, respectively and the ratio of Fe : O of 0.74-0.78 like oxide prepared with high heating rate (850 K) but the thickness of iron oxide with low heating rate is rather thicker, about 10-14 Å. This thickness indicates that the slow heating of the sample allows oxygen gas to slowly go through the surface to form iron oxide. XPS of 12-16 Å thick iron oxide prepared at 650 K is shown in Fig 3.31(c) and (d).

The streaky LEED pattern of thick iron oxide film is similar to the thin iron oxide (Fig 3.32). The pattern is blurred as expected due to the deformation of surface and interlayer or disorientations several layers deep in the surface. This is a unique LEED pattern of prepared  $\text{Fe}_3\text{O}_4$  on Cu(100) substrate.

After oxidation at a very slow rate at high temperature (850 K), obviously the thickness of the iron oxide film was higher and there are many islands with straight shape in Fig 3.33. The shapes of the islands are rectangular, triangular and hexagonal. The entire substrate is covered mostly by rectangular, hexagonal crystallites 5 Å high corresponding to the  $\text{Fe}_3\text{O}_4$  (111) surface.

Fig 3.34 shows a STM image of the iron oxide film in another area with fairly square shaped island (14 Å thick oxide). The height of the iron oxide terrace is ~ 4 Å (Fig 3.34 (b)) corresponding to the double AB layer of the  $\text{Fe}_3\text{O}_4$ (100) termination.

The STM image shows the interesting topographic structure of oxide film prepared at 650 K. Obviously the shape of the island after oxidation at low temperature is slightly round. Some islands are obtained as hexagonal-like shapes. The temperature is rather low so that iron oxide film prepared is not well-ordered. Many small round islands were obtained as shown in Fig 3.35. The round islands are ca.10 Å high indicating that 2 layers of  $\text{Fe}_3\text{O}_4$ (111) or (100) termination occur at this slow heating rate condition.



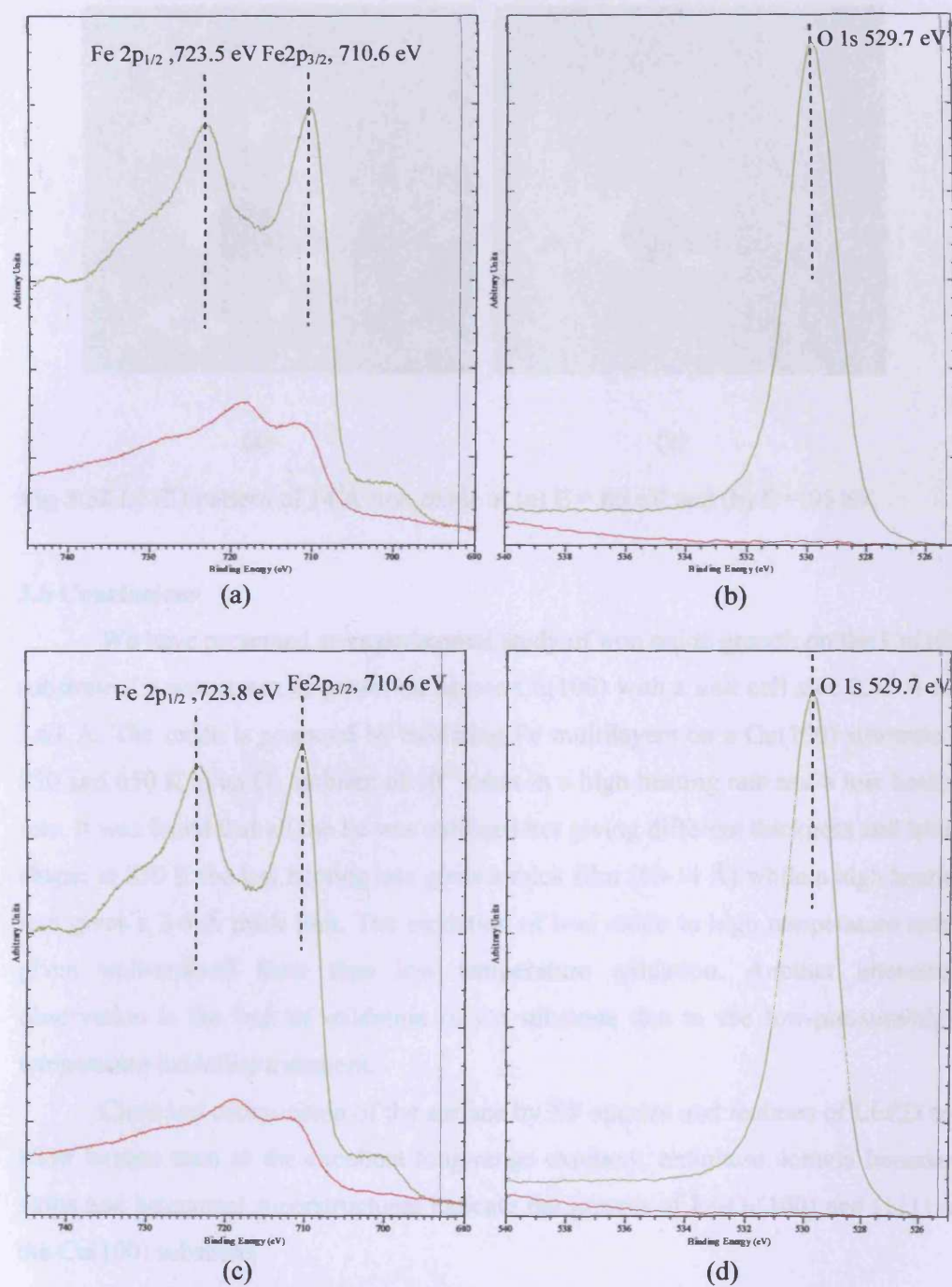


**Fig 3.31** XPS spectra of iron oxide thick film prepared by oxidation at 850 K (a) and (b) Fe 2p (b) O (1s) peaks and oxidation at 650 K (c) Fe 2p and (d) O 1s peaks.

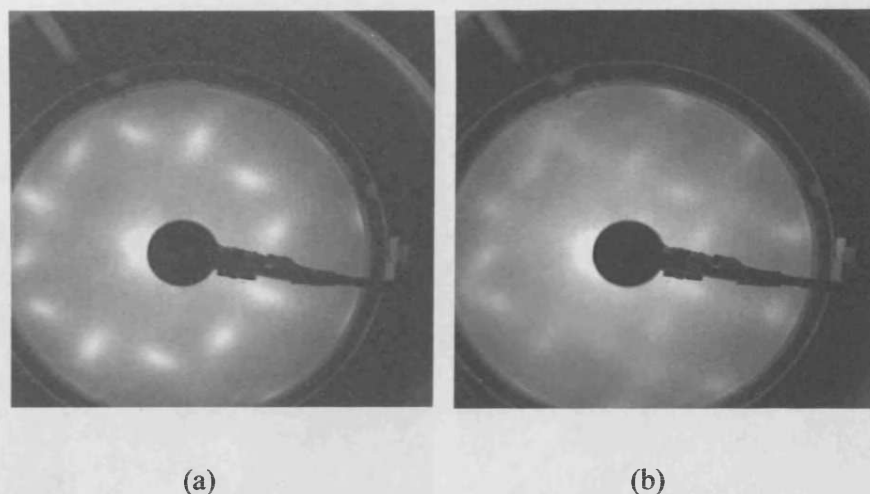


**Fig 3.32** LEED pattern of 14 Å iron oxide at (a)  $E = 65$  eV and (b)  $E = 95$  eV.

### 3.5 Conclusions

We have presented an experimental study of iron oxide growth on the Cu(100) substrate. Fe was epitaxial grown on square Cu(100) with a unit cell side 2.55 Å and 3.61 Å. The oxide is prepared by oxidizing Fe multilayers on a Cu(100) substrate at 850 and 650 K in an  $O_2$  ambient of  $10^{-6}$  mbar in a high heating rate and a low heating rate. It was found that all the Fe was oxidized but giving different thickness and island shape; at 850 K the low heating rate gives a thick film (10-14 Å) while a high heating rate gives a 3-5 Å thick film. The oxidation of iron oxide in high temperature rather gives well-ordered form than low temperature oxidation. Another interesting observation is the lack of oxidation of Cu substrate due to the low-pressure/high-temperature oxidation treatment.

Chemical composition of the surface by XP spectra and features of LEED and STM images such as the excellent long-range epitaxy, antiphase domain boundary strips and hexagonal superstructures indicate the growth of  $Fe_3O_4(100)$  and (111) on the Cu(100) substrate.

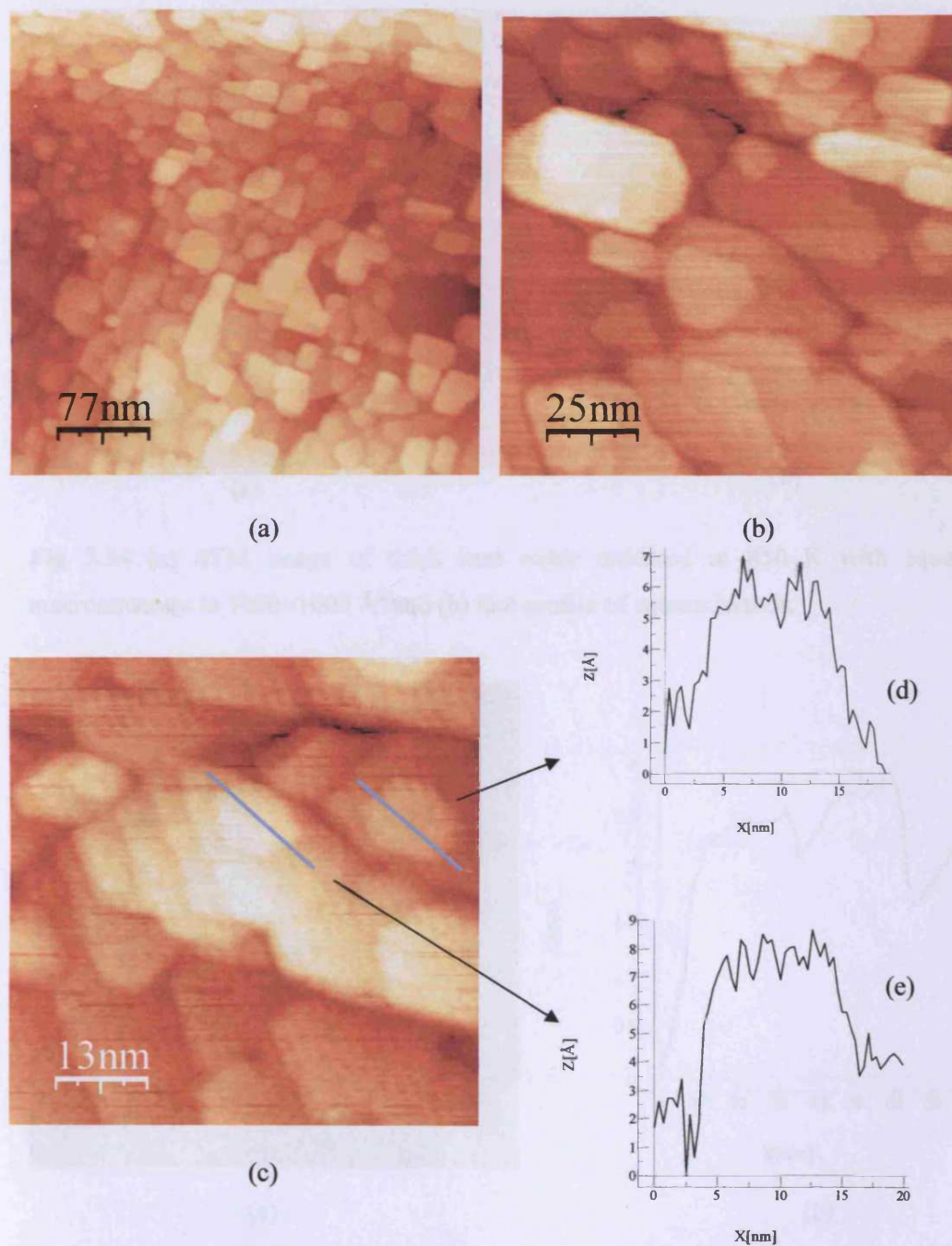


**Fig 3.33** STM images of thick iron oxide oxidized at 850 K in area (a)  $3840 \times 3830 \text{ \AA}^2$ , (b)  $1250 \times 1250 \text{ \AA}^2$  and (c)  $670 \times 670 \text{ \AA}^2$ , (d) and (e) are line profiles of the structure.



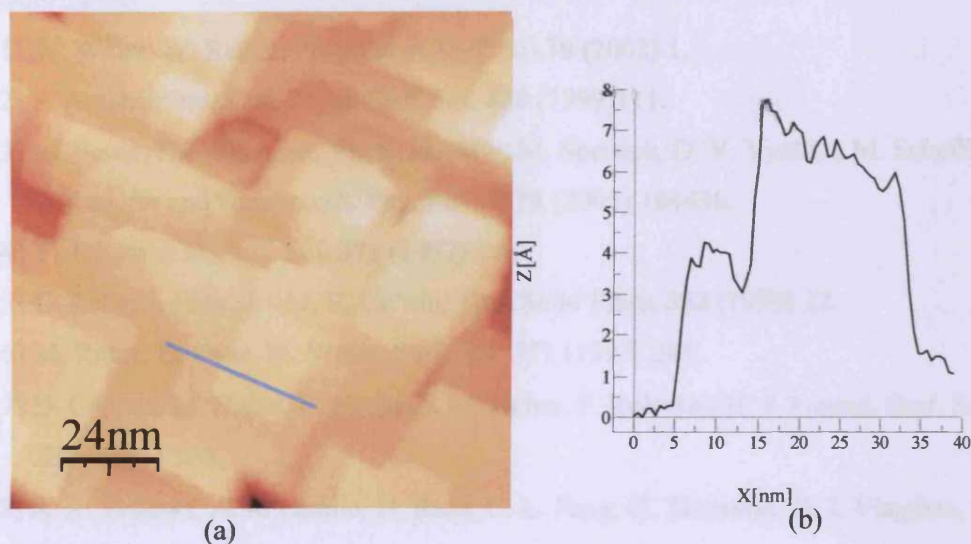


**Fig 3.34** (a) STM image of thick iron oxide oxidized at 850 K with square macrostructure in  $1000 \times 1000 \text{ Å}^2$  and (b) line profile of square islands.

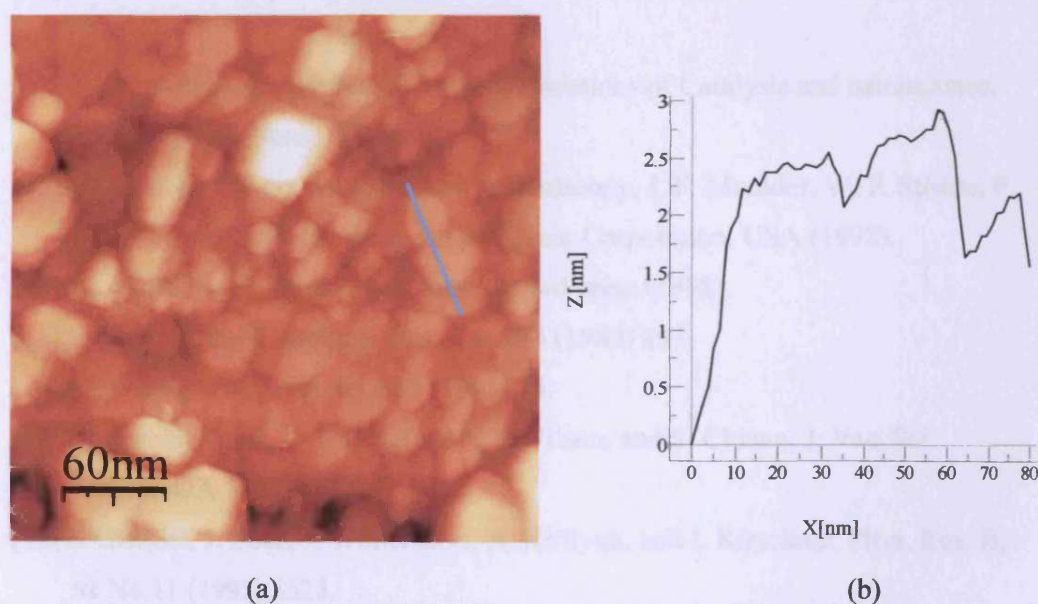


**Fig 3.35** STM image of iron oxide oxidized 650 K (a)  $3000 \times 3000 \text{ Å}^2$  (b) line profile of the structure.

**References:**

- [1] W. Weiss, W. Ranke, *Progress in Surf. Sci.* **70** (2002) 1.
- [2] S. A. Chamber, S. A. Joyel, *Surf. Sci.* **420** (1999) 111.
- [3] M. Fonin, R. Pentcheva, Yu. S. Dedkov, M. Sperlich, D. V. Vyalikh, M. Scheffler, U. Rudiger and Guntherodt, *Phy. Rev. B* **72** (2005) 104436.
- [4] Y. J. Kim et al, *Surf. Sci.* **371** (1997) 358.
- [5] C. Ruby, J. Fusy, J. –M. R. Ge'nin, *Thin Solid Films* **352** (1999) 22.
- [6] M. Ritter, H. Over, W. Weiss, *Surf. Sci.* **371** (1997) 245.
- [7] D. Cappus, M. Haßel, E. Neuhaus, M. Heber, F. Rohr and H. J. Freund, *Surf. Sci.* **337** (1995) 268.
- [8] R. A. Fellows, A. R. Lennie, H. Raza, C. L. Pang, G. Thornton, D. J. Vaughan, *Surf. Sci.* **445** (2000) 11.
- [9] J. Karunamuni, R. L. Kurtz, R. L. Stockbaver, *Surf. Sci.* **442** (1999) 223.
- [10] C. Pflitsh, R. David, L. K. Verhej, R. Franchy, *Surf. Sci.* **488** (2001) 32.
- [11] F. Qin, N. P. Magtoto, M. Garza, J. A. Kelber, *Thin Solid Films* **444** (2003) 179.
- [12] K. W. Kolasinski, *Surface Science: Foundations of Catalysis and nanoscience*, John Willey & Sons LTD, 2001.
- [13] *Handbook of X-ray Photoelectron spectroscopy*, J. F. Moulder, W. F. Stickle, P. E. Sobol and K. D. Bomben, Perkin-Elmer Corporation, USA (1992).
- [14] G. Attard and C. Barnes, *Surfaces*, Oxford press (1998).
- [15] F. Jona and P. M. Marcus, *Surf. Sci.* **223** (1989) 897.
- [16] M. Wuttig et al, *Surf. Sci.* **291** (1993) 14.
- [17] K. E. Johnson, D. D. Chambliss, R. J. Wilson, and S. Chiang, *J. Vac. Sci. Technol. A* **11** (1993) 4.
- [18] J. Giergiel, J. Shen, J. Woltersdorf, A. Kirilyuk, and J. Kirschner, *Phys. Rev. B*, **52** No.11 (1995) 8528.
- [19] Y. J. Y. Gao, S.A. Chambers, *Surf. Sci.* **371** (1997) 358.
- [20] C. Ruby, J. Fusy, J. –M. R. Ge'nin, *Thin Solid Films* **352** (1999) 22.
- [21] E. Yagasaki, K. Kishi, *J. electron Spectrosc. Relat. Phenom.* **69** (1994) 133.
- [22] G.C. Allen, M. T. Curtis, A. J. Hooper and P. M. Tucker, *J. Chem. Soc. Dalton Trans.* (1974) 1525.



- [23] J. Zang, G. Cao, Chinese J. of Chemical Physics **19** No.3 (2006)197.
- [24] S. F. Ceballos, G. Mariotto, K. Jordan, S. Murphy, C. Seoighe, I. V. Shvets, Surf. Sci. **548** (2004) 106.
- [25] M. Ritter, W. Weiss, Surf. Sci. **432** (1999) 81.

## Chapter 4

### Gold Nanoparticles Deposited on Iron Oxide

#### 4.1 Introduction to gold nanoparticles deposited on iron oxide

Gold metal is chemically inert compared to other metals and has been less studied as catalyst. Hammer and Norskov [1] have found that the low activity of the gold surface relates to the degree of orbital overlap and the degree of filling of the antibonding states. Those factors determine the strength of the adsorbate-metal interaction and dissociation energy. According to density functional theory, the d-band of gold is only weakly coupled to adsorbate electronic states. This coupling is not strong enough to drive the antibonding state above the Fermi level of Au metal resulting in a repulsive interaction. The reactivity of the Au metal surface is poor even with reactive molecules such as O<sub>2</sub> and H<sub>2</sub>. However, the gold nanoparticles have a high catalytic activity and nowadays attract much attention from scientists.

Haruta's group reported that catalytic properties of Au depend on the oxide support, preparation methods and size of Au clusters [2]. For CO oxidation, the hemispherical shape of Au gives higher reactivity than spherical shaped Au particles due to more extensive perimeter interface of hemispherical Au clusters. Moreover, Au clusters with diameter ~ 35 Å gave a maximum rate of CO oxidation and STS results shows nonmetallic properties of Au clusters at this size[2]. These results suggest that the catalytic properties of a Au cluster supported on oxide may deviate from the bulk metal.

The structure of nanoparticles has been the subject of much interest over recent years due to their remarkable electronic, geometric and chemical properties which are important for both fundamental research and applications [3]. Au nanoparticles supported on metal oxide powders such as TiO<sub>2</sub> or α-Fe<sub>2</sub>O<sub>3</sub> are very active for catalytic reactions [4, 5]. It was found that deposition of Au nanoparticles on single crystal rutile TiO<sub>2</sub>(110) is also very high reactive. Model systems are studied in order to investigate the mechanisms for the high catalytic activity, and are in agreement with Au particle size effect.

The supported model system would make possible an enhanced understanding of catalytic activity of metal oxide supported Au catalysts.

Again studies of catalytic reaction at the molecular level are difficult on oxide surfaces due to surface charging, impurities and reproducible sample preparation [6]. These problems can be avoided by using thin films of metal oxide grown on metal substrates and consequent Au particle deposition. This is the procedure that has been undertaken in the current work.

In this chapter the preparation of iron oxide films (more detail of iron oxide preparation are given in chapter 3) and subsequent deposition of Au nanoparticles is studied. Our core target in this work is to make a well-defined model catalyst consisting of Au particles supported on iron oxide( $\text{Fe}_3\text{O}_4$ ) on a Cu(100) surface. The combination of XPS, LEED and STM was performed to characterize the surface. Au nanoparticles deposited on high temperature oxidized Cu and clean Cu were also studied.

#### **4.2 Literature reviews: Au nanoparticles supported on substrates**

Au nanoparticles supported on model substrate systems with high catalytic reactivity, have been studied for several years. Au and Ag nanoparticles grown on sputtered Highly Ordered Pyrolytic Graphite (HOPG) surface were studied by Lopes-Salido et al [3]. It was found that at high Au coverages, the structure of Au films deviate from the truncated octahedral form. Many steps exist between different Au atom layers due to a high activation barrier for diffusion of Au atoms across the step edges. Au hexagonal shapes could also be obtained indicating favored growth of Au nanostructures aligned with the (111) direction normal of surface. XPS studies show a small core level shift with decreasing particle size and Auger analysis reveals the metal/substrate charge transfer. Ag is (partially) positively charged while Au is negatively charged on HOPG.

Chusuei et al [7] studied model catalysts consisting of Au and Ag clusters on single crystal  $\text{TiO}_2(110)$  and ultra-thin films of  $\text{TiO}_2$ ,  $\text{SiO}_2$  and  $\text{Al}_2\text{O}_3$ . It was found that the unique cluster size  $< 50 \text{ \AA}$  was obtained. The dispersions of Ag and Au depend on the underlying surface structure (roughness, plateaus and defects density). Relative differences in XPS core level binding energy shifts as a function of cluster

coverage reveal that the electronic structure reflects chemical compositions of the underlying oxide support. Admetal cluster size and the cluster-substrate interactions influence the catalytic activity. The application of metal clusters supported on thin oxide films presents new insights into the special electronic and chemical properties that direct their unique catalytic chemistry.

Au/TiO<sub>2</sub>/Ru(0001) model catalysts and their interaction with CO were studied by Zhao et al [6]. An epitaxial thin TiO<sub>2</sub> film was grown on Ru(0001) by high temperature oxidation of Ti on a Ru substrate. Au particles 20-60 Å high (one to three atomic layers) were distributed homogeneously on oxidized and reduced TiO<sub>2</sub> surfaces. Au particles distribution on oxidized TiO<sub>2</sub> was slightly higher than that of on reduced TiO<sub>2</sub>; however, Au clusters supported on reduced TiO<sub>2</sub> are more stable than those on oxidized TiO<sub>2</sub>. Annealing at 770 K resulted in more hemispheric particles and 3D islands. After exposure of CO to Au/TiO<sub>2</sub>/Ru(0001) model catalysts, both Au clusters and the TiO<sub>2</sub> substrate adsorbed CO molecules.

Our aim is the preparation of Au supported on an iron oxide film grown on Cu(100). Our model catalyst was produced in UHV and characterized by XPS, LEED and STM.

### 4.3 Experimental Details

The experiments were performed in a UHV system. Oxide films were produced by oxidizing Fe multilayers deposited on Cu(100). More information on iron oxide film preparation is provided in chapter 3.

The Au doser was made by wrapping high purity wires (99 %) of Au around a molybdenum filament, which was then resistively heated by passing current through the filament wire. This wire was thoroughly out-gassed to remove impurities before use. A 1 ML surface coverage was defined as  $1.5 \times 10^{15}$  atoms cm<sup>-2</sup> [1 Cu unit cell is  $6.5 \times 10^{-16}$  cm<sup>2</sup> which is  $1.5 \times 10^{15}$  atoms cm<sup>-2</sup> for 1 ML]. Au deposition on the iron oxide surface film was performed in the C chamber with a current of 3.8 A. Overall the C chamber pressure did not exceed  $2 \times 10^{-9}$  mbar during deposition.

### 4.4 Characterization of Au deposited on iron oxide films

Au nanoparticles deposited on iron oxide film were analyzed by XPS, LEED and STM to monitor the changes in chemical composition and morphology.

#### 4.4.1 Characterization of Au deposited on thin iron oxide films (~5 Å thick)

This section shows results and discussion of XPS and STM analysis of Au nanoparticles on ~5 Å thin iron oxide  $\text{Fe}_3\text{O}_4$  films.

##### 4.4.1.1 XPS results

In this experiment, an  $\text{Fe}_3\text{O}_4$  film (oxidized in  $10^{-6}$  mbar at 850 K) grown on Cu(100) was used as a support for Au (0.2-0.4 ML) deposition. The combination of a 4.8 Å superstructure and strips 2.0-4.0 Å wide which cover almost the whole sample surface, indicate iron oxide  $\text{Fe}_3\text{O}_4(111)$  and (100) terminations.

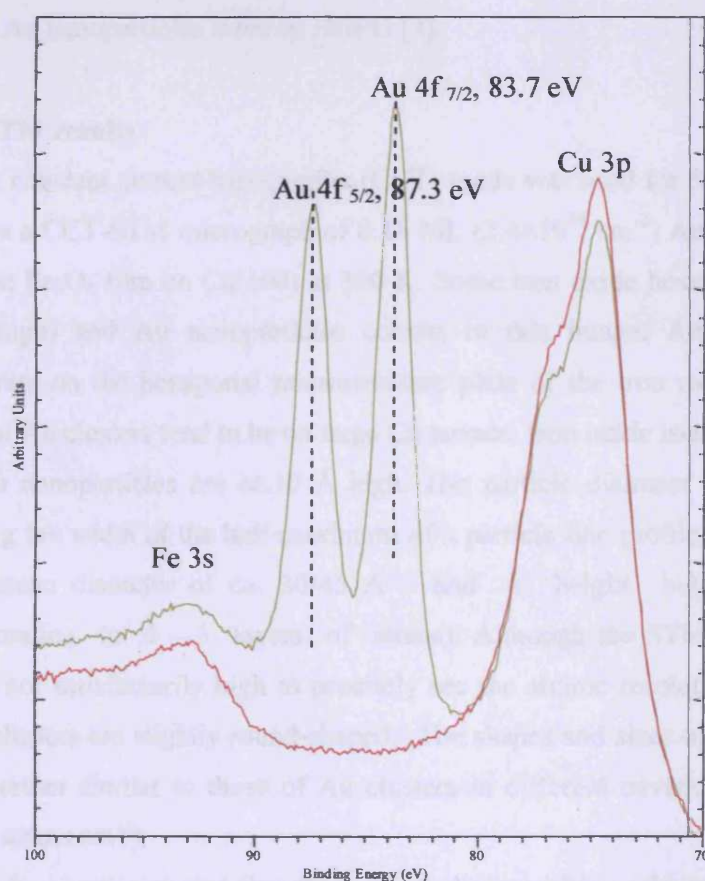


**Fig 4.1** XP spectra of Au 4f peak on  $\text{Fe}_3\text{O}_4/\text{Cu}(100)$  surface at 300 K, Al  $K\alpha$  anode (1486.6 eV); — iron oxide surface on Cu and — after Au deposition on thin iron oxide grown on Cu.



The surface concentration of Au is  $3.0\text{--}6.0 \times 10^{14}$  atoms  $\text{cm}^{-2}$  (ca. 0.2–0.4 ML). Surface concentration of carbon and oxygen impurities were low ( $1\text{--}2 \times 10^{14}$  atoms  $\text{cm}^{-2}$ ). Fig 4.1 shows XP spectra of 0.4 ML Au 4f at 300 K. The Au 4f photoemission peak is in between the Cu 3p and Fe 3s peaks; binding energy of Au 4f<sub>7/2</sub> and Au 4f<sub>5/2</sub> peaks are 83.7 and 87.3 eV, respectively. It has been reported [7] that at high Au coverage (0.02–6.0 ML) the Au 4f<sub>7/2</sub> core levels shift toward lower binding energy (84.3 eV) due to emission from large Au clusters. A lower Au coverage gives a Au 4f<sub>7/2</sub> core level shift toward higher binding energy due to the finite cluster size effects or small Au clusters grown on the defect sites/ step edges rather than flat terraces. However, it has also been reported that no significant core level shifts occur for different Au nanoparticles sizes on HOPG [3].

#### 4.4.1.2 STM results

A constant current topographic (CCT) mode was used for STM imaging. Fig 4.2 shows a CCT-STM micrograph of 0.16 ML ( $2.4 \times 10^{14}$   $\text{cm}^{-2}$ ) Au deposited on 5 Å iron oxide Fe<sub>3</sub>O<sub>4</sub> film on Cu(100) at 300 K. Some iron oxide hexagonal flat terraces (4.8 Å high) and Au nanoparticles coexist in this image. Au clusters tend to agglomerate on the hexagonal microstructure plate of the iron oxide surface while individual Au clusters tend to be on large Cu terrace. Iron oxide islands are 4.8 Å high while Au nanoparticles are ca. 10 Å high. The particle diameter was evaluated by measuring the width of the half-maximum of a particle line profile. Au nanoparticles have a mean diameter of ca. 30–45 Å and a height below 10 – 15 Å (Corresponding to 3 – 5 layers of atoms). Although the STM resolution in the image is not satisfactorily high to precisely see the atomic resolution, we can argue that the clusters are slightly round-shaped. The shapes and sizes of Au nanoparticles are also rather similar to those of Au clusters in different coverages (between  $3.0\text{--}6.0 \times 10^{14}$  atoms  $\text{cm}^{-2}$ ).

It has been reported that there are 3 distinguishing admetal growth modes; layer-by-layer (Frank van der Merwe), an initial monolayer, followed by 3D growth (Stranski-Krastanov) and 3D cluster growth (Volmer-Weber) modes. Au, Pd and Ag admetals have been found to nucleate and grow on oxides as quasi-2D clusters (flat 3-Dimensional island) at < 1 ML coverage while at coverages > 1 ML these admetals grow as 3D structures [7]. It also has been reported that the top layer of oxygen on the

support material might be a significant factor in Au nanoparticles growth. In our studies, Au clusters on iron oxide were found as 3D particles at a coverage of 0.2 ML Au.

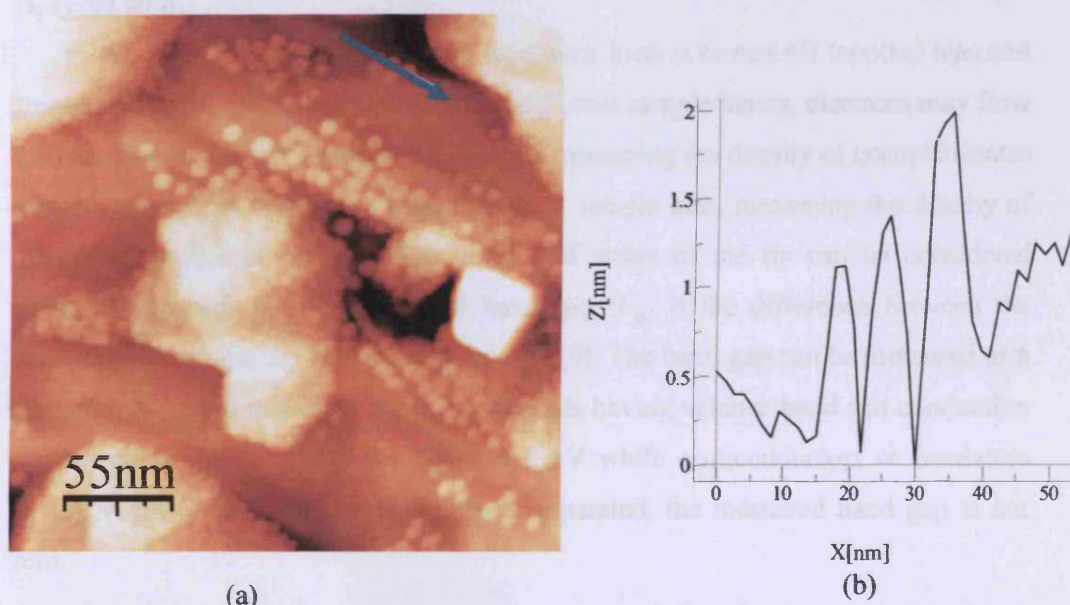


**Fig 4.2** STM image of 0.2 ML Au on 4 Å  $\text{Fe}_4\text{O}_4$  on Cu(100) surface (1nA, 1V, 2700×2700 Å<sup>2</sup>) and (b) line profile of Au nanoparticles.

Fig 4.3(a) shows the agglomeration of Au clusters on a Cu terrace oxidized at high temperature. Au clusters with diameter 40-50 Å tend to agglomerate to big islands rather than be isolated on the substrate. The line profile of these islands with maxima 20 Å high is shown in Fig 4.3(b). Some individual Au clusters are also located on the Cu edge.

Interestingly, Au clusters tend to grow as 3D islands on iron oxide islands (Fig 4.2); otherwise they agglomerate themselves on the surface (Fig 4.3). As mentioned in the previous chapter the top of oxide film could be terminated by either Fe cations or oxygen; oxygen could be the promising element to induce Au nanoparticles to stick on the oxide film.

The combination of scanning tunneling spectroscopy (STS) and CCT-STM imaging is a very good method to determine the local electronic structure of surfaces on nanometer scale [8]. A map of local density of states (DOS) could be obtained by varying the applied voltage and measuring the tunneling current. Both occupied and

unoccupied electronic states can be investigated by holding the tip position and tunneling gap constant and measuring the tunneling current as a function of bias voltage. The I-V curve gives the information about the chemical environment of the analyzed atom.

At equilibrium gap spacing the feed back loop is turned off (applied bias and tunneling current for milliseconds). Under different sample biases, electrons may flow from surface to the tip (negative sample bias, measuring the density of occupied states of surface) or from the tip to surface (positive sample bias, measuring the density of unoccupied states of surface). The density of states of the tip can be considered constant with respect to voltage. The band gap ( $E_g$ ) is the difference between the conduction band and the valence band energy [9]. The band gap can be measured as a zero-current period in the I-V curve; for metals having valence band and conduction band overlap, the measured band gap is 0 eV while semiconductors or insulators having valence band and conduction band separated, the measured band gap is not zero.

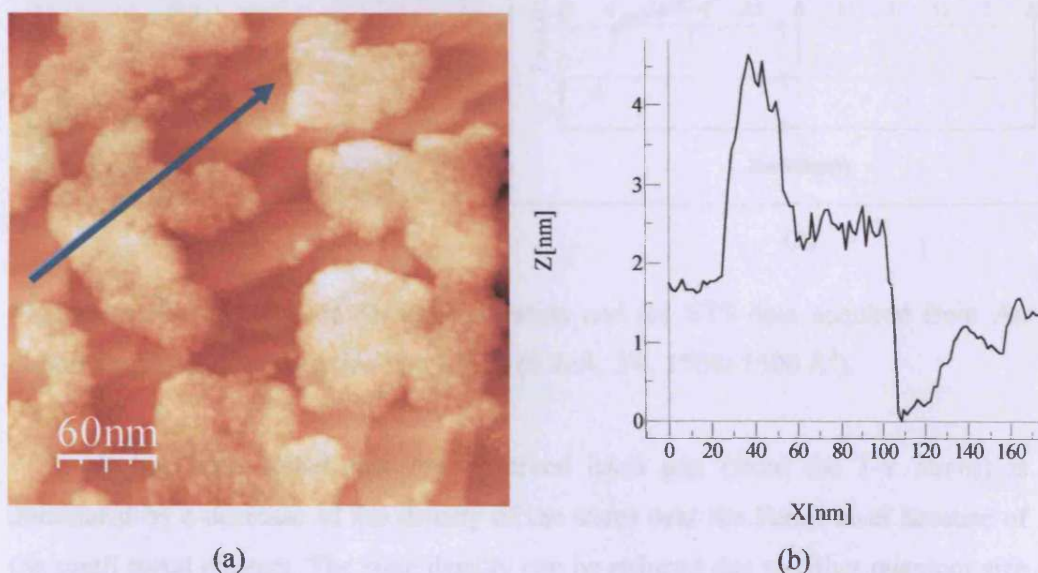


**Fig 4.3** (a) STM image of agglomeration of Au clusters in  $3000 \times 3000 \text{ \AA}^2$ , (0.2 nA, 1V) and (b) line profile of Au agglomeration on oxidized surface.

Fig 4.4(a) shows a closer STM image of Au clusters islands and Fig 4.4(b) shows STS taken at different points on the sample surface area. The ST spectra had been obtained by pointing the STM tungsten tip at a preferred point and locking the



STM feedback loop. The tunneling current ( $I$ ) as a function bias voltage ( $V$ ) across the tip is measured. The tunneling current and bias voltage ( $I$ - $V$ ) curves are correlated with different areas on surface. As Fig 4.4(b) shows the agglomeration of Au clusters in various areas have a non-metallic character resulting in significant band gaps ( $\sim 0.5$  V) (curves 1-5). However, high temperature oxidized Cu still has metallic properties giving no band gap (curve 6). It has been reported that the measured band gap for the substrate is related to the number and conductivity of oxygen vacancies and defect sites. The coexistence between Au clusters and iron oxide can also affect the Au cluster electronic properties.

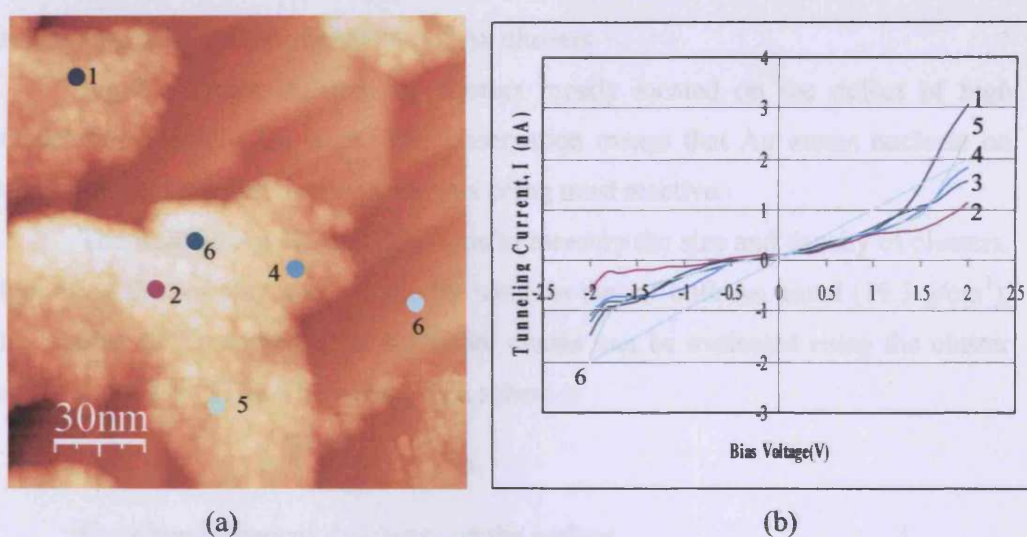


**Fig 4.4** (a) STM image of Au agglomeration and (b) STS data acquired from Au cluster agglomeration on oxide Fe<sub>3</sub>O<sub>4</sub> film (0.2 nA, 1 V, 1500×1500 Å<sup>2</sup>).

It has been stated that the observed band gap (from the  $I$ - $V$  curve) is dominated by a decrease of the density of the states near the Fermi level because of the small metal clusters. The state density can be reduced due to either quantum size effects or to spillover of oxide from the support to the metal cluster [9]. For quantum size effect, electronic properties of small clusters start to change when the metal size decrease ( $\sim 5$  Å). The wave functions deviate and energy level spectrum narrows and splits into sub-bands. This splitting of orbital bands results in extension of the band gap between the valence and conduction bands.

Fig 4.5(a) shows a large area of pseudo-hexagonal arrangements of Au clusters in another area on the same sample. The 2D Fourier transformation inset in Fig 4.5(b) shows the preferred Au cluster periodicity on the pseudo hexagonal superstructure of iron oxide  $\text{Fe}_3\text{O}_4(111)$  termination. The hexagon inset in Fig 4.5(b) is similar to that inset in Fig 4.5(c) indicating underlying Au clusters could be on the pseudo-hexagonal structure of iron oxide  $\text{Fe}_3\text{O}_4(111)$ . 50 Å hexagonal dimension of Au cluster measured is also similar to the hexagonal superstructure of  $\text{Fe}_3\text{O}_4$ . This suggests that 1 layer of Au clusters are grown on pseudohexagonal structure of the oxide. The cluster height is rather difficult to be measured due to the fully covering of Au cluster on that oxide terrace. The band gap of the Au clusters is  $< 0.1$  V designating semi-metallic behaviour of Au clusters.

Fig 4.6 shows isolated Au clusters mostly located on the defect of high temperature oxidized Cu steps. This observation means that Au atoms nucleate on surface defect sites first due to those sites being most reactive.

The isolated Au clusters enable us to measure the size and density of clusters. Supposing the Au cluster density is the same as that of bulk Au metal ( $19.3 \text{ g/cm}^3$ ), the number of Au contained in a singular cluster can be evaluated using the cluster size measured by STM. The volume of a sphere is

$$V = \frac{4}{3} \pi r^2 \times h$$

For a hemispherical Au cluster on the surface

$$V = \frac{2}{3} \pi r^2 \times h$$

The radius of Au hemisphere (for the maximum value) is 22.5 Å with 15 Å high

$$\begin{aligned} V &= \frac{2}{3} \pi (22.5 \times 10^{-8} \text{ cm})^2 \times 15 \times 10^{-8} \text{ cm} \\ &= 1.59 \times 10^{-20} \text{ cm}^3 \end{aligned}$$

From Au density,  $19.3 \text{ g/cm}^3$ , It is about  $3.06 \times 10^{-19} \text{ g}$ .

Molecular weight of Au is 196.9665 amu. Therefore, 1 mole of Au weighs 196.9665 g. Therefore,  $1.22 \times 10^{-18} \text{ g}$  is  $1.55 \times 10^{-21} \text{ mole}$  which is ~930 atoms.

Therefore, the volumetric sphere of Au particles is 930 atoms.



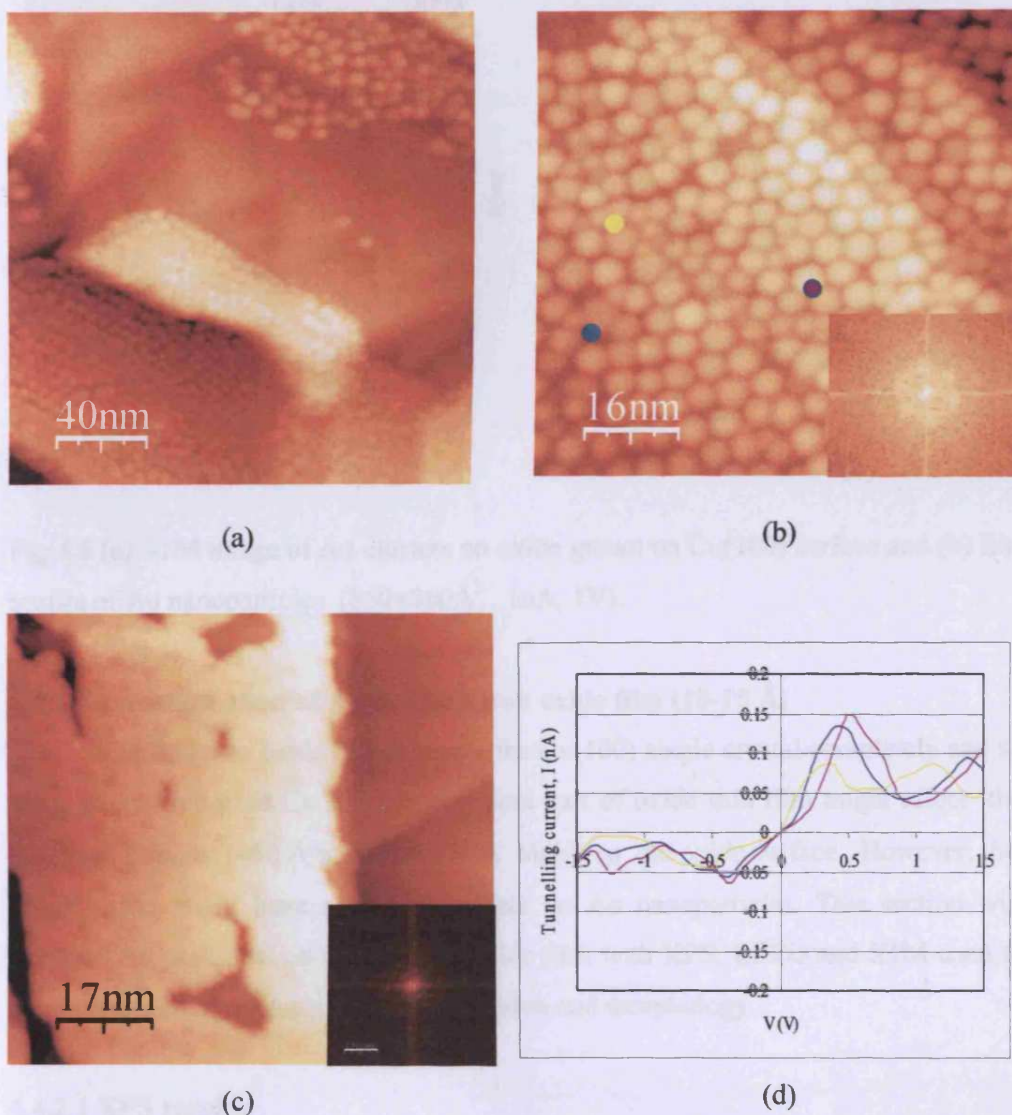


**Fig 4.5** (a) A large area of hexagonal structure arrangement of Au clusters in  $2000 \times 2000 \text{ \AA}^2$  (0.35 nA, 0.8 V), (b) a closer image with  $820 \times 820 \text{ \AA}^2$  (0.4 nA, 0.9 V) and (c) hexagonal structure arrangement of iron oxide film surface ( $860 \times 860 \text{ \AA}^2$ ), and (d) I-V curve of Au clusters in (b).

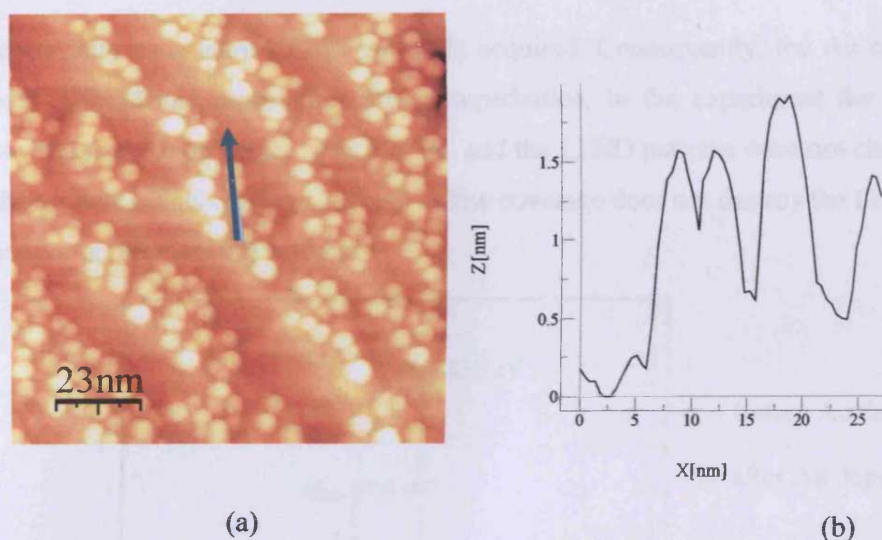


**Fig 4.6** (a) STM image of Au clusters on oxide grown on Cu(100) surface and (b) line profile of Au nanoparticles ( $860 \times 860 \text{ \AA}^2$ , 1 nA, 1 V).

#### 4.4.2 Characterization of Au on thick iron oxide film (10-15 Å)

The thin iron oxide did not cover the Cu(100) single crystal completely and so some part of oxidized Cu substrate or some part of oxide thin film might affect the Au nanoparticles ( $\sim 50 \text{ \AA}$  wide and  $\sim 15 \text{ \AA}$  high) on the oxide surface. However, the thick oxide might have a different effect on Au nanoparticles. This section will describe Au deposited on a thick iron oxide film with XPS, LEED and STM used to examine the changes in chemical composition and morphology.

##### 4.4.2.1 XPS results

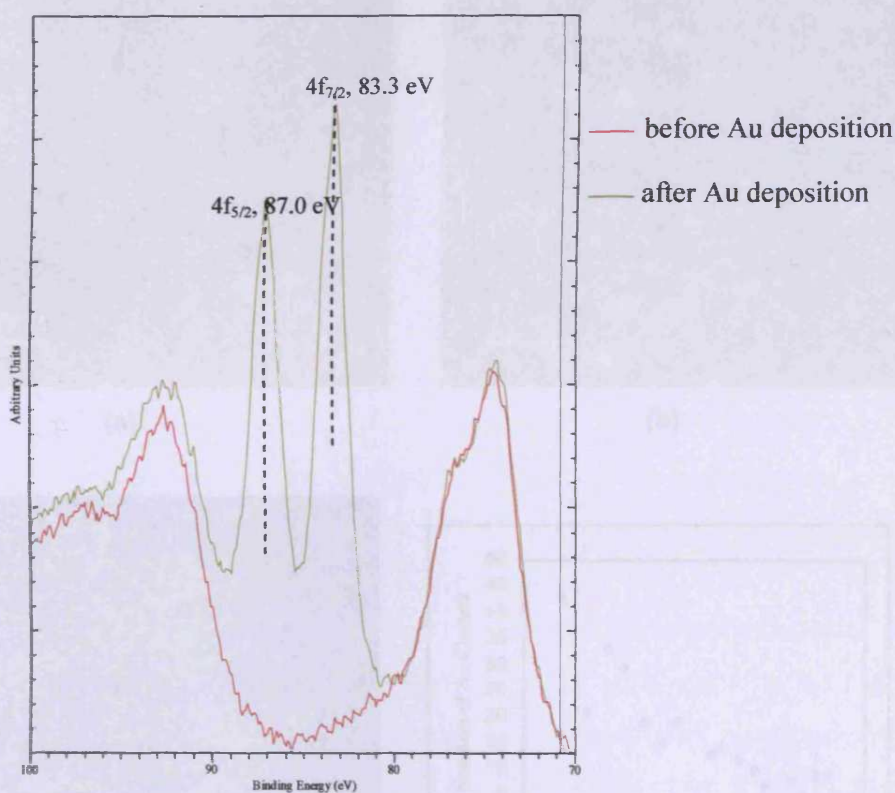
0.3-0.6 ML Au was deposited on a 10-15 Å thick iron oxide film. XP spectra show Au(4f) regions obtained after deposition of Au at 300 K. The Au(4f<sub>7/2</sub>) is at 83.3. The XP spectrum in Fig 4.7 shows a weak interaction between deposited Au and iron oxide film, otherwise the core level might shift.

##### 4.4.2.2 LEED results

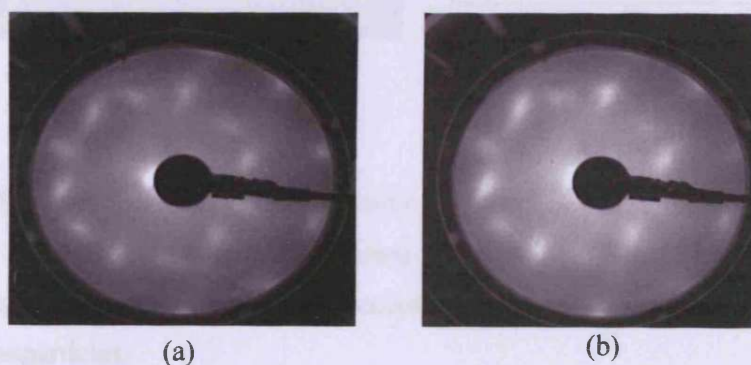
The LEED patterns before and after depositing Au on 10 Å Fe<sub>3</sub>O<sub>4</sub> surface are shown in Fig 4.8. No square pattern of Cu(100) substrate is seen due to the thick iron oxide preparation. LEED measurements suggest that Au clusters might grow



epitaxially as a sharp LEED pattern is acquired. Consequently, the Au clusters are well defined and repeat the surface superlattice. In the experiment the maximum coverage of Au on  $\text{Fe}_3\text{O}_4$  was 0.6 ML and the LEED patterns were not changed (not shown here). This confirms that Au at low coverage does not destroy the  $\text{Fe}_3\text{O}_4$  LEED pattern on the Cu(100) surface.



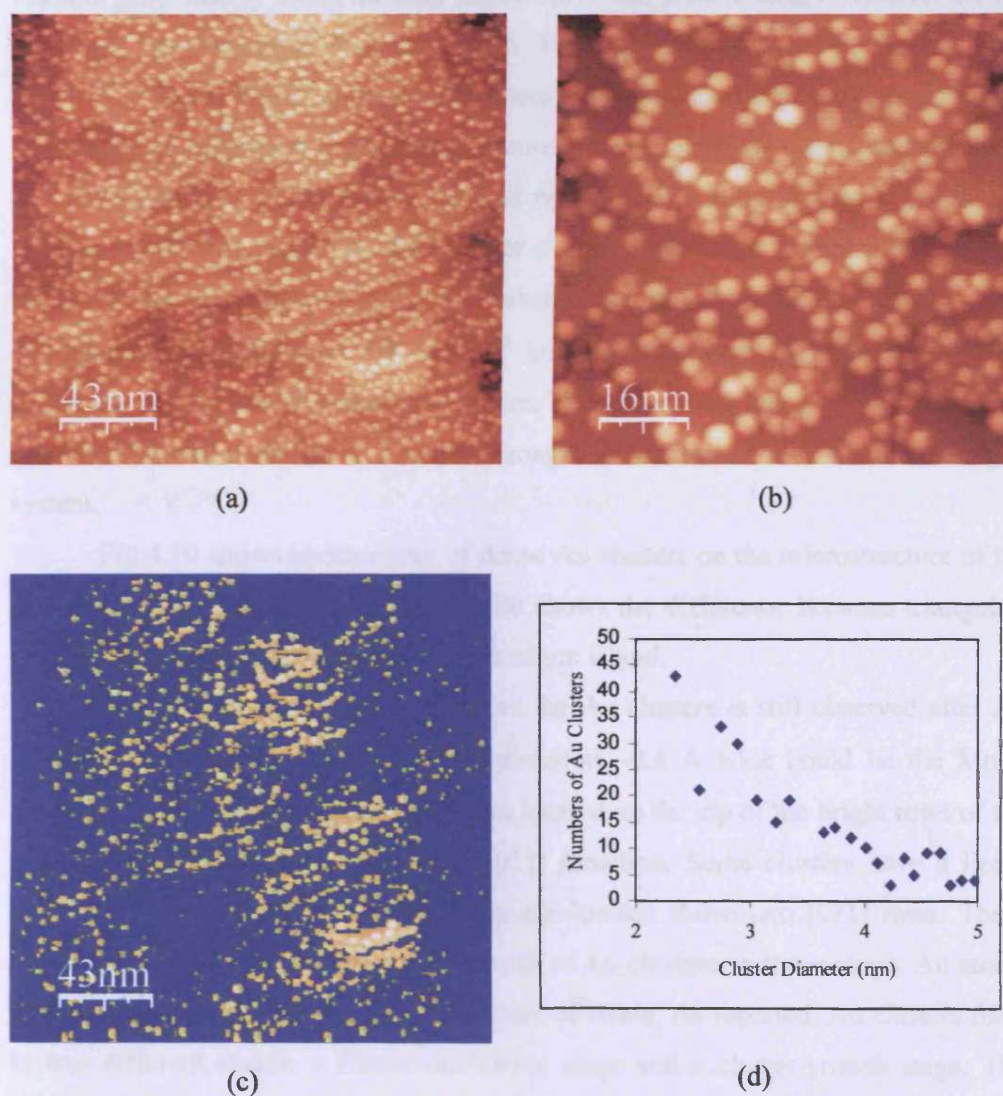
**Fig 4.7** XPS spectra of Au 4f region obtained after deposition of Au on thick  $\text{Fe}_3\text{O}_4/\text{Cu}$  (100) at 300 K



**Fig 4.8** LEED pattern of (a)  $\text{Fe}_3\text{O}_4$  at  $E = 84$  eV and (b) 0.35 ML Au deposition at  $E = 82$  eV.

#### 4.4.2.3 STM results

STM measurements were performed on the Au/thick iron oxide surfaces after Au deposition.



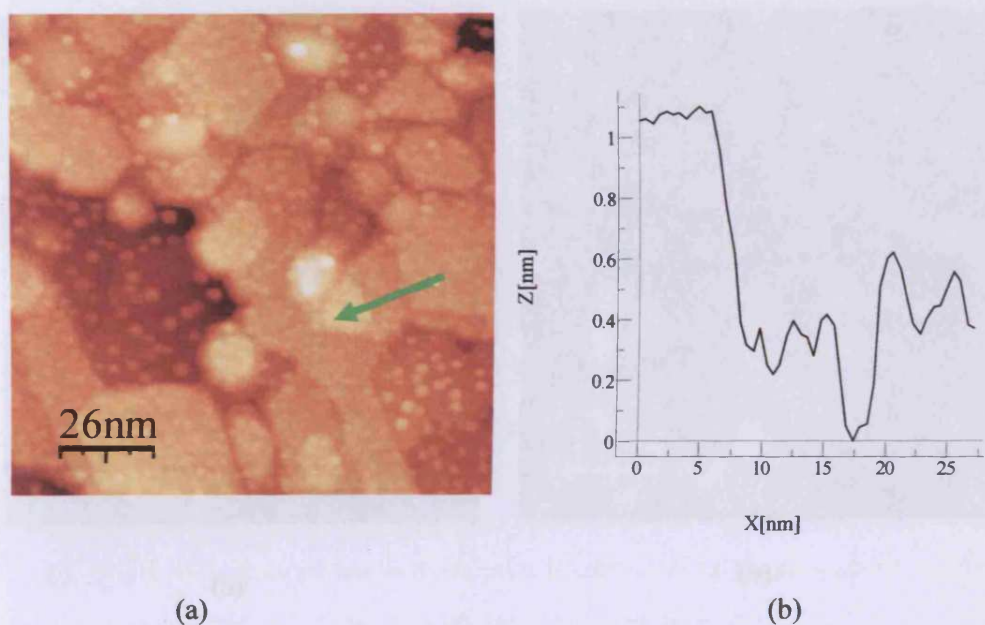
**Fig 4.9** Au decorates the step-edges and on the terraces of iron oxide surface in (a) an image  $2150 \times 2150 \text{ \AA}^2$ , (b) a closer image  $800 \times 800 \text{ \AA}^2$ , (1nA, 1.4V) (0.35 ML Au) (c) image of selected particles to be counted by WSxM and (d) distribution graph of Au nanoparticles.

Fig 4.9 was obtained after depositing 0.35 ML Au. This image shows Au clusters are decorated at the edge and on the flat area of iron oxide terrace. It suggests that Au atoms nucleate on the surface defect sites. In this image hemispherical clusters grow mainly along the step edges. However, some clusters locate on the flat terraces. The step height is about 10-15 Å. The majority of Au clusters size are about 25-50 Å as in Fig 4.9(d). In general, clusters grow on the support by 2 processes [9]. First, clusters migrate to coalesce and second clusters grow by intercluster transport, driven by capillary action, called Ostwald ripening. The latter process is because of surface free energy reduction of the larger cluster. Intercluster transport of atom can occur by surface diffusion along the substrate or by vapor phase transport. The sublimation energy of Au  $\approx 370 \text{ kJ mol}^{-1}$  implying the intercluster transport by free Au atoms will be slow at room temperature. The intercluster transport will be mainly made by the surface diffusion. The STM images of Au clusters are stable in our UHV system.

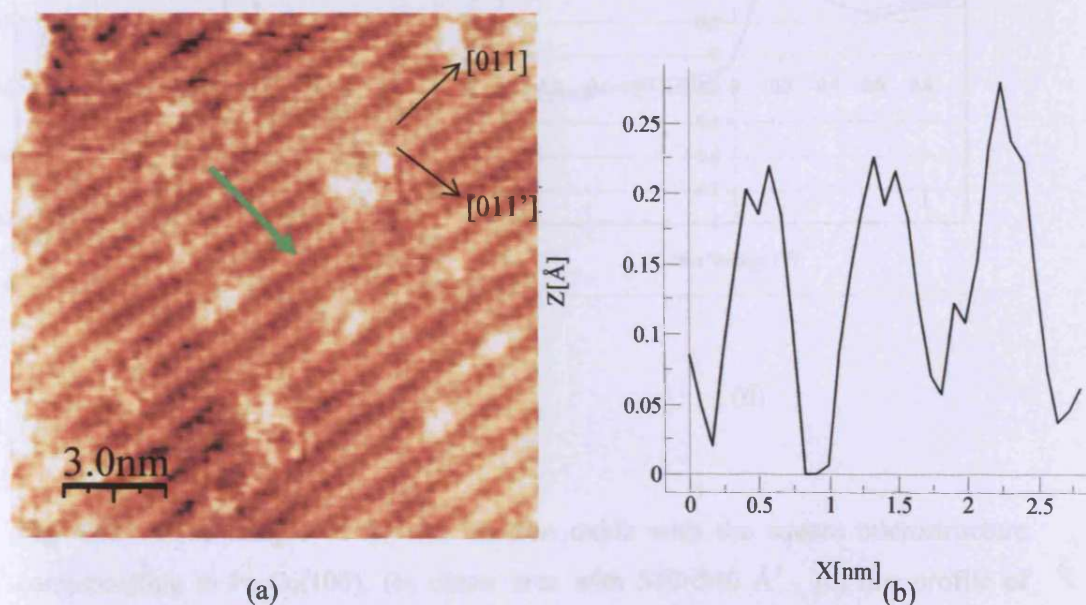
Fig 4.10 shows another area of dense Au clusters on the microstructure of the iron oxide film. The height of line profile shows the difference between triangular-shaped island and microstructure of the hexagon island.

Some surface of iron oxide around the Au clusters is still observed after Au deposition. The strips along the [011] direction  $\sim 0.8 \text{ Å}$  wide could be the Moiré pattern (Fig 4.11). Most of Au clusters are located on the top of the bright rows of the substrate. They are aligned along the [011] direction. Some clusters have a linear shape above one [011] row while others are located above two [011] rows. These dimensions specify a pseudomorphic growth of Au clusters on those strips. Au atoms might nucleate on top of the defect structure of oxide. As reported, Au clusters form in two different stages; a cluster-nucleation stage and a cluster-growth stage. The difference between the two stages is the Au coverage. At low coverage, Au atoms adsorb generally on surface defect sites and form 2D clusters that become nuclei for further growth. Then 3D cluster formation occurs after further depositing Au. Fig 4.11 could be the image of a cluster-nucleation stage and Fig 4.12 is the image of a cluster-growth.

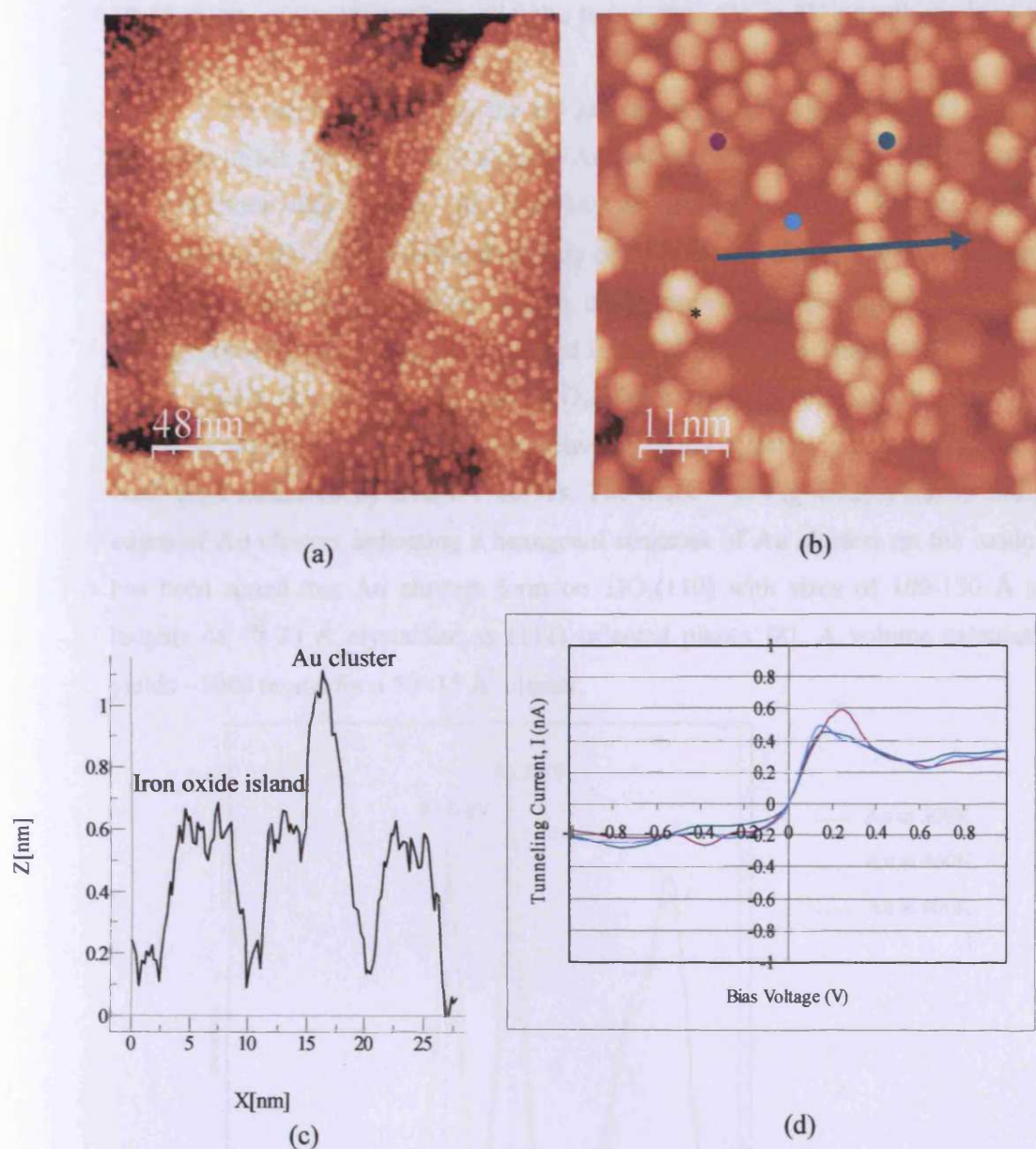




**Fig 4.10** (a) STM of 0.6 ML Au clusters on iron oxide and (b) line profile of Au modified iron oxide in different terrace  $1300 \times 1300 \text{ \AA}^2$  (0.8 nA, 0.9 V).



**Fig 4.11** (a) STM image of Au clusters on the  $\text{Fe}_3\text{O}_4$  surface as quasi-2D Au clusters (strips 1-1.5  $\text{\AA}$  wide),  $150 \times 150 \text{ \AA}^2$  (1 nA, 1 V) and (b) line profile of oxide strips.



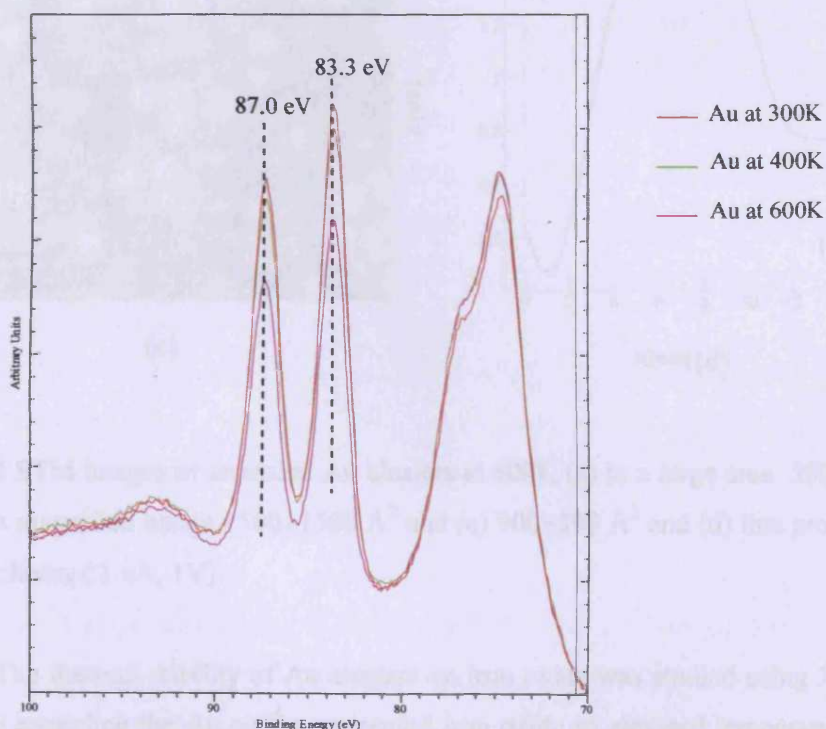
**Fig 4.12** STM images of (a) Au on iron oxide with the square microstructure corresponding to Fe<sub>3</sub>O<sub>4</sub>(100), (b) closer area with 540×540 Å<sup>2</sup>, (c) line profile of surface structure in (b) showing different heights of Fe<sub>3</sub>O<sub>4</sub> islands and Au clusters and (d) I-V curve of Au nanoparticles on Au supported iron oxide surface; (0.9 nA, 1V).

Fig 4.12 was acquired after a 0.2 ML Au deposition on a 10 Å thick iron oxide film. It shows a homogeneous distribution of hemispherical Au clusters with diameter



30-45 Å on iron oxide surface. Clearly, the clusters are in 3D growth mode at this coverage.

It has been reported that the 3D growth of Au clusters on  $\text{TiO}_2(110)$  occurs around 0.10 ML [8]. Our aim is to make Au particles with diameter  $< 50$  Å supported on iron oxide film to study the reactivity on a model catalyst. We observed the formation of 3D clusters having diameters of 40-50 Å and heights of  $\sim 10$  Å. Areas of Au clusters and microstructure of iron oxide coexist on the surface and can be distinguished by the height of the island in Fig 4.12(c). The height of the oxide is about 4.0-5.0 Å (corresponding to  $\text{Fe}_3\text{O}_4(100)$  and (111)) whereas the Au cluster height is about 10 Å. Semi-metallic behavior of Au clusters is denoted by narrow band gaps measured by STS-I-V curves. The mark \* in Fig 4.12(b) shows straight edges of Au clusters indicating a hexagonal structure of Au clusters on the oxide. It has been stated that Au clusters form on  $\text{TiO}_2(110)$  with sizes of 100-150 Å and heights of 40-70 Å crystallize as (111) oriented planes [8]. A volume calculation yields  $\sim 1000$  atoms for a  $50 \times 15$  Å<sup>2</sup> cluster.



**Fig 4.13** XPS spectra shows decrease of Au intensity peaks after annealing the surface of Au nanoparticles /iron oxide/Cu substrate at 300 K, 400 K and 600 K.

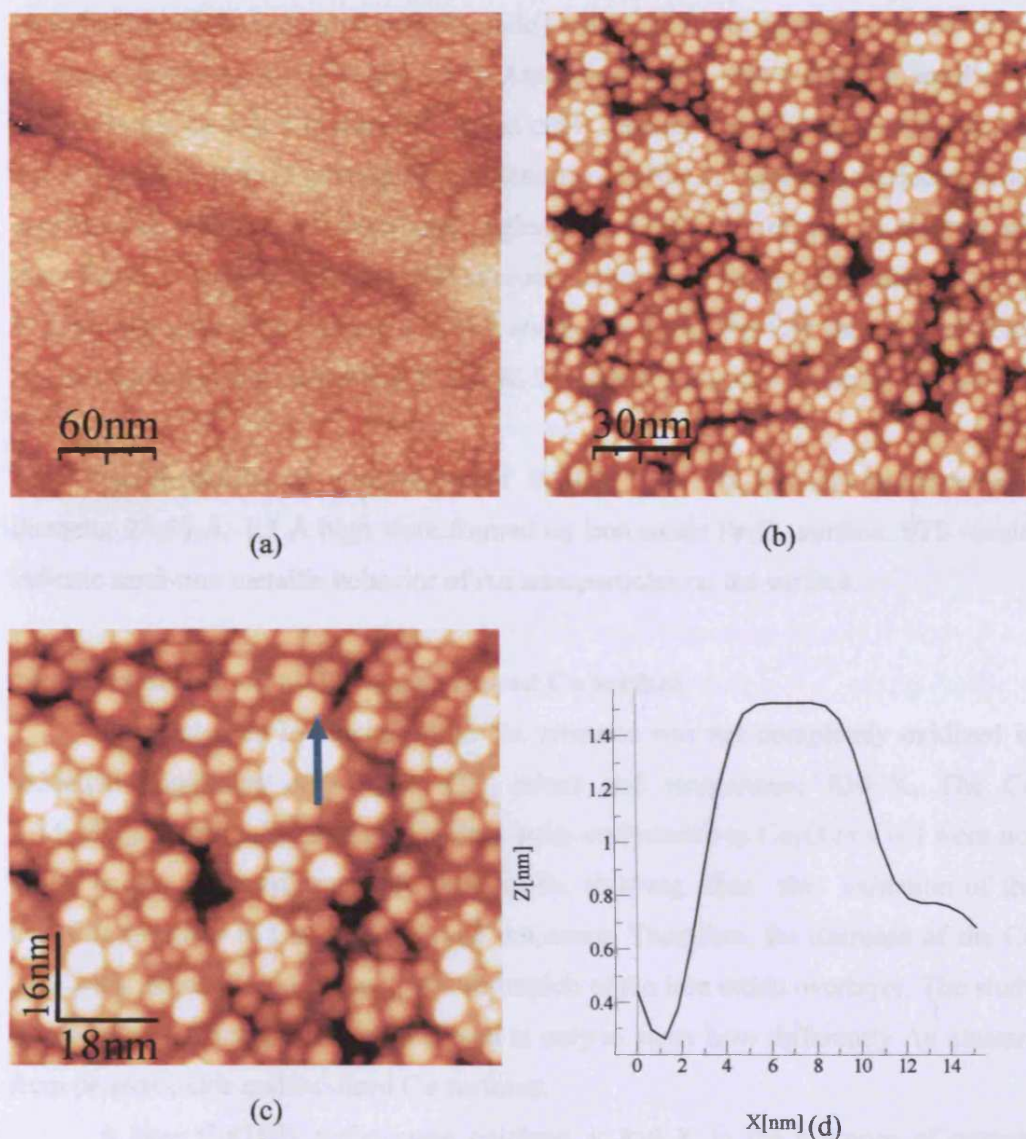


**Fig 4.14** STM images of annealed Au clusters at 600K (a) in a large area  $3000 \times 3000 \text{ \AA}^2$ , (b) a magnified image  $1500 \times 1500 \text{ \AA}^2$  and (c)  $900 \times 890 \text{ \AA}^2$  and (d) line profile of a flat Au cluster (1 nA, 1V).

The thermal stability of Au clusters on iron oxide was studied using XPS and STM by annealing the Au on the supported iron oxide to elevated temperatures. XP spectra (Fig 4.13) show that the Au 4f binding energy is constant. It was found that Au clusters were stable after annealing at 400 K for 10 min indicated by the unchanging clusters sizes in STM images. Annealing did not significantly change the

morphology of Au supported on iron oxide surface but the quantitative amount of Au decreases as shown by XPS (Fig 4.13). Annealing at 300, 400 and 600 K resulted in Au coverages of 5.4, 5.0,  $4.0 \times 10^{14}$  atoms  $\text{cm}^{-2}$ , respectively. The intensity of the Fe and Cu peaks increased after heating indicating only the Au signal was reduced. After annealing at 600 K Au atoms might agglomerate on the top of the Au clusters and then form a large flat hexagonal microcrystal (more likely close-packed (111) oriented planes) with a diameter of 120 Å and height 15 Å. Fig 4.14 shows STM of the Au nanoparticles after annealing at 600 K. The flat top particle is shown in Fig. 4.14 (d).

Consequently, at a coverage of 0.3-0.6 ML, 3D Au nanoparticles with diameter 25-50 Å, 1.5 Å high were formed on iron oxide  $\text{Fe}_3\text{O}_4$  surface. STS results indicate semi-non metallic behavior of Au nanoparticles on the surface.

#### 4.5 Characterization of Au on an oxidized Cu surface

As mentioned in chapter 3 the Cu substrate was not completely oxidized in oxidation conditions of oxygen ( $10^{-6}$  mbar) and temperature 850 K. The Cu  $L_{3/2}M_{4,5}M_{4,5}$  Auger peaks and the Cu  $2p_{3/2}$  peak attributable to  $\text{Cu}_2\text{O}$  or  $\text{CuO}$  were not found in the preparation of the iron oxide, showing that the oxidation of the Cu(100) substrate to  $\text{Cu}_2\text{O}$  or  $\text{CuO}$  did not occur. Therefore, the decrease of the Cu  $2p_{3/2}$  peak intensity is only due to the formation of the iron oxide overlayer. The study of oxidation of a clean Cu single crystal is only to show how differently Au clusters form on iron oxide and oxidized Cu surfaces.

A bare Cu(100) surface was oxidized at 850 K in the presence of oxygen ( $1 \times 10^{-6}$  mbar) for 5 min (similar to the conditions for iron oxide preparation). XPS, LEED and STM were used to characterize the surface.

##### 4.5.1 XPS results

Core level spectra of Cu, O and Au shown in Fig 4.15 are used to determine the composition of the surface. Those spectra are for a clean Cu, oxidized Cu and Au deposited on Cu. Binding energies are 932.1 eV, 567.3 eV, 529 eV, and 83.8 eV for Cu  $2p_{3/2}$ , Cu Auger (LMM), O 1s, and Au ( $4f_{7/2}$ ), respectively. The Cu  $2p_{3/2}$



intensity successively decreased after oxidization and Au deposition. The surface concentration of oxygen on oxidized Cu and Au is  $4.8$  and  $2.8 \times 10^{14}$  atoms  $\text{cm}^{-2}$ , respectively. The Cu 2p binding energy does not change after oxidation but there is an additional oxygen peak. We observe a chemical shift of the Cu 2p peaks associated with the oxygen interaction. The energy of this peak is known to very insensitive to the state of Cu oxidation. Moreover, no sign of a satellite peak correlated with this oxidized Cu peak in this surface.

It has been reported that a Cu metal surface was oxidized in a presence of oxygen (1 torr) at 670 K for 1.5 hour for a CuO preparation while  $\text{Cu}_2\text{O}$  was prepared by heating CuO in vacuum at 570 K for 1 hr [11]. The Cu 2p satellite is a fingerprint of CuO. It was mentioned that Cu  $L_{2,3}M_{4,5}M_{4,5}$  Auger spectra on  $\text{Cu}_2\text{O}$  should be similar to that of Cu metal. The XP main peak of CuO is broad (FWHM 3.4 eV) at  $933.2 \pm 0.2$  eV and has an associated satellite on the high-binding-energy at about 9 eV separation. This satellite is a characteristic of materials having a  $d^9$  configuration in the ground state. The XP of Cu 2p of  $\text{Cu}_2\text{O}$  has a narrow (FWHM 1.9 eV) peak at  $932.4 \pm 0.2$  eV. From the discussion above, our surface could not be either CuO (no strong shake up satellite) or  $\text{Cu}_2\text{O}$  (surface was oxidized in a low pressure of oxygen gas in short time).

#### 4.5.2 LEED results

Fig 4.16(b) shows the diffraction pattern of Cu(100) after oxidation at 850 K in the presence of oxygen ( $1 \times 10^{-6}$  mbar). The LEED pattern of oxidized Cu(100) and Au deposited Cu(100) gives additional spots running in a  $45^\circ$  direction to clean Cu in Fig 4.16(b) and (c). The LEED pattern after deposition of Au was not changed suggesting that Au grows epitaxially on the substrate giving a sharp LEED pattern. This confirms that Au at low coverage does not damage the oxidized Cu(100) surface. Manipulation of matrices [10] could derive the unit cell of the oxidized Cu in real space. From Fig 4.16(b) can be derived :

The real space of the overlayer as follows.

$$\begin{aligned} a_o &= 1 a_s + 1 b_s \\ b_o &= -1 a_s + 1 b_s \end{aligned} \quad \text{equation 4.1}$$

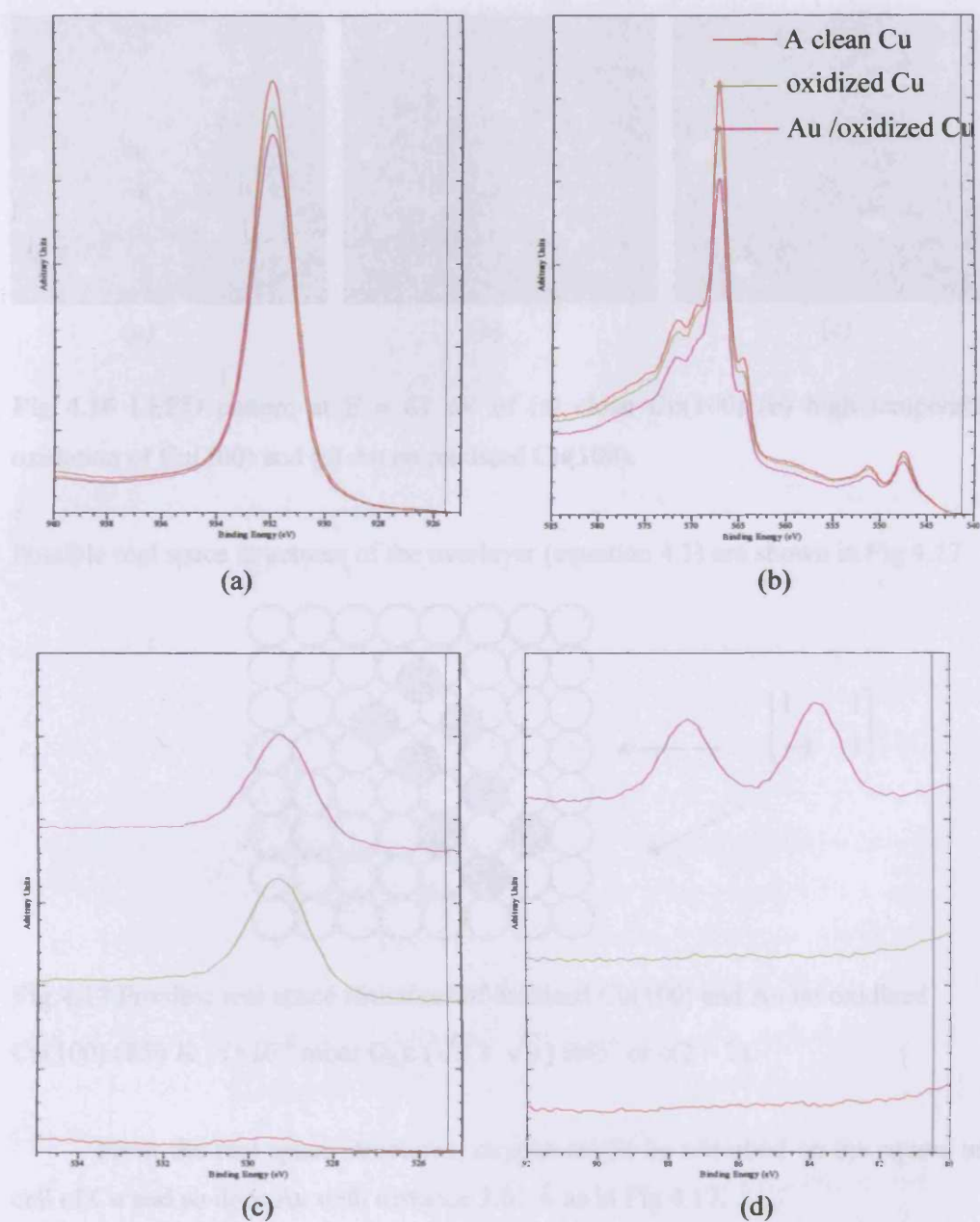


**Fig 4.15** XPS spectra of (a) Cu 2p<sub>3/2</sub>, (b) Cu Auger peak, (c) O 1s and (d) Au 4f<sub>7/2</sub> and 4f<sub>5/2</sub> after the Cu substrate was oxidized in oxygen (10<sup>-6</sup> mbar) at 850 K.

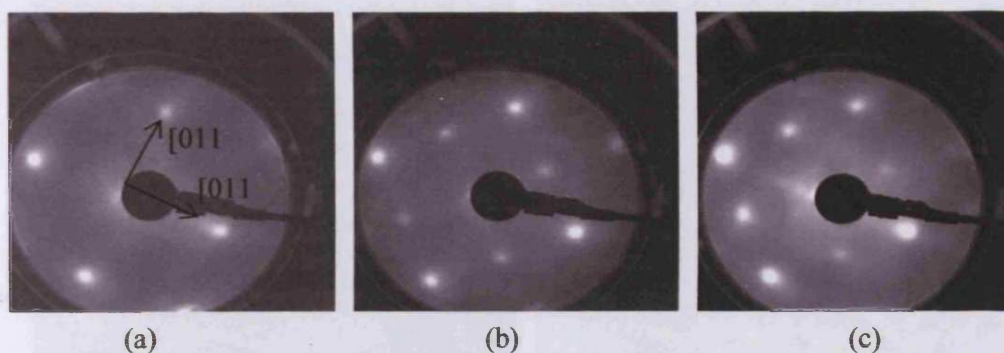


**Fig 4.16** LEED pattern at  $E \approx 61$  eV of (a) clean Cu(100) (b) high temperature oxidation of Cu(100) and (c) Au on oxidized Cu(100).

Possible real space structures of the overlayer (equation 4.1) are shown in Fig 4.17

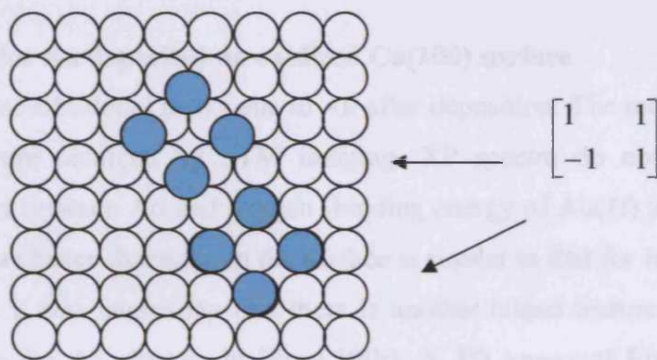


**Fig 4.17** Possible real space structures of oxidized Cu(100) and Au on oxidized Cu(100) (850 K,  $1 \times 10^{-6}$  mbar  $O_2$ ):  $(\sqrt{2} \times \sqrt{2}) R45^\circ$  or  $c(2 \times 2)$ .

From the real space structures, oxygen might be adsorbed on the square unit cell of Cu and so does Au with distance 3.61 Å as in Fig 4.17.

#### 4.5.3 STM results for oxidized Cu

An atomically resolved STM image of clean Cu(100) was not obtained but after oxidation the square microstructure image was acquired. Fig 4.18 shows an extended area image of oxygen adsorbed on Cu(100). The square microstructures of Cu terraces were obtained. Unfortunately, atomically resolved images could not be accomplished. XPS confirms that oxygen has adsorbed on the Cu(100) surface.



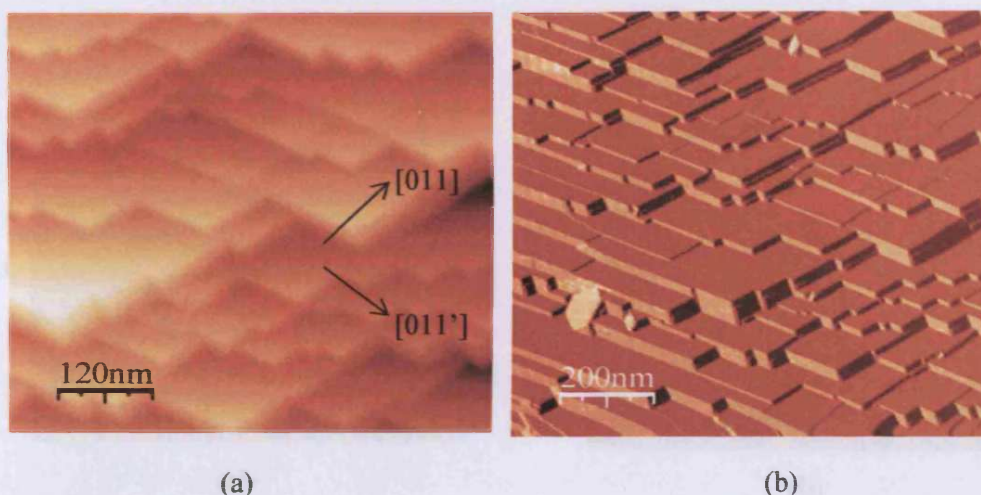


**Fig 4.18** STM images of oxidized Cu(100) in a big area as (a)  $4900 \times 4900 \text{ \AA}^2$  and (b)  $1 \times 1 \mu\text{m}^2$  (0.5 nA, 1.1V).

#### 4.5.4 STM results for Au deposited on oxidized Cu(100) surface

XPS confirms additional peaks due to Au after deposition. The morphological surface changes were obtained by STM imaging. XP spectra do not show any chemical interaction between Au and oxygen (binding energy of Au(4f) and O(1s) is unaffected). The Au cluster character on the surface is similar to that for iron oxide as shown in Fig 4.19. It was interesting that there is another island feature with lower height compared to the Au clusters in Fig 4.19(b). A 3D image of Fig 4.19(b) is shown in Fig 4.19(e) indicating an obvious lower feature. Fig 4.19(c) is the selected area for the calculation of the distribution of Au clusters on the surface. The STM line profile in Fig 4.19(f) shows Au clusters with diameters 20-80 Å and 10-15 Å high similar to Au clusters on iron oxide as shown in the chapter 3.

Fig 4.20(a) shows Au clusters on the hexagonal microstructure terrace of oxidized Cu surface. Atomically resolved images were not obtained on Cu due to the delocalized conduction band. Au is supposed to be involved on the top surface of the substrate giving hexagonal microstructures as stable fcc(111) plane. The band gap of a Au nanoparticle is ~0.1 V indicating nonmetallic behavior while that of a small square-like island is less than 0.1 V. The band gap of copper terraces containing the small islands is zero indicating a metallic area.

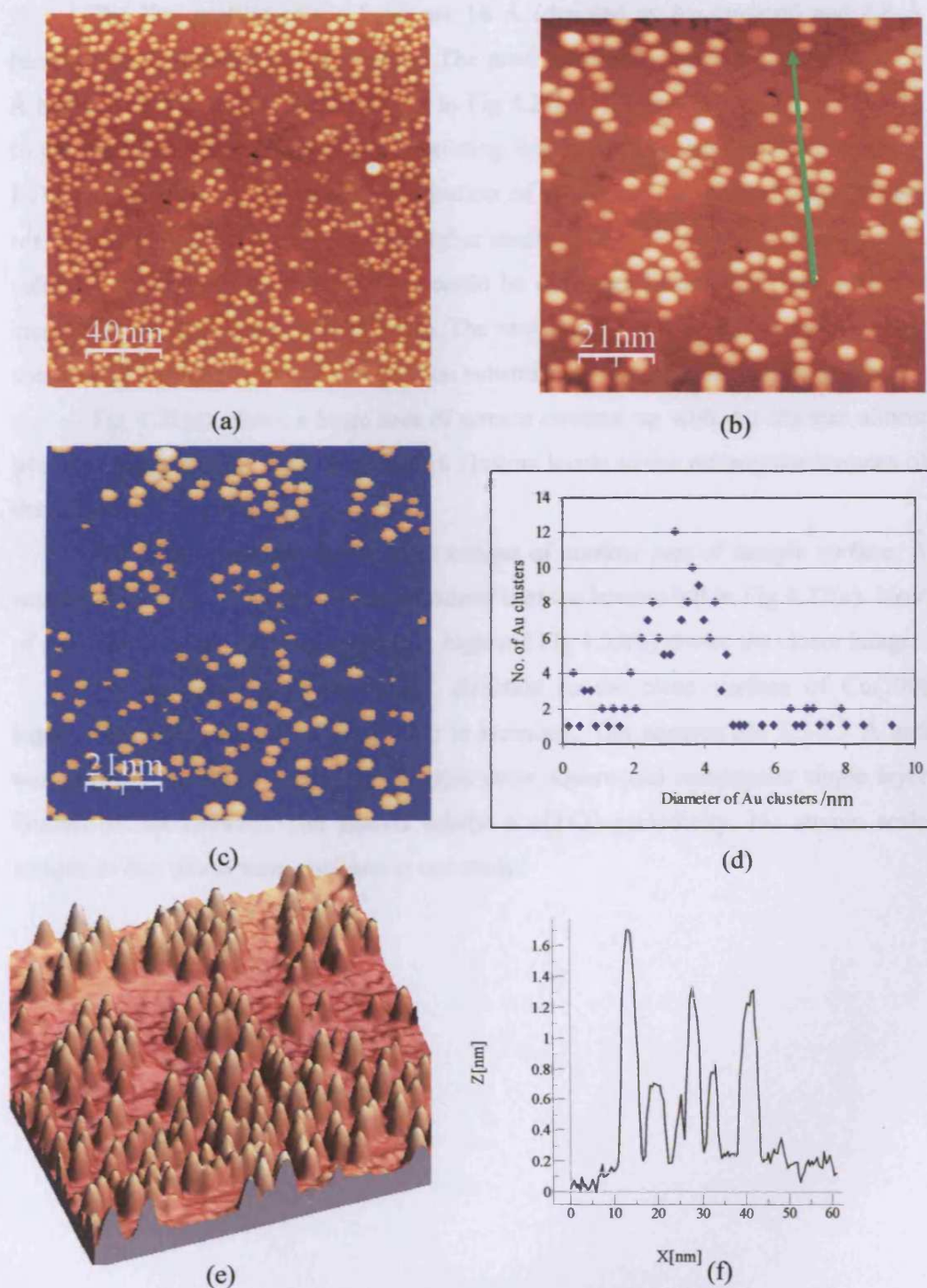


**Fig 4.19** STM images of Au deposited on oxidized Cu surface in (a) a large area  $2000 \times 2000 \text{ \AA}^2$  (1.2 V, 1 nA) and (b) a closer area  $1000 \times 1000 \text{ \AA}^2$ , (1.2V, 1 nA), (c) selected Au clusters area for counting, (d) graph of Au clusters distribution, (e) 3D of image (b) and (f) line profile of Au nanoparticles on oxidized Cu surface.

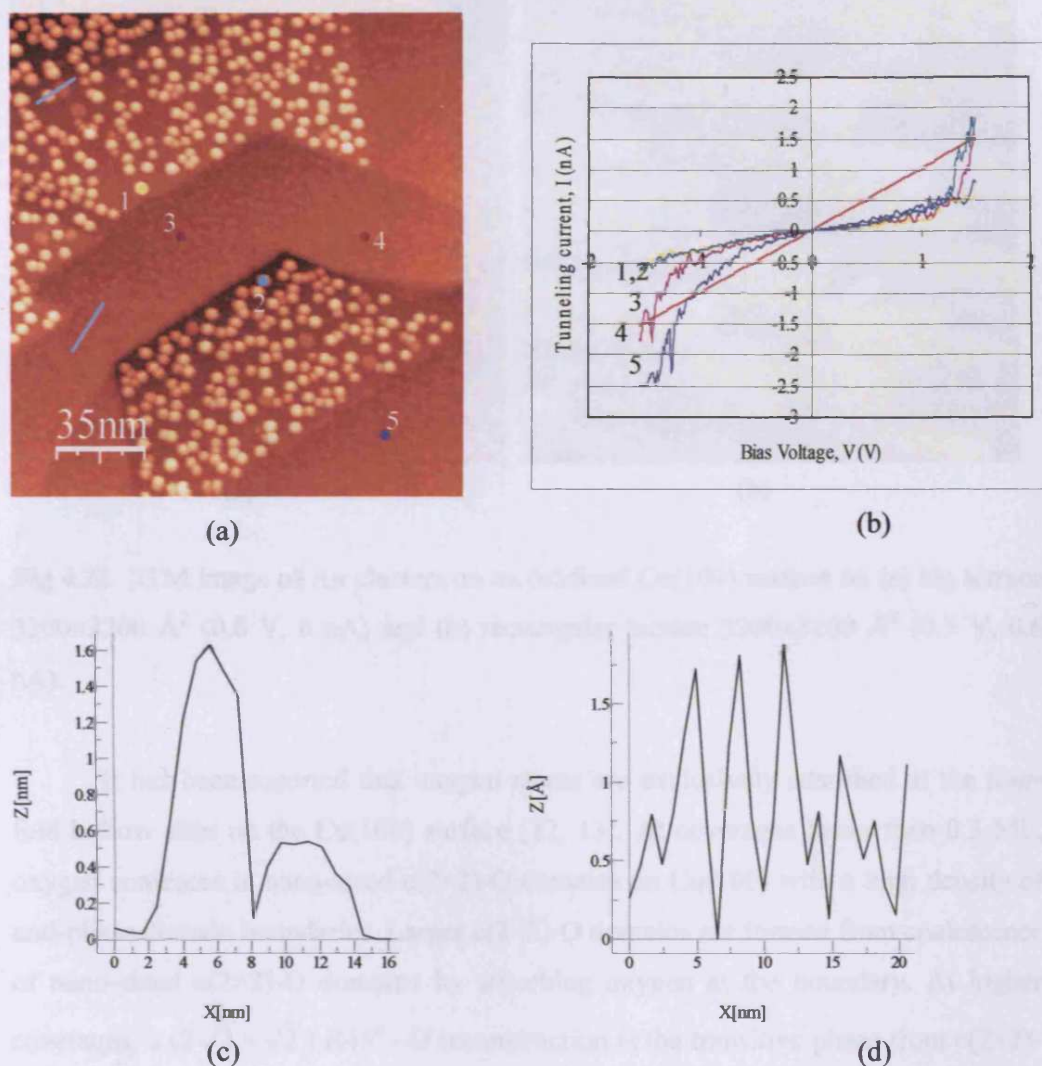


The line profiles of top layer are 16 Å (denoted as Au clusters) and 4.8 Å (denoted as oxide) high in Fig 4.20 (c). The profile of small structure islands (1.5-1.6 Å high) distribute around the surface is in Fig 4.20(d). No area is allowed to measure to get the right height. It was very interesting that before Au deposition no close-up STM image could be obtained. Mobilisation of atoms on the surface might be the reasonable reason for not getting any higher resolved images. After Au deposition on substrate surface, closer STM images could be obtained; however, it was not good enough to see the atom resolved image. The remarkable morphological images show some Au clusters and oxygen adsorbed on substrate giving different height profiles.

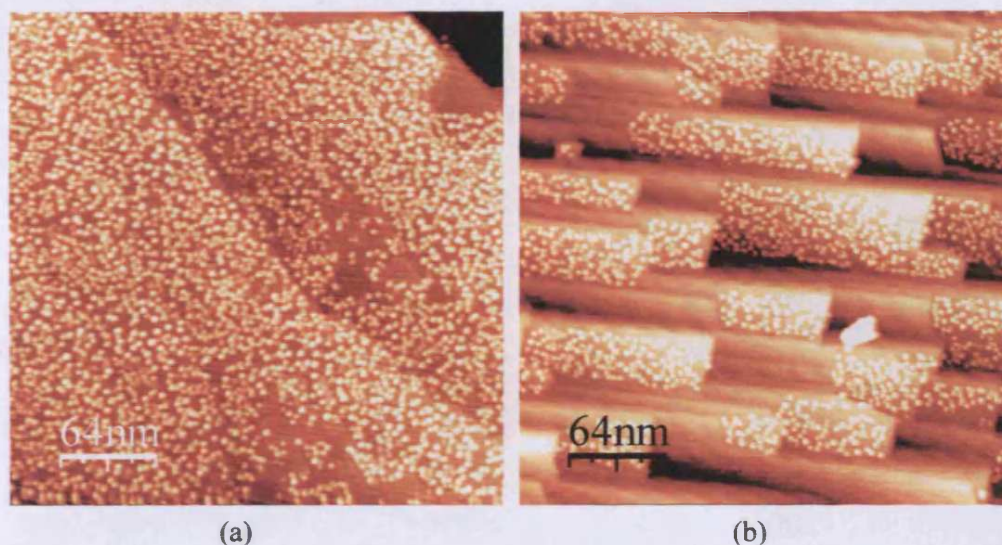
Fig 4.21(a) shows a large area of terrace covered up with Au clusters almost over the whole surface area. Besides, Au clusters locate to the rectangular terraces of the substrate in Fig 4.21(b).

Fig 4.22(a) and (b) shows STM images of another part of sample surface. A small part of image with Au clusters obtained is at the bottom left in Fig 4.22(a). Most of area contains square islands with 2 Å high and Fig 4.22(b) shows the closer image.

The square islands are in 45° direction to the clean surface of Cu(100) suggesting STM and LEED results are in harmony. The squares are 3.5-3.7 Å and multiples of 3.5-3.7 Å wide. STM images show square and rectangular single layer islands on the terraces. The islands exhibit a c(2×2) periodicity. No atomic scale images of this phase were obtained in our study.



**Fig 4.20** (a) STM image of the surface after Au deposition in  $1700 \times 1700 \text{ \AA}^2$  (1.2 V, 0.7 nA), (b) I-V curve on surface in (a) and (c) and (d) line profiles of Au clusters and oxygen adsorbed on Cu surface, respectively.



**Fig 4.21** STM image of Au clusters on an oxidized Cu(100) surface on (a) big terrace  $3200 \times 3200 \text{ \AA}^2$  (0.8 V, 6 nA) and (b) rectangular terrace  $3200 \times 3200 \text{ \AA}^2$  (0.5 V, 0.6 nA).

It has been reported that oxygen atoms are exclusively adsorbed at the four-fold hollow sites on the Cu(100) surface [12, 13]. At coverages lower than 0.3 ML, oxygen coalesces in nano-sized  $c(2 \times 2)$ -O domains on Cu(100) with a high density of anti-phase domain boundaries. Larger  $c(2 \times 2)$ -O domains are formed from coalescence of nano-sized  $c(2 \times 2)$ -O domains by adsorbing oxygen at the boundary. At higher coverages, a  $(2\sqrt{2} \times \sqrt{2}) R45^\circ$  -O reconstruction is the transitive phase from  $c(2 \times 2)$ -O domains by missing Cu atoms from a  $c(2 \times 2)$ -O structure along the [001] and [010] directions.

No large  $c(2 \times 2)$ -O domains are formed in Fig 4.22. The anti-phase domain boundaries are observed as the bright zig-zag lines. Unfortunately, an atomically resolved STM image could not be obtained to verify the mechanisms above. Square structure indicates that oxygen atoms tend to minimize the surface energy by coalescing themselves.

The band gap of a square island from Fig 4.22(c) is  $\sim 1 \text{ V}$  while the bare Cu surface is 0 V indicating metallic behaviour. Fascinatingly, the band gap of the square island is rather the same as Au clusters on adsorbed on Cu(100).



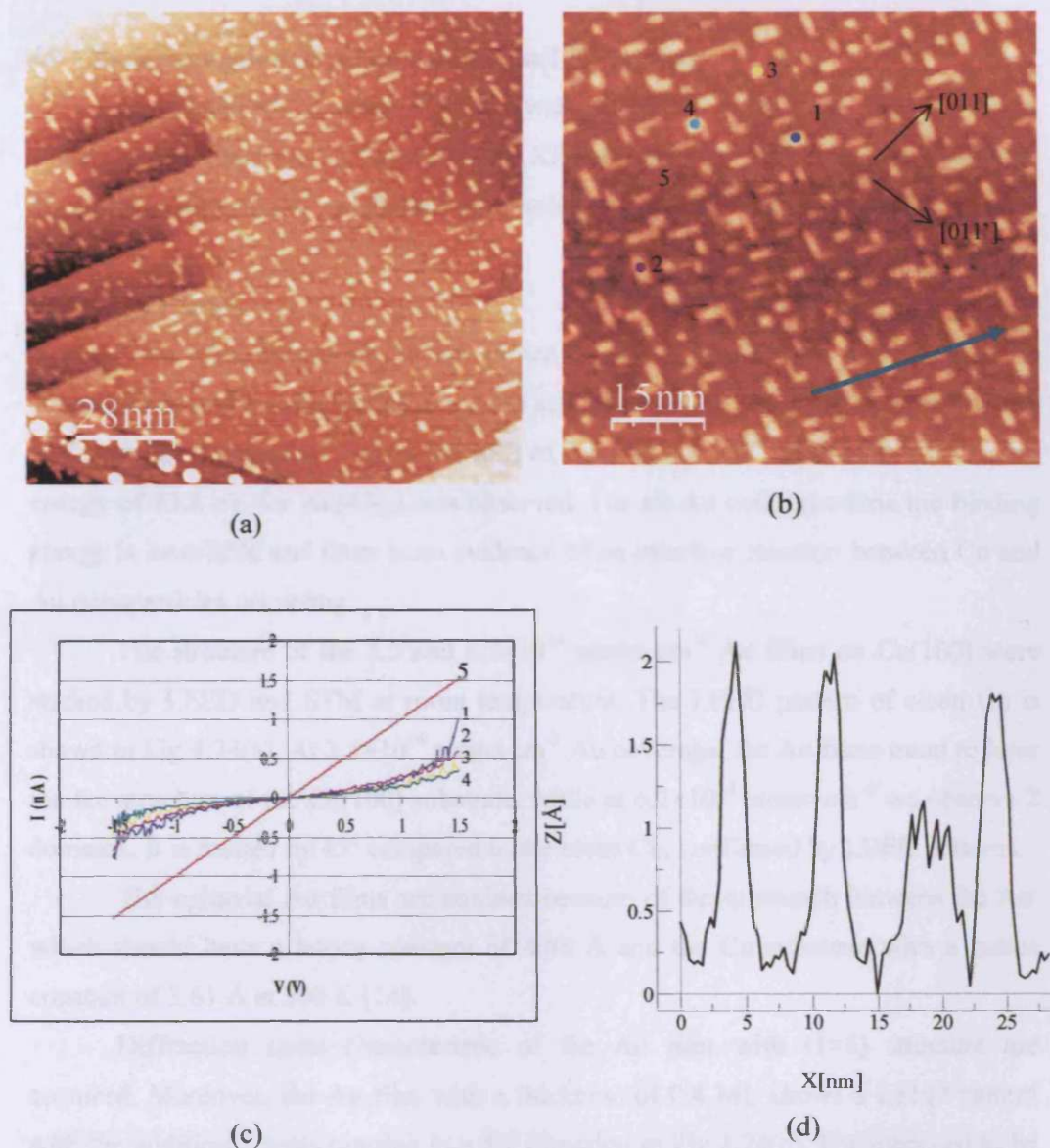


**Fig 4.22** (a) STM image ( $1400 \times 1400 \text{ \AA}^2$ ) of  $c(2 \times 2)\text{-O}$  surface on Cu(100), (b) a closer view  $810 \times 810 \text{ \AA}^2$  (1.2 V, 0.8 nA), (c) and (d) I-V curve and line profile of image (b), respectively.

It has been reported the crystallographic parameters of  $\text{Cu}_2\text{O}$  and  $\text{CuO}$  are 1.84 and 1.95 Å, respectively [11]. The line profile of square islands is 2 Å high indicating oxygen adsorption on the Cu(100) surface. It's unlikely those square islands would be due to the Au because the diameter of Au is about 2.9 Å. Therefore, all square and rectangular islands are monoatomic layers of oxygen adsorbed on the Cu substrate.

#### 4.6 Characterization of Au on a clean Cu(100) surface

Au deposited on clean Cu(100) was studied to investigate how the oxide surface could affect the Au cluster shape. XPS, LEED and STM are used to examine the surface composition and surface morphology.

##### 4.6.1 XPS results

Core level spectra of Au are shown in Fig 4.23 and used to determine the composition on the surface. Those spectra are for clean Cu, Au deposited on Cu with surface concentrations of Au on Cu(100) of  $2.5$  and  $6.2 \times 10^{14}$  atoms  $\text{cm}^{-2}$ ; a binding energy of  $83.8$  eV for Au( $4f_{7/2}$ ) was observed. For all Au concentrations the binding energy is invariable and there is no evidence of an interface reaction between Cu and Au nanoparticles occurring.

The structure of the  $2.5$  and  $6.2 \times 10^{14}$  atoms  $\text{cm}^{-2}$  Au films on Cu(100) were studied by LEED and STM at room temperature. The LEED pattern of clean Cu is shown in Fig 4.24(a). At  $2.5 \times 10^{14}$  atoms  $\text{cm}^{-2}$  Au coverage, the Au films trend to have the fcc structure of the Cu(100) substrate, while at  $6.2 \times 10^{14}$  atoms  $\text{cm}^{-2}$  we observe 2 domains. It is rotated by  $45^\circ$  compared to the clean Cu, confirmed by LEED patterns.

The epitaxial Au films are strained because of the mismatch between fcc Au, which should have a lattice constant of  $4.08$  Å and the Cu substrate with a lattice constant of  $3.61$  Å at  $300$  K [14].

Diffraction spots characteristic of the Au film with  $(1 \times 1)$  structure are acquired. Moreover, the Au film with a thickness of  $0.4$  ML shows a LEED pattern with the additional spots running in a  $45^\circ$  direction in Fig 4.24(c). It's supposed to be 2 domains of Au on the surface of Cu(100) surface: Cu- $(1 \times 1)$ -Au and c $(2 \times 2)$ -Au. Spots on the pattern are blurred due to again the small mismatch of Au and Cu.

Manipulation of matrices [10] could derive the unit cell of the Au overlayer in real space of the Cu(100) clean surface.



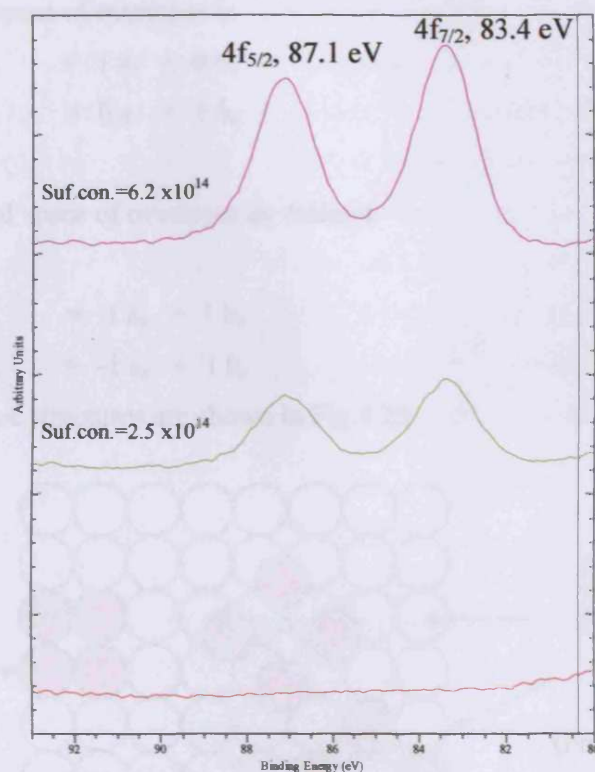


**Fig 4.23** XP Spectra of Au 4f after Au deposition on the oxidized Cu surface with surface concentrations  $2.5$  and  $6.2 \times 10^{14}$  atoms  $\text{cm}^{-2}$ .

#### 4.6.2 LEED results

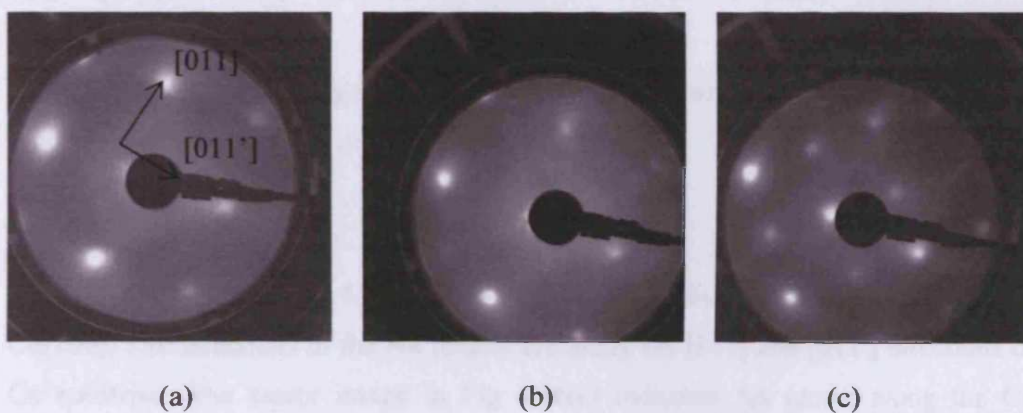


**Fig 4.24** LEED pattern of (a) clean Cu ( $E = 82$  eV), (b)  $2.5 \times 10^{14}$  atoms  $\text{cm}^{-2}$  Au ( $E = 81$  eV) and (c)  $6.2 \times 10^{14}$  atoms  $\text{cm}^{-2}$  Au on Cu(100) ( $E = 75$  eV).

Fig 4.24(b) real space of overlayer is

$$a_o = 1 a_s + 0 b_s \quad \text{equation 4.2}$$

$$b_o = 0 a_s + 1 b_s$$

In Fig 4.24(c) real space of overlayer as follows

Hence

$$a_o = 1 a_s + 1 b_s \quad \text{equation 4.3}$$

$$b_o = -1 a_s + 1 b_s$$

Possible real space structures are shown in Fig 4.25

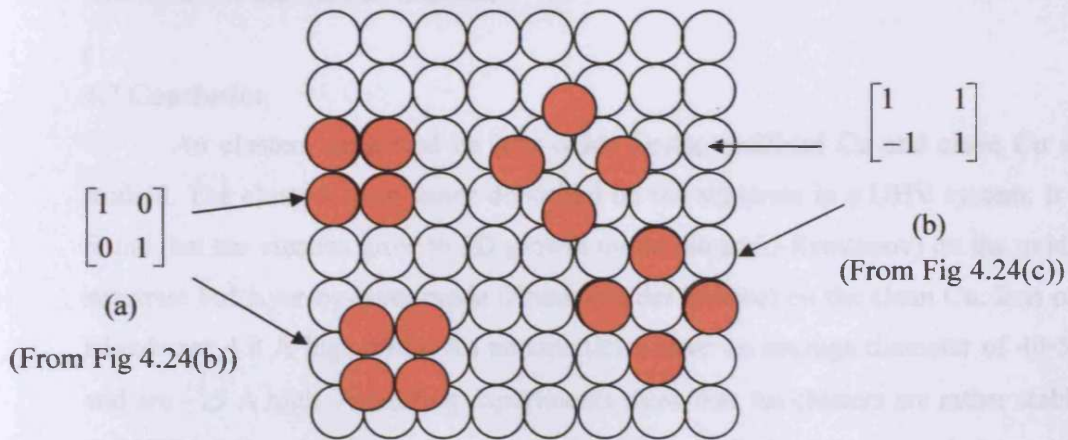


**Fig 4.25** Possible real space structures of Au (a)  $p(1 \times 1)$  (from fig 4.24(b)) and (b)  $(\sqrt{2} \times \sqrt{2}) R45^\circ$  or  $c(2 \times 2)$  (from Fig 4.24(c)) on Cu(100) substrate.

From the real space structure, Au might be grown on square unit cell of Cu with distance either 2.55 Å or 3.61 Å as in Fig 4.25.

#### 4.6.3 STM results

STM images in Fig 4.26(a) and (b) show square Au islands on clean surface of Cu(100). The directions of the Au islands are along the  $[011]$  and  $[0\bar{1}1]$  directions of Cu substrate. The closer image in Fig 4.26(c) indicates Au grows along the Cu substrate directions as a monoatomic layer. Therefore, the growth mode of Au ( $2.5 \times 10^{14}$  atoms  $\text{cm}^{-2}$ ) on clean Cu is layer by layer (Frank van der Merwe). The line

profile shows Au islands with 2.75-3.0 Å high indicating Au atomic diameter. The images are noisy but it is clear that only one atomic layer of Au is on the Cu surface. The Au growth on Cu could be layer growth by island coalescence (2 dimension growth). In this type of growth, the nucleation of islands is more rapid than terrace diffusion. This growth mode is decided by the extent of interlayer transport.

An STM image of Au with a surface concentration  $6.2 \times 10^{14}$  atoms  $\text{cm}^{-2}$  on a Cu(100) surface is shown in Fig 4.27. Larger squares of Au terraces 2.8-3.0 Å high indicate layer by layer growth of Au on the Cu surface. Au would rather grow on Cu terrace than grow on step edge of Cu due to a big mismatch of atomic distances of overlayer Au and the Cu substrate.

#### 4.7 Conclusion

Au clusters supported on iron oxide  $\text{Fe}_3\text{O}_4$ , oxidized Cu and clean Cu were studied. The clusters were vapor-deposited on the substrate in a UHV system. It was found that the clusters grow in 3D growth mode (Stranski-Krastanov) on the oxidized substrate but layer-by-layer mode (Frank van der Merwe) on the clean Cu. Iron oxide islands are 4.8 Å high while Au nanoparticles have an average diameter of 40-50 Å and are ~15 Å high. Annealing experiments show that Au clusters are rather stable in the UHV system and form microcrystals with well-defined hexagonal shapes. STS results show that Au clusters on oxide substrate exhibit nonmetallic properties. Au wets a clean Cu surface as LEED and STM show Au epitaxial grown on clean Cu.

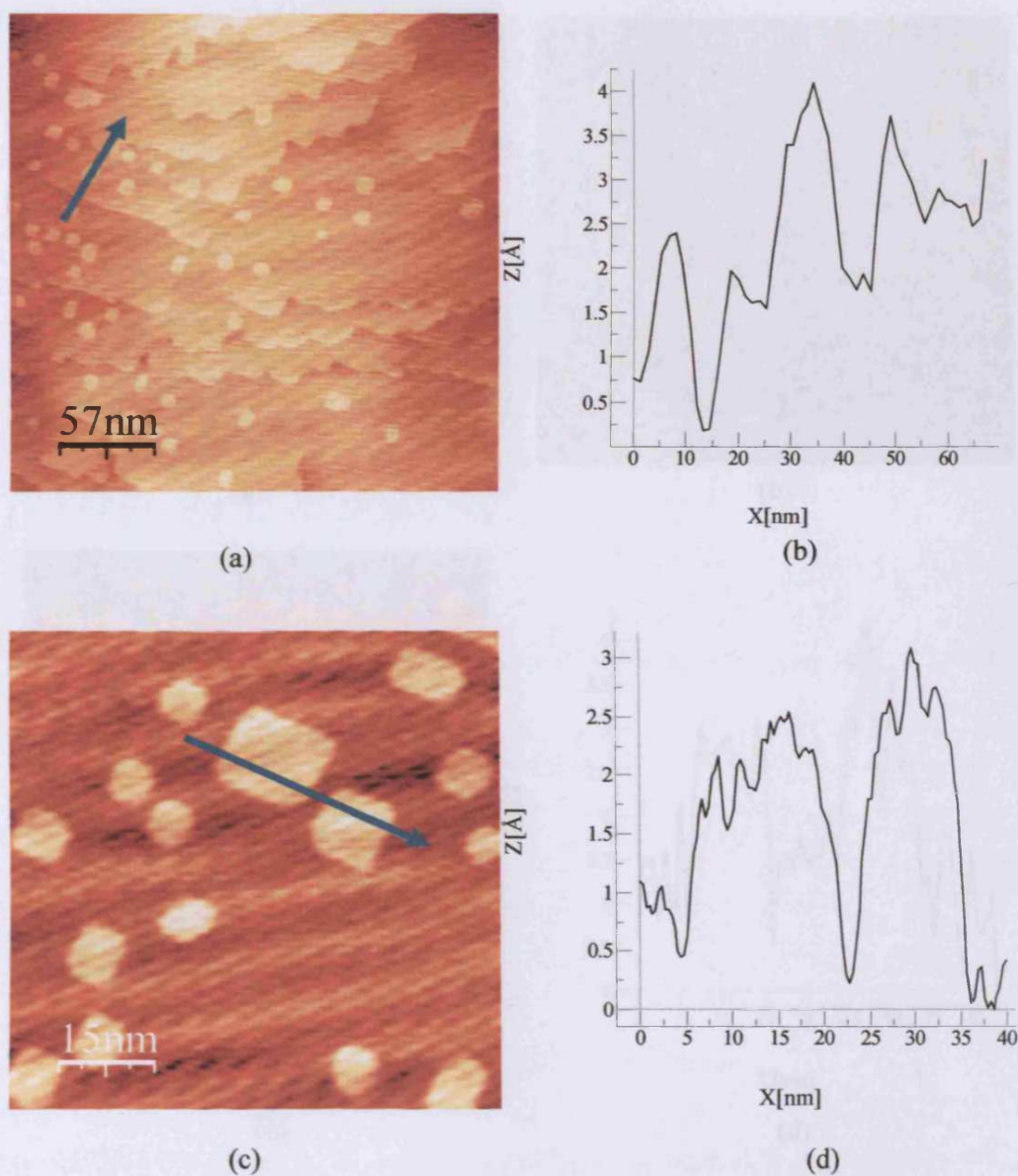


**Fig 4.26** STM of (a)  $2.5 \times 10^{14}$  atoms  $\text{cm}^{-2}$  of Au films on clean Cu in area  $3200 \times 3200 \text{ Å}^2$  (0.4V, 0.6nA) and (b) line profile of island in (a) , (c) closer image in  $760 \times 760 \text{ Å}^2$  (0.3 V, 0.4 nA) and (d) line profile of Au square island in (c).



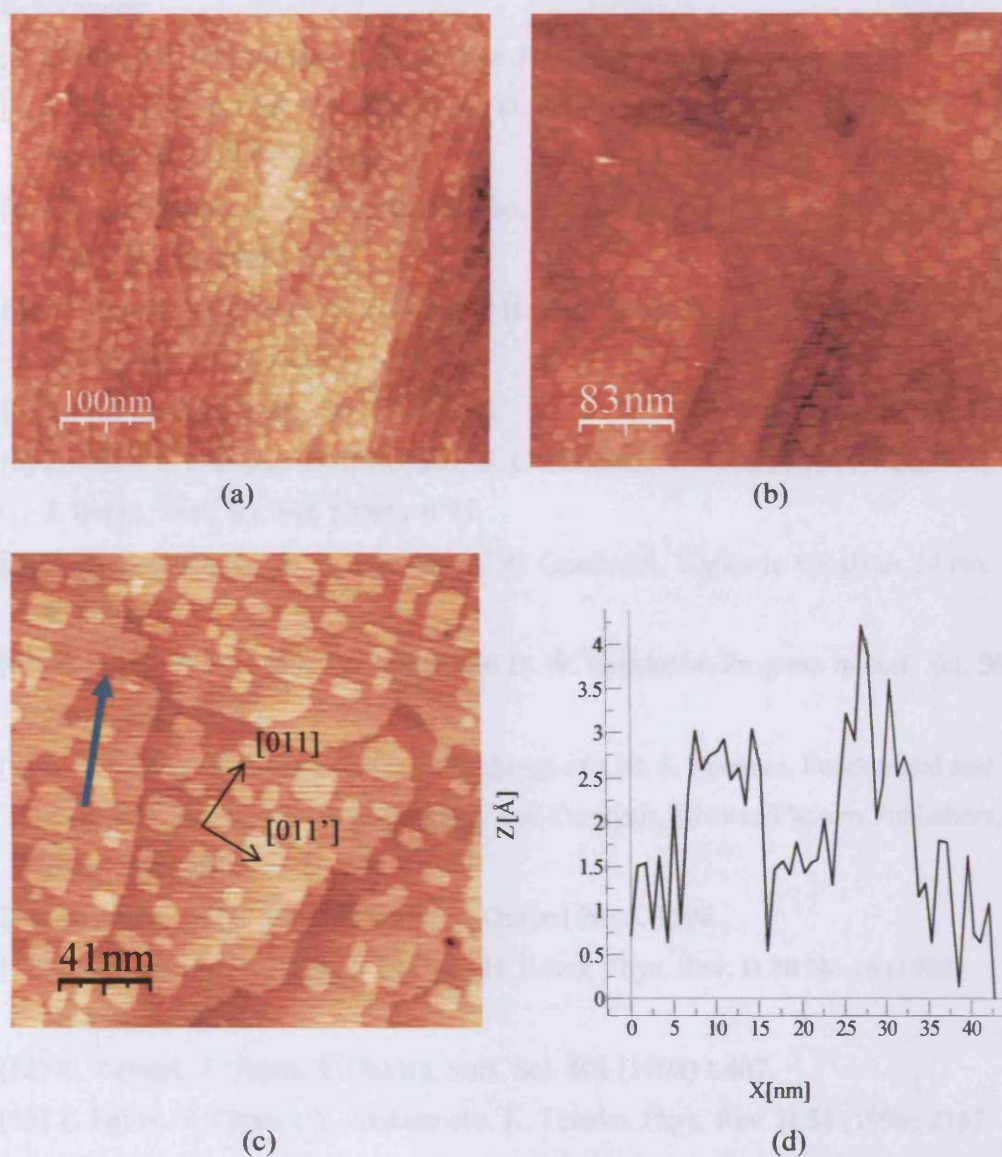


**Fig 4.27** STM images of  $6.2 \times 10^{14}$  atoms  $\text{cm}^{-2}$  Au on Cu(100) in a large area (a)  $5000 \times 5000 \text{ \AA}^2$  and (b)  $4000 \times 4000 \text{ \AA}^2$  (0.5 V, 0.2 nA), (c) closer image in  $2000 \times 2000 \text{ \AA}^2$  (0.6 V, 0.26 nA) and (d) a line profile of Au films from image (c).



**References:**

- [1] Hammer B. and Norskov J. K., *Nature* **376** (1995) 238.
- [2] X. Lai, T. P. St. Clair, M. Valden and D. W. Goodman, *Progress in Surface Science* **59** no.1-4 (1988) 25.
- [3] I. Lopes-Salido, D. C. Lim, R. Dietsche, N. Bertram and Y. D. Kim, *J. Phys, Chem. B* **110** (2006) 1128.
- [4] M. Haruta, S. Tsubota, T. Kobayashi, H. Kageyama, M. J. Genet, B. Delmon, *J. Catal.* **144** (1993) 175.
- [5] M. Haruta, *Cal. Today* **36** (1997) 153.
- [6] Z. Zhao, T. Diemant, D. Rosenthal, K. Christmann, J. Bansmann, H. Rauscher, R. J. Behm, *Surf. Sci.* **600** (2006) 4992.
- [7] C. C. Chusuei, X. Lai, K. Luo and D. W. Goodman, *Topics in Catalysis* **14** No. 1-4 (2001) 71.
- [8] X. Lai, T. P. St. Clair, M. Valden and D. W. Goodman, *Progress in surf. Sci.* **59** No. 1-4 (1998) 25.
- [9] A. F. Carley, P. R. Davies, G. J. Hutchings and M. S. Spencer, *Fundamental and Applied Catalysis, Surface Chemistry and Catalysis*, Kluwer/Plenum Publishers, New York, 2002.
- [10] G. Attard and C. Barnes, *Surfaces*, Oxford Press, 1998.
- [11] J. Ghijsen, L. H. Tjeng, J. van Elp, H. Eskes, *Phys. Rev. B* **38** No.16 (1988) 11332.
- [12] K. Tanaka, T. Fujita, Y. Okawa, *Surf. Sci.* **401** (1998) L407.
- [13] T. Fujita, Y. Okawa, Y. Matsumoto, K. Tanaka, *Phys. Rev. B* **54** (1996) 2167.
- [14] M. J. Mehl and D. A. Panagiotopoulos, *Phys. Rev. B* **54** No.7 (1996) 4519.

## Chapter 5

### Reactions on iron oxide surfaces

#### 5.1 Introduction to reactions on iron oxide surfaces

Understanding the interaction between organic molecules and metal oxide surfaces is very important in a theoretical context as well as a functional one (e.g. catalysis, corrosion) [1]. A significant knowledge about simple molecules adsorbed on well-defined single crystals of metal, and metal particles on a support material, has been developed over the last decade.

Iron oxide is used in many industries as a heterogeneous catalyst support but there is not a detailed understanding about structure-reactivity relationships and reaction mechanisms on this surface at the atomic scale. The understanding of molecular events during the reaction and chemical information are crucial for catalyst development.

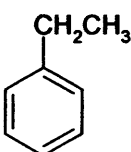
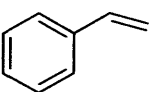
In this Chapter we examine the adsorption of acrylic acid,  $\text{CO}_2$  and  $\text{NH}_3$  at iron oxide, predominantly  $\text{Fe}_3\text{O}_4$ , and modified oxide surfaces.

#### 5.2. Literature review of reactions on iron oxide surfaces

The delocalized electrons in pure metal catalysts can be transferred easily between surface and reactants, resulting in redox reactions, whereas redox chemistry is less likely on oxides because electronic states are separated by the band gap. Acidic and basic sites in a metal oxide are a characteristic of ionic compounds, and could control the surface chemical mechanism. Metal oxides with a small band gap allow a combination of acid-base and redox chemistry whereas highly ionic oxides with large band gaps become pure acid-base reactions [2]. Iron oxide has a low metal-oxygen bond strength [3] and the bulk oxide has pH 7 [4]. It would be good to control the surface chemical processes as a combination of acid-base and redox reactions. A number of molecules have been used to study and reveal reactions on iron oxide surfaces.

The surface structure of iron oxide films on a Pt(111) substrate was studied by Weiss et al [2, 5]. LEED and STM reveal that the  $\text{FeO}(111)$  film is oxygen-terminated

resulting in basic oxygen sites. The surfaces of the  $\text{Fe}_3\text{O}_4(111)$  films are terminated by hexagonal  $\frac{3}{4}$  oxygen layer which cover a  $\frac{1}{4}$  monolayer of iron cations while the nature of the  $\text{Fe}_2\text{O}_3(0001)$  surface is still under discussion. However, Fe cations on both  $\text{Fe}_3\text{O}_4$  and  $\text{Fe}_2\text{O}_3$  films are Lewis acidic in character. Studies of the adsorption of

ethylbenzene (  ) and styrene (  ), soft bases, on the

oxide can be understood in terms of the acid-base properties of the surface [5]. On the Fe-terminated  $\text{Fe}_3\text{O}_4(111)$  and  $\alpha\text{-Fe}_2\text{O}_3(0001)$  surfaces, ethylbenzene and styrene are chemisorbed *via* the  $\pi$ -electron system of the phenyl ring, the molecules adsorbed in an almost flat configuration ( $\eta^6$ -like ring adsorption geometry). At monolayer saturation, the aromatic ring tilts to greater than  $40^\circ$ . In contrast, O-terminated  $\text{FeO}(111)$  surfaces only weakly physisorb ethylbenzene and styrene. In this system, the molecules are tilted due to adsorbate-adsorbate interactions.

$\text{H}_2\text{O}$  is one of the soft small bases that researchers have been interested in. Molecularly adsorbed  $\text{H}_2\text{O}$  binds as a base via the O atom to a metal or cation site (Lewis acid). The Lewis acid of the substrate can interact with the oxygen lone pair orbital of  $\text{H}_2\text{O}$ . The interaction of water with well characterized epitaxial  $\text{FeO}(111)$  and  $\text{Fe}_3\text{O}_4(111)$  films on  $\text{Pt}(111)$  was studied by Joseph et al [6]. O-terminated  $\text{FeO}(111)$  surfaces did not undergo reaction with the water. Physisorption of water forms a hydrogen-bonded bilayer with an ice-like structure at saturation point and consequently ice multilayers are condensed. Adsorbed hydroxyl and hydrogen species from the dissociative adsorption of the water are obtained on the Fe-terminated  $\text{Fe}_3\text{O}_4(111)$  surface exposing both Fe and O atoms. It is proposed that  $\text{OH}^-$  groups are bound to Fe cations and  $\text{H}^+$  species to O anions exposed in the topmost layer of  $\text{Fe}_3\text{O}_4(111)$ .

$\text{CCl}_4$  adsorption at iron oxide is one of useful relevance to the degradation of chlorinated compounds in soil, sediments and the catalytic destruction and corrosion of metal surfaces [7]. Degradation of  $\text{CCl}_4$  on a single crystal  $\alpha\text{-Fe}_2\text{O}_3(0001)$  surface

was studied by Rim et al [7]. STM revealed that 85 % of surface  $\text{Fe}_3\text{O}_4(111)$  is a  $2\times 2$  termination and 15% terminated by a  $1\times 1$  and superstructure phase. It was found that Cl atoms are adsorbed only on the  $\text{Fe}_3\text{O}_4(111)$   $2\times 2$  termination after  $\text{CCl}_4$  dosing at room temperature and subsequently flashing to 600 K. Both  $\text{CCl}_4$  and  $\text{Cl}_2$  dissociative reaction occurs at iron atoms in the surface as revealed by AES, LEED, TPD and XPS.

Finely dispersed Au on a metal oxide support has been discovered to be highly reactive for a number of catalytic reactions such as hydrochlorination of acetylene, propene epoxidation, hydrogenation of unsaturated aldehydes and CO oxidation [8]. For many applications using Au catalysts, the understanding of molecular processes during the reaction is little known and therefore the reactions of molecules with model systems of Au deposited on an iron oxide surface are one of the targets of researchers recently. CO adsorption on Au deposited on a thin  $\text{FeO}(111)$  film grown on a  $\text{Pt}(111)$  has been studied by Lemire et al [9]. It was found that the small Au clusters strongly adsorb more CO at low temperature. However, after 500 K the CO desorbed. The interaction of CO at low Au coverage on the iron oxide surface is similar to that at high coverage. They proposed that CO adsorption involves low coordinated atoms and is consequently independent of particle dimensions. Therefore, the controlling factor in the CO adsorption on Au nanoparticles is not quantum size effects as postulated by some researchers, but the presence of highly uncoordinated Au atoms in very small particles. Not only Au but also Pd is used to modify iron oxide films for reaction study. Meyel et al [10] have studied CO adsorption on Pd deposited on a thin  $\text{FeO}(111)$  film grown on a  $\text{Pt}(111)$  substrate. It was found that typical CO adsorption occurred after Pd particles were deposited on  $\text{FeO}(111)$  surface at 70-100 K. After annealing to 600 K, a complex CO adsorption behavior was observed. Hence, there are several factors for surface reaction such as final temperature, heating and cooling rate, annealing time etc.

The experiments reported in this chapter are an attempt to investigate the possibility of reactions on oxide surfaces and Au nanoparticles on  $\text{Fe}_3\text{O}_4$  films grown on a Cu (100) surface with (1) acrylic acid, (2)  $\text{CO}_2$  (acid) and (3)  $\text{NH}_3$  (base). Further information about the preparation of the iron oxide film and Au nanoparticles deposited on oxides has been discussed in Chapter 3 and 4, respectively.

### 5.3 Reaction of acrylic acid on thin iron oxide ( $\text{Fe}_3\text{O}_4$ , 3–4 Å) and thick iron oxide ( $\text{Fe}_3\text{O}_4$ , 7–14 Å)

#### 5.3.1 Introduction

Aldehydes are widely used in the food and chemical industries. The hydrogenation of carboxylic acid is one of the important catalyzed reactions for aldehyde synthesis. Ponec et al [11, 12] studied acetaldehyde formation from acetic acid using various metal oxide catalysts, and iron oxide showed the highest selectivity. Therefore, it is fascinating to study the reaction on this oxide surface. Acrylic acid is used for studying the reaction on the surface due to the vinyl group associated with the carboxylic group in the molecule being a good leaving group for further reaction studies.

This work studies the adsorption of acrylic acid on prepared iron oxide and oxide supported Au nanoparticles at 295 K and desorption of acrylic acid on those model catalyst at 500 K in UHV system. The investigations are carried out by XPS, LEED and STM to characterize those reactions on surfaces.

#### 5.3.2 Experimental details

Thin iron oxide films (3–4 Å) were produced by oxidizing an iron multilayer deposited on a Cu(100) surface. The substrate was exposed to oxygen at the pressure of  $10^{-6}$  mbar at room temperature and simultaneously the sample was heated at a high rate to 850 K and cooled down to room temperature in  $\text{O}_2$ .

Thick iron oxide films (7–14 Å) were produced by oxidizing iron multilayer deposited on Cu(100) in a presence of oxygen at a pressure of  $10^{-6}$  mbar at room temperature and simultaneously, the sample was heated at a slow rate to 850 K, maintained at this temperature for 10 min, then cooled in  $\text{O}_2$ .

Au nanoparticles were deposited by passing a current through a Mo filament wrapped with Au wire. The Mo wire was resistively heated resulting in the evaporation of gold.

Acrylic acid was purified by several freeze-pump-thaw cycles before admission to the vacuum chamber. The sample was exposed to purified acrylic acid at the pressure of  $1 \times 10^{-6}$  mbar (1 Langmuir =  $10^{-6}$  torr s $^{-1}$ ) at room temperature. Desorption of acrylic acid was performed at 500 K.



In this work, a combination of XPS, LEED and STM was used to examine the chemical composition and surface structure. The experiments were performed in a multichamber ultrahigh vacuum (UHV) system as described in Chapter 2.

### 5.3.3 Reaction of acrylic acid on a thin iron oxide surface ( $\text{Fe}_3\text{O}_4$ , 3-4 Å)

#### 5.3.3.1 XPS results

Acrylic acid represents an ethylene-like molecule, with one hydrogen atom of ethylene replaced by the  $-\text{COOH}$  functional group. The conjugation of the  $\text{C}=\text{C}$  bond with the  $\text{COOH}$  group leads to delocalized orbitals so the reactivity of molecule could be influenced by either  $\text{C}=\text{C}$  bond,  $-\text{COOH}$  group or both functions [13].

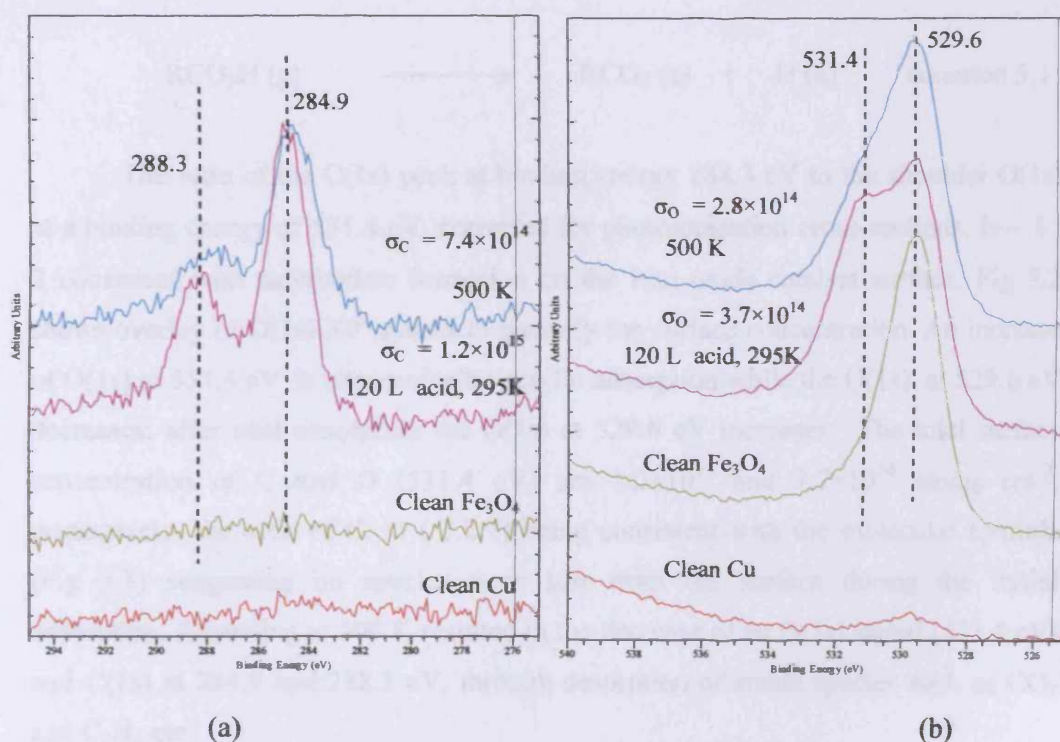


**Fig 5.1** (a) C(1s) and (b) O(1s) XP spectra of a clean Cu,  $\text{Fe}_3\text{O}_4$  and exposure acrylic acid adsorption at 295 K and desorption at 500 K on Cu substrate, respectively.

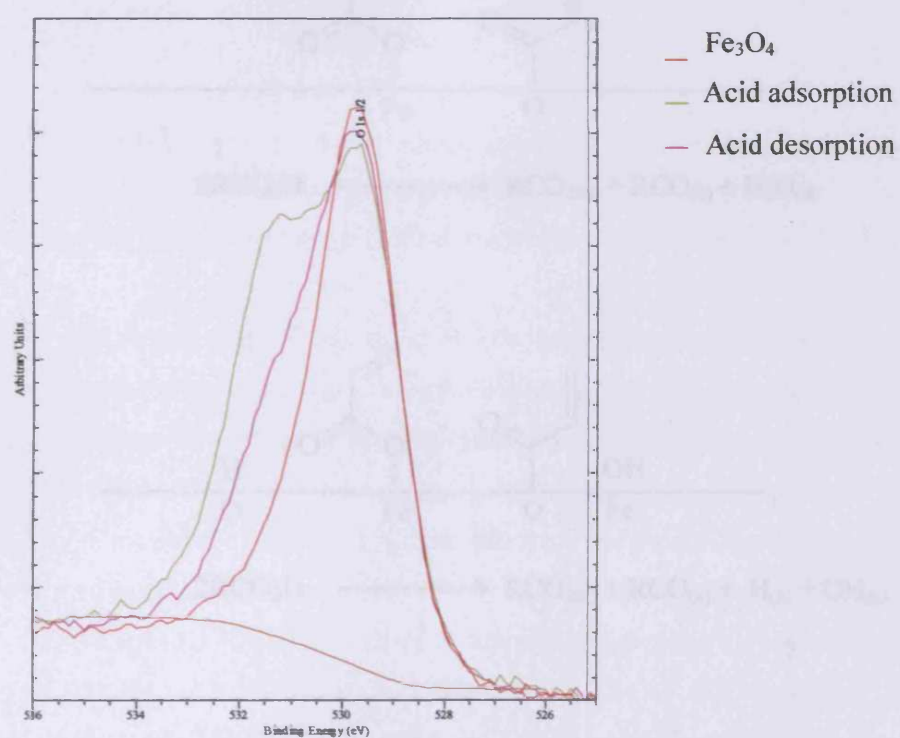
C(1s) and O(1s) signals in the XP spectra (Fig 5.1). The presence of C(1s) and signals is indicative of acrylic acid adsorption. An extra O(1s) peak at 531.4 eV appears. The binding energy of lattice oxygen in an iron oxide film surface is 529.6 eV while that of the oxygen in the adsorbed acrylic acid molecule is 531.4 eV (Fe and OH adsorption) in Fig 5.1(b). 2 species of carbon appear at binding energy 284.9 and 288.3 eV with an intensity ratio 2:1. There might be H dissociation of the acid on oxide surface shown in equation 5.1



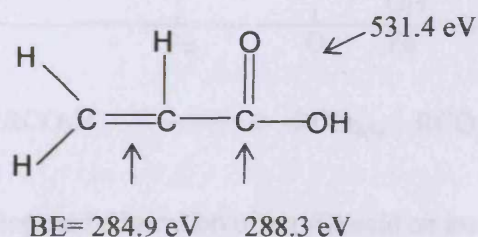
The ratio of the C(1s) peak at binding energy 288.3 eV to the shoulder at a binding energy of 531.4 eV, corrected for photoionisation cross-sections, is 2 consistent with carboxylate formation on the iron oxide catalyst surface. Fig 5.3 shows overlay of O(1s) XP spectra to quantify the surface concentration. An increase of O(1s) at 531.4 eV is observed after acrylic adsorption while the O(1s) at 529.6 eV decreases; after acid desorption the O(1s) at 529.6 eV increases. The total surface concentration of C and O (531.4 eV) are  $1.2 \times 10^{15}$  and  $3.7 \times 10^{14}$  atoms respectively, the ratio of C: O ( 3.2:1) being consistent with the molecular formula of acrylic acid (Fig 5.3) suggesting no species were lost from the surface during the adsorption. Annealing to 500 K resulted in the decrease of an O(1s) signal (531.4 eV) and C(1s) at 284.9 and 288.3 eV, through desorption of stable species such as  $\text{CO}$  and  $\text{C}_2\text{H}_4$  etc.

Fig 5.3 shows acrylic formula giving different binding energy in different environments in the observed XP spectra in Fig 5.1.

Fig. 5.4 shows the proposed adsorption geometry of acrylic acid on the oxide surface. It is assumed that the exposed basic O anion and acidic Fe cation in the film surface would be a host for acid adsorption. Acid could possibly be adsorbed on a single atom of Fe and O or 2 atoms of Fe and O. Either the vinyl group ( $-\text{C}=\text{C}-$ ) reacts with the O terminated oxide film as the addition reaction of an alkene or the carboxylic acid group ( $-\text{COOH}$ ) reacts with Fe cations resulting in carboxylate formation. The possibility also exists for long range interactions (such as H-bond interaction) between molecular adsorbates (Fig 5.4(a) and (d)).



**Fig 5.2** Overlay of O(1s) spectra of  $\text{Fe}_3\text{O}_4$ , acrylic acid adsorption (295 K) and desorption (500 K).



**Fig 5.3** Acrylic acid formula and binding energy at different environments.

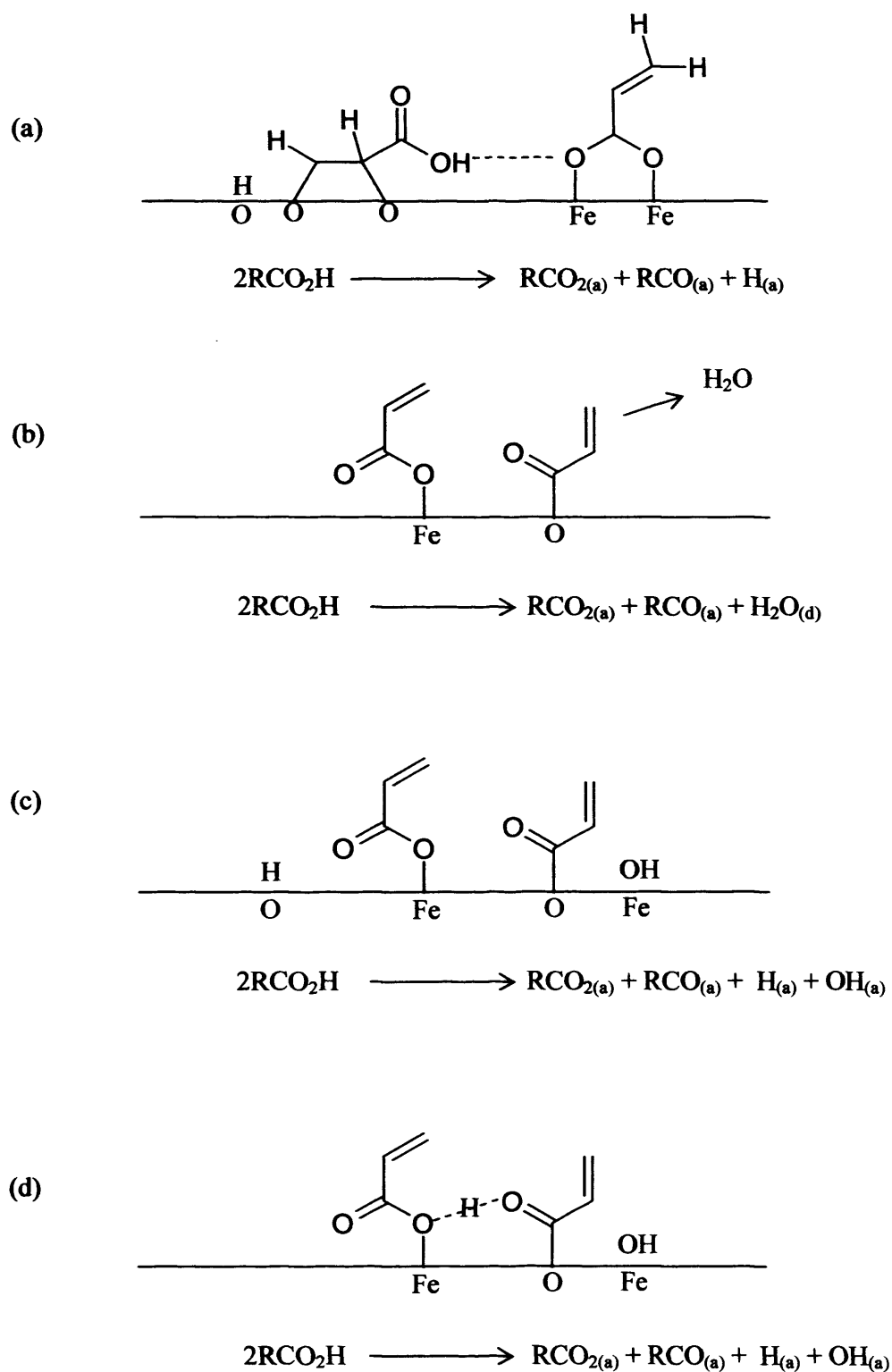


**Fig 5.4** Proposed adsorption of acrylic acid on iron oxide.



### 5.3.3.2 LEED results

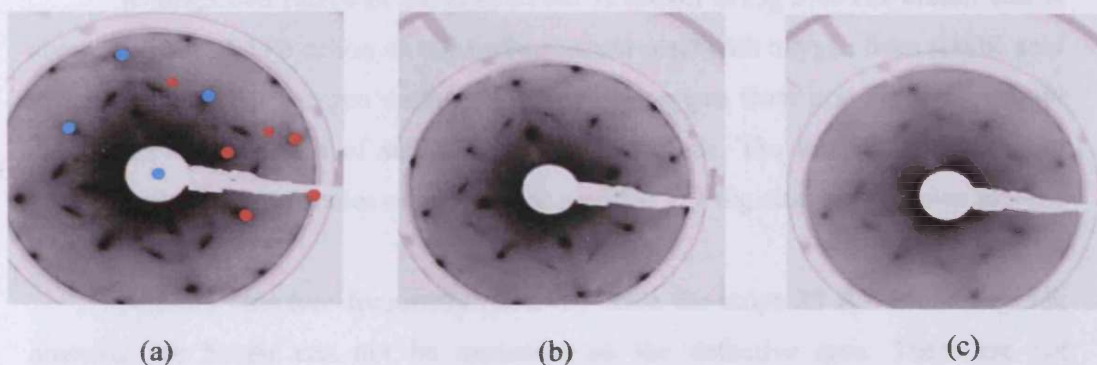


**Fig 5.5** LEED patterns at  $E = 98$  eV of (a) 3 Å iron oxide ( $\text{Fe}_3\text{O}_4$ ) film (b) after (300L) exposure of this film to acrylic acid (c) after heating the sample to 500 K; blue represents the Cu substrate atoms and red oxide overlayer.

Fig. 5.5 shows the LEED patterns of iron oxide ( $\text{Fe}_3\text{O}_4$ ), after acid adsorption and following partial desorption. Acrylic acid adsorption does not destroy the LEED pattern of the surface. The pattern of spots is rather similar to before dosing the acid. After heating at 500 K for 3 min, some spots disappear. The blue-spot unit cell (Fig 5.5(a)) represents the Cu(100) substrate and the red-spots additional structure from the oxide film. The disappeared red spots could be either Fe cation or O anion from the oxide surface. XP spectra show that C and O intensities are reduced. The desorbed species could be e.g.  $\text{CO}_2$ ,  $\text{CH}_2\text{CH}_2$ ,  $\text{CH}_3\text{CH}_2\text{OH}$  or  $\text{CH}_3\text{OH}$  etc. Therefore, the disappeared spots on the LEED could possibly be only O atoms from iron oxide or Cu surface.

### 5.3.3.3 STM results

Fig 5.6 depicts the dramatic change after exposure of the iron oxide surface to acrylic acid. The population of acid clusters is concentrated on the edge of the iron oxide steps due to high surface free energy (Fig 5.6(a)). Acrylic acid clusters were also obvious on the edges of iron oxide strips in different directions, as shown in Fig 5.6(b). The gap between acid cluster rows is ca. 50 Å (Fig.5.6(d)), which is the same



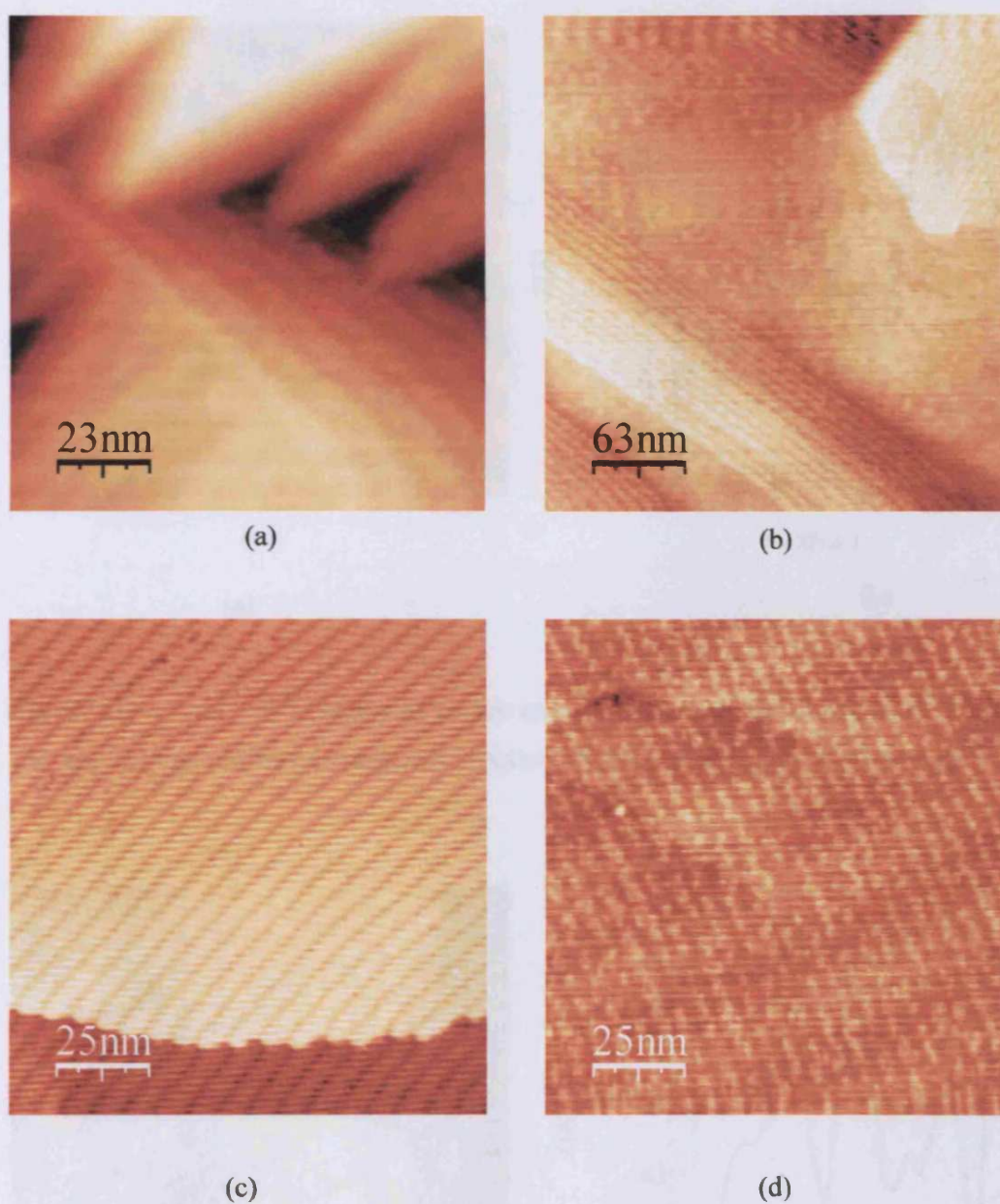
as the oxide strips in Fig 5.6(c). The clusters of acrylic acid could be formed *via* long range interaction between molecular adsorption of acid as proposed in Fig 5.4.

A magnified image of the acid cluster is shown in Fig 5.7. The cluster size is about 25-30 Å. An Fe cation on the surface would react with oxygen from acrylic acid to form carboxylate oxygen on the surface while oxygen from iron oxide film could react with ethylene part of acid parallel to the surface. The long range interaction between adsorbed molecules on the surface resulted in a big clusters as shown in STM image.

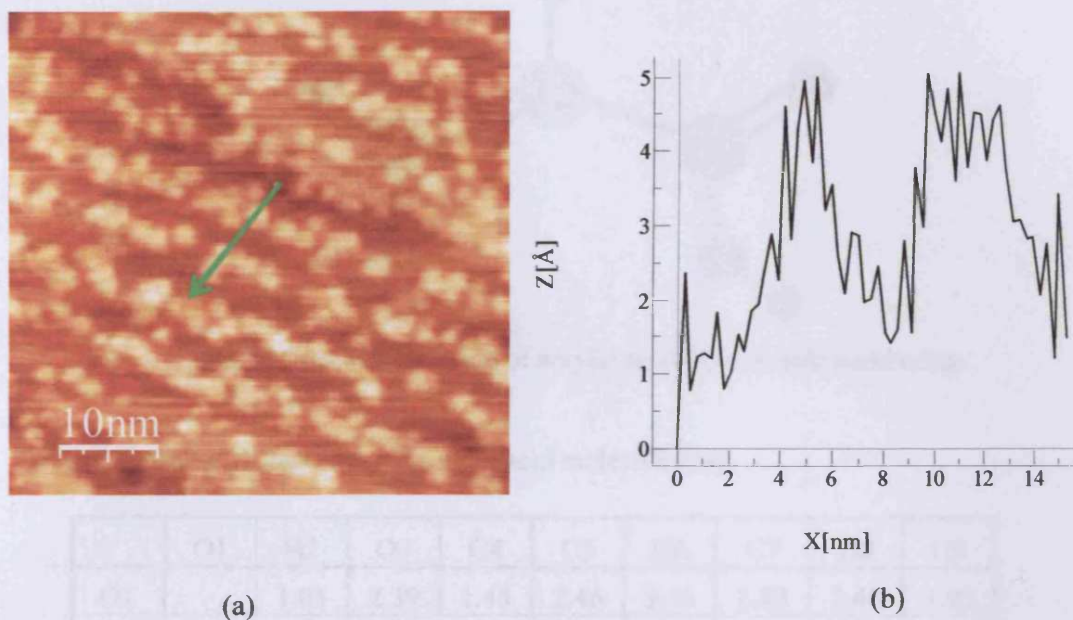
Another structure frequently observed were the strips 25 Å wide in Fig 5.8; however the height can not be measured on the defective area. These are not consistent with the iron oxide structure; therefore the product of acid adsorption could be on the Cu substrate itself. I-V analysis was not performed on this image.

Fig 5.9 shows the molecular structure of acrylic acid together with the atomic distances in Table 5.1 [14]. Fig 5.10 and Fig 5.11 show models of the iron oxide  $\text{Fe}_3\text{O}_4(100)$  and  $(111)$  surfaces. Adsorption of acrylic acid could take place in either of those models. As proposed mechanisms in Fig 5.4, the acid might be adsorbed on single Fe atom, O atom, 2 Fe atoms or 2 O atoms on oxide surface. The maximum atomic distance for whole molecule of acid is 4.95 Å. From the size of clusters in Fig 5.7, they would consist of 3-6 molecules of acrylic acid. Table 5.1 shows atomic distances between O(1) and O(3) (2.39 Å) and C(5) and C(7) (1.35 Å). The shortest atomic distance of O-O atoms in the  $\text{Fe}_3\text{O}_4(111)$  surface is ca. 2.8-3.0 Å and Fe-Fe ca. 2.9-3.4 Å (in Fig 5.10). In the  $\text{Fe}_3\text{O}_4(100)$  surface (Fig 5.11) the atomic distance of O-O atoms is 2.8-3.0 Å and Fe-O atoms is 2.0 Å. Therefore, adsorption of the acrylic acid may take place on single atoms of Fe or O on the surface rather than bond on double atoms.

The step edges of the strips are fully covered by acid clusters as shown in Fig 5.7. The cluster height is ca. 3-4 Å, similar to the height of the acid molecule. From Table 5.1 the maximum atomic distance is 4.95 Å between H(2) and H(9). This implies single layer adsorption of acrylic acid on the oxide surface. The acrylic acid clusters of size 30 Å indicate long range interaction between acid molecules.



**Fig 5.6** (a) Clusters of acrylic acid on iron oxide step edges in surface area  $1100 \times 1100 \text{ \AA}^2$  (0.6 nA, 1 V) (b) rows of acrylic acid clusters on oxide strips in different directions (c) on iron oxide strips (50 Å wide) before acrylic acid adsorption (1.5 nA, 1 V) and (d) after 120 L of acid clusters on the oxide surface in  $1240 \times 1240 \text{ \AA}^2$  (0.7 nA, 0.63 V).



**Fig 5.7** (a) A closer STM image of acrylic acid clusters in an area  $510 \times 510 \text{ Å}^2$  (1 nA, 1V) and (b) line profile of acrylic acid clusters with 3-4 Å high and 30-40 Å wide.

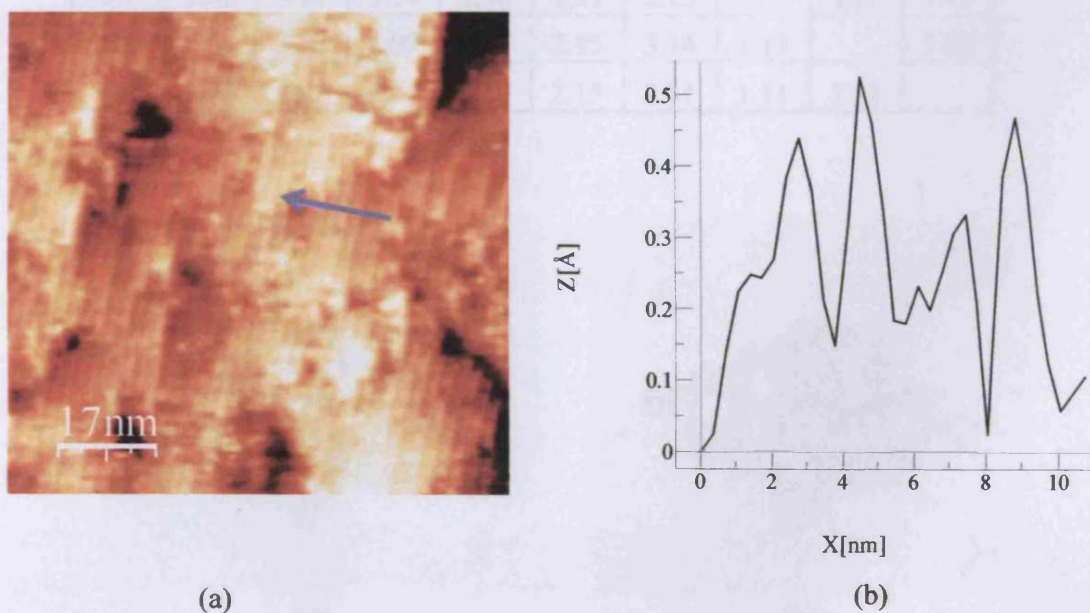


**Fig 5.8** STM image shows (a) strips 25 Å wide in an area  $840 \times 840 \text{ Å}^2$  (0.3 nA, 0.25 V) after acrylic acid adsorption (b) line profile of the strip structure.



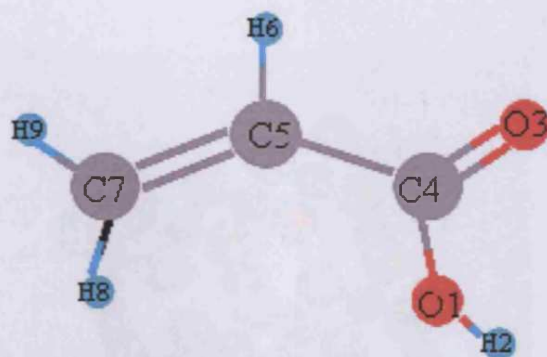
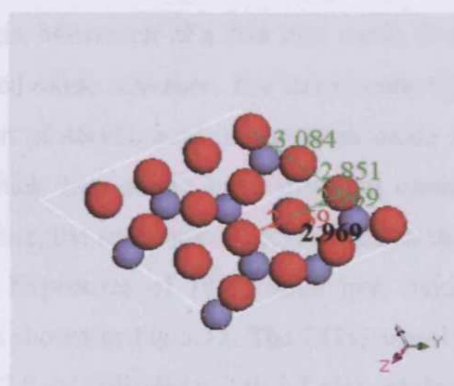


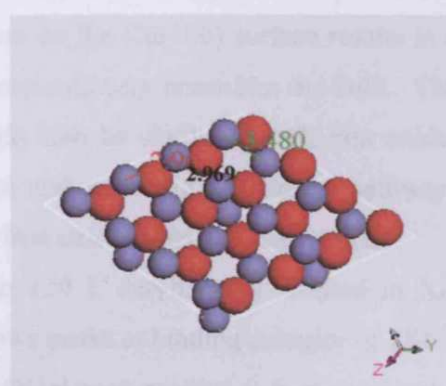
Fig 5.9 Molecular structure of acrylic acid with atomic numbering.

Table 5.1 Atomic distance (Å) in acrylic acid molecule [14]

	O1	H2	O3	C4	C5	H6	C7	H8	H9
O1		1.05	2.39	1.45	2.46	3.45	2.83	2.48	3.93
H2	1.04		2.32	1.93	3.30	4.16	3.84	3.52	4.95
O3	2.39	2.32		1.27	2.52	2.76	3.73	4.09	4.67
C4	1.45	1.93	1.27		1.53	2.23	2.56	2.81	3.57
C5	2.46	3.29	2.52	1.54		1.11	1.35	2.15	2.15
H6	3.45	4.15	2.76	2.23	1.10		2.15	3.14	2.51
C7	2.82	3.84	3.74	2.56	1.35	2.15		1.11	1.11
H8	2.48	3.52	4.09	2.81	2.15	3.14	1.11		1.88
H9	3.93	4.95	4.67	3.57	2.15	2.51	1.11	1.88	



(a)



(b)

Fig 5.10 Model of  $\text{Fe}_3\text{O}_4(111)$  termination with (a) topmost O atoms with atomic distance 2.8-3.0 Å and (b) topmost Fe atoms with atomic distance 2.9-3.5 Å.

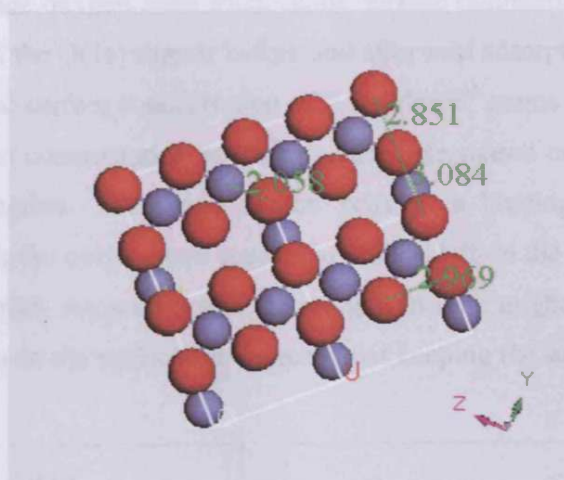


**Fig 5.11** Model of  $\text{Fe}_3\text{O}_4(100)$  termination show O-O atomic distance with 2.8-3.0 Å and Fe-O atomic distance with 2.0 Å.

In conclusion, adsorption of acrylic acid results in either the formation of carboxylate or ethylene adsorption laying flat and parallel on the surface. Heating to 500 K results in acid desorption from the surface as illustrated in XPS. LEED show that O atoms on the oxide surface are involved in desorption, and STM images shows that the edge of iron oxide strips are more reactive to acrylic acid cluster formation.

#### 5.3.4 Reaction of acrylic acid on thick iron oxide ( $\text{Fe}_3\text{O}_4$ , 7-14 Å)

A thick iron oxide film might better mimic the iron oxide powder used often in catalysis. Mismatch of a thin iron oxide structure on the  $\text{Cu}(100)$  surface results in a distorted oxide structure. The thick oxide film more closely resembles the bulk. The reaction of acrylic acid on the thick oxide might also be similar to bulk iron oxide. This thick film might have different character and react via a different pathway. Therefore, the reactions of acrylic acid on thick iron oxide films has been studied.

Exposures of 10 Å thick iron oxide to 120 L acrylic acid resulted in XP spectra shown in Fig 5.12. The  $\text{C}(1s)$  signal shows peaks at binding energies of 284.3 and 287.8 eV (FWHM = 2.0, 2.5 eV) while the  $\text{O}(1s)$  peak position is fairly constant at a binding energy of 529.4 eV. The ratio of  $\text{C}_{284.3}$  to  $\text{C}_{287.8}$  is ~ 1.8: 1.1. Compared to the  $\text{O}(1s)$  peak before dosing acrylic acid, the XP intensity of  $\text{O}(1s)$  is rather



constant due to lattice oxygen from thick oxide surface dominating the whole peak area. The FWHM of the O(1s) signals before and after acid adsorption are 1.9 and 2.0 eV, respectively. The surface concentration of C is  $1.4 \times 10^{15}$  atoms  $\text{cm}^{-2}$ . After heating to 500 K the carbon concentration at both positions decreased consistent with  $\text{CO}_2$  and  $\text{CH}_2\text{CH}_2$  desorption. The broad carbon peak at a binding energy of 283.7 (FWHM= 3.7 eV) is the only carbon species of carbon left on the surface. The O(1s) intensities are constant suggesting that the oxygen in bulk might emerge to replace the desorbed oxygen on the surface for the reason of keeping the surface being stable.

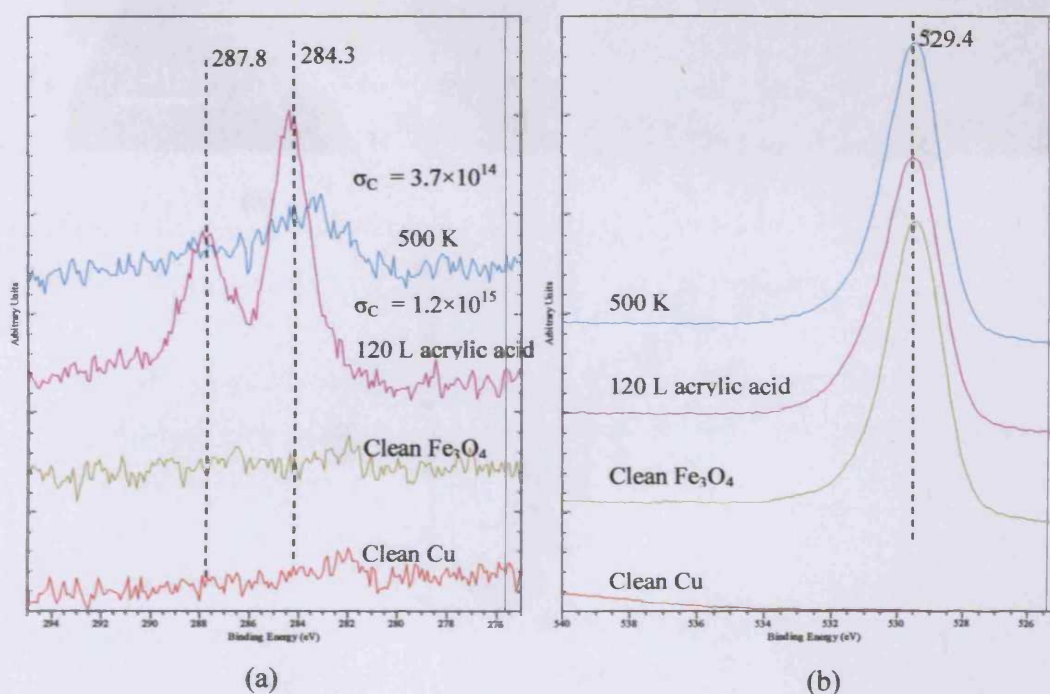


**Fig 5.12** (a) C(1s) and (b) O(1s) XP spectra of clean Cu , 10 Å Fe<sub>3</sub>O<sub>4</sub> , 120 L acrylic acid adsorption (295 K) and desorption at 500 K, respectively.

STM images (Fig 5.13) show the surface of the thick iron oxide surface after exposure to acrylic acid. As in Chapter 3, the high densities of round structures of iron oxide are observed, the bright islands scattered around the surface indicating either oxide islands decrease or acid clusters adsorbed on oxide surface. STS was not obtained in the experiment. Compared with the case of the oxide film and Au modified oxide substrates in Chapters 3 and 4, the bright islands 2-3 Å high in Fig 5.13 should be acid molecules or iron oxide, however hexagonal microstructure

terraces with ca. 5 Å high indicate  $\text{Fe}_3\text{O}_4(111)$  termination.

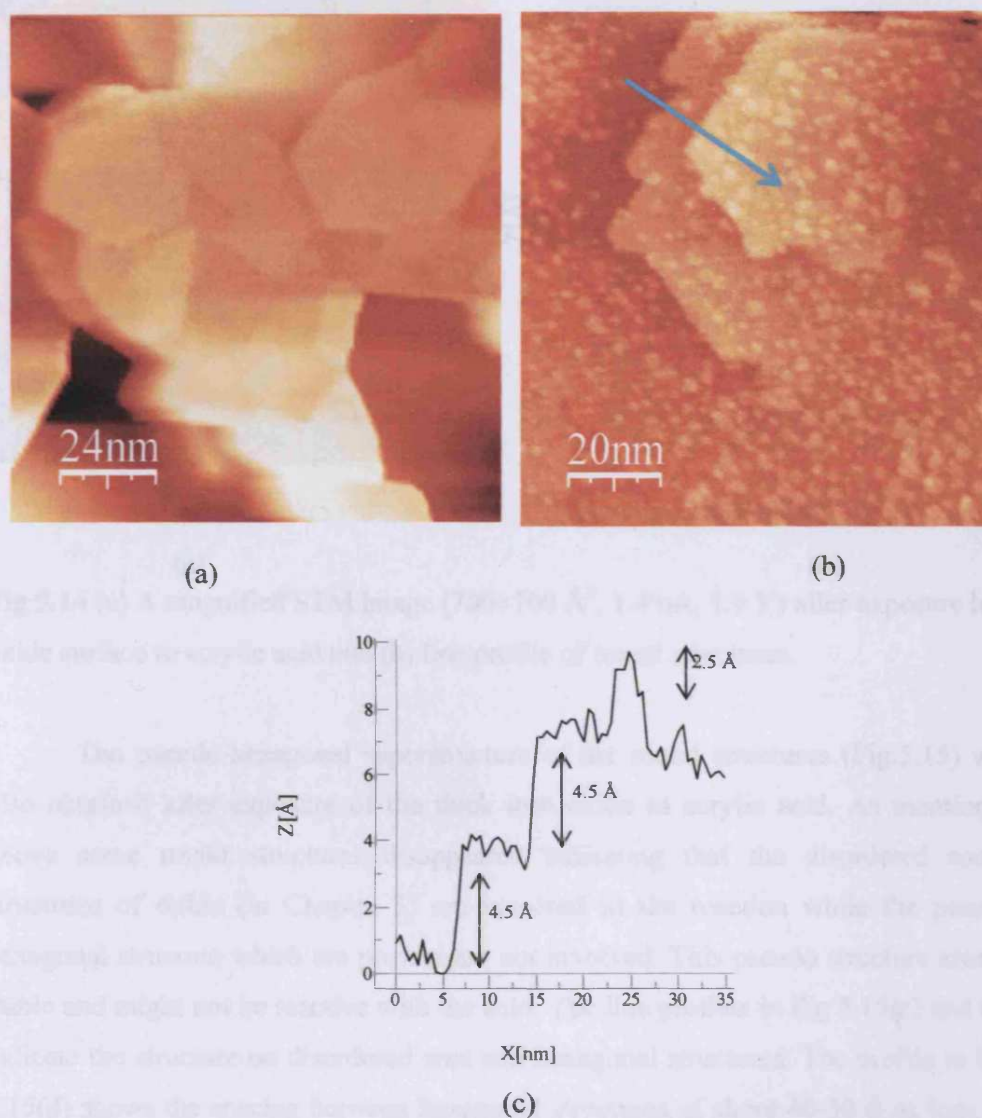


**Fig 5.13** STM image of catalyst surface before (a) and (b) after exposure the surface to 120 L acid in about  $1000 \times 1000 \text{ Å}^2$  (1 nA, 1 V) and (c) line profile show 7 Å  $\text{Fe}_3\text{O}_4$  with 4.5 Å high and acrylic acid with 2-3 Å high.

A magnified image in Fig 5.14 shows the round structures 25-30 Å diameter as iron oxide character in Chapter 3 but the population of round structures are not as much as before the reaction. This suggests that the round particles could be due to the oxide surface or acid adsorption. The height of the round structures is about 2-3 Å.



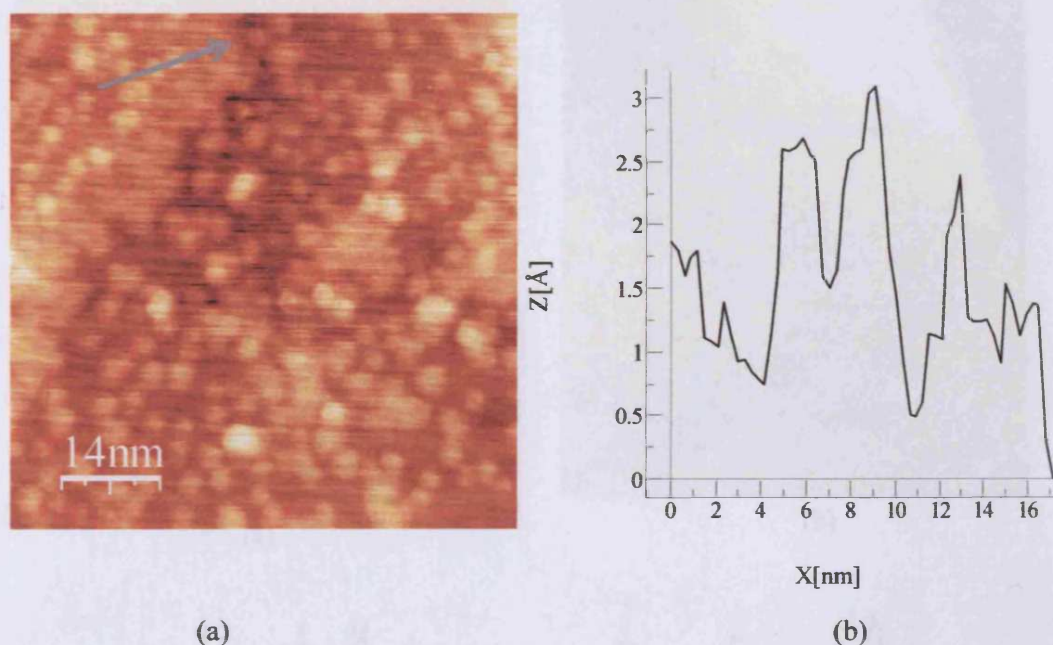


**Fig 5.14** (a) A magnified STM image ( $700 \times 700 \text{ Å}^2$ , 1.4 nA, 1.9 V) after exposure iron oxide surface to acrylic acid and (b) line profile of round structures.

The pseudo-hexagonal superstructure of the round structures (Fig.5.15) was also obtained after exposure of the thick iron oxide to acrylic acid. As mentioned above some round structures disappeared indicating that the disordered round structures of oxide (in Chapter 3) are involved in the reaction while the pseudo hexagonal structure which are present are not involved. This pseudo structure area is stable and might not be reactive with the acid. The line profiles in Fig 5.15(c) and (d) indicate the structure on disordered area and hexagonal structures. The profile in Fig 5.15(d) shows the spacing between hexagonal structures of about 40-50 Å as long as before the reaction.

STM images of rows of acrylic acid clusters acquired in Fig 5.16(a) are similar to acrylic acid on thin iron oxide film, as are the gaps between the rows which are an average 50 Å. Fig 5.16(b) shows another area of the sample surface. Acid rows on iron oxide strips and disordered structures are observed.

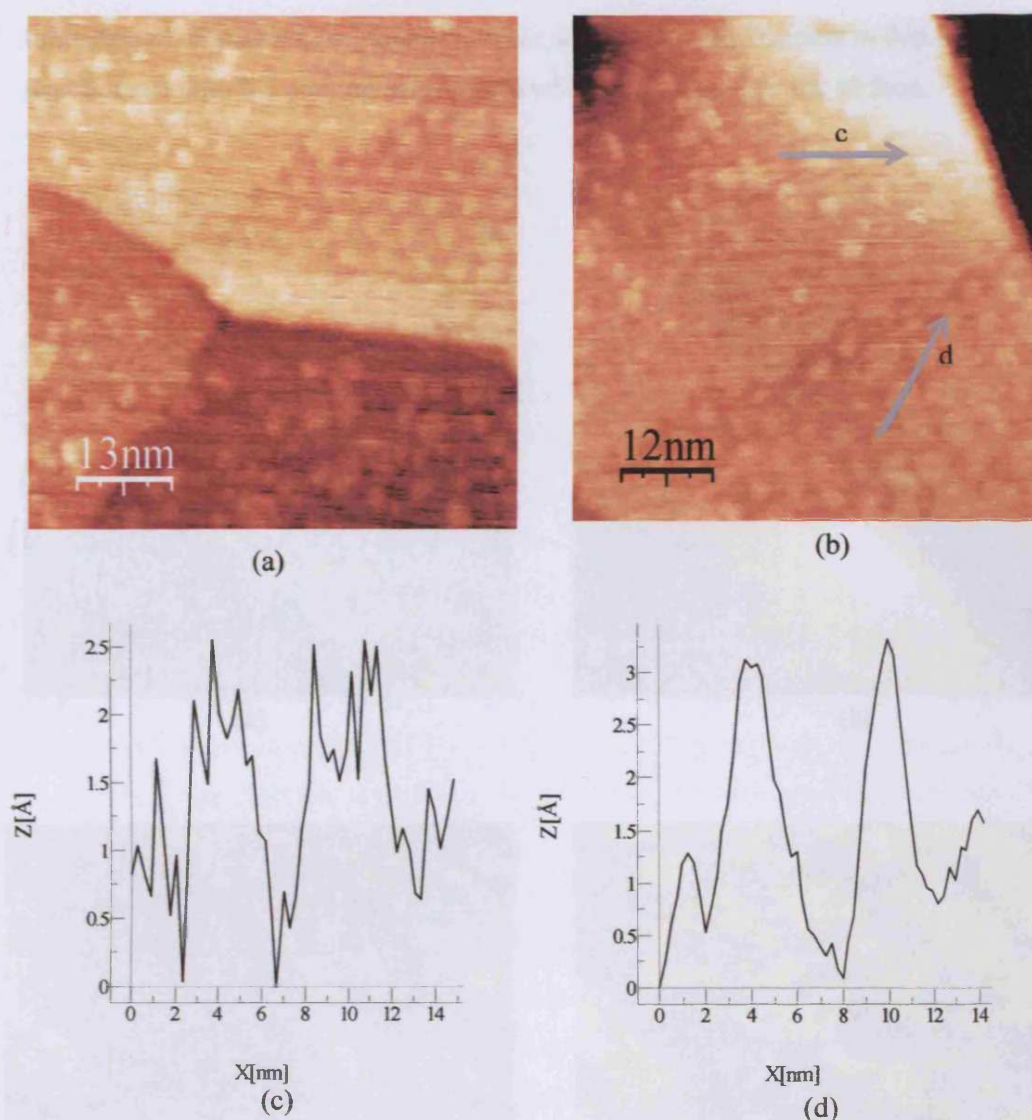


**Fig 5.15** STM images of sample surface (a) after acrylic acid adsorption (600 L)  $1760 \times 1760 \text{ \AA}^2$  (1 nA, 0.81 V) and (b) a magnified image in  $370 \times 370 \text{ \AA}^2$  (1 nA, 1.4V) and line profile of (c) the round structure and (d) arranged hexagonal pattern.

The iron oxide strips are shown in Fig 5.16(c) are for a wide area and (d) in a magnified area. Note that in some areas acid forms as a cluster on iron oxide strips while in some areas iron oxide strips are destroyed. It is possible that the thick oxide survives due to the loss of surface O being replaced by O from the bulk. This may explain why destructive strips were only obtained for the thick oxide film. However, the destructive iron oxide strips were not found on the thin iron oxide due to a



limitation of available O on this iron oxide surface. Lattice O atoms in thin iron oxide tend to react with the coming acrylic acid which is adsorbed on the surface.

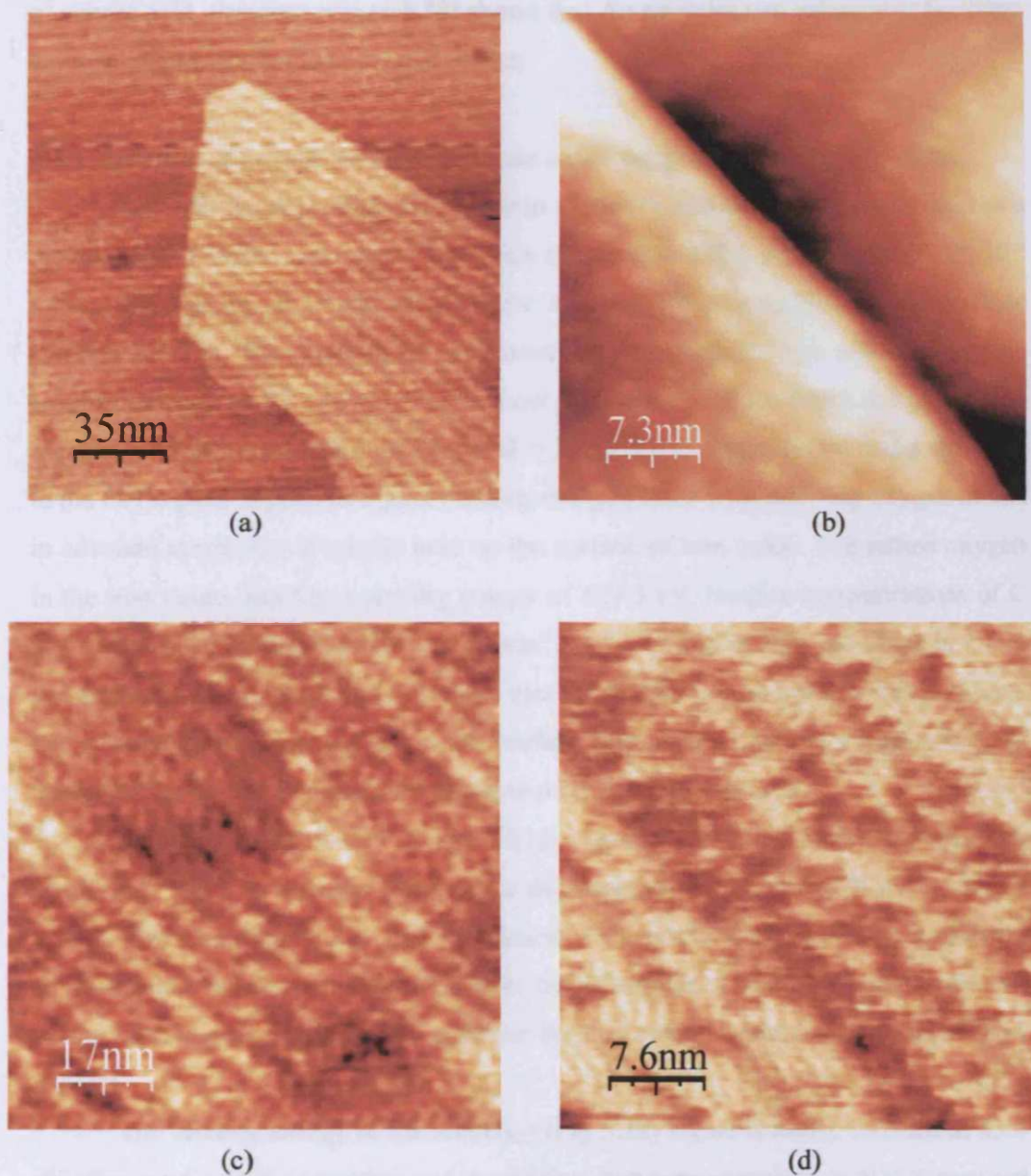


**Fig 5.16** STM images of surface show strips of acrylic acid rows (a)  $1800 \times 1800 \text{ \AA}^2$  (0.9 nA, 0.8 V) and (b)  $350 \times 350 \text{ \AA}^2$  and (c) destroyed iron oxide strips in  $850 \times 850 \text{ \AA}^2$  (1.1 nA, 0.99 V) and (d) a closer area of strips in  $380 \times 380 \text{ \AA}^2$  (1.2 nA, 1 V).



#### 5.4 Reaction of acrylic acid on thin and thick iron oxide films in the presence of Au nanoparticles

Au modified thin and thick iron oxide films were used to study the adsorption of acrylic acid. Previous research [8] shows that Au particles can enhance or facilitate the reaction on the surface of metal oxides.

##### 5.4.1 Reaction of acrylic acid on thin iron oxide supported Au nanoparticles

0.47 ML Au deposited on a 4 Å iron oxide ( $\text{Fe}_3\text{O}_4$ ) film surface was used as a model catalyst. After exposure of the oxide substrate to 120 L acrylic acid ( $P_{\text{O}_2} = 10^{-6}$  mbar), XP spectra of C and O(1s) show acrylic acid components on the surface (section 5.3.3.1). Thin iron oxide supported Au nanoparticles also adsorbed acrylic acid molecules, as XP spectra results show in Fig 5.17. C(1s) peaks are at binding energies of 284.2 and 288.0 eV (FWHM = 2.3, 2.5 eV, respectively) and a shoulder to the O(1s) peak appears at higher binding energy (530.6 eV), showing oxygen atoms in covalent molecules of acrylic acid on the surface of iron oxide. The lattice oxygen in the iron oxide film has a binding energy of 529.5 eV. Surface concentrations of C and O are  $1.3 \times 10^{15}$  and  $3.4 \times 10^{14}$  atoms  $\text{cm}^{-2}$ , and the ratio of  $\text{C}_{284.2}$  to  $\text{C}_{288.0}$  is 2.1: 1 and ratio of  $\text{C}_{288.0}$  to  $\text{O}_{530.6}$  is 1.3:1. Note that the surface concentrations and C(1s) and O(1s) binding energies on Au oxide surface and iron oxide are comparable. Au nanoparticles do not enhance acid adsorption on the oxide surface.

After annealing to 500 K, the C(1s) signal at 288.0 eV shows a reduction, signifying  $\text{CO}_2$  is lost as the carboxylate decomposes; the peak at 284 eV is shifted toward lower binding energy and broadened. This would suggest that no  $\pi$  electron delocalization between  $\text{C}=\text{C}$  and  $\text{COO}$  in the molecules. The ethylene molecule left on the surface gave a C(1s) peak at lower binding energy which was broad (FWHM 3.0 eV).

The binding energy of the  $\text{Au}(4f_{7/2})$  (Fig 5.18) signal is rather constant at 83.4 eV after acrylic acid adsorption and desorption; however annealing to 500 K resulted in reduction of the  $\text{Au}(4f_{7/2})$  intensity possibly due to sintering of the particles.

In conclusion, acrylic acid is adsorbed on the Au modified iron oxide surface (295 K). Carboxylate formation and ethylene adsorption were found at this surface similar to the reaction on thin and thick iron oxide films. Acrylic acid desorption (at 500 K) indicate that some C-C remains though  $\text{CO}_2$  has left. Surface concentrations

and C(1s) and O(1s) binding energies on the Au supported oxide surface and thin and thick iron oxide films are similar. Therefore, Au nanoparticles do not enhance acid adsorption on Au modified oxide surface.

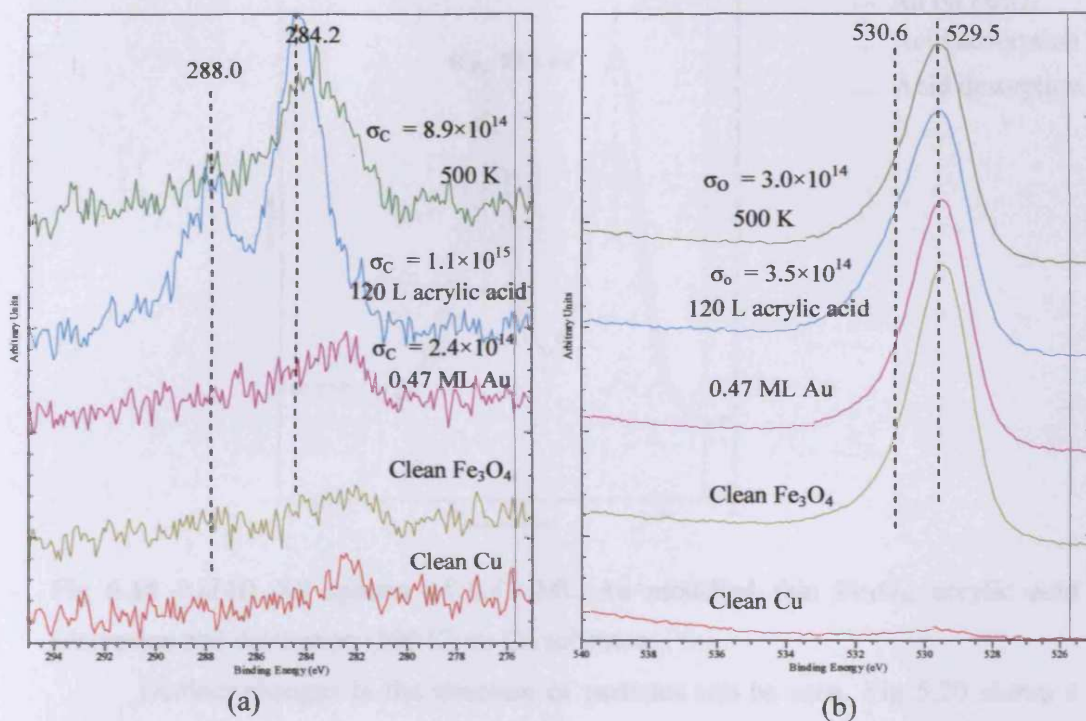


**Fig 5.17** (a) C(1s) and (b) O(1s) XP spectra of clean Cu, Fe<sub>3</sub>O<sub>4</sub>, 0.47 ML Au modified thin iron oxide surface, acrylic acid adsorption and desorption at 500 K on a Cu substrate, respectively.

#### 5.4.2 Reaction of acrylic acid on thick iron oxide supported Au nanoparticles

Exposure of a 0.4 ML Au modified 14 Å thick iron oxide film to 120 L acrylic acid resulted in the XP spectra shown in Fig 5.19. Before acid dosing, the C(1s) signal at binding energy 283.9 eV represents impurities and after dosing the additional C(1s) peaks are obtained at binding energies of 284.1 and 288.1 eV (3.1: 1.5) while a small O(1s) shoulder is obtained at binding energy of 530.2 eV. The reason for that observed C ratio might be CO<sub>2</sub> formation and desorption. The surface concentration of C after acrylic acid exposure is  $1.2 \times 10^{15}$  atoms cm<sup>-2</sup>. After heating to 500 K, the C(1s) components decrease in intensity while the O(1s) intensity seems to be

unchanged. The broadened C(1s) peak remaining indicates at least 2 species at a binding energy of around 284 eV on the surface.

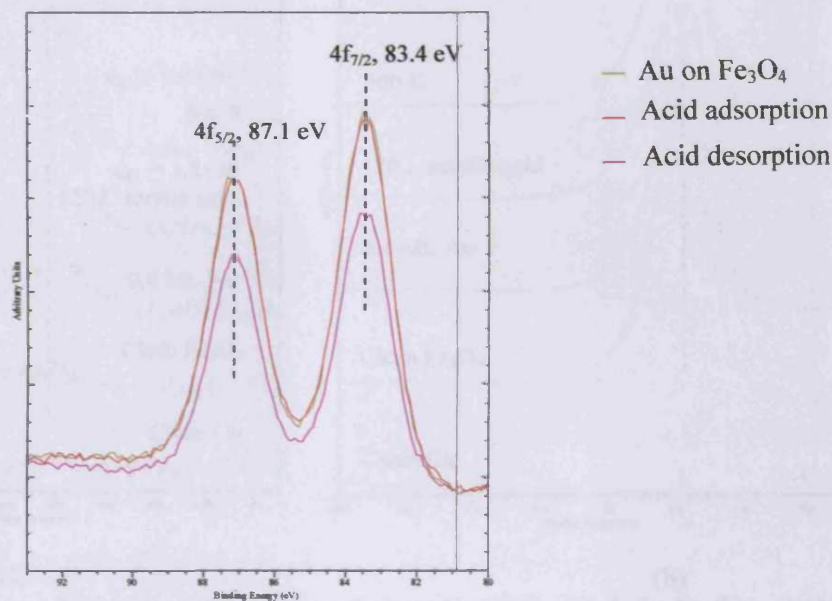


**Fig 5.18** Au(4f) XP spectra of 0.47 ML Au modified thin  $\text{Fe}_3\text{O}_4$ , acrylic acid adsorption and desorption (500 K) on Cu substrate.

Distinct changes in the structure of particles can be seen. Fig 5.20 shows a large surface before and after exposure of Au modified iron oxide to acrylic acid.

Fig 5.21 (b) z-image and (c) current image show a closer picture at the step edges of the modified oxide surface. Small round structures are on the top of distorted Au nanoparticles. Some Au nanoparticles have 2-3 round structures on the top suggesting adsorbed acrylic acid. 3 D images of the sample surface are also shown in Fig 5.21(d) which demonstrates more clearly Au nanoparticles are involved in acrylic acid adsorption.

Au nanoparticles distribute around the iron oxide surface. Some areas are fully covered by Au nanoparticles while elsewhere they are located only on the edge of oxide areas. Interestingly many Au nanoparticles are arranged in straight lines e.g. in Fig 5.22(a). The surface underneath those Au nanoparticles would be iron oxide strips, which would direct the Au nanoparticles growth. Fig 5.22(b) shows distorted Au nanoparticles and acrylic acid clusters inserting between Au clusters and on the edge of big step. The small round structures are similar to those seen on the thin iron oxide with the same size and assigned to acrylic acid clusters.



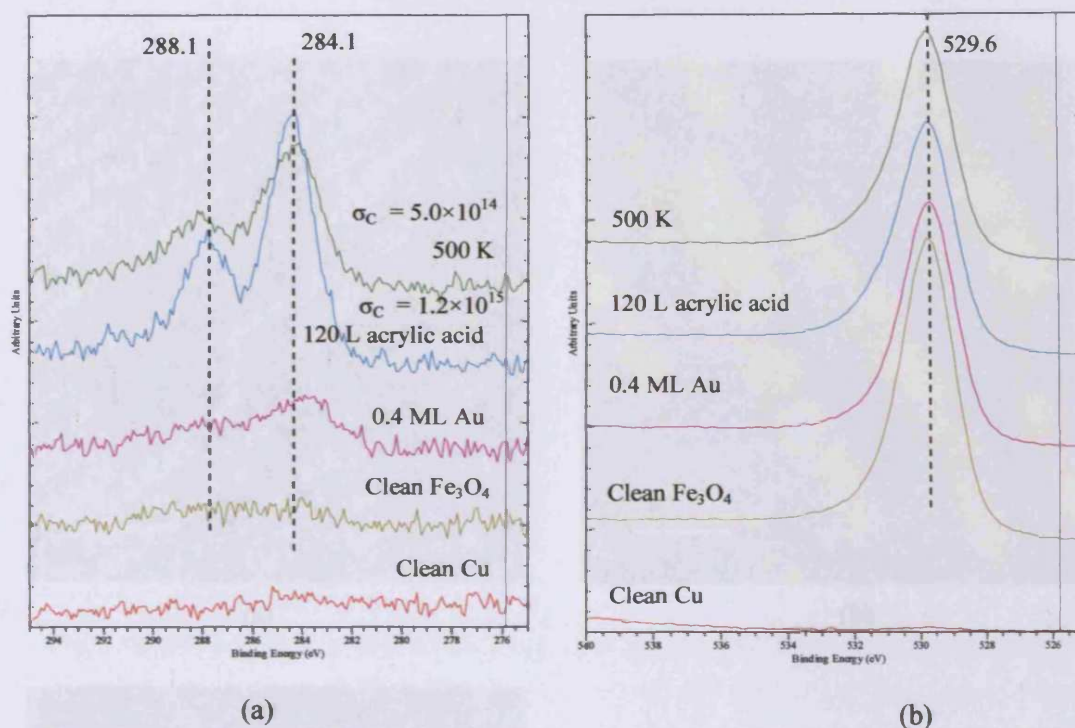


**Fig 5.19** (a) C(1s) and (b) O(1s) XP spectra of clean Cu(100), 14 Å Fe<sub>3</sub>O<sub>4</sub> film, 0.40 ML Au modified iron oxide surface, acrylic acid adsorption and desorption at 500 K, respectively.

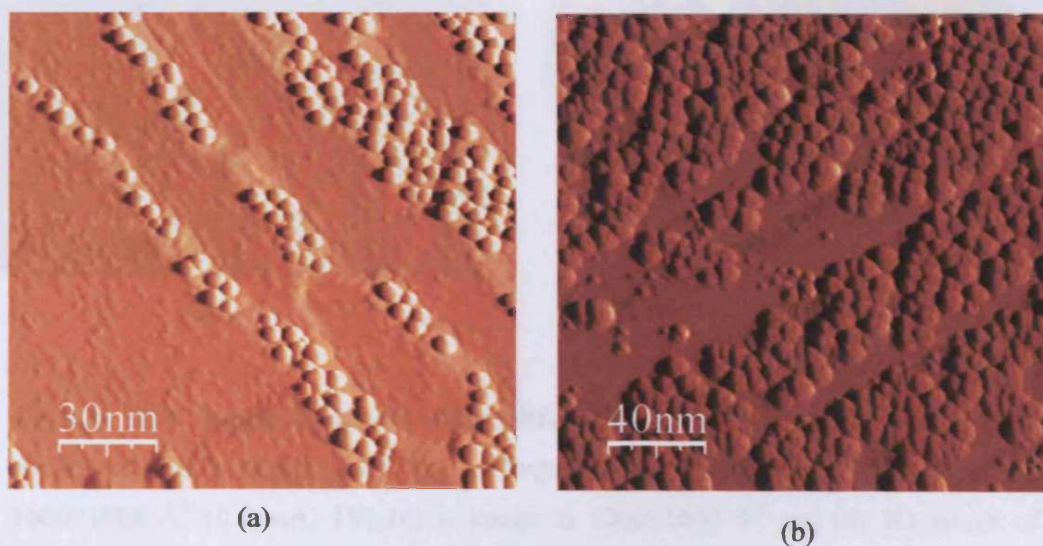


**Fig 5.20** The current image of Au modified iron oxide surface (a) before acrylic acid adsorption (1500×1500 Å<sup>2</sup>) (1 nA, 1V) (b) after acrylic acid adsorption (2000×2000 Å<sup>2</sup>) (0.9 nA, 1V).

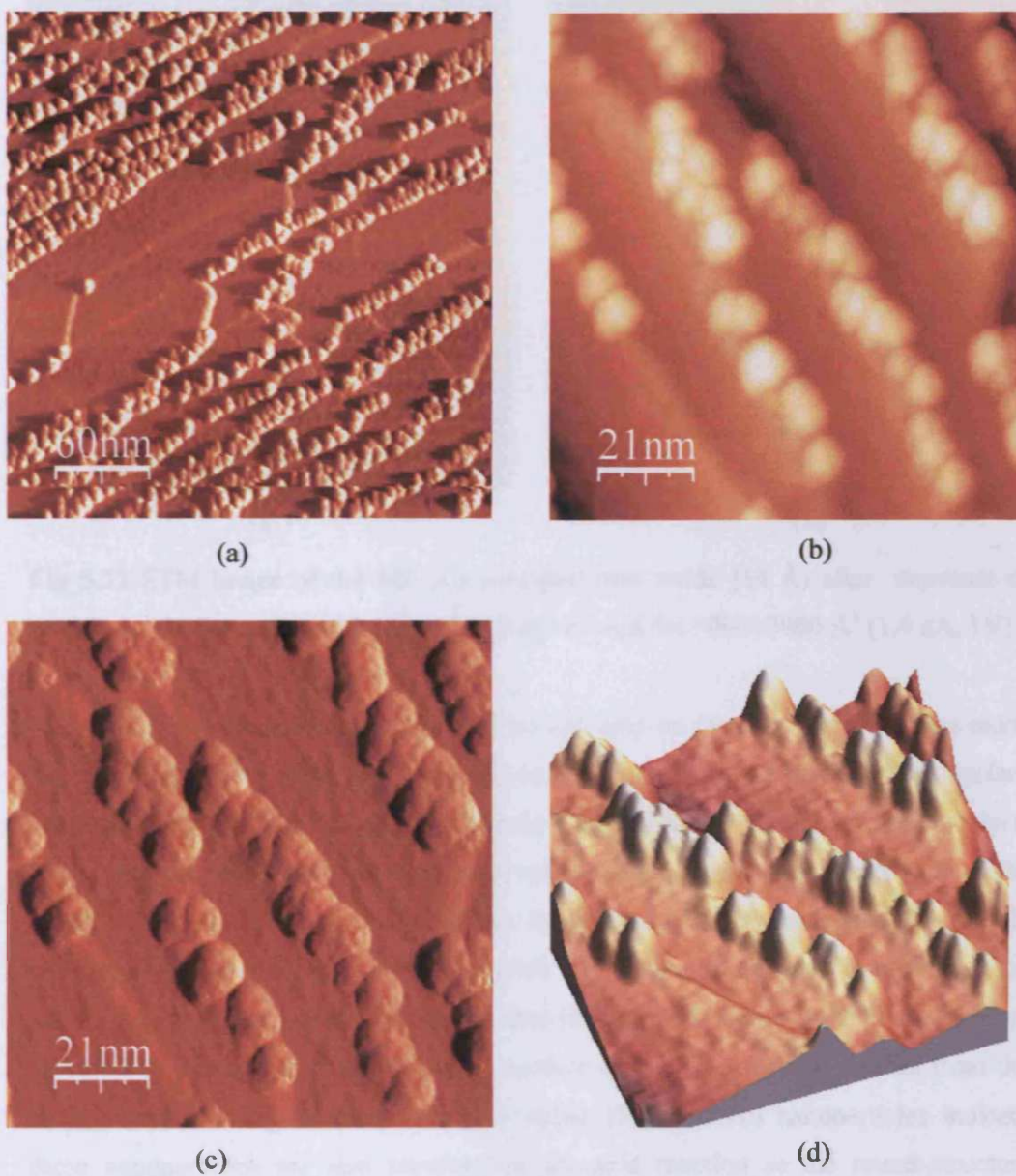


**Fig 5.21** STM images of 0.4 ML Au modified iron oxide ( $14 \text{ \AA}$ ) after exposure the surface to 120 L acrylic acid (a) in large area  $3000 \times 3000 \text{ \AA}^2$  (b) z-image in  $1000 \times 1000 \text{ \AA}^2$  (0.9, nA, 1V) (c) i- image in  $1000 \times 1000 \text{ \AA}^2$  and (d) 3D image of surface in (b).



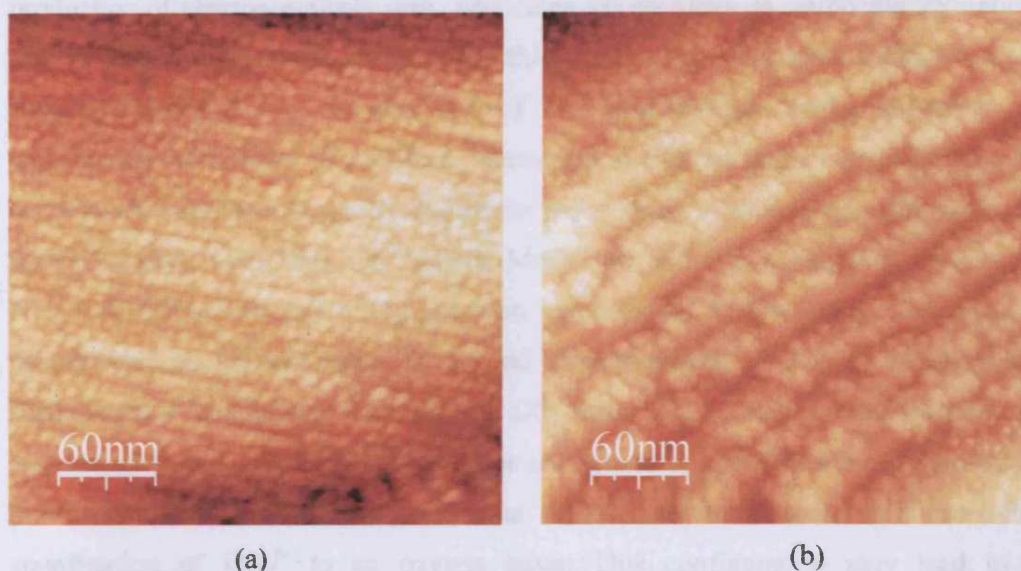


**Fig 5.22** STM image of 0.4 ML Au modified iron oxide (14 Å) after exposure of sample to 120 L acrylic acid (a)  $3000 \times 3000 \text{ Å}^2$  and (b)  $3000 \times 3000 \text{ Å}^2$  (1.4 nA, 1V).

In conclusion, the adsorption of acrylic acid on the thin and thick iron oxide and Au modified thin and thick iron oxides show similar carbon surface concentrations (by XPS) suggesting that the reaction on the surface of those catalysts is possibly the same. However, there are differences in the thermal desorption of the adsorbed acid: at the thick oxide and Au modified thin oxide desorption was mainly  $\text{CO}_2$  while at the surface of thin iron oxide and Au modified thick iron oxide some carboxylate is left on the surface. It was also found that O atoms in the thick oxide are involved in the acid adsorption on the surface and form a leaving species from the oxide films resulting in the destructive strips. Distorted Au nanoparticles indicate these nanoparticles are also involved in the acid reaction as the round structure adsorbed on the top of Au clusters in STM image. Note that the Au oxidation state before and after reaction does not change.

## 5.5 Reaction of iron oxide and Au modified iron oxide surfaces with $\text{CO}_2$

### 5.5.1 Introduction and literature review

$\text{CO}_2$  is used mainly in 4 industrial processes [15] :  $\text{CO}_2$  interaction with (1)  $\text{NH}_3$  leading to the nitrogen containing nutrient, urea; (2) salicylic acid in the

production of pharmaceuticals and pesticides, (3) epoxides in carbonate formation and (4) methanol synthesis in water gas-shift reaction. This has led to interest in CO<sub>2</sub> surface chemistry. CO<sub>2</sub> is also one of the most suitable acidic molecules to characterize the basicity of a surface. Interaction of CO<sub>2</sub> on single crystal surfaces of metal oxide substrates has been studied for many years. A variety of substrates such as BaO (poly), CaO(100), Cr<sub>2</sub>O<sub>3</sub>(111), MnO(100) and (111), Na<sub>2</sub>(100) and (111), NiO(100), TiO<sub>2</sub>(110) and ZnO have been investigated. At low temperature CO<sub>2</sub> is physisorbed on all substrates. In general chemisorption of CO<sub>2</sub> on metal oxide surfaces leads to carbonate formation but CO<sub>2</sub> formed CO<sub>2</sub><sup>-</sup> (carboxylate structure) on a ZnO surface [15]. Carboxylate structures are formed by coordination of a bent CO<sub>2</sub><sup>δ-</sup> molecule to a metal, whereas carbonate (CO<sub>3</sub><sup>2-</sup>) structures could be formed by coordination of CO<sub>2</sub><sup>δ-</sup> to an oxygen atom. This configuration may lead to a monodentate carbonate; however, it has not been confirmed yet. Kuhlenbeck et al [16] have found carbonate formation at low temperature by bidentate coordination for CO<sub>2</sub> adsorption on Cr<sub>2</sub>O<sub>3</sub>(111). This carbonate forms at 100 K and is stable above room temperature. At above room temperature, CO<sub>2</sub> is chemically adsorbed at the surface defect sites of alkaline earth oxide and forms carbonate (CO<sub>3</sub>). Fukuda et al [17] stated that mono- and bidentate carbonate are formed from CO<sub>2</sub> adsorption on MgO at room temperature. Idriss et al [18] reported that carbonate formation does not only reflect the titration of surface Lewis base sites but also the ability of a surface to share or donate oxygen atoms to adsorbates. Moreover, cations on metal oxide surfaces should be considered especially for bidentate carbonate formation.

There has been discussion about the chemisorption of CO<sub>2</sub> on Cu surface which is insignificant at room temperature and even pressures up to 5 atm; however, partially adsorbed O on a Cu surface will react with high pressures of CO<sub>2</sub> to form carbonate [19]. XPS spectra show O(1s) and C(1s) binding energy at 530.8 and 288.2 eV indicating carbonate formation. Moreover, it was found that the use of CO<sub>2</sub>-rich CO<sub>2</sub>-O<sub>2</sub> mixtures also give rise to carbonate formation. The mixture is another promising target for carbonate formation on prepared iron oxide systems.

In the present work, exposure of iron oxide and Au modified iron oxide films on Cu(100) to CO<sub>2</sub> rich CO<sub>2</sub>-O<sub>2</sub> mixtures were studied. The formation of carbonate compound species on oxide and modified oxide surface was investigated by XPS, LEED and STM.

### 5.5.2 Experimental details

Oxide films were prepared according to the recipe described in Chapter 3. In brief, Fe is evaporated onto Cu(100) single crystal at 300 K and subsequently oxidized at  $10^{-6}$  mbar of  $O_2$  at 850 K.

Au particles were deposited on iron oxide film by passing current through the Mo filament wire to heat the Au drop.

At a back ground pressures of less than  $5.0 \times 10^{-9}$  mbar, exposures of the sample to mixtures of  $CO_2$  rich  $CO_2$ - $O_2$  mixture (ratio 3-10 :1) were performed at the pressure  $1 \times 10^{-6}$  mbar at 295 K.  $CO_2$  (99.999%) and  $O_2$  (99.999%) are from gas cylinder. The gas was introduced into P chamber and controlled by a leak valve connected to the gas line. The  $CO_2$  and  $O_2$  gas were mixed in the gas line the composition checked by mass spectrometer. The ratio of the mixture was determined by the intensities of peaks the in the mass spectra at 44 ( $CO_2$ ) and 32 ( $O_2$ ) amu. The ionization probabilities of  $CO_2$  and  $O_2$  are 1.4 and 1.0 respectively.

The sample chemical composition was examined using X-ray photoelectron spectroscopy followed by low-electron diffraction (LEED) and scanning tunneling microscopy (STM) for surface structure.

### 5.5.3 Results and discussion

3 different experiments will be discussed in this section. The reaction of thick iron oxide, regenerated thick iron oxide and iron oxide in the presence of Au nanoparticles with  $CO_2$  rich  $CO_2$ - $O_2$  mixtures. The regenerated iron oxide films were annealed to desorb carbonate and other adsorbed species and their subsequent reactivity studied without further treatment. All reactions were performed at room temperature. Molecular adsorption can lead to the formation of  $CO_2^-$  and  $CO_3^{2-}$  species [20]. Carbonate, a stable species, is supposed to be the main product on the iron oxide surface.

### 5.5.3.1 Reaction of iron oxide surfaces with CO<sub>2</sub> rich CO<sub>2</sub>-O<sub>2</sub> mixtures

For the reaction of iron oxide films to CO<sub>2</sub>, a small level of carbon contamination (surface concentration,  $2.0 \times 10^{14}$  atom.cm<sup>-2</sup>) was observed on the surface of oxide film before dosing the mixtures. Exposures of the oxide surface (10 Å) to CO<sub>2</sub> were carried out at room temperature. There are no additional C(1s) and O(1s) XP peaks.

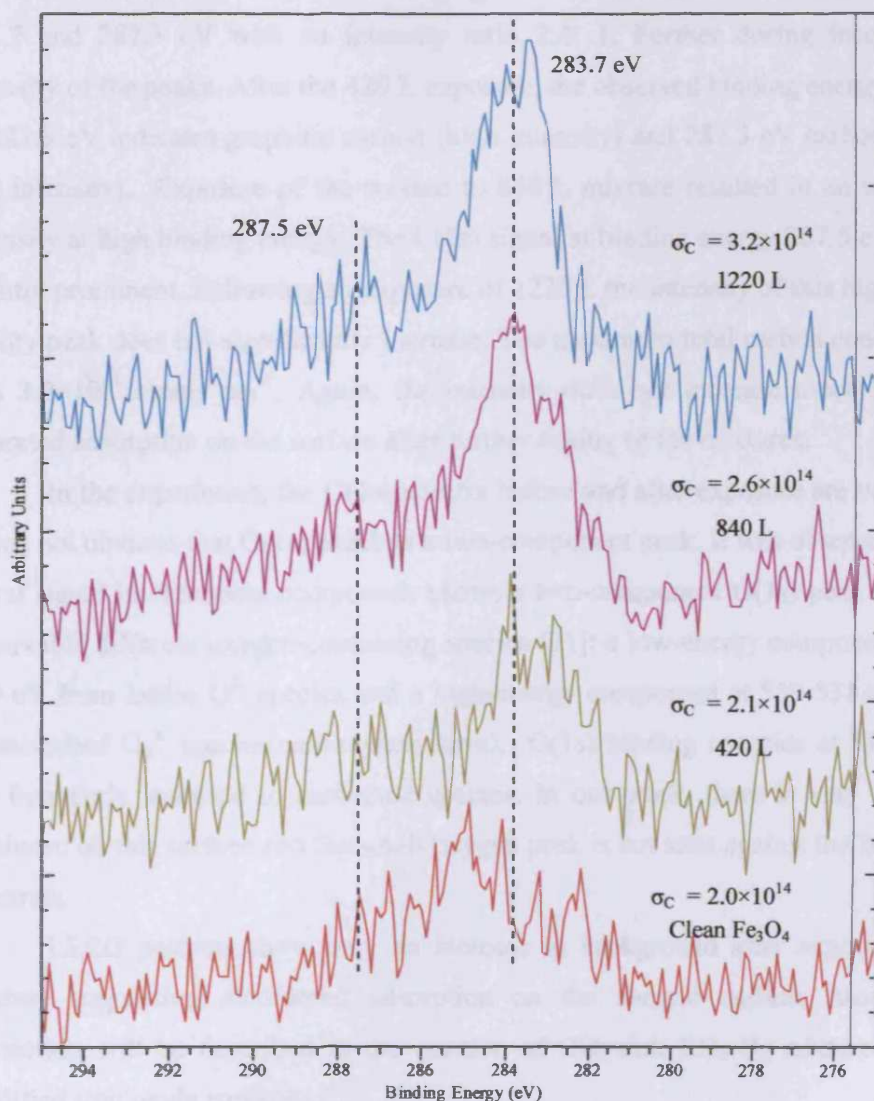


**Fig 5.23** C(1s) XP spectra after exposure of the Fe<sub>3</sub>O<sub>4</sub> surface to CO<sub>2</sub> rich CO<sub>2</sub>-O<sub>2</sub> (~8 : 1) : 420 L, 840 L and 1220 L of the mixture.



Since there is no CO<sub>2</sub> reaction it may be that the prepared iron oxide surface lacks oxygen species for carbonate formation. Therefore, exposure to CO<sub>2</sub> rich CO<sub>2</sub>-O<sub>2</sub> mixtures was an interesting option for studying carbonate formation. Fig 5.23 shows the result of a thick iron oxide surface after dosing the CO<sub>2</sub> rich CO<sub>2</sub>-O<sub>2</sub> mixture.

Carbon atoms in carbonate species should give a C(1s) peak at a binding energy of 286-290 eV. 2 species of C(1s) from carbonate and graphitic carbon resulted in broad carbon signals developing in the C(1s) region at binding energies of 283.7 and 287.3 eV with an intensity ratio 2.4: 1. Further dosing increased the intensity of the peaks. After the 420 L exposure, the observed binding energy of C(1s) at 283.8 eV indicates graphitic carbon (high intensity) and 287.3 eV carbonate (very low intensity). Exposure of the surface to 840 L mixture resulted in an increase in intensity at high binding energy. The C(1s) signal at binding energy 287.5 eV became slightly prominent. Following an exposure of 1220 L the intensity of this high binding energy peak does not significantly increase. The maximum total carbon concentration was  $3.2 \times 10^{14}$  atoms cm<sup>-2</sup>. Again, the intensity does not increase much indicating saturated adsorption on the surface after further dosing of the mixtures.

In the experiment, the O(1s) spectra before and after exposure are unchanged. It was not obvious that O(1s) exhibits a two-component peak. It was observed that the O(1s) signal in carbonate compounds shows a two-component O(1s) peak indicating observable different oxygen-containing species [21]: a low-energy component at 528-529 eV from lattice O<sup>2-</sup> species and a high-energy component at 530-531 eV from a chemisorbed O<sub>2</sub><sup>x-</sup> species(carboxylate form). O(1s) binding energies at 532-533 eV are frequently assigned to carbonate species. In our work, there is very little CO<sub>3</sub> produced on this surface and the small oxygen peak is not seen against the large oxide substrate.

LEED patterns show only an increase in background after exposure to the mixture suggesting disordered adsorption on the sample surface. More LEED discussion will be described in the reaction of CO<sub>2</sub>-rich CO<sub>2</sub>-O<sub>2</sub> mixture with Au modified iron oxide surfaces.

Fig 5.24(a) shows STM images after exposure of the iron oxide surface to the CO<sub>2</sub> rich CO<sub>2</sub>-O<sub>2</sub> mixture. Magnified images are in Fig 5.24(b) and (c).

Bright structures are located around on the top of oxide terrace being possibly both graphitic carbon and some carbonate (as XP spectra confirmed). The square patterns below the bright lumps could be Moire' patterns from the iron oxide surface. Interestingly, the edges of iron oxide have been roughened signifying reaction is occurring here. The line profile of the lumps are  $1 < \text{\AA}$  high indicating the small structures on the surface.

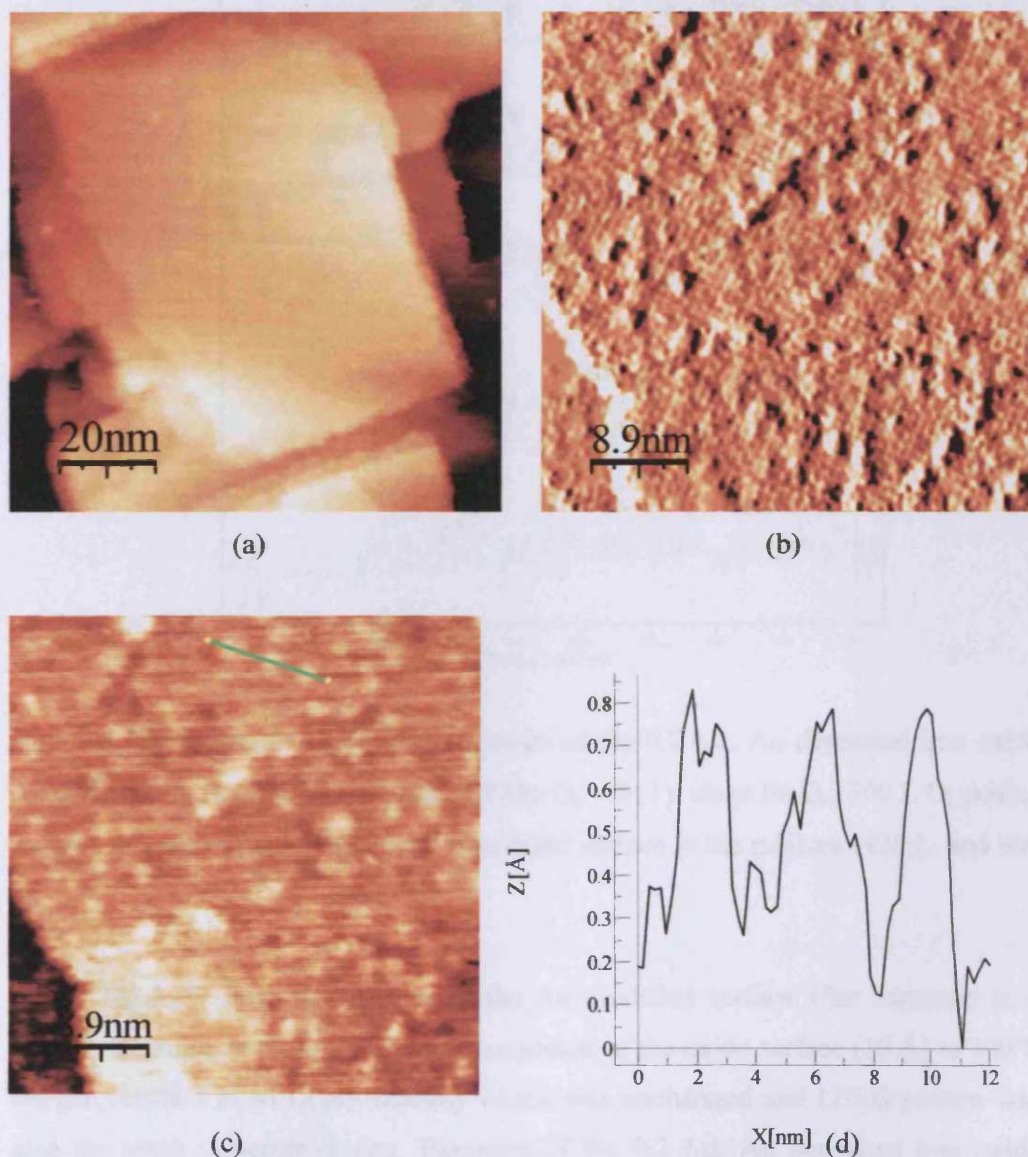


**Fig 5.24** STM image of iron oxide surface after dosing a mixture of  $\text{CO}_2$  rich  $\text{CO}_2\text{-O}_2$ : (a) a large area in  $1000 \times 1000 \text{ nm}^2$  (0.2 nA, -0.7 V), (b) i-image and (c) z-image in  $450 \times 450 \text{ \AA}^2$  (0.3 nA, -0.7 V) and (d) line profile of bright structures.

### 5.5.3.2 Reaction of Au modified iron oxide surface with CO<sub>2</sub> rich CO<sub>2</sub>-O<sub>2</sub> mixtures

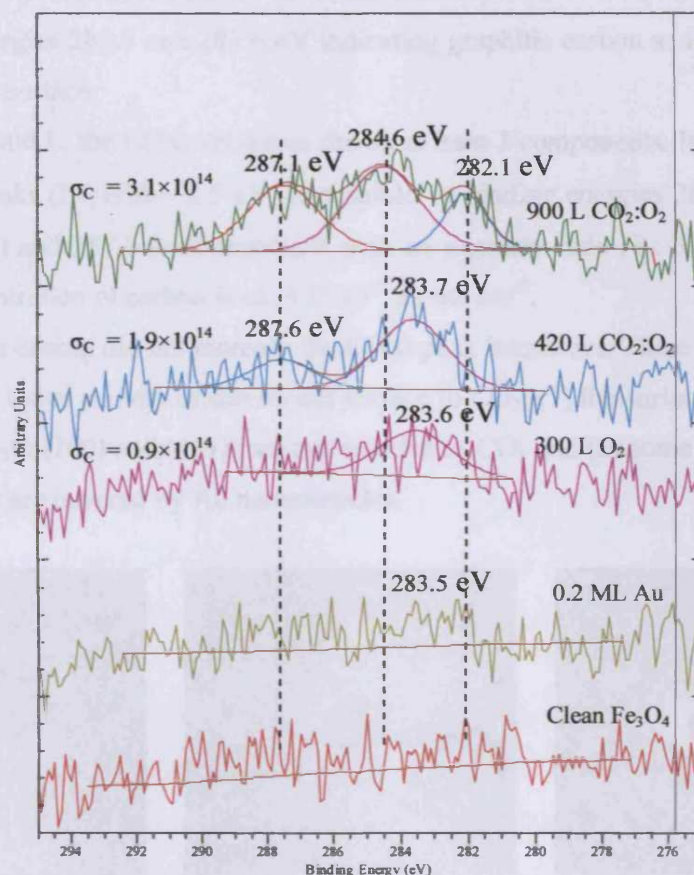


**Fig 5.25** XP spectra of C(1s) after exposure of the 0.2 ML Au deposited iron oxide catalyst to CO<sub>2</sub> rich CO<sub>2</sub> – O<sub>2</sub> mixture (CO<sub>2</sub>: O<sub>2</sub>  $\approx$  8: 1): clean Fe<sub>3</sub>O<sub>4</sub>, 300 L O<sub>2</sub> dosing, after exposure of the Au deposited iron oxide surface to the mixture (420 L and 900 L).

Fig.5.25 shows XP spectra of the Au modified surface after exposure to a CO<sub>2</sub>/O<sub>2</sub> mixture. At room temperature, exposure of the oxide surface (10 Å) to 300 L oxygen resulted in an O(1s) intensity which was unchanged and LEED pattern was also the same as before dosing. Exposure of the 0.2 ML Au deposited iron oxide surface to 300 L of a CO<sub>2</sub>-rich CO<sub>2</sub>-O<sub>2</sub> mixture (CO<sub>2</sub>: O<sub>2</sub>  $\approx$  8 : 1) resulted in a broad carbon signal developing in the C(1s) region. The O(1s) XP signal did not change due



to the dominant contribution of lattice oxygen in the iron oxide thin film. Au(4f<sub>7/2</sub>) signals with binding energy at 83.4 eV before and after reaction are observed.

After exposure to a further 420 L, the intensity of the carbon signal increases at binding energies 283.7 and 287.6 eV indicating graphitic carbon and carbonate are formed on the surface.

After 900 L, the C(1s) spectrum shows at least 3 components. In Fig 5.25, the fitting of 3 peaks (FWHM ~ 2.5 eV) is possible, at binding energies 282.1 (carbide), 284.6 (carbon) and 287.6 (carbonate) eV with an intensity ratio (1 : 5.9 : 3.8). Total surface concentration of carbon is ca.  $3.1 \times 10^{14}$  atoms cm<sup>-2</sup>.

Further dosing did not increase the C(1s) peak intensities. There are possibly 2 factors for the lower activity of this model surface to CO<sub>2</sub>; (1) the surfaces of prepared iron oxide (Fe<sub>3</sub>O<sub>4</sub>(100) and (111)) are not reactive to CO<sub>2</sub> and (2) some active sites of these catalysts are covered by Au nanoparticles.

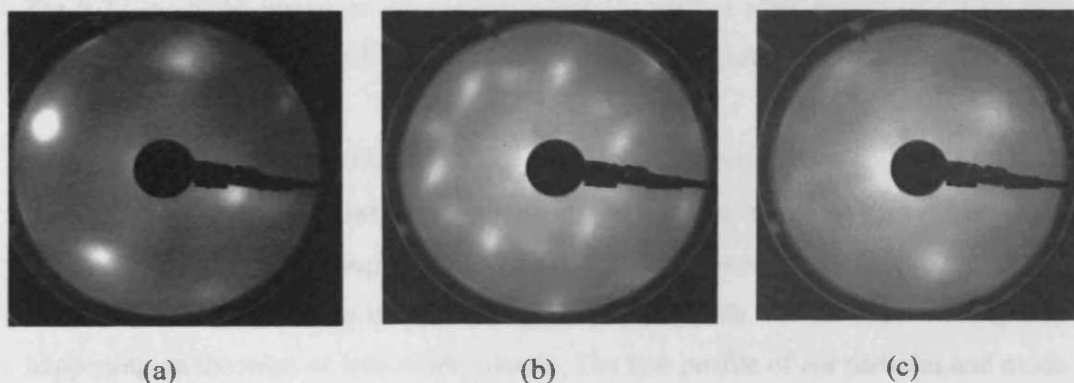


**Fig 5.26** LEED of (a) clean Cu ( $E = 75$  eV) and (b) Au modified iron oxide before and (c) after exposure of the surface to the mixture of CO<sub>2</sub> rich CO<sub>2</sub>-O<sub>2</sub> ( $E = 82$  eV).

LEED patterns obtained before and after exposure of Au modified iron oxide to a CO<sub>2</sub> rich CO<sub>2</sub>-O<sub>2</sub> mixture (Fig 5.26) are similar to those after reaction on the iron oxide surface. Fig 5.26 shows exposure to the mixture degrades the LEED pattern of the surface. There are only blurred spots present in a square unit cell rotated in 45° to the clean Cu lattice. It could be the twin unit cell of the Cu substrate as square unit cell with 2.55 Å on the surface. The disappearance of additional spots for iron oxide explains that the gas mixture reacted with atoms on iron oxide surface.



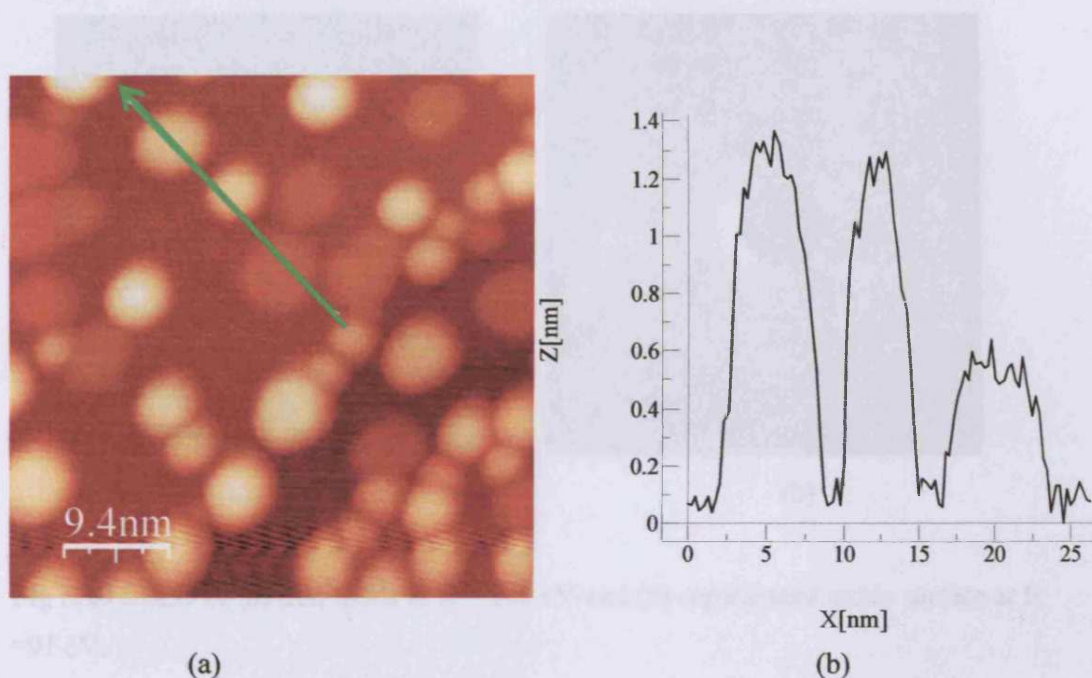


**Fig 5.27** (a) STM image of Au modified sample surface after dosing of a CO<sub>2</sub> rich CO<sub>2</sub>-O<sub>2</sub> mixture (470×470 Å<sup>2</sup>) and (b) line profile of features on the surface.

Fig 5.27 shows STM of the surface after exposure to a CO<sub>2</sub>-rich CO<sub>2</sub>-O<sub>2</sub> mixture. The topography image is similar to the surface of Au modified iron oxide before the reaction, although, oxide hexagonal-like shaped islands become round while the Au nanoparticles are not changed. This suggests that the reaction might be happening on the edge of iron oxide islands. The line profile of Au particles and oxide islands on the surface are similar to the surface before the reaction.

### 5.5.3.3 Reaction of regenerated thick iron oxide surface with CO<sub>2</sub> rich CO<sub>2</sub>-O<sub>2</sub> mixtures

It is of interest to know if the iron oxide catalyst could react with the mixtures again after being first used and the regenerated. Heating the sample in an O<sub>2</sub> atmosphere would be a possible method to regenerate the oxide catalyst to its original state and the carbonate might be desorbed as CO<sub>2</sub>, during oxidation. After treatment of the surface with high temperature oxidation (500 K), the surface was used to study the reaction with the CO<sub>2</sub> rich CO<sub>2</sub>-O<sub>2</sub> mixture.

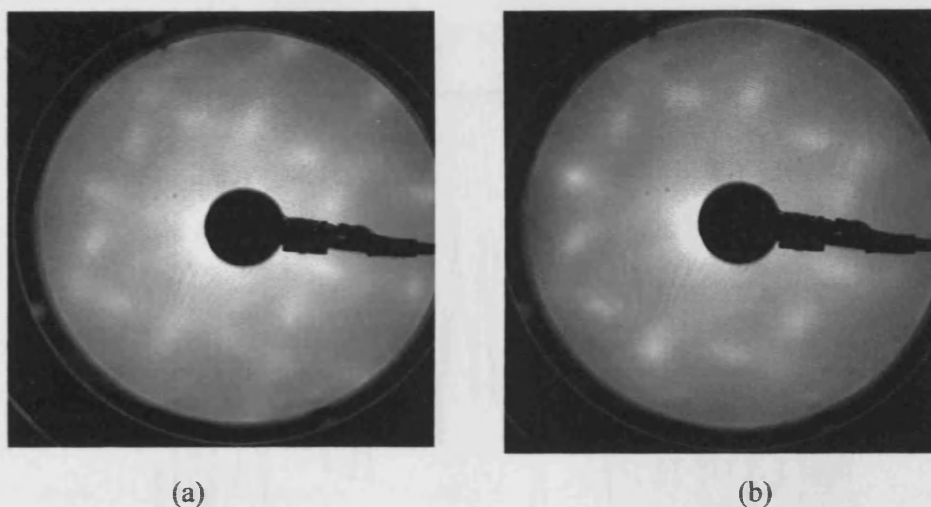


**Fig 5.28** LEED of (a) iron oxide at  $E = 100$  eV and (b) regenerated oxide surface at  $E = 91$  eV.

After an experiment dosing a  $\text{CO}_2$  rich  $\text{O}_2/\text{CO}_2$  mixture, the surface was heated in the presence of  $\text{O}_2$  ( $1 \times 10^{-6}$  mbar) at 500 K for 3 min. The LEED pattern in Fig 5.28 shows that surface of the catalyst could be recovered. The LEED pattern after re-oxidization is similar to that for the 'fresh' oxide surface. However, the reactivity is much less than the freshly-prepared oxide as XPS results in Fig 5.29. The C(1s) signal shows that there was some carbon left after regeneration. The C(1s) signal left after re-oxidizing resulted in a low activity for carbonate formation. It is possible that the carbon shown in Fig 5.29 is more likely to be carbon from the bulk otherwise the LEED pattern from the iron oxide could not have been observed. Carbon in the oxide film might terminate the reaction on the surface. The ratio of Fe to O is about 0.72 indicating iron oxide  $\text{Fe}_3\text{O}_4$ . The surface concentration of C is fairly constant at about  $1 \times 10^{14}$  atoms  $\text{cm}^{-2}$ . It is interesting that regenerated iron oxide surface exhibits a similar LEED pattern to a fresh preparation but it is not as reactive with the mixture. Moreover, there is not even additional C graphite at a C(1s) binding energy of 284 eV after further dosing the mixture.

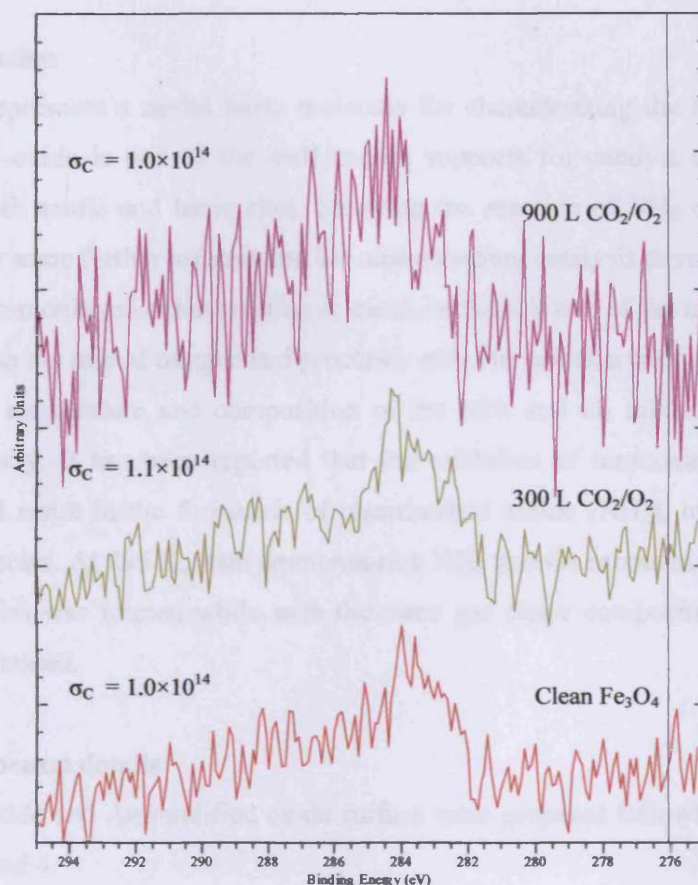


**Fig 5.29** C(1s) XP spectra of the regenerated iron oxide film reacted with  $\text{CO}_2$  rich  $\text{CO}_2\text{-O}_2$  mixture : exposure the surface to 300 L and 900 L of the mixture.

In summary, carbonate formation can be observed on the iron oxide surface ( $\text{Fe}_3\text{O}_4$ ) surface, although in very small quantity. Au deposition enhances the reaction. Studying this reaction at low temperature would be interesting and worthy to understand the reaction mechanism.

## 5.6 Reaction of iron oxide and Au modified iron oxide surfaces with NH<sub>3</sub>

### 5.6.1 Introduction

NH<sub>3</sub> represents a useful basic molecule for characterizing the acidity of the surfaces. Iron oxide is one of the well-known supports for catalyst as its surface consists of both acidic and basic sites. Studying the reaction of NH<sub>3</sub> on iron oxide would provide some further information for understanding catalysis development.

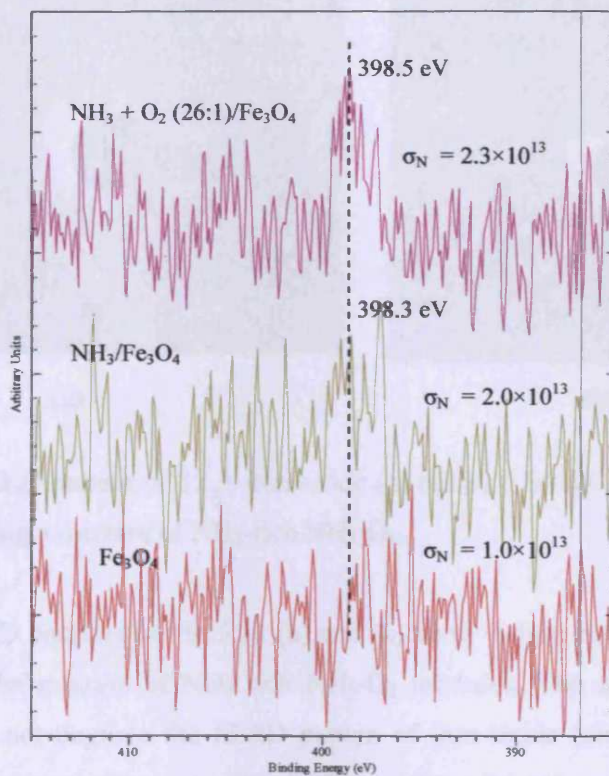
The ammonia oxidation reaction at metal surfaces is one of the model systems used to develop the role of oxygen and precursor states in reaction pathways [22]. The conditions of temperature and composition of the NH<sub>3</sub> and O<sub>2</sub> mixtures direct the reaction pathway. It has been reported that the oxidation of ammonia on Cu(110) surfaces could result in the formation of chemisorbed amide (NH<sub>2</sub>), imide (NH) or nitride (N) species. At 295 K, with ammonia-rich NH<sub>3</sub> and O<sub>2</sub> mixtures, a monolayer of imide species was formed while with the same gas phase composition at 475 K, nitride was obtained.

### 5.6.2 Experimental details

Iron oxide and Au modified oxide surface were prepared following the recipe in Chapter 3 and 4.

At background pressures of less than  $5.0 \times 10^{-9}$  mbar, exposures of sample to mixtures of NH<sub>3</sub> rich NH<sub>3</sub>-O<sub>2</sub> (ratio 5-15 :1) were performed at the pressure  $1 \times 10^{-6}$  mbar at 300 K. NH<sub>3</sub> (99.999%) and O<sub>2</sub> (99.999%) are from gas cylinders. The gas mixtures were introduced into the P chamber and controlled by a leak valve connected to the gas line. The NH<sub>3</sub> and O<sub>2</sub> gas were mixed in the gas line and the composition checked by a mass spectrometer. The ratio of the mixture was determined by the intensities of peaks in the mass spectra at 17 (NH<sub>3</sub>) and 32 (O<sub>2</sub>) amu. The ionization probabilities of NH<sub>3</sub> and O<sub>2</sub> are 1.3 and 1.0, respectively.



5.6.3 Reaction of iron oxide with  $\text{NH}_3$ -rich  $\text{NH}_3$ - $\text{O}_2$  mixtures

**Fig 5.30** N(1s) spectra of the surface of the 12 Å iron oxide and after exposures of the sample to  $\text{NH}_3$  (200 L) and a  $\text{NH}_3$ - $\text{O}_2$  mixture (300L).

Successive exposures of the 12 Å iron oxide surface to  $\text{NH}_3$  (200 L) and then  $\text{NH}_3$  rich  $\text{NH}_3$ - $\text{O}_2$  mixture ( $\text{NH}_3$  :  $\text{O}_2$  with ratio 26 : 1, 200 L) at room temperature were made. The surface concentration of N(1s) species of both experiments was significant ( $2.3 \times 10^{13}$  atoms  $\text{cm}^{-2}$ ) at binding energies of 398.3 and 398.5 eV ( $\text{NH}_2$  or  $\text{NH}$  molecule) (Fig 5.30). It has been reported in previous work [23, 24] that  $\text{NO}_{\text{ad}}$ ,  $\text{NH}_3_{\text{ad}}$ ,  $\text{NH}_{\text{ad}}$  and  $\text{N}_{\text{ad}}$  have binding energies of 400.0, 399.0, 397.5 and 396.6 eV respectively. Moreover, it was suggested that  $\text{NH}_2_{\text{ad}}$  is a very unstable intermediate that decomposes instantly after formation on the way to  $\text{NH}_{\text{ad}}$ . The N(1s) spectra could prove that  $\text{NH}_2$  or  $\text{NH}$  can be adsorbed on the surface of iron oxide. Surface reaction with nitrogen indicates that the iron oxide surface are partially acidic and basic (react with  $\text{CO}_2$ (acid) in the previous topic).

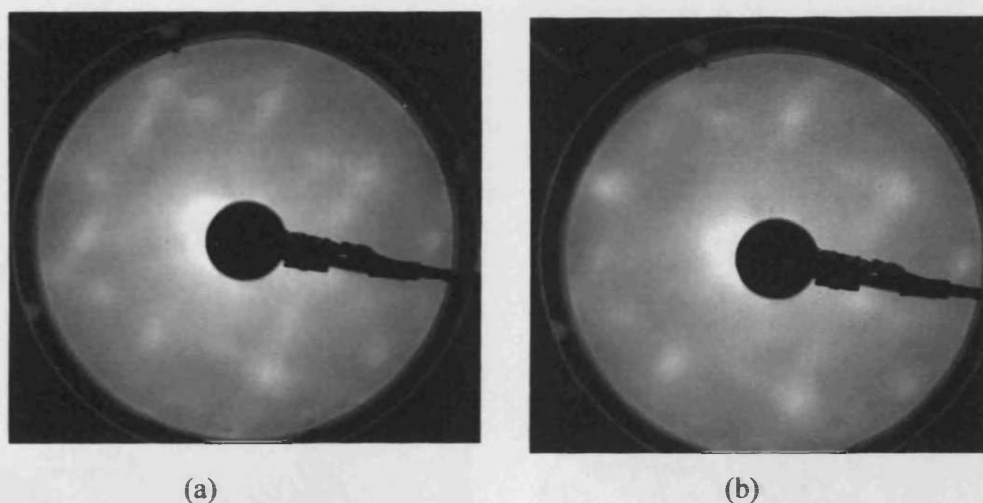
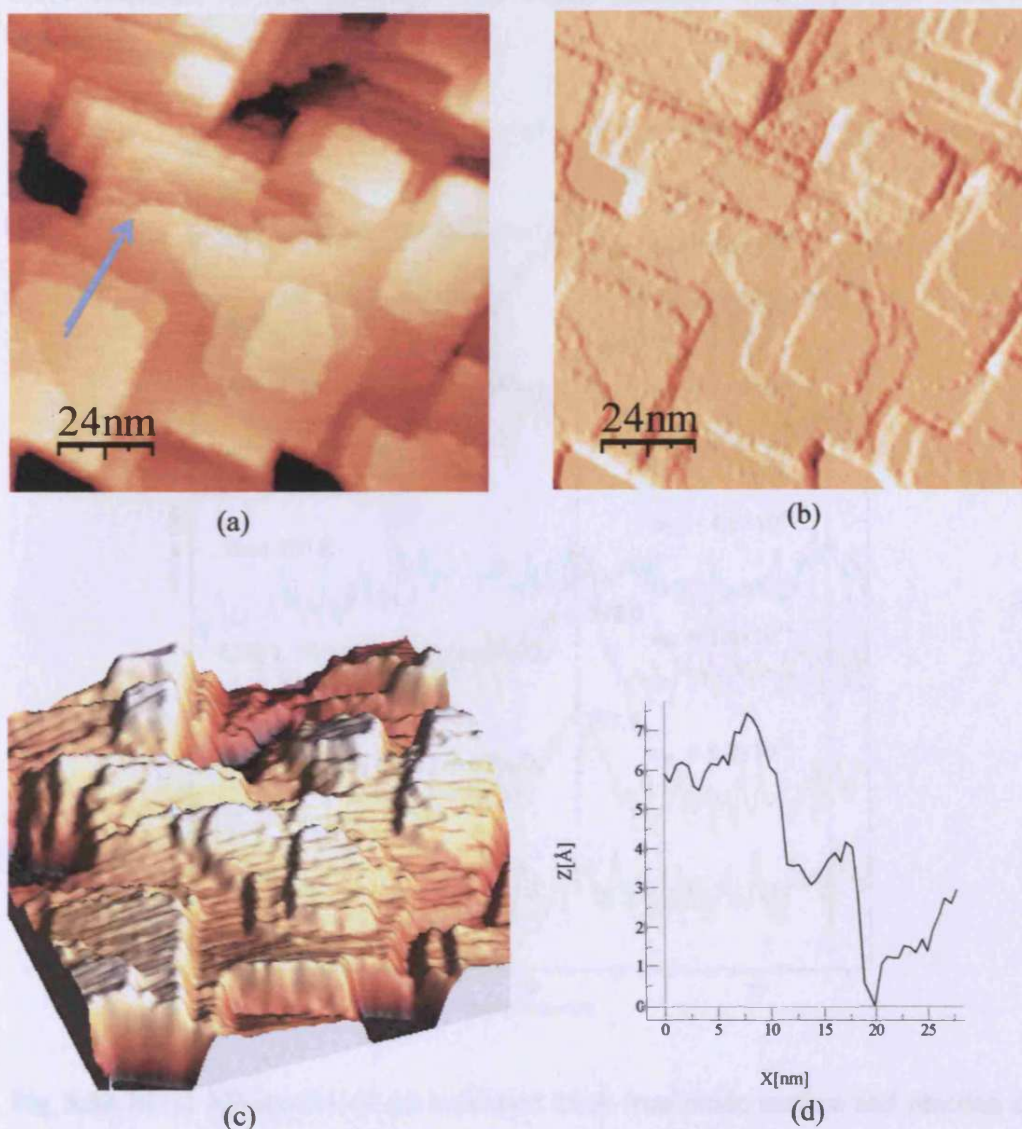


Fig 5.31 LEED pattern of 12 Å iron oxide (a) before (  $E = 83$  eV ) and (b) after (  $E = 79$  eV ) dosing a mixture of NH<sub>3</sub>-rich NH<sub>3</sub>-O<sub>2</sub>.

LEED patterns in Fig 5.31 (a) and (b) show before and after exposure of the sample to the mixture of NH<sub>3</sub> rich NH<sub>3</sub>-O<sub>2</sub> mixtures. The atoms adsorbed on the surface did not degrade the LEED pattern of iron oxide (unlike the reaction with CO<sub>2</sub>). This shows either an epitaxial N species adsorption on iron oxide catalyst model or the small N compound species is not high enough to damage the pattern of iron oxide LEED pattern.

The STM images in Fig 5.32(a) show rough terrace edges of iron oxide islands in the wide range image. The current image and 3D images (Fig 5.32(b) and (c)) shown are clearly the rough edges of square terrace 4 Å high. The 4 Å high square terraces indicate iron oxide Fe<sub>3</sub>O<sub>4</sub>(100) termination. Interestingly, the edges of the flat oxide islands have developed rims up to ~1.5 Å high above the plane. This indicates that the step edge of the oxide is more reactive than the terraces. However, the surfaces of the big terraces are also roughened indicating that reaction has also taken place. Unfortunately, no atomically resolved image was acquired.



**Fig 5.32** STM image of iron oxide surface after exposure the surface to a  $\text{NH}_3$ -rich mixture of  $\text{NH}_3$  and  $\text{O}_2$  : (a) z-image, (b) i-image, (c) 3-D image in  $1200 \times 1200 \text{ \AA}^2$  and (d) line profile in image (a).



#### 5.6.4 Reaction of Au modified iron oxide surfaces with $\text{NH}_3$ -rich $\text{NH}_3$ - $\text{O}_2$ mixtures

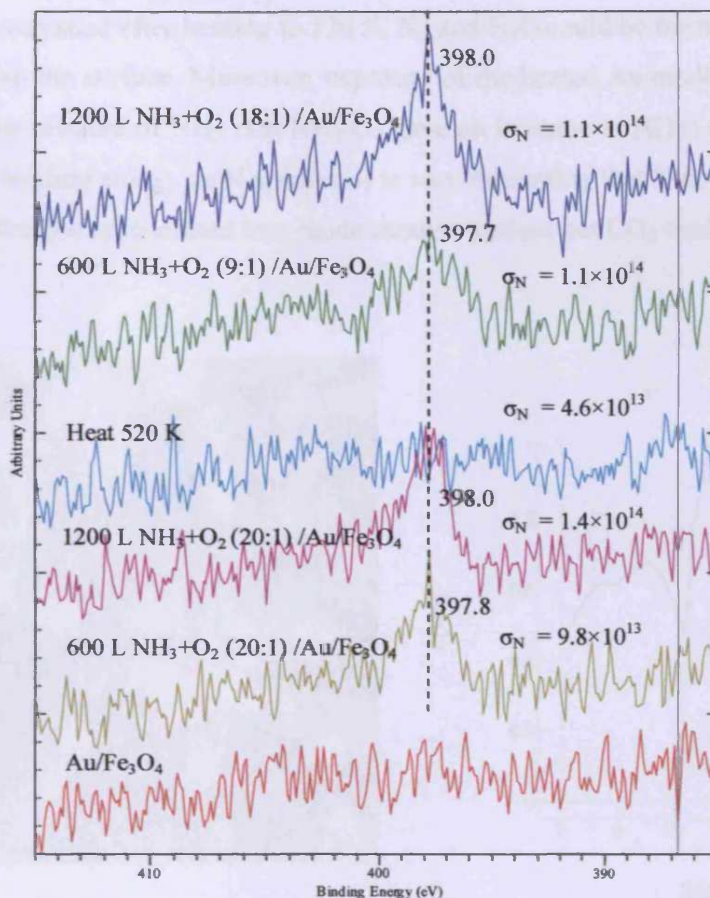


**Fig 5.33** N(1s) XP spectra of Au modified 14 Å iron oxide surface and reaction of oxide surface with  $\text{NH}_3$  rich  $\text{NH}_3$ - $\text{O}_2$  mixtures.

0.1 ML Au deposited on an 12 Å iron oxide films was used to study  $\text{NH}_3$  adsorption and reaction. Fig 5.33 shows the N(1s) spectra peaks with binding energies of ca. 397.8–398.0 eV were obtained indicating either  $\text{NH}_3$ ,  $\text{NH}_2$  or  $\text{NH}$  compounds located on the surface. Au(4f<sub>7/2</sub>) signals are observed at a binding energy of 83.4 eV before and after reaction. The carbon surface concentration is about  $2 \times 10^{14}$  atoms  $\text{cm}^{-2}$  at a binding energy of 284 eV (graphitic carbon) indicating impurities on the surface.



The maximum nitrogen surface concentration is about  $1.1 \times 10^{14}$  atoms  $\text{cm}^{-2}$ . The N(1s) spectra show that the Au modified iron oxide surface is more reactive than the iron oxide surface. The peaks are more prominent as depicted in Fig 5.33. N compounds vanished after heating to 520 K.  $\text{N}_2$  and  $\text{H}_2\text{O}$  could be the main desorption products from the surface. Moreover, exposure of the heated Au modified iron oxide surface to the mixture of  $\text{NH}_3$  rich  $\text{NH}_3\text{-O}_2$  gave an increase in N(1s) signal intensity at the same binding energy as N species. It is very interesting that N compounds could be adsorbed on the regenerated iron oxide catalyst surface but  $\text{CO}_2$  could not.

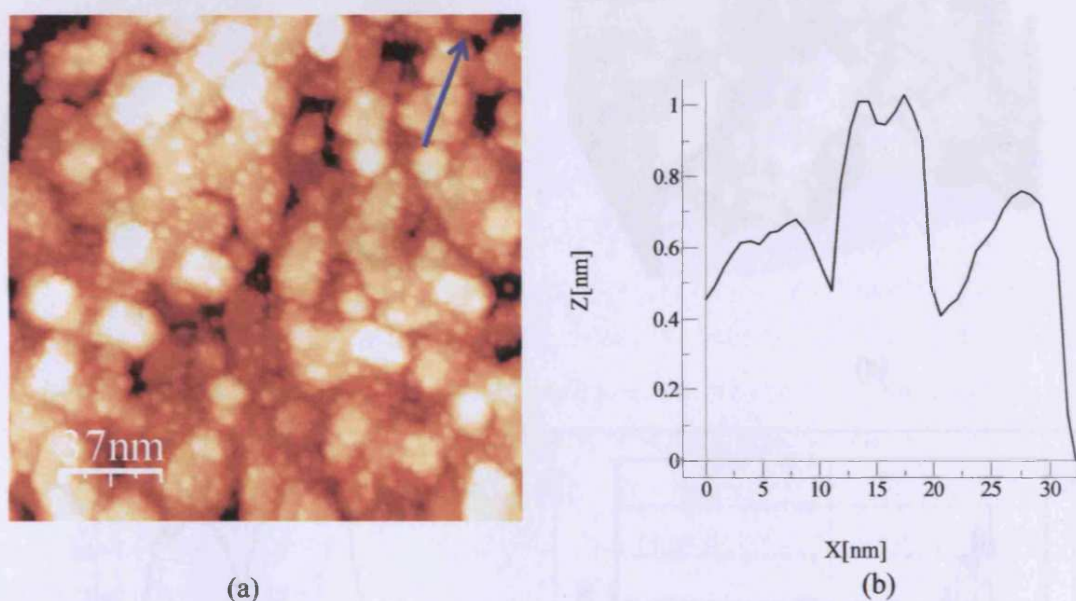


**Fig 5.34** STM image of Au modified iron oxide surface after dosing the surface to  $\text{NH}_3$  rich  $\text{NH}_3\text{-O}_2$  mixture ( $1800 \times 1800 \text{ \AA}^2$ ).

The STM image in Fig 5.34(a) was acquired after exposure of the Au modified sample to the  $\text{NH}_3$  rich  $\text{NH}_3\text{-O}_2$  mixture. Interestingly, a reduction of the height of Au nanoparticles height (less than 6–8 Å in Fig 5.34(b)) was observed. It could be that the tunnelling characteristics have changed due to adsorption on the Au clusters involved in the reaction; however  $\text{NH}_x$  adsorption is unlikely on Au, and an alternative explanation is that for adsorption on the iron oxide surface has modified its imaging characteristics. The surface of the iron oxide terraces are covered by Au clusters, and therefore it is hard to see the structure change of oxide surface.

Fig 5.35(a) shows a magnified image of the sample after exposure of Au deposited iron oxide to the mixtures. The 3D image in Fig 5.35(b) shows a noticeable topography of surface. The Au clusters are 6 Å high in Fig 5.35(c) indicating that Au shapes were contracted by the reaction on the surface or a changed in tunneling current.

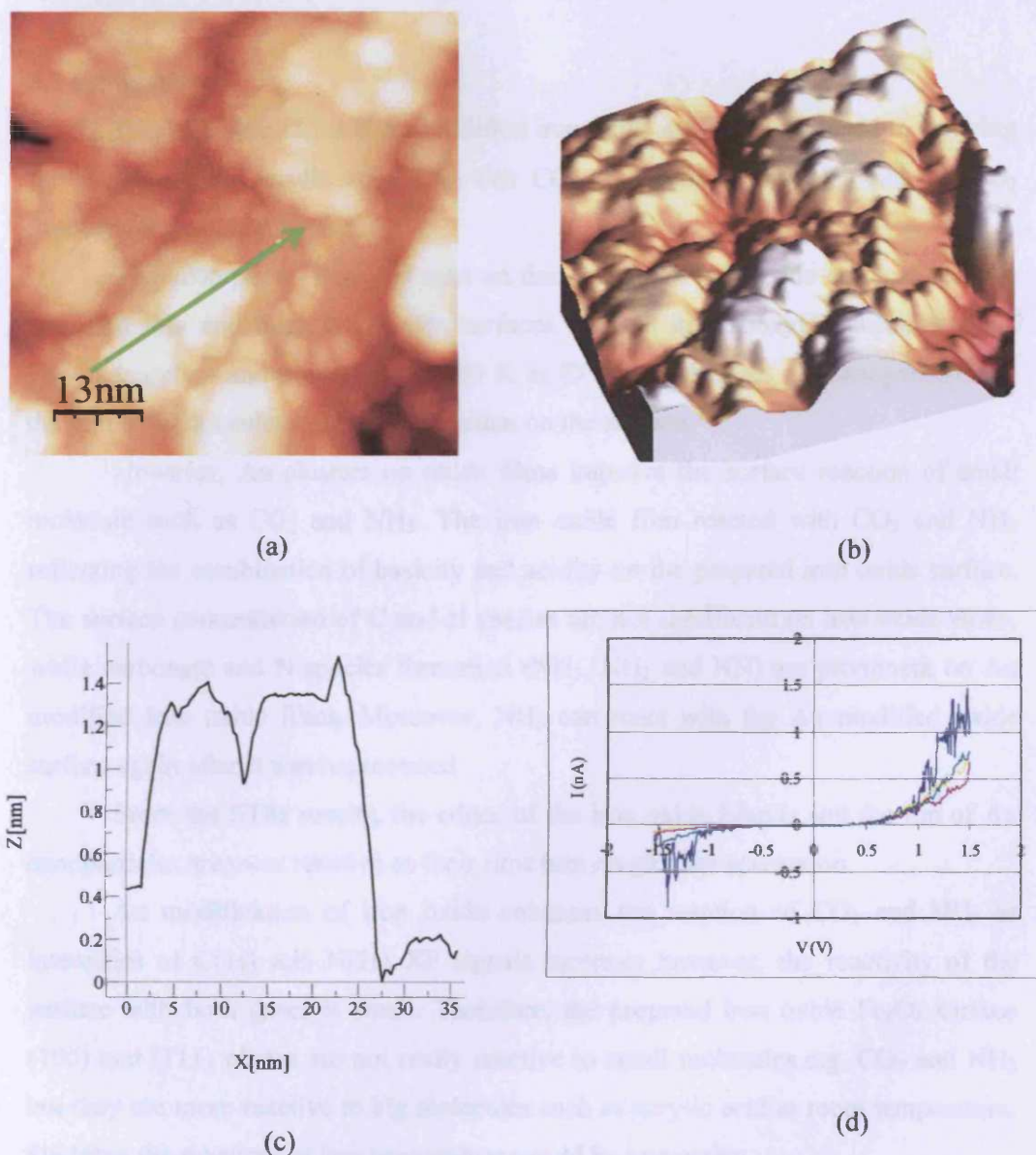


**Fig 5.35** (a) STM image and (b) 3 D image of Au deposited iron oxide surface exposed to  $\text{NH}_3$  rich  $\text{NH}_3\text{-O}_2$  mixture ( $640 \times 640 \text{ \AA}^2$ ), (c) line profile of structure in (a) and (d) IV curve of Au modified iron oxide surface after the mixture dosing.

Au nanoparticles were involved in the reaction. The IV curve still shows the semimetal behavior of Au nanoparticles with band gap of 1.0 eV.

In conclusion, the formation of N species was observed on iron oxide and Au modified iron oxide surfaces. Au nanoparticles enhance the number of N species formed on the iron oxide surface. The LEED pattern of the oxide was not destroyed by N species adsorption.

## 5.7 Conclusions

Iron oxide( $\text{Fe}_3\text{O}_4$ ) and Au modified iron oxide surfaces were used to studying the reaction with acrylic acid,  $\text{CO}_2$ -rich  $\text{CO}_2$ - $\text{O}_2$  mixtures and  $\text{NH}_3$ -rich  $\text{NH}_3$ - $\text{O}_2$  mixtures at room temperature.

The adsorption of acrylic acid on thin and thick iron oxide surfaces and Au modified thin and thick iron oxide surfaces resulted in carboxylate formation and vinyl adsorption and desorption at 500 K as  $\text{CO}_2$  and ethylene. Au nanoparticles on the oxide did not enhance the acid reaction on the surface.

However, Au clusters on oxide films improve the surface reaction of small molecule such as  $\text{CO}_2$  and  $\text{NH}_3$ . The iron oxide film reacted with  $\text{CO}_2$  and  $\text{NH}_3$  reflecting the combination of basicity and acidity on the prepared iron oxide surface. The surface concentration of C and N species are not significant on iron oxide alone, while carbonate and N species formation ( $\text{NH}_3$ ,  $\text{NH}_2$  and  $\text{NH}$ ) are prominent on Au modified iron oxide films. Moreover,  $\text{NH}_3$  can react with the Au modified oxide surface again after it was regenerated.

From the STM results, the edges of the iron oxide islands and the top of Au nanoparticles are most reactive as their rims turn rough after adsorption.

Au modification of iron oxide enhances the reaction of  $\text{CO}_2$  and  $\text{NH}_3$  as intensities of C(1s) and N(1s) XP signals increase; however, the reactivity of the surface with both gases is small. Therefore, the prepared iron oxide  $\text{Fe}_3\text{O}_4$  surface (100) and (111) planes are not really reactive to small molecules e.g.  $\text{CO}_2$  and  $\text{NH}_3$  but they are more reactive to big molecules such as acrylic acid at room temperature. Studying the reactions at low temperature would be interesting.

**References:**

- [1] F. Bournel, C. Laffon, Ph. Parent and G. Tourillon, *Surf. Sci.* **350**(1996) 60.
- [2] W. Weiss, W. Ranke, *Progress in surface Science* **70** (2002) 1.
- [3] R. Pestman, A. van Duijne, J. A. Z. Pieterse, V. Ponec, *J. of Molecular Catalysis A : Chemical* **103** (1995) 175.
- [4] S. R. Leadley, J. F. Watts, *J. of Electron Spectroscopy and related Phenomena*, **85** (1997) 107.
- [5] Y. Joseph, M. Wühn, A. Niklewski, W. Ranke, W. Weiss, C. Wöll and R. Schlögl, *Phys. Chem. Chem. Phys.* **2** (2000) 5314.
- [6] Y. Joseph, W. Ranke and W. Weiss, *J. Phys. Chem. B*, **204** (2000) 3224.
- [7] K. T. Rim, J. P. Fitts, T. Müller, K. Adib. N. Camillone III, R. M. Osgood, S. A. Joyce, G. W. Flynn, *Surf. Sci.* **541** (2003) 59.
- [8] G. J. Hutchings, M. S. Hall, A. F. Carley, P. Landon, B. E. Solsona, C. J. Kiely, A. Herzing, M. Makkee, J. A. Moulijn, A. Overweg, J. C. Fierro-Gonzalez, J. Guzman, B. C. Gates, *J. of Catal.* **242** (2006) 71.
- [9] C. Lemire, R. Meyer, Sh. K. Shaikhutdinov, H. –J. Freund, *Surf. Sci.* **552** (2004) 27.
- [10] R. Meyer, D. Lahav, T. Schalow, M. Laurin, B. Brandt, S. Schauermaun, S. Guimond, T. Klüner, H. Kühlenbeck, J. Libuda, Sh. Shaikhutdinov, H.-J. Freund, *Surf. Sci.* **586** (2005) 174.
- [11] R. Pestman, A. van Duijne, J. A. Z. Pieterse, V. Ponec, *J. of Molecular Catalysis A : Chemical* **103** (1995) 175.
- [12] T. Yokoyama, N. Yamagata, *Applied Cat. A : General* **221** (2001) 227.
- [13] F. Bournel, C. Laffon, Ph. Parent and G. Tourillon, *Surf. Sci.* **350** (1996) 60.
- [14] <http://srdata.nist.gov/cccbdb/geom3.asp?method=13&basis=20>
- [15] H. –J. Freund and M. W. Roberts, *Surface Science Reports* **25** (1996) 225.
- [16] H. Kühlenbeck, C. Xu, B. Dilmann, M. Häfel, B. Adam, D. Ehrlich, S. Wohlrab, H.-J. Freund, U. A. Ditzinger, H. Heddermeyer, M. Neuber and M. Neumann, *Ber. Bunsenges, Phys. Chem.* **96** (1992) 15.
- [17] Y. Fukuda. Y. Tanabe, K. Bull. Chem. Soc. Jpn. **46** (1973) 1616.
- [18] H. Idriss, E. G. Seebauer, *Catal. Lett.* **66** (2000) 139.
- [19] A. F. Carley, A. Chambers, P. R. Davies, G. G. Mariotti, R. Kurian and M. W. Roberts, *Faraday Discuss* **105** (1996) 225.



- [20] R. G. Copperthwaite, P. R. Davies, M. A. Morris, M. W. Roberts and R. A. Ryder, *Catal. Lett.* **1** (1988) 11.
- [21] H. M. Ismail, D. A. Cadenhead, and M. I. Zaki, *J. of Colloid and Interface Science*, **194** (1997) 482.
- [22] A. F. Carley, P. R. Davies, K. R. HArikummar, R. V. Jones, G. U. Kullkarni and M. W. Roberts, *Topics in Catalysis* **14** No.1-4 (2001) 101.
- [23] A. C. M. van den Broek, J. van Grondelle, R. A. van Santen, *J. Catal.* **185** (1999) 297.
- [24] C. J. Weststrate, J. W. Bakker, E. D. L. Rienks, S. Lizzit, L. Petaccia, A. Baraldi, C. P. Vinod, B. E. Nieuwenhuys, *Phys. Chem. Chem. Phys.* **7** No. 13 (2005) 2629.

## Chapter 6

### Conclusion

As iron oxide is an important catalyst component in many applications and Au has been shown to enhance reactions of this oxide surface, the preparation of iron oxide and Au modified iron oxide surfaces were made and then the reactivity of the catalyst models were also studied. In the experiments, the iron oxide and Au modified iron oxide films were made on a Cu(100) substrate and their reactivity with acrylic acid, CO<sub>2</sub> and NH<sub>3</sub> studied. This Chapter will summarize the results and discussion from those experiments.

Fe was deposited on the Cu(100) substrate using an evaporator with a small flux of Fe evaporation resulting in layer and island growth mode (Stranski-Krastanov). A step height of the topmost island shows monatomic steps ~2 Å high. An Fe overlayer grew epitaxially on the substrate with 2 domains with a square unit cells of sides 2.55 Å and 3.61 Å signifying domains p(1×1) and c(2×2) on the substrate surface.

The oxide is prepared by oxidizing Fe multilayers at temperature 850 K using a high and low heating rate. A low heating rate gives a thick film (10-14 Å) while a high heating rate gives a thinner (3-5 Å) film. Both conditions give a well-ordered surface. However, the Cu substrate was not oxidized in this low-pressure/high-temperature oxidation treatment. Fe<sub>3</sub>O<sub>4</sub>(100) and (111) surfaces are identified by the chemical composition of the surface from XP spectra and LEED and STM images. Excellent long-range epitaxy, antiphase domain boundary strips and hexagonal superstructures were observed.

The Fe 2p<sub>3/2</sub> core level of the iron oxide film is 710.5 eV binding energy while O1s appears at 529.5 eV. The ratio Fe: O was about 0.74 - 0.78 from XPS data indicating Fe<sub>3</sub>O<sub>4</sub>. The spectra of Fe<sub>3</sub>O<sub>4</sub> are made complicated by the presence of two oxidation states (Fe<sup>2+</sup> and Fe<sup>3+</sup>) of Fe. The O 1s binding energy is fixed at 529.5 eV because the O 1s binding energy is in general not sensitive to the oxidation state of the

iron. The observed broad Fe 2p<sub>3/2</sub> peak (FWHM ~4.3 eV) of the prepared oxide also suggests Fe<sub>3</sub>O<sub>4</sub>.

Iron oxide having a complicated structure would produce additional spots compared with LEED pattern of the Fe multilayer. LEED structures of both hexagonal and square lattices were observed which is well-oriented relative to the Cu(100) substrate. Three possible diffraction structures corresponding to Cu(100) are: (1) real space structure Cu(100)-( $\sqrt{2} \times \sqrt{2}$ )R45 or Cu-(100)-  $\begin{bmatrix} 1 & -1 \\ 1 & 1 \end{bmatrix}$  with a square unit cell 3.61 Å, (2) real structure Cu(100)-c(4×2) or Cu-(100)-  $\begin{bmatrix} 2 & -1 \\ 2 & 1 \end{bmatrix}$  with a hexagonal unit cell 5.7 Å and (3) the real space structure Cu(100)-( $\sqrt{5} \times \sqrt{5}$ )R26.6° or Cu-(100)-  $\begin{bmatrix} 2 & 1 \\ -1 & 2 \end{bmatrix}$  with a square unit cell 5.1 Å. The nature of these domains could be exploded in a detailed LEED study of structure and Fe coverage.

STM images show domain boundary strips and hexagonal superstructures with the antiphase domain boundary strips of Fe<sub>3</sub>O<sub>4</sub>(100) underneath the hexagonal Fe<sub>3</sub>O<sub>4</sub>(111) structures. Strips might be formed in the first layer of oxide formation on Cu(100) surface and the next layer could be either strips or hexagonal structure. The pseudo-hexagonal superstructure has 50 Å hexagonal spacing with atomically flat ~5 Å high corresponding to Fe<sub>3</sub>O<sub>4</sub>(111) termination. Strips grown and aligned with the Cu(100) substrate structure with the size ca. 50 Å wide and 2.1 ± 0.2 Å high. More detailed studies of the structures of layers and their reactivities would be useful.

Au was deposited on the substrates to study the electronic, geometric and chemical properties. Au clusters were vapor-deposited on iron oxide Fe<sub>3</sub>O<sub>4</sub>, oxidized Cu and clean Cu surfaces. It was found that the clusters grow in a 3D mode (Stranski-Krastanov) on the oxidized substrate but in a layer-by-layer mode (Frank van der Merwe) on clean Cu. On iron oxide the Au nanoparticles have an average diameter of 30-50 Å and are ~10 Å high. Annealing experiments show that the Au clusters are stable in the system to at least 600 K and form well-defined hexagonal microcrystals. STS showed that the Au clusters on the oxide substrate have nonmetallic properties (0.5-1 V). The development of STS with concentration would be worth studying. The LEED patterns before and after depositing Au on iron oxide surface are the same.

The epitaxial Au films on Cu are strained because of lattice mismatch. Two domains of Au on Cu(100) surface: Cu-(1×1)-Au and c(2×2)-Au were observed. STM images show square Au islands with 2.75-3.0 Å high.

Iron oxide (Fe<sub>3</sub>O<sub>4</sub>) and Au modified iron oxide surfaces were used for studies of the chemistry of acrylic acid, CO<sub>2</sub>-rich CO<sub>2</sub>-O<sub>2</sub> mixtures and NH<sub>3</sub>-rich NH<sub>3</sub>-O<sub>2</sub> mixtures at room temperature. The adsorption of acrylic acid on thin and thick iron oxide surfaces and Au modified thin and thick iron oxide surfaces resulted in carboxylate formation and vinyl adsorption together with the desorption of CO<sub>2</sub> and ethylene at 500 K. Au nanoparticles on the oxide did not enhance the acid reaction on the surface.

However, Au clusters on oxide films increased the surface reaction of small molecules such as CO<sub>2</sub> (acid) and NH<sub>3</sub> (base). STM results show the edges of the iron oxide islands and the top of Au nanoparticles are more reactive as their rims turn “uneven” after adsorption. Carbonate is a main product of reaction of Au modified iron oxide with CO<sub>2</sub> whereas for NH<sub>3</sub>, NH<sub>2</sub> and NH compounds are adsorbed on those modified oxide surfaces. N<sub>2</sub> and H<sub>2</sub>O could be the main desorption products but these were not measured directly. Moreover, exposure of the regenerated Au modified iron oxide surface could react to NH<sub>3</sub> as shown by an increase in N(1s) signal intensity at the same binding energy. Therefore, N compounds could react on the regenerated oxide catalyst surface but CO<sub>2</sub> could not. STM images also show a reduction of the height of Au nanoparticles height after reaction and annealing.

For future work a study of the reactivity of oxide and Au modified iron oxide at low temperatures might aid surface science characterization. Also, as Au nanoparticles are relatively high, a study of the reactivity of those nanoparticles with a macromolecule (bulky molecular structure) will be able to provide more clues to the mechanisms and the reaction on the nanoparticles surfaces.

